

IMAGING AND VELOCITY ANALYSIS BY TARGET-ORIENTED
WAVEFIELD INVERSION

A DISSERTATION
SUBMITTED TO THE DEPARTMENT OF GEOPHYSICS
AND THE COMMITTEE ON GRADUATE STUDIES
OF STANFORD UNIVERSITY
IN PARTIAL FULFILLMENT OF THE REQUIREMENTS
FOR THE DEGREE OF
DOCTOR OF PHILOSOPHY

Yaxun Tang
July 2011

© Copyright by Yaxun Tang 2011
All Rights Reserved

I certify that I have read this dissertation and that, in my opinion, it is fully adequate in scope and quality as a dissertation for the degree of Doctor of Philosophy.

(Biondo L. Biondi) Principal Adviser

I certify that I have read this dissertation and that, in my opinion, it is fully adequate in scope and quality as a dissertation for the degree of Doctor of Philosophy.

(Jon F. Claerbout)

I certify that I have read this dissertation and that, in my opinion, it is fully adequate in scope and quality as a dissertation for the degree of Doctor of Philosophy.

(Jerry Harris)

Approved for the University Committee on Graduate Studies

Abstract

This thesis develops a novel target-oriented inversion framework that uses wavefields as carriers of information to image both low- and high-wavenumber components of the earth model in complex geological settings, such as subsalt regions. The low-wavenumber component of the earth model is often known as background velocity, whereas the high-wavenumber component of the earth model is often known as reflectivity. I address the problem of reflectivity imaging with *target-oriented wavefield least-squares migration*, and the problem of velocity estimation with *target-oriented wavefield tomography*.

Reflectivity images of the subsurface are commonly produced by prestack depth migration. When the overburden is complex and the reflectors are unevenly or insufficiently illuminated, the migration operator alone is inadequate to provide an optimal image.

I tackle the problem of distorted illumination in reflectivity imaging by wavefield least-squares migration. I formulate least-squares migration in the image domain and solve it in a target-oriented fashion. In the image-domain formulation, explicit computation of the Hessian operator (the resolution function that measures the illumination deficiency of the imaging system) is the most important and challenging step. I develop a novel method based on phase encoding to efficiently and accurately compute the target-oriented Hessian operator. By design, the phase-encoded Hessian converges to the exact Hessian either deterministically (for plane-wave phase encoding) or statistically (for random phase encoding), while having the important advantages that no Green's functions need to be stored during computation and that

the number of wavefield propagations is also drastically reduced. The target-oriented Hessian operator is then used to recover the reflectivity by iterative inverse filtering. I regularize the inversion with dip constraints, which naturally incorporate interpreted geological information into the inversion.

Accurate imaging of the reflectivity also requires an accurate background velocity model. High-quality velocity model-building in complex geology requires wavefield-based velocity analysis to properly model band-limited wave phenomena. However, the high cost and lack of flexibility of target-oriented model-building prevent this method from being widely used in practice.

I overcome the cost and flexibility issues of wavefield-based migration velocity analysis by developing target-oriented wavefield tomography. Target-oriented wavefield tomography is achieved by synthesizing a new data set specifically for velocity analysis. The new data set is generated based on an initial unfocused target image and by a novel application of generalized Born wavefield modeling, which correctly preserves velocity kinematics by modeling both zero and non-zero subsurface-offset-domain images. The new data set can be synthesized for a chosen target region with velocity inaccuracies. The reduced data size and computation domain, therefore, greatly improve the efficiency and flexibility of wavefield tomography, allowing fast and interpretation-driven interactive wavefield-based velocity analysis, where different geological scenarios or hypotheses can be tested in quasi-real time.

The proposed target-oriented inversion framework successfully estimates subsalt velocities and recovers subsalt reflectivities from distorted illumination from 2-D synthetic and 3-D field data.

Preface

The electronic version of this report¹ makes the included programs and applications available to the reader. The markings **ER**, **CR**, and **NR** are promises by the author about the reproducibility of each figure result. Reproducibility is a way of organizing computational research that allows both the author and the reader of a publication to verify the reported results. Reproducibility facilitates the transfer of knowledge within SEP and between SEP and its sponsors.

ER denotes Easily Reproducible and are the results of processing described in the paper. The author claims that you can reproduce such a figure from the programs, parameters, and makefiles included in the electronic document. The data must either be included in the electronic distribution, be easily available to all researchers (e.g., SEG-EAGE data sets), or be available in the SEP data library². We assume you have a UNIX workstation with Fortran, Fortran90, C, X-Windows system and the software downloadable from our website (SEP makerules, SEPScons, SEPlib, and the SEP latex package), or other free software such as SU. Before the publication of the electronic document, someone other than the author tests the author's claim by destroying and rebuilding all ER figures. Some ER figures may not be reproducible by outsiders because they depend on data sets that are too large to distribute, or data that we do not have permission to redistribute but are in the SEP data library, or that the rules depend on commercial packages such as Matlab or Mathematica.

¹<http://sepwww.stanford.edu/private/docs/sep144>

²<http://sepwww.stanford.edu/public/docs/sepdata/lib/toc.html>

CR denotes Conditional Reproducibility. The author certifies that the commands are in place to reproduce the figure if certain resources are available. The primary reasons for the CR designation is that the processing requires 20 minutes or more.

NR denotes Non-Reproducible figures. SEP discourages authors from flagging their figures as NR except for figures that are used solely for motivation, comparison, or illustration of the theory, such as: artist drawings, scannings, or figures taken from SEP reports not by the authors or from non-SEP publications.

Our testing is currently limited to LINUX 2.6 (using the Intel Fortran90 compiler) and the SEPlib-6.4.6 distribution, but the code should be portable to other architectures. Reader's suggestions are welcome. For more information on reproducing SEP's electronic documents, please visit <http://sepwww.stanford.edu/research/redoc/>.

Acknowledgments

It has been a long journey for me to finish this thesis. When I look back, I realize that it would be impossible for me to accomplish this work without the valuable help from others.

I am grateful to Biondo Biondi, my adviser, for his guidance and constant encouragement throughout the past six years. I appreciate him for giving me the complete research freedom, allowing me to explore at will in the uncharted research territory. I also thank him for his patience and always being available for discussion. I am grateful to Jon Claerbout for his insights in geophysical inverse problems. I admire his wisdom, passion and energy for geophysics. Jon made me realize that great ideas should be ideas with practical values. Bob Clapp has always been a great source of help whenever I encountered problems. I have benefited a lot from his rich knowledge in geophysical computing, which turned out to be quite helpful when I was dealing with 3-D field data. I thank my thesis committee member Jerry Harris for his valuable and constructive suggestions to my thesis. I also thank Tapan Mukerji for chairing my defense.

My journey to Stanford would have not been possible without the encouragement from my previous advisers, Huazhong Wang and Zaitian Ma from Tongji University, and Guanquan Zhang from Chinese Academy of Sciences. Unfortunately, Professor Ma passed away on June 5, 2011. Nevertheless, he will always live in my memory, and I wish him rest in peace.

The majority of the time that I spent at SEP was with my fellow students, both

senior and junior to me. I always consider Guojian Shan to be my SEP mentor. I would like to thank him for helping me adapt to the SEP environment and being a very close friend. I have found myself fortunate to share offices with many SEPs. The most influential ones are Alejandro Valenciano, Claudio Guerra, Sjoerd de Ridder and Yang Zhang, off whom, I have bounced many interesting ideas. Gboyega Ayeni is also a good source of discussion on inverse problems. As a system administrator at SEP, I know how difficult and time-consuming it is to maintain our computers. I thank Bill Curry, our previous system administrator, for his hard work, and Ohad Barak, our current system administrator, for his kindness in taking over all my computer duties so that I can concentrate on finishing my thesis. I also thank the many students who arrived before and after me, in particular, Jesse Lomask, Daniel Rosales, Brad Artman, Gabriel Alvarez, Jeff Shragge, Madhav Vyas, Pierre Jouselin, Ben Witten, Roland Gunther, Xukai Shen, Adam Halpert, Abdullah Al Theyab, Mohammad Maysami, Yunyue Li, Mandy Wong, Nader Moussa, Ali Almomin, Chris Leader, Kittinat Taweestananon, Yi Shen and Qiang Fu for being great friends, sharing ideas and discussing about geophysics and the world at large.

Diane Lau deserves special credit for her continuous effort to smoothly run SEP, which makes our lives as students much easier. I also thank Dawn Burges for carefully proofreading my thesis draft.

Finally, I would like to thank my parents and my parents-in-law for their encouragement and moral support. I cannot say enough how much I thank my wife, Huawei Chen. I thank her for having the strength and courage to stick with me through this long journey and for supporting me through thick and thin all these years. Without her love, patience and understanding, I simply cannot finish this Ph.D. degree.

Contents

Abstract	v
Preface	vii
Acknowledgments	ix
1 Introduction	1
2 Target-oriented wavefield least-squares migration	15
3 Target-oriented wavefield tomography	57
4 3-D field-data examples	99
5 Conclusions	175
A Convergence property of plane-wave phase encoding	179
B Convergence property of random phase encoding	182
C Wave-equation tomographic operator	186

D	3-D conical-wave migration	196
E	Seismic visibility analysis	199

List of Tables

2.1	Cost comparison for a marine acquisition geometry.	31
2.2	Cost comparison for an OBS or a land acquisition geometry.	32
4.1	The spacings of B-spline nodes for different iterations.	118

List of Figures

1.1	An example based on the Sigsbee2A model illustrating the challenges for imaging subsalt reflectivity. Panel (a) is the subsurface illumination, and panel (b) is the image obtained using a conventional imaging technique. [CR]	4
1.2	The resolution functions (a.k.a. the point spread functions) for the Sigsbee2A example. Panels (a) and (b) are resolution functions for image points A and B, respectively, as shown in Figure 1.1(a). In each panel, the left plot shows the space-domain resolution function, while the right plot shows its amplitude spectrum in the Fourier domain. [CR]	5
1.3	Comparison between rays and wavefields. Panel (a) shows a snapshot of the rays overlaid by the Sigsbee2A velocity model, (b) shows a snapshot of the wavefields. [ER]	6
1.4	Velocity sensitivity kernel for the Sigsbee2A model at a frequency of 7 Hz. Panels (a) and (b) are the real and imaginary parts of the kernel, respectively. [ER]	7
1.5	Velocity sensitivity kernel for the Sigsbee2A model at a frequency of 20 Hz. Panels (a) and (b) are the real and imaginary parts of the kernel, respectively. [ER]	7

1.6	A simple cartoon illustrating different types of scattered waves due to the anomaly in the center. Waves A and D that transmit through the anomaly are forward scatterings. Waves B and C that are reflected by the anomaly are backward scatterings. [NR]	9
1.7	The wavenumber spectrum resolved by (a) the backward scatterings and (b) the forward scatterings. The results are obtained using a single frequency, assuming that there is infinite surface acquisition and that all waves transmitting through the anomaly can be recorded by receivers on the surface. Under these assumptions, the maximum incident and scattered angles can reach $\pm 90^\circ$ with respect to vertical, which is the ideal case for surface seismic. [CR]	10
1.8	The wavenumber spectrum resolved by (a) the backward scatterings and (b) the forward scatterings. The results are obtained using a single frequency and limiting the maximum incident and scattered angles to $\pm 45^\circ$ with respect to vertical, which represents a more realistic situation for surface seismic. [CR]	10
1.9	The wavenumber spectrum resolved by (a) the backward scatterings and (b) the forward scatterings. The results are obtained using three frequencies and limiting the maximum incident and scattered angles to $\pm 45^\circ$ with respect to vertical. Blue, green and red colors denote low, middle and high frequencies, respectively. [CR]	11
2.1	Diagonal of the Hessian for a constant-velocity model with one shot and two receivers. (a) The exact diagonal of the Hessian (equation 2.7); (b) the Hessian contaminated by crosstalk (equation 2.8 with $\alpha(\mathbf{x}_r, \mathbf{p}_r, \omega) = 1$); (c) the receiver-side plane-wave phase-encoded Hessian; (d), (e) and (f) are the receiver-side randomly phase-encoded Hessians obtained with 1, 5 and 20 random realizations, respectively. [CR]	35

2.2	The local Hessian operator for image point $x = 0.5$ km, $z = 1.5$ km (a row of the Hessian matrix). The acquisition geometry is the same as that in Figure 2.1. The size of the Hessian operator is 81 samples in both x and z directions. (a) The exact Hessian; (b) The Hessian contaminated by crosstalk; (c) the receiver-side plane-wave phase-encoded Hessian; (d), (e) and (f) are the receiver-side randomly phase-encoded Hessian obtained with 1, 5 and 20 random realizations, respectively. [CR]	36
2.3	Diagonal of the Hessian for a constant-velocity model with one shot and 401 receivers. (a) The exact diagonal of the Hessian; (b) the Hessian contaminated by crosstalk; (c) the receiver-side plane-wave phase-encoded Hessian; (d), (e) and (f) are the receiver-side randomly phase-encoded Hessians obtained with 1, 5 and 20 random realizations, respectively. [CR]	38
2.4	The local Hessian operator for image point $x = 0.5$ km, $z = 1.5$ km. The acquisition geometry is the same as that in Figure 2.3. (a) The exact Hessian; (b) The Hessian contaminated by crosstalk; (c) the receiver-side plane-wave phase-encoded Hessian; (d), (e) and (f) are the receiver-side randomly phase-encoded Hessian obtained with 1, 5 and 20 random realizations, respectively. [CR]	39
2.5	Diagonal of the Hessian with 401 shots and 401 receivers. (a) The exact diagonal of the Hessian; (b) the receiver-side randomly phase encoded Hessian with only one random realization. [CR]	40
2.6	The local Hessian operator for image point at $x = 0.5$ km and $z = 1.5$ km. (a) The exact diagonal of the Hessian; (b) the receiver-side randomly phase encoded Hessian with only one random realization. [CR]	40
2.7	Sigsbee2A stratigraphic velocity model. [ER]	42

2.8	Diagonal of the Hessian for the Sigsbee2A model. The Hessian is obtained by using receiver-side random-phase encoding, which takes the limited receiver array into consideration. The result shows the Hessian for a frequency band from 5 Hz to 35 Hz. [CR]	43
2.9	Source-wavefield intensity for the Sigsbee2A model, which assumes the receiver-side Green's functions to be constant; it ignores the effects of the limited receiver aperture and over-estimates the total energy that enters the earth and returns to be recorded by the receivers. [CR]	44
2.10	Conventional one-way wave-equation shot-profile migration result of the Sigsbee2A model. Note the uneven illumination below the salt. [CR]	46
2.11	The migrated image (Figure 2.10) is normalized by the diagonal of the Hessian shown in Figure 2.8. [CR]	47
2.12	The migrated image (Figure 2.10) is normalized by the source-wavefield intensity shown in Figure 2.9. [CR]	48
2.13	Receiver-side randomly phase-encoded Hessian operators for the Sigsbee2A model. Panel (a) shows the diagonal part for a particular region of interest under the salt. Note the uneven illumination due the complex salt body and limited acquisition geometry. Panel (b) shows the result obtained by convolving the Hessian operator (with a size 21×21) with a collection of point scatterers. Note the non-stationarities of the operators. [CR]	50
2.14	Comparison between migration and inversion. Panel (a) shows the migrated result, (b) shows the inversion result using the receiver-side randomly phase-encoded Hessian operator, and (c) is the filtered true reflectivity. All three panels are plotted with the same scale. [CR]	51
2.15	Normalized residual vs. number of iterations for the Sigsbee2A model; the inversion converges after about 12 iterations. [CR]	52

2.16	A close-up view of (a) the migrated image, (b) the inverted image and (c) the filtered true reflectivity model. [CR]	52
2.17	The amplitude spectrum of (a) the migrated image (Figure 2.16(a)) and (b) the inverted image (Figure 2.16(b)). Note the inverted image contains a broader range of spatial frequencies. [CR]	53
2.18	A horizontal trace at depth 5.2 km extracted from images shown in Figure 2.16. The dotted line, solid line and dashed line represent traces extracted from the true reflectivity model, the migrated image and the inverted image, respectively. [CR]	53
3.1	Flow diagrams of seismic data mapping. [NR]	62
3.2	Initial images used for Born modeling. Panel (a) is the image cube with the third dimension being the subsurface offset, and (b) is the zero-subsurface-offset image. [ER]	68
3.3	Comparison among (a) the original data set, (b) the new data set modeled using SODCIGs and (c) the new data set modeled using only zero-subsurface-offset image. [ER]	68
3.4	The extracted SODCIGs obtained using (a) the original data set, (b) the data set modeled using generalized Born modeling and (c) the data set modeled using conventional Born modeling. The three data sets are migrated using a velocity 15% slower than the true velocity. [ER]	69
3.5	The extracted SODCIGs obtained using (a) the original data set, (b) the data set modeled using generalized Born modeling and (c) the data set modeled using conventional Born modeling. The three data sets are migrated using the true velocity. [ER]	69
3.6	The true migration velocity of the Sigsbee2A model. [ER]	73
3.7	The initial velocity model for the Sigsbee2A example. The black box outlined area is the target region for velocity analysis. [ER]	73

3.8	The zero-subsurface-offset image (top) and SODCIGs (bottom) for the target region, obtained by using the original data set and the initial velocity model. The SODCIGs are located at CMP location 7.62, 9.14, 10.67, 12.19, 13.72, 15.24, 16.76, 18.29 km, from left to right. [CR]	74
3.9	The diagonal of the Hessian computed using the initial velocity model and the original acquisition geometry. View descriptions are the same as in Figure 3.8. [CR]	75
3.10	The initial target image and SODCIGs normalized by the diagonal of the Hessian shown in Figure 3.9. View descriptions are the same as in Figure 3.8. [CR]	76
3.11	The target image and SODCIGs obtained by using the new data set (31 planewave-source gathers) and the initial velocity model. View descriptions are the same as in Figure 3.8. [CR]	78
3.12	ADCIGs obtained using (a) the original data set and (b) the new data set. They are located at the same CMP location as the SODCIGs shown in Figure 3.8. [CR]	79
3.13	The initial velocity model for the target region (a), the inverted velocity model (b), and the true velocity model (c). [CR]	80
3.14	Panel (a) shows the ratio between the inverted velocity and the initial velocity, whereas panel (b) shows the ratio between the true velocity and the initial velocity. Notice the similarity of the estimated velocity anomaly to the one I introduced in the initial model. [CR]	81
3.15	Zero-subsurface-offset image and SODCIGs obtained using the inverted velocity model and the original data set. View descriptions are the same as in Figure 3.8. [CR]	82
3.16	Zero-subsurface-offset image and SODCIGs obtained using the true velocity model and the original data set. View descriptions are the same as in Figure 3.8. [CR]	83

3.17	ADCIGs obtained using (a) the initial velocity model, (b) the inverted velocity model and (c) the true velocity model. The ADCIGs are located at CMP location 7.62, 9.14, 10.67, 12.19, 13.72, 15.24, 16.76, 18.29 km, respectively. [CR]	84
3.18	The initial velocity model for the selected 2-D line of the GOM data set. The area inside the black box is the target region for velocity analysis. Velocities outside the region are assumed to be accurate. [ER]	85
3.19	The zero-subsurface-offset image (top) and SODCIGs (bottom) obtained using the original data set and the initial velocity model. The SODCIGs are extracted at CMP locations 2.21, 3.74, 5.27, 6.79, 8.31, 9.84, 11.36, 12.89, 14.41 km, from left to right. The minimum and maximum subsurface offsets in the bottom panel are -0.75 km and 0.75 km, respectively. [CR]	86
3.20	The diagonal of Hessian computed using the initial velocity model and the original acquisition geometry. View descriptions are the same as in Figure 3.19. [CR]	87
3.21	The initial target image and SODCIGs normalized by the diagonal of Hessian shown in Figure 3.20. View descriptions are the same as in Figure 3.19. [CR]	89
3.22	The target image and SODCIGs obtained by using the new data set and the initial velocity model. View descriptions are the same as in Figure 3.19. [CR]	90
3.23	The inverted velocity model after 30 nonlinear iterations. [CR] . . .	91
3.24	Zero-subsurface-offset images obtained using (a) the initial velocity model and (b) the inverted velocity model. The original data set is used for migration. [CR]	92

3.25	A close-up view of the upper section in Figure 3.24. Panels (a) and (b) are obtained using the initial and inverted velocity model, respectively. [CR]	93
3.26	A close-up view of the lower section in Figure 3.24. Panels (a) and (b) are obtained using the initial and inverted velocity model, respectively. [CR]	94
3.27	SODCIGs obtained using (a) the initial velocity model and (b) the inverted velocity model. The original data set is used for migration. The SODCIGs are extracted at the same CMP locations as those shown in Figure 3.19. [CR]	95
3.28	ADCIGs obtained using (a) the initial velocity model and (b) the inverted velocity model. The original data set is used for migration. The ADCIGs are extracted at the same CMP locations as those shown in Figure 3.27. [CR]	96
3.29	The amplitude spectrum of the prestack resolution functions (the Fourier transform of one row of the Hessian operator) at image point $x = 12.68$ km, $z = 5.49$ km for the Sigsbee2A model. Panel (a) is obtained using the original acquisition geometry, and (b) using the new acquisition geometry. Both resolution functions are computed using the velocity model shown in Figure 3.7. [CR]	97
4.1	One typical shot gather for the GOM data set. The shot gather has only inline offset due to narrow azimuth acquisition and AMO transform. [CR]	107
4.2	The initial 3-D velocity model. The area inside the black box is the target region for velocity analysis. Velocities above the target region and the salt interpretation are known to be accurate. [ER]	108
4.3	The zero-subsurface-offset image for the target region, obtained by migrating the original data set using the initial velocity model. [CR]	110

4.4	The 3-D SODCIGs obtained using the original data set and the initial velocity model. Panels (a), (b) and (c) are extracted at (3.04, 1.34) km, (6.09, 2.86) km and (9.13, 4.38) km, from left to right. [CR]	111
4.5	The diagonal components of the Hessian matrix for the target region obtained using the initial velocity model. Hot colors denote high illumination, whereas cold colors denote low illumination. [CR]	112
4.6	The subsurface-offset-domain illumination gathers. They are extracted at the same locations as those in Figure 4.4. [CR]	112
4.7	The zero-subsurface-offset image after illumination compensation. Compare the figure with Figure 4.3. [CR]	113
4.8	The 3-D SODCIGs after illumination compensation. Compare the figure with Figure 4.4. [CR]	113
4.9	The initial zero-subsurface-offset image after muting the events in the salt body. The muted image and gathers are used for the generalized Born wavefield modeling. [CR]	114
4.10	The average source visibility (data-domain illumination) for the target region using 3-D plane-wave acquisition geometry for the Born wavefield modeling. Note that most of the energy contributing to the target region falls within the range where $\tilde{p}_{s_x} \in (-213, 213)$, and $\tilde{p}_{s_y} \in (-180, 180)$. [CR]	115
4.11	The synthesized 3-D plane-wave data. Panel (a) is the plane-wave source function with both incident dip and azimuth angles equal 10° at the top of the target region shown in Figure 4.2, and (b) is the corresponding plane-wave gather collected also at the top of the target region. [CR]	116
4.12	The zero-subsurface-offset image obtained using the synthesized Born data set. Compare the figure with Figure 4.9. [CR]	117

4.13	The 3-D SODCIGs obtained using the synthesized Born data set and the initial velocity model. Panels are extracted at (a) inline 3.04 km, crossline 1.34 km, (b) inline 6.09 km, crossline 2.86 km and (c) inline 9.13 km, crossline 4.38 km. Compare the figure with Figure 4.8. [CR]	118
4.14	The mask operator applied to the gradient to prevent updating velocities inside the salt. [ER]	119
4.15	The normalized gradient at iteration one (a) before and (b) after applying the smoothing and mask operators. [CR]	120
4.16	The normalized gradient at iteration 11 (a) before and (b) after applying the smoothing and mask operators. [CR]	121
4.17	The normalized gradient at iteration 21 (a) before and (b) after applying the smoothing and mask operators. [CR]	122
4.18	The normalized gradient at iteration 31 (a) before and (b) after applying the smoothing and mask operators. [CR]	123
4.19	The evolution of the objective function over the first 40 DSO iterations. The objective function values have been normalized to 1. [CR]	124
4.20	Step length versus the number of iterations. The initial step length is about 20 m/s. [CR]	124
4.21	The inverted velocity model in the target region after (a) 10 iterations, (b) 20 iterations, (c) 30 iterations and (d) 40 iterations. [CR]	125
4.22	The final velocity model after merging the inverted velocity model in the target region (Figure 4.21(d)) with the velocity model above the target. [CR]	126
4.23	The zero-subsurface-offset image obtained using the synthesized Born data set and the updated velocity model. [CR]	127

4.24	Comparison between the inline SODCIGs (a) before and (b) after updating the velocity. The results are obtained by migrating the synthesized Born data set. [CR]	128
4.25	The zero-subsurface-offset image obtained by using the original data set and the updated velocity model. [CR]	129
4.26	The diagonal components of the Hessian matrix obtained using the updated velocity model. [CR]	130
4.27	Comparison between the zero-subsurface-offset image (a) before and (b) after updating the velocities. Both results are obtained using the original surface-recorded data set. In both panels, the crosshair is taken at inline 11.55 km, crossline 1.00 km and relative depth 4.94 km. [CR]	131
4.28	Comparison between the zero-subsurface-offset image (a) before and (b) after updating the velocities. Both results are obtained using the original surface-recorded data set. In both panels, the crosshair is taken at inline 7.55 km, crossline 3.70 km and relative depth 4.57 km. [CR]	132
4.29	Comparison between the zero-subsurface-offset image (a) before and (b) after updating the velocities. Both results are obtained using the original surface-recorded data set. In both panels, the crosshair is taken as inline 5.35 km, crossline 4.40 km and relative depth 1.46 km. [CR]	133
4.30	Comparisons between SODCIGs (a) before and (b) after updating the velocities. Both results are obtained using the original surface-recorded data set. All of the SODCIGs are extracted at the same crossline (1.00 km), but at inlines 1.52, 3.05, 4.57, 6.10, 7.62, 9.14 and 10.67 km, from left to right. [CR]	134

4.31	Comparisons between SODCIGs (a) before and (b) after updating the velocities. Both results are obtained using the original surface-recorded data set. All of the SODCIGs are extracted at the same crossline (3.70 km), but at inlines 1.52, 3.05, 4.57, 6.10, 7.62, 9.14 and 10.67 km, from left to right. [CR]	135
4.32	Comparisons between SODCIGs (a) before and (b) after updating the velocities. Both results are obtained using the original surface recorded data set. All of the SODCIGs are extracted at the same crossline (4.40 km), but at inlines 1.52, 3.05, 4.57, 6.10, 7.62, 9.14 and 10.67 km, from left to right. [CR]	136
4.33	Comparisons between ADCIGs (a) before and (b) after updating the velocities. Both results are obtained using the original surface-recorded data set. All of the ADCIGs are extracted at the same crossline (1.00 km), but at inlines 1.52, 3.05, 4.57, 6.10, 7.62, 9.14 and 10.67 km, from left to right. [CR]	137
4.34	Comparisons between ADCIGs (a) before and (b) after updating the velocities. Both results are obtained using the original surface-recorded data set. All of the ADCIGs are extracted at the same crossline (3.70 km), but at inlines 1.52, 3.05, 4.57, 6.10, 7.62, 9.14 and 10.67 km, from left to right. [CR]	138
4.35	Comparisons between ADCIGs (a) before and (b) after updating the velocities. Both results are obtained using the original surface recorded data set. All of the ADCIGs are extracted at the same crossline (4.40 km), but at inlines 1.52, 3.05, 4.57, 6.10, 7.62, 9.14 and 10.67 km, from left to right. [CR]	139
4.36	Target area selected (outlined by a box) for wavefield least-squares migration. [CR]	140
4.37	Migrated image for the selected target region. [CR]	141

4.38	The Hessian matrix for the target region. The top panel shows the diagonal components of the matrix; the bottom left panel shows one row of the matrix taken from the image point at inline 7.45 km, crossline 2.50 km and relative depth 0.30 km (the intersection of the crosshairs in the top panel); the bottom right panel shows the amplitude spectrum of the bottom left panel. [CR]	143
4.39	The Hessian matrix for the target region. The top panel shows the diagonal components of the matrix; the bottom left panel shows one row of the matrix taken from the image point at inline 8.65 km, crossline 1.60 km and relative depth 0.80 km (the intersection of the crosshairs in the top panel); the bottom right panel shows the amplitude spectrum of the bottom left panel. [CR]	144
4.40	Hessian filter response for point scatterers. Panels (a) and (b) show different slices of the same 3-D cube. Note the nonstationarities of the filters. [CR]	145
4.41	Hessian filter response for horizontal reflectors. Panels (a) and (b) show different slices of the same 3-D cube. Note the imprint of shadow zones on the reflectors. [CR]	146
4.42	Inversion without any regularization for the horizontal-reflector model. Panels (a) and (b) show two different slices of the same 3-D cube. [CR]	150
4.43	Inversion preconditioned by dip filters that smooth horizontally. Panels (a) and (b) show two different slices of the same 3-D cube. [CR] . . .	151
4.44	Inversion preconditioned by dip filters that smooth along a plane dipping -30° inline and 30° crossline. Panels (a) and (b) show two different slices of the same 3-D cube. [CR]	152
4.45	A mask operator used during inversion. [ER]	153

4.46	The migrated image of the 3-D GOM data set. Panels (a) and (b) show different slices of the same 3-D cube. The image has been masked using the mask operator shown in Figure 4.45 to focus on comparing sediment reflectivities. [CR]	154
4.47	The inverted image without applying any regularization. Panels (a) and (b) show different slices of the same 3-D cube. [CR]	155
4.48	The inverted image with a damping regularization ($\varepsilon = 0.02$). Panels (a) and (b) show different slices of the same 3-D cube. [CR]	156
4.49	The inverted image with a damping regularization ($\varepsilon = 0.05$). Panels (a) and (b) show different slices of the same 3-D cube. [CR]	157
4.50	Interpreted horizons from the migrated image. The horizons are then used to build the dip field for dip filtering. [CR]	158
4.51	The estimated dip field from the interpreted reflectors. Panels (a) and (b) are the slopes in the inline and crossline directions, respectively. [CR]	159
4.52	The impulse responses of dip filters with weak smoothing. [CR] . . .	160
4.53	The impulse responses of dip filters with moderate smoothing. [CR] .	160
4.54	The impulse responses of dip filters with strong smoothing. [CR] . .	161
4.55	The inverted image when preconditioned using dip filters with weak smoothing (Figure 4.52). Panels (a) and (b) show different slices of the same 3-D cube. [CR]	162
4.56	The inverted image when preconditioned using dip filters with moderate smoothing (Figure 4.53). Panels (a) and (b) show different slices of the same 3-D cube. [CR]	163
4.57	The inverted image when preconditioned using dip filters with strong smoothing (Figure 4.54). Panels (a) and (b) show different slices of the same 3-D cube. [CR]	164

4.58	The image residual ($\mathbf{H}\mathbf{m} - \mathbf{m}_{\text{mig}}$) at the last iteration for different methods. Panel (a) is obtained using inversion without regularization. Panels (b) and (c) are obtained using inversion regularized by a damping term with $\varepsilon = 0.02$ and $\varepsilon = 0.05$, respectively. Panels (d), (e) and (f) are obtained using inversion preconditioned with weak, moderate and strong dip filtering, respectively. All panels are clipped to the same value. Symbol “S” denotes coherent signal, whereas “N” denotes coherent noise. [CR]	167
4.59	Evolution of the image misfit ($\frac{1}{2} \mathbf{H}\mathbf{m} - \mathbf{m}_{\text{mig}} ^2$) for different inversion methods. [CR]	168
4.60	The migrated image (Figure 4.46) after applying AGC. Panels (a) and (b) show different slices of the same 3-D cube. [CR]	169
4.61	The migrated image (Figure 4.46) after applying both weak dip filtering and AGC. Panels (a) and (b) show different slices of the same 3-D cube. [CR]	170
4.62	The inverted image with damping regularization (Figure 4.48) after applying AGC. Panels (a) and (b) show different slices of the same 3-D cube. [CR]	171
4.63	The inverted image with weak dip preconditioning (Figure 4.55) after applying AGC. Panels (a) and (b) show different slices of the same 3-D cube. [CR]	172

Chapter 1

Introduction

Accurate 3-D images of the earth’s subsurface obtained from seismic data are crucial to the success of petroleum reservoir exploration. Because the majority of the “easy oil”—i.e. nearer to surface, in simple geological settings—is currently being produced, future reservoir discoveries will be located increasingly in frontier areas characterized by more complex geology, such as deep water and subsalt regions. Accordingly, the search for new hydrocarbon reserves continuously motivates the development of 3-D seismic imaging techniques able to better image complex subsurface structures. This thesis presents a step toward improving the seismic images obtained in complex geologies, with greater accuracy, efficiency and flexibility than conventional methods.

CHALLENGES OF IMAGING COMPLEX GEOLOGIES

Seismic imaging is an inverse problem that uses seismic data acquired from the surface to infer geological information in the subsurface. In general, seismic imaging requires two main elements: velocity estimation and reflectivity imaging. The former estimates the low-wavenumber component of the earth model (background velocity), while the latter estimates the high-wavenumber component of the earth model (reflectivity). Decoupling the low- and high-wavenumber components is justified because seismic data are insensitive to the middle-wavenumber component of the earth model

(Claerbout, 1985; Jannane et al., 1989). Therefore, each component can be estimated more or less independently. In areas where the overburden is complex, as exemplified by targets below salt bodies, recovering both components of the earth model can be a very challenging seismic imaging problem.

There are two main challenges inherent in subsalt imaging: poor subsalt illumination and difficulties in estimating subsalt velocities. Poor subsalt illumination is largely due to the fact that the salt velocity is usually twice as fast as the surrounding sediment velocity. That characteristic, combined with the complexity of the salt shape, especially the rugosity of the top and base of the salt, prevents seismic energy from penetrating the salt itself. Limited surface acquisition geometry can also reduce subsalt illumination. For example, in the standard marine-streamer acquisition system, only narrow-azimuth data with limited offsets are acquired; this significantly reduces the angular coverage for subsalt targets. Recently developed multi-azimuth, rich-azimuth and wide-azimuth acquisition systems (Michell et al., 2006; Keggin et al., 2006; Howard and Moldoveanu, 2006) can significantly improve subsalt illumination by providing a much richer data-coverage in azimuth. However, these acquisition methods still use cables with a limited length, and crossline sampling may still be coarse because of various economical and logistical reasons. As a result, illumination holes and aliasing may still occur when the overburden is complex. Figure 1.1(a) shows a subsalt illumination map for a typical marine acquisition experiment on the Sigsbee2A model (Paffenholz et al., 2002), where the subsalt illumination is greatly distorted by the salt body.

The distorted illumination, if not properly corrected, has a blurring effect on the reflectivity image. The distortion can be quantitatively measured by the resolution function (or point-spread function) of the imaging system (Lecomte and Gelius, 1998; Gelius et al., 2002; Valenciano, 2008), which is highly non-stationary, and which has a shape that depends on the subsurface illumination. The non-stationary property of the resolution function is illustrated in Figure 1.2. In areas of good illumination, as exemplified by image point A in Figure 1.1(a), the filter is relatively focused in the space domain (the left panel in Figure 1.2(a)), indicating relatively good spectrum

coverage in the Fourier domain (the right panel in Figure 1.2(a)). On the other hand, in areas of poor illumination, as exemplified by image point B in Figure 1.1(a), the filter is broader in the space domain (the left panel in Figure 1.2(b)), indicating narrower Fourier spectrum coverage (the right panel in Figure 1.2(b)). Unfortunately, the state of the art in reflectivity imaging, represented by prestack depth migration, does not properly take into account the non-stationary spreading effects of the resolution function, and consequently, the reflectivity image suffers from unbalanced amplitudes and the shadow-zone effect (Figure 1.1(b)). The distorted image may cause significant difficulties for seismic interpretation.

Besides the amplitude issue mentioned above, accurate imaging of the reflectivity also requires an accurate background velocity model. The state of the art in velocity analysis is represented by ray-based tomography (Bishop et al., 1985; Al-Yahya, 1989; Stork, 1992; Etgen, 1993; Kosloff et al., 1996). Such methods are efficient and accurate in relatively simple geologies with small velocity contrasts, such as the areas above the salt. However, ray-based tomography often fails due to the instability of ray tracing for complex velocity structures with sharp boundaries, such as subsalt regions. The infinite-frequency approximation and the caustics inherent in ray theory also prevent ray-based methods from accurately modeling complicated wave phenomena, such as the band-limited effect and multi-pathing. Figure 1.3 compares rays with wavefields for the Sigsbee2A model; it is obvious that the rays oversimplify the wavefields, resulting in loss of important information. Hence, in such situations, it is desirable to use wavefield-based method to define the velocity model.

Another important motivation for wavefield-based tomography is illustrated by Figures 1.4 and 1.5, which demonstrate the velocity sensitivity kernel under the Born approximation (Woodward, 1989) for the Sigsbee2A model at frequencies of 7 and 20 Hz, respectively. Note that they differ dramatically for different frequencies. This frequency-dependence of the velocity sensitivity suggests that accurate velocity updates require using band-limited wavefields as carriers of information.

Despite its advantages in modeling band-limited wavefields, practical application of wavefield-based tomography is still rare and small in scale for two reasons: First,

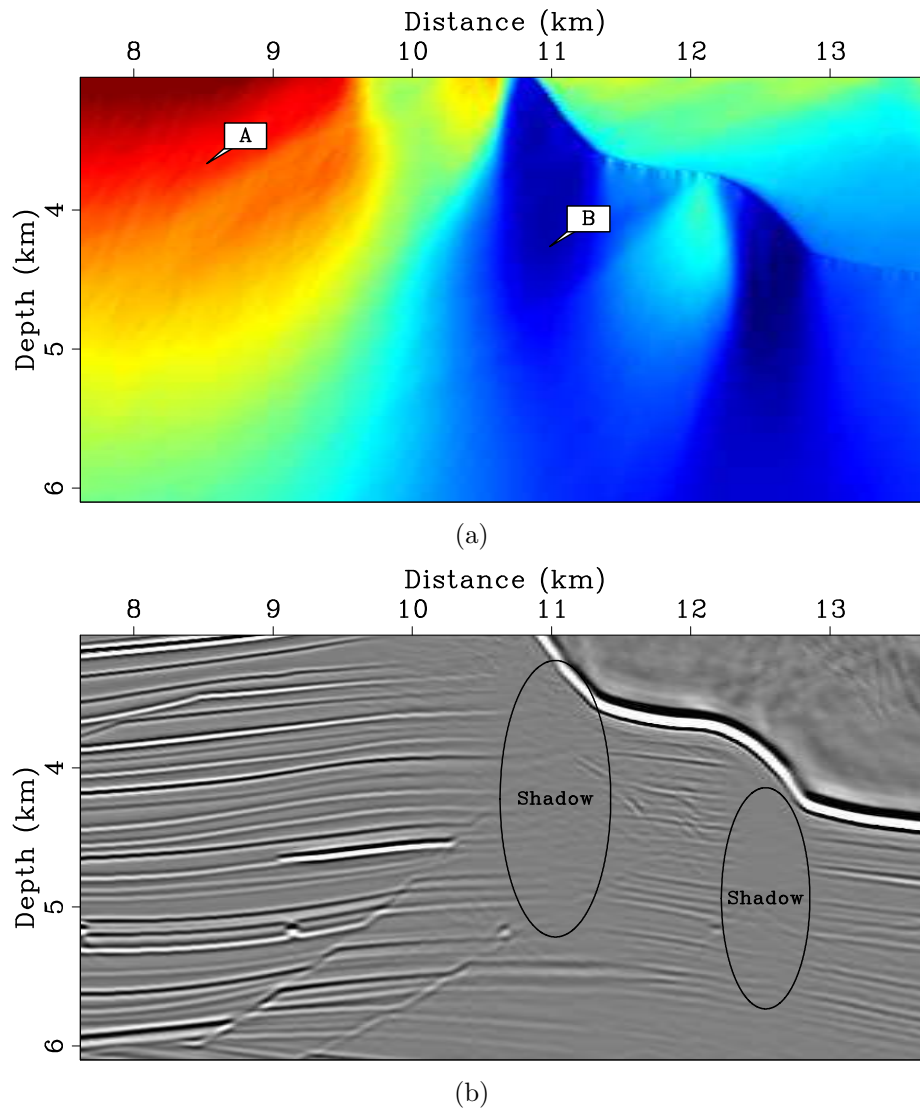


Figure 1.1: An example based on the Sigsbee2A model illustrating the challenges for imaging subsalt reflectivity. Panel (a) is the subsurface illumination, and panel (b) is the image obtained using a conventional imaging technique. [CR] chap1/. sigsb2a-hess-diag,sigsb2a-imag

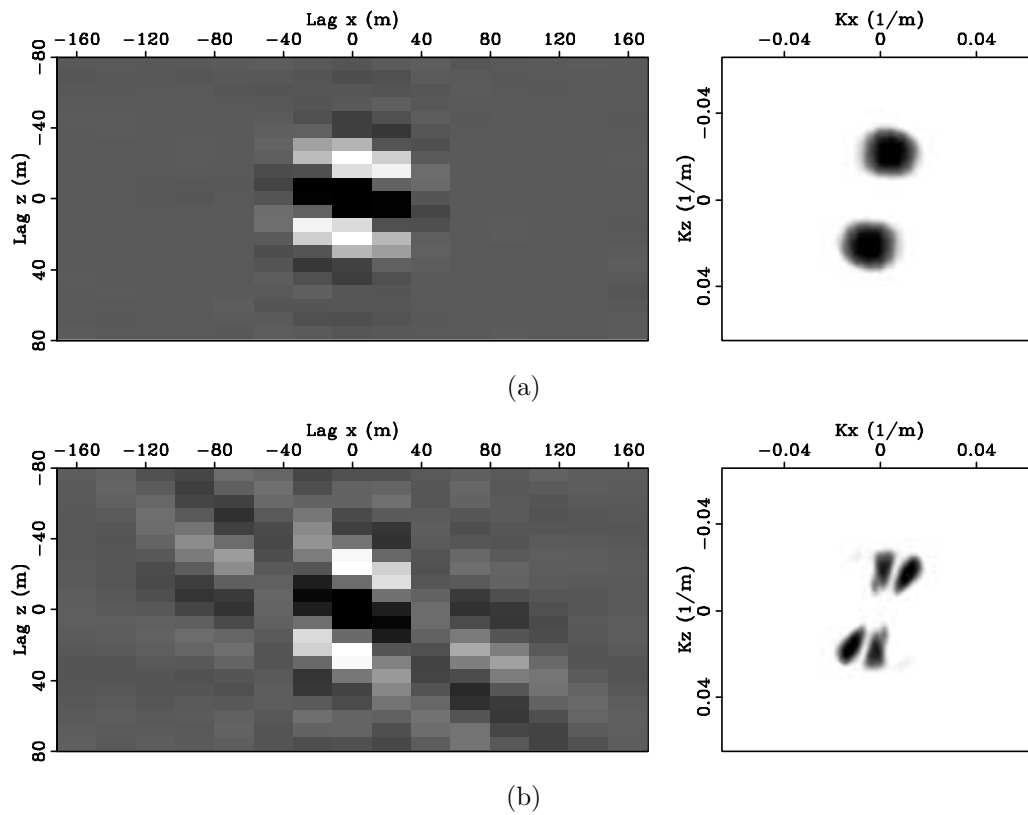


Figure 1.2: The resolution functions (a.k.a. the point spread functions) for the Sigbee2A example. Panels (a) and (b) are resolution functions for image points A and B, respectively, as shown in Figure 1.1(a). In each panel, the left plot shows the space-domain resolution function, while the right plot shows its amplitude spectrum in the Fourier domain. [CR] chap1/. space-a,space-b

the method is computationally demanding (Biondi and Sava, 1999; Shen et al., 2005; Albertin et al., 2006; Fei et al., 2009), because it uses expensive wavefield modeling engines. Second, the method lacks flexibility and usually requires the use of the whole recorded data set for velocity analysis.

Overcoming the illumination problem in subsalt reflectivity imaging, and meanwhile improving the accuracy, efficiency and flexibility of wavefield-based tomography for subsalt velocity analysis, motivate the development of the target-oriented wavefield inversion technique reported in this thesis.

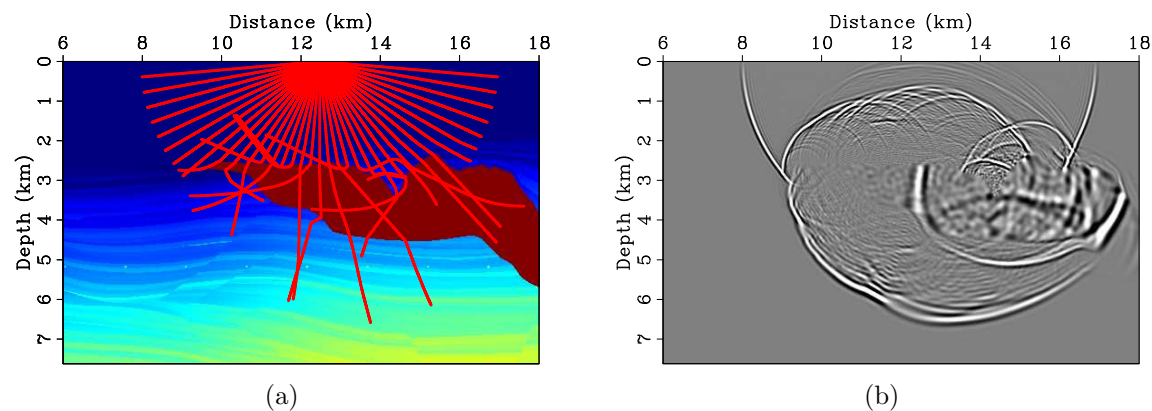


Figure 1.3: Comparison between rays and wavefields. Panel (a) shows a snapshot of the rays overlaid by the Sigsbee2A velocity model, (b) shows a snapshot of the wavefields. [ER] `chap1/. sigsb2a-rays-vmod,sigsb2a-wave-snapshot`

IMAGING BY TARGET-ORIENTED WAVEFIELD INVERSION

In this thesis, I develop techniques that use wavefields as carriers of information to recover both low- and high-wavenumber components of the earth model. Instead of estimating both components simultaneously, as in full waveform inversion (FWI) (Tarantola, 1987; Mora, 1987; Pratt, 1999), I estimate them sequentially by solving two independent inverse problems. In particular, I first use wavefield-based tomography (a.k.a. wavefield migration velocity analysis), a nonlinear inversion technique

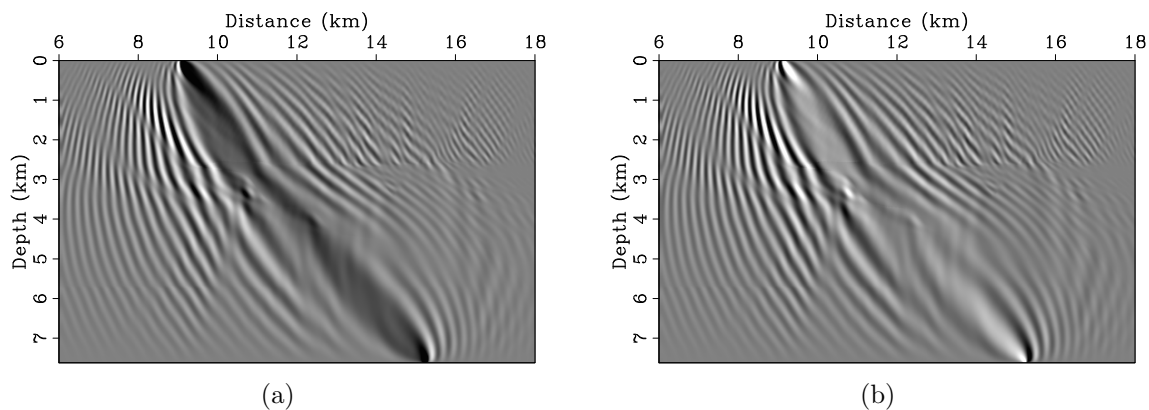


Figure 1.4: Velocity sensitivity kernel for the Sigsbee2A model at a frequency of 7 Hz. Panels (a) and (b) are the real and imaginary parts of the kernel, respectively. **[ER]** `chap1/. sigsb2a-vker-7hz-real,sigsb2a-vker-7hz-imag`

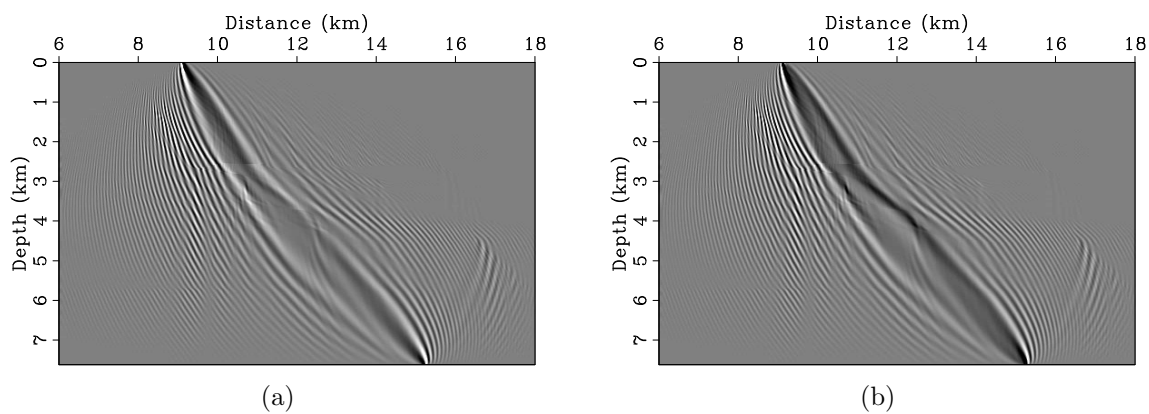


Figure 1.5: Velocity sensitivity kernel for the Sigsbee2A model at a frequency of 20 Hz. Panels (a) and (b) are the real and imaginary parts of the kernel, respectively. **[ER]** `chap1/. sigsb2a-vker-20hz-real,sigsb2a-vker-20hz-imag`

that uses primarily the kinematic information of the wavefields, to recover the background (low-wavenumber) velocity model. Next, I use wavefield least-squares migration, a linear inversion technique that utilizes mainly the dynamic information of the wavefields, to recover the reflectivity of the subsurface.

The reason that we can invert different components of the earth model separately is because different seismic waves sample different wavenumbers of the earth model. These wavenumbers have very little overlap due to the lack of long-offset and low-frequency information in the recorded surface seismic data (Jannane et al., 1989). Without loss of generality, Figure 1.6 shows a cartoon illustrating four different types of scattered wavefields. Based on how they interact with the anomaly in the center, the scattered wavefields can be classified into two categories: forward scattering and backward scattering. The forward scatterings are waves transmitting through the anomaly (wave A and D in Figure 1.6), and the backward scatterings are waves reflected directly by the anomaly (wave B and C in Figure 1.6). Through a simple K-space analysis (Wu and Toksöz, 1987; Mora, 1989), it is easy to show that the backward scatterings mainly sample the high-wavenumber component of the earth model, whereas the forward scatterings mainly sample the low-wavenumber component of the earth model (Figures 1.7, 1.8 and 1.9). Therefore, the high-wavenumber component can be recovered by a migration-type technique, which mainly takes advantage of the backward scatterings, while the low-wavenumber component can be recovered by a tomography-type technique, which mainly takes advantage of the forward scatterings.

As will be demonstrated in this thesis, one important advantage of solving two sequential inversion problems is that we can formulate both problems in the image domain and solve them in a target-oriented fashion. The idea of target-oriented inversion is very useful and has a lot of practical advantages. It allows us to apply the powerful, but expensive, wavefield-based technique only in areas where it is necessary, such as in subsalt regions with complex overburdens, and leave areas with relatively simple geologies to be handled by conventional imaging and velocity-analysis methods, which are sufficient to produce accurate results. By localizing the computation within a selected target zone, the target-oriented inversion strategy dramatically improves

the efficiency and flexibility of wavefield-based inversion methods. Therefore, it can greatly shorten the cycle time from seismic processing to interpretation, enabling interpretation-driven interactive wavefield-based imaging and velocity analysis, where different geological scenarios can be tested in quasi-real time.

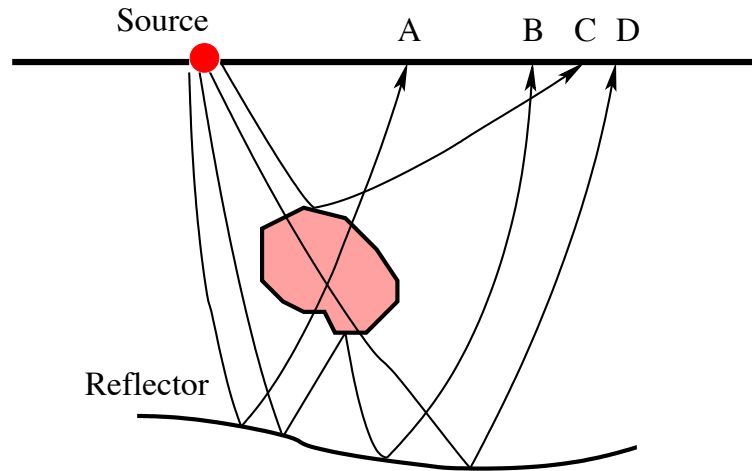


Figure 1.6: A simple cartoon illustrating different types of scattered waves due to the anomaly in the center. Waves A and D that transmit through the anomaly are forward scatterings. Waves B and C that are reflected by the anomaly are backward scatterings. [NR] [chap1/. scattered-waves](#)

THESIS OVERVIEW AND CONTRIBUTIONS

Target-oriented wavefield least-squares migration: In Chapter 2, I demonstrate how to pose the reflectivity imaging problem as a linear inversion problem. The linear relationship between the observed data and the reflectivity is established by a formal linearization of the acoustic wave equation, where the multiply scattered waves are ignored and the low-wavenumber component of the earth model (the background velocity) is assumed to be known. Instead of solving the inverse problem in the data domain, I solve it in the image domain, following an approach similar to one discussed by Valenciano (2008). The image-domain formulation allows a target-oriented application of the proposed inversion technique, enabling accurate reflectivity imaging at the reservoir level. However, as

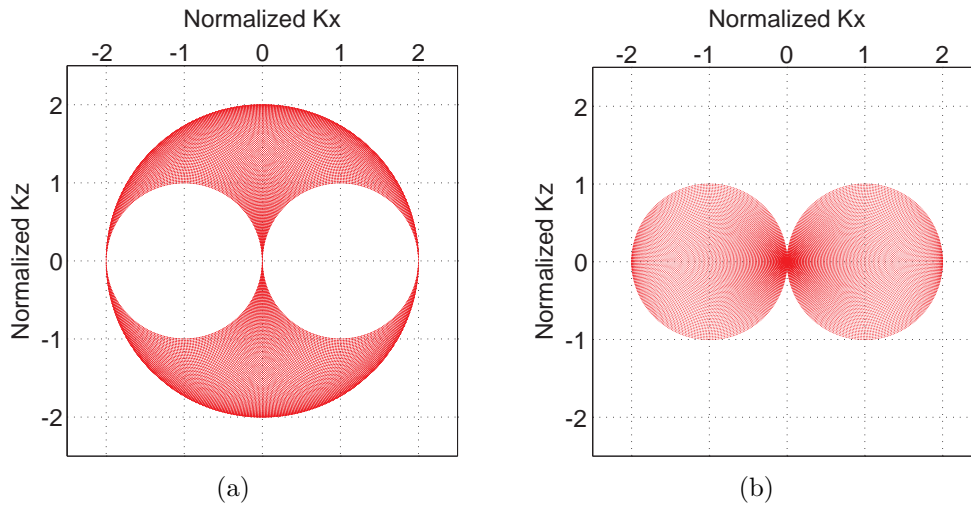


Figure 1.7: The wavenumber spectrum resolved by (a) the backward scatterings and (b) the forward scatterings. The results are obtained using a single frequency, assuming that there is infinite surface acquisition and that all waves transmitting through the anomaly can be recorded by receivers on the surface. Under these assumptions, the maximum incident and scattered angles can reach $\pm 90^\circ$ with respect to vertical, which is the ideal case for surface seismic. [CR] `chap1/. K-bwd-full,K-fwd-full`

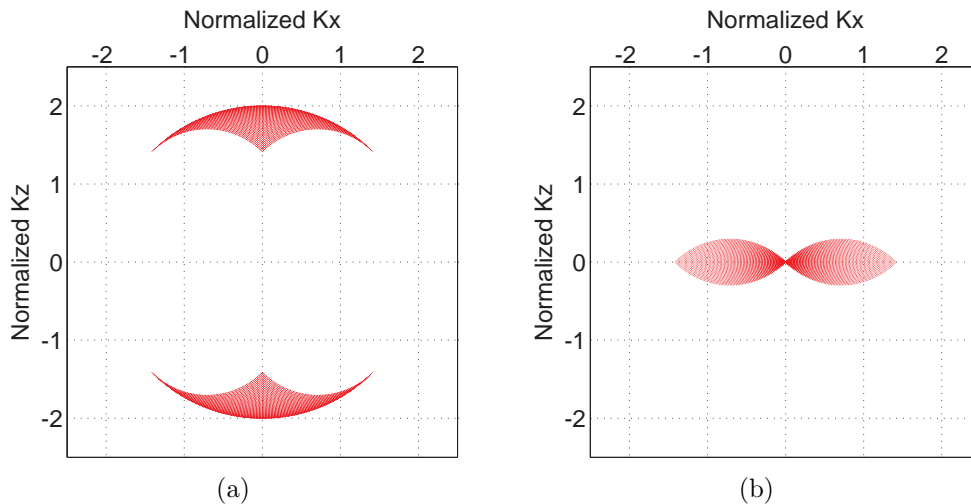


Figure 1.8: The wavenumber spectrum resolved by (a) the backward scatterings and (b) the forward scatterings. The results are obtained using a single frequency and limiting the maximum incident and scattered angles to $\pm 45^\circ$ with respect to vertical, which represents a more realistic situation for surface seismic. [CR] `chap1/. K-bwd-part,K-fwd-part`

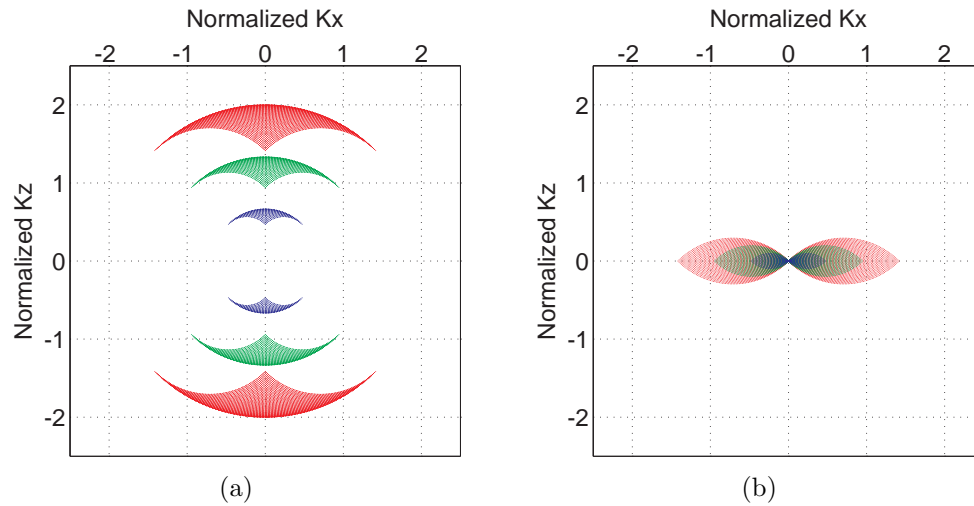


Figure 1.9: The wavenumber spectrum resolved by (a) the backward scatterings and (b) the forward scatterings. The results are obtained using three frequencies and limiting the maximum incident and scattered angles to $\pm 45^\circ$ with respect to vertical. Blue, green and red colors denote low, middle and high frequencies, respectively. [CR] chap1/. K-bwd-multi,K-fwd-multi

I will explain in Chapter 2, one big obstacle for the image-domain inversion is the huge computational cost of the Hessian operator (the resolution function), an operator containing all necessary information for correcting the effects of distorted illumination. As a solution to this difficulty, I develop a novel method based on the idea of phase encoding to very efficiently and accurately calculate the target-oriented Hessian operator. Numerical examples validate the proposed method. At the end of the chapter, I apply the target-oriented inversion technique to 2-D synthetic data sets. Results from this chapter have been published as Tang (2009).

Target-oriented wavefield tomography: In Chapter 3, I develop the theory of target-oriented wavefield tomography to estimate the background velocity. The idea is to synthesize a new data set specifically for velocity analysis. The new data set is designed to be much smaller than the originally surface recorded data set, but contains all necessary information for velocity updating. The same idea

has also been explored by Guerra (2010), who uses prestack-exploding-reflector modeling (PERM) to generate a new data set. PERM, however, generates crosstalk when multiple image events (reflectors) are modeled simultaneously. This limits the number of reflectors it can model. Manual picking and stochastic encoding methods, such as random-phase encoding, are required to mitigate the impact of the crosstalk.

The method discussed in Chapter 3 differs substantially from Guerra (2010). I formulate the problem under seismic data mapping (SDM) framework (Hubral et al., 1996; Bleistein and Jaramillo, 2000) and use generalized Born wavefield modeling as the mapping operator to synthesize a new data set for velocity analysis. Generalized Born wavefield modeling is extended from conventional Born modeling (Chapter 2) to include prestack parameters, such as the subsurface offset. As will be shown, the inclusion of the prestack parameters in the modeling process preserves the correct velocity information and is crucial to the success of this method. The phase-encoded Hessian discussed in Chapter 2 is used to calculate the pseudo-inverse of the generalized Born modeling operator, required by SDM. As will be shown, in contrast to PERM, generalized Born wavefield modeling does not require any picking, but picking can be incorporated if it is desired. Another advantage of generalized Born wavefield modeling is that it can model arbitrary number of reflectors simultaneously and is very little affected by the crosstalk artifacts.

The synthesized new data set is then used for image-domain wavefield tomography, which minimizes a residual field (or equivalently maximizes a coherence field) defined in the image domain using nonlinear optimization. At the end of the chapter, I apply the proposed methodology to 2-D synthetic and field data sets to improve subsalt velocities in a target-oriented fashion. Results from this chapter have been accepted for publication as Tang and Biondi (2011).

3-D field-data examples: In Chapter 4, I apply the target-oriented wavefield inversion theory developed in Chapter 2 and Chapter 3 to a 3-D field data set acquired from the Gulf of Mexico. I image the data in the 3-D conical-wave

domain, and show how the 3-D Hessian matrix can be efficiently computed in this domain using a version of simultaneous phase encoding.

To image below the salt, I first estimate the subsalt velocities using target-oriented wavefield tomography, where I synthesize a 3-D Born plane-wave data set for velocity analysis. The new data set is about two orders of magnitude smaller than the original surface-recorded data set. With academic-scale computing resources, I am able to obtain the 3-D inversion result in only a few days. The updated velocity model significantly improves the coherence and continuity of subsalt reflectors. The excellent velocity inversion result shows that target-oriented wavefield tomography is an efficient, accurate and flexible tool for velocity model-building in complex geology.

After obtaining a more accurate subsalt velocity model, I proceed to recover the subsalt reflectivity using target-oriented wavefield least-squares migration. Because the linear inversion is performed in the image domain in a target-oriented fashion, the computational cost is extremely low. Therefore, different regularization parameters or schemes can be easily tested at little cost. I show inversion results with different regularizations, and demonstrate that regularization with nonstationary dip filters (Clapp, 2003, 2005; Hale, 2007) helps incorporate interpreted geological information into the inversion process, making possible interpretation-driven interactive reflectivity inversion. The dip-regularized inversion successfully recovers subsalt reflectivities from the effects of uneven illumination, yielding more balanced amplitudes and higher spatial resolution in the inverted image.

Conclusions: In Chapter 5, I summarize the main results and conclusions obtained in this thesis. I also briefly discuss possible research directions to improve this method.

Chapter 2

Target-oriented wavefield least-squares migration

This chapter shows how to pose the reflectivity imaging as a linearized inversion problem and solve it in the image domain in a target-oriented fashion. Conventional reflectivity-imaging approach, as represented by prestack depth migration, produces blurred images resulting from limited acquisition apertures, complexities in the velocity model, and band-limited characteristics of seismic waves. This distortion can be optimally corrected using the image-domain least-squares migration approach, where a target-oriented wave-equation Hessian operator is computed explicitly and then inverse filtering is applied iteratively to deblur or invert for the reflectivity. However, one difficulty of this procedure is the cost of computing the explicit Hessian operator, which requires storing a large number of Green's functions, making it challenging for large-scale applications. In this chapter, I describe a novel method for computing the Hessian operator for the wavefield least-squares migration problem. The proposed method modifies the original explicit Hessian formula, enabling efficient computation of this operator. An advantage is that the method eliminates disk storage of Green's functions. The modifications, however, also introduce undesired crosstalk artifacts. Two different phase-encoding schemes, plane-wave-phase encoding and random-phase encoding, suppress the crosstalk. A 2-D numerical test using the Sigsbee2A synthetic

data set demonstrates that linear inversion with the phase-encoded Hessian can produce superior subsalt imaging results than conventional migration alone.

INTRODUCTION

Migration is an important tool for imaging subsurface structures using reflection seismic data. The classic imaging principle for shot-based migration states that reflectors are located where the forward-propagated source wavefield correlates with the backward-propagated receiver wavefield (Claerbout, 1971). However, this imaging principle is only the adjoint of the forward Born-modeling operator (Lailly, 1983), which provides reliable structural information of the subsurface, but blurs the image because of the non-unitary nature of the Born modeling operator. To deblur the migrated image and correct the effects of limited acquisition geometry, complex overburden and band-limited wavefields, the imaging problem can be posed as a linearized inversion problem based on the minimization of a least-squares functional. The inverse problem can be formulated either in the data domain (Lailly, 1983; Tarantola, 1984; Nemeth et al., 1999; Kühn and Sacchi, 2003; Clapp, 2005) or in the image domain (Beylkin, 1985; Chavent and Plessix, 1999; Rickett, 2003; Sjöberg et al., 2003; Guitton, 2004; Plessix and Mulder, 2004; Valenciano et al., 2006; Yu et al., 2006; Symes, 2008). The data-domain approach can be solved iteratively using gradient-based methods (Nemeth et al., 1999; Kühn and Sacchi, 2003; Clapp, 2005) without explicit construction of the Hessian, the matrix of the second derivatives of the error functional with respect to the model parameters. The iterative solving, however, is relatively costly and converges slowly without proper preconditioning.

On the other hand, the image-domain approach requires explicitly constructing the Hessian and applying its pseudo-inverse to the migrated image. The full Hessian of the least-squares functional is too big and expensive to compute in practical applications; hence some authors (Chavent and Plessix, 1999; Rickett, 2003; Plessix and Mulder, 2004; Symes, 2008) approximate it by a diagonal matrix. In the case of high-frequency asymptotics, and with an infinite aperture, the Hessian is diagonal in most cases

(Beylkin, 1985). For a finite range of frequencies and limited acquisition geometry, however, the Hessian is no longer diagonal and not even diagonally dominant (Pratt et al., 1998; Chavent and Plessix, 1999; Plessix and Mulder, 2004; Valenciano et al., 2006). It has been shown by Albertin et al. (2004) and Valenciano (2008) that, in areas of poor illumination, e.g., subsalt regions, the Hessian’s main diagonal energy is smeared along its off-diagonals. Therefore, a diagonal matrix has limited effect in deblurring the migrated image, especially in poorly illuminated areas. That is why several authors, e.g., Albertin et al. (2004) and Valenciano (2008), suggest computing a limited number of the Hessian off-diagonals to compensate for poor illumination and improve the inversion/deblurring result.

Since the exact Hessian off-diagonals are expensive to compute, some attempts have been made to reduce the cost by computing the non-diagonal Hessian in an approximate sense. Yu et al. (2006) introduce a lateral invariant non-diagonal Hessian by assuming a 1-D layered medium; Guitton (2004) uses a bank of non-stationary filters to approximate a non-diagonal inverse of the Hessian; with local plane-wave assumptions, Lecomte and Gelius (1998), Gelius et al. (2002) and Lecomte (2008) compute the Hessian in the local phase domain using a ray-based approach. They demonstrate that, since ray tracing conveniently gives local propagation angles of both source and receiver rays, the local scattering wavenumber for image points in the subsurface can be efficiently constructed. However, the high-frequency asymptotic approximation and the caustics inherent in ray theory may prevent the ray-based approach from accurately handling complex geologies (Hoffmann, 2001). To better model the band-limited characteristics of the seismic waves, Xie et al. (2006) use an one-way wave-equation-based approach to compute the phase-domain Hessian through local plane-wave decomposition. The above theories of computing the local phase-domain Hessian operator assume the velocity model is locally homogeneous. Although this is a reasonable assumption for most cases, when there are sharp velocity contrasts as in the vicinities of salt boundaries, this assumption becomes less reliable.

Another way of computing the wave-equation non-stationary Hessian operator is through crosscorrelation of the source and receiver Green’s functions in the space

domain (Plessix and Mulder, 2004; Valenciano et al., 2006). This approach does not introduce any assumptions to the velocity model. However, computing even a limited number of the Hessian off-diagonals in the space domain, by directly implementing the explicit Hessian formula, is very cumbersome. A huge number of Green's functions (easily several hundred terabytes for a typical 3-D survey with a reasonable frequency band) must be pre-computed and stored and then read from the disk to generate the Hessian. Such operations not only require high-volume storage, but also high-speed I/O and network communication. Though computer speed continues to improve rapidly, computing the Hessian in such a way still presents a challenge.

To make the space-domain Hessian more affordable, I describe a method based on the phase-encoding technique. In this method, the original explicit Hessian formula is slightly modified to enable efficient computation of this operator. The proposed method makes the Hessian computation similar to the shot-profile migration, but with slightly modified imaging and boundary conditions for the wavefields. The new method eliminates the need to store Green's functions, but it also introduces crosstalk artifacts. I examine two phase-encoding schemes, plane-wave-phase encoding (Whitmore, 1995; Zhang et al., 2005; Liu et al., 2006) and random-phase encoding (Romero et al., 2000), to attenuate the crosstalk.

This chapter is organized as follows. First, I briefly review the theory of Born wavefield modeling and show how to pose the reflectivity imaging as an image-domain inversion problem. Next, I discuss how the explicit Hessian can be efficiently computed using phase encoding. Finally, I apply the phase-encoded Hessian to deblur the migrated image for the Sigsbee2A model.

IMAGING BY LINEAR INVERSION

The use of inverse problem theory to recover the best migrated section from multishot and multitrace seismic data requires the choice of a forward model to build the cost function. In this chapter, I consider an acoustic earth with a constant density, as in acoustic migration. (This formalism, however, allows us to consider a more accurate

model, such as an elastic or viscoelastic earth.) The parameter is then the acoustic velocity. It is convenient to split this velocity field into a slowly varying part, (the low-wavenumber component, i.e., the background velocity), and a rapidly varying part (the high-wavenumber component, i.e., the reflectivity). By slowly varying, I mean that the scale length of the variations is much greater than the wavelength of the seismic waves under consideration. Therefore, it does not generate meaningful reflections to be recorded by receivers. On the other hand, the rapidly varying component represents discontinuities in the subsurface that generates reflections. In an acoustic earth with a constant density, the discontinuities are mainly caused by velocity variations that are comparable to the wavelength of the seismic waves under consideration. The variations are small enough that they do not affect the kinematics of the wavefield. I refer Clayton and Stolt (1981); LeBras and Clayton (1988); Docherty (1991); Chavent and Clement (1993) for more detailed discussions of the background velocity/reflectivity decomposition in the case of Born approximation.

Therefore, the seismic data $d(\mathbf{x}_r, \mathbf{x}_s, \omega)$ recorded by a receiver at $\mathbf{x}_r = (x_r, y_r, 0)$ due to a point source at $\mathbf{x}_s = (x_s, y_s, 0)$ can be modeled using the following equation (Stolt and Benson, 1986):

$$d(\mathbf{x}_r, \mathbf{x}_s, \omega) = \omega^2 \sum_{\mathbf{x}} f_s(\omega) G(\mathbf{x}, \mathbf{x}_s, \omega) G(\mathbf{x}, \mathbf{x}_r, \omega) m(\mathbf{x}), \quad (2.1)$$

where ω is the angular frequency; $f_s(\omega)$ is the source signature; and $m(\mathbf{x})$ denotes the reflectivity (a perturbed quantity from the background velocity) at image point $\mathbf{x} = (x, y, z)$ in the subsurface; $G(\mathbf{x}, \mathbf{x}_s, \omega)$ and $G(\mathbf{x}, \mathbf{x}_r, \omega)$ are the Green's functions connecting the source and receiver respectively, to the image point $\mathbf{x} = (x, y, z)$. In this definition, I do not take into account multiple reflections as is usually the case for wave-equation migration. This explains why the data d , which contains only primaries, are linear in m . In equation 2.1, I also assume that the background velocity \mathbf{v} used for computing the Green's functions is sufficiently accurate and it can explain all kinematics in the data. Therefore, the reflectivity term, m , only contributes to the amplitude in the modeled primaries. In Chapter 3, I discuss how to obtain an accurate background velocity model required by this linear inversion.

In equation 2.1, we assume \mathbf{x}_s and \mathbf{x}_r are infinite in extent and independent of each other. For a real survey, however, we do not have infinitely long cable and infinitely many sources; thus we must introduce the following acquisition mask matrix to limit the size of the modeling:

$$W(\mathbf{x}_r, \mathbf{x}_s) = \begin{cases} 1 & \text{if } \mathbf{x}_r \text{ is within the recording} \\ & \text{range of a shot at } \mathbf{x}_s; \\ 0 & \text{otherwise .} \end{cases} \quad (2.2)$$

In 2-D, for a marine acquisition geometry, $W(\mathbf{x}_r, \mathbf{x}_s)$ is similar to a band-limited diagonal matrix; for an Ocean Bottom Seismometer (OBS) or a land acquisition geometry, where all shots share the same receiver array, $W(\mathbf{x}_r, \mathbf{x}_s)$ is a rectangular matrix. In 3-D, the structure of the matrix is slightly more complicated.

To find a reflectivity model that best fits the observed data, we can minimize the following objective function in the least-squares sense:

$$F = \frac{1}{2} \sum_{\omega} \sum_{\mathbf{x}_s} \sum_{\mathbf{x}_r} |W(\mathbf{x}_r, \mathbf{x}_s)[d(\mathbf{x}_r, \mathbf{x}_s, \omega) - d_{\text{obs}}(\mathbf{x}_r, \mathbf{x}_s, \omega)]|^2, \quad (2.3)$$

where $d_{\text{obs}}(\mathbf{x}_r, \mathbf{x}_s, \omega)$ represents the observed data. It can be written in a more compact notation as follows:

$$F(\mathbf{m}) = \frac{1}{2} \|\mathbf{W}(\mathbf{d} - \mathbf{d}_{\text{obs}})\|^2 = \frac{1}{2} \|\mathbf{W}(\mathbf{L}\mathbf{m} - \mathbf{d}_{\text{obs}})\|^2, \quad (2.4)$$

where \mathbf{L} is the forward modeling operator defined in equation 2.1, \mathbf{W} is the acquisition mask operator described by equation 2.2, and $\|\cdot\|$ stands for the ℓ_2 norm. In this chapter, we assume that the background velocity \mathbf{v} for Green's functions construction is known and sufficiently accurate. In other words, the Born modeling operator \mathbf{L} explains all kinematics in the recorded primaries \mathbf{d}_{obs} . The accurate background velocity model guarantees that reflectors are positioned at correct locations in the recovered reflectivity image. Therefore, the misfit function described by equation 2.4 is sensitive mainly to reflectors' amplitudes.

The data-domain objective function $F(\mathbf{m})$ is usually minimized with a gradient-based optimization solver, which iterates until an acceptable image is obtained (Nemeth et al., 1999; Kühn and Sacchi, 2003; Clapp, 2005). However, the data-domain inversion scheme lacks flexibility and cannot be implemented in a target-oriented fashion. Full-domain migration/demigration has to be carried out within each iteration; and the optimization converges slowly without a proper preconditioner. Therefore, the data-domain inversion scheme is computationally challenging for large-scale applications.

Alternatively, we can reformulate the inverse problem and solve it in the image domain. Because \mathbf{L} is a linear operator, $F(\mathbf{m})$ is a quadratic function. $F(\mathbf{m})$ reaches its minimum when \mathbf{m} satisfies (Tarantola, 1987):

$$\mathbf{m} = \mathbf{H}^{-1}\mathbf{L}^*\mathbf{W}^*\mathbf{d}_{\text{obs}}, \quad (2.5)$$

where $*$ means adjoint (complex conjugation and transpose) and $\mathbf{H} = \mathbf{L}^*\mathbf{W}^*\mathbf{W}\mathbf{L}$ is the weighted Hessian operator. Equation 2.5 has only symbolic meaning, because the Hessian is often singular and its inverse is not easy to obtain directly. A more practical way would be reconstructing the reflectivity \mathbf{m} through iterative inverse filtering by minimizing an image-domain objective function defined as follows (Valenciano et al., 2006):

$$J(\mathbf{m}) = \frac{1}{2} \|\mathbf{H}\mathbf{m} - \mathbf{m}_{\text{mig}}\|^2, \quad (2.6)$$

where $\mathbf{m}_{\text{mig}} = \mathbf{L}^*\mathbf{W}^*\mathbf{d}_{\text{obs}}$ is the migrated image.

One advantage of the image-domain formulation is that it can be implemented in a target-oriented fashion, which can substantially reduce the size of the problem and hence the computational cost (Valenciano et al., 2006; Valenciano, 2008). For example, we can choose to invert only areas of particular interest, such as subsalt regions, where potential reservoirs are located and migration often fails to provide reliable images. In fact, the image-domain approach divides the inversion problem into two stages: computing the explicit Hessian (only once) and minimizing the objective function $J(\mathbf{m})$. Since the cost of minimizing the objective function $J(\mathbf{m})$ is

relatively small once the explicit Hessian is obtained, various regularization schemes incorporating different *a priori* information can be easily tested at very little cost.

Each element of the Hessian is given as follows by taking the second derivative of the objective function $F(\mathbf{m})$ with respect to the model parameters (Plessix and Mulder, 2004; Valenciano et al., 2006); note that $W^2(\mathbf{x}_r, \mathbf{x}_s) = W^*(\mathbf{x}_r, \mathbf{x}_s) = W(\mathbf{x}_r, \mathbf{x}_s)$:

$$\begin{aligned}
 H(\mathbf{x}, \mathbf{x}') = & \sum_{\omega} \omega^4 \sum_{\mathbf{x}_s} |f_s(\omega)|^2 G(\mathbf{x}, \mathbf{x}_s, \omega) G^*(\mathbf{x}', \mathbf{x}_s, \omega) \\
 & \times \sum_{\mathbf{x}_r} W(\mathbf{x}_r, \mathbf{x}_s) G(\mathbf{x}, \mathbf{x}_r, \omega) G^*(\mathbf{x}', \mathbf{x}_r, \omega), \quad (2.7)
 \end{aligned}$$

where \mathbf{x}' is a neighbor point around the image point \mathbf{x} in the subsurface. The diagonal part of the Hessian (when $\mathbf{x} = \mathbf{x}'$), which contains autocorrelations of both source- and receiver-side Green's functions, can be interpreted as a subsurface illumination map with contributions from both sources and receivers. The rows of the Hessian (for fixed \mathbf{x} 's and varying \mathbf{x}' 's), which contain crosscorrelations of both source- and receiver-side Green's functions, can be interpreted as resolution functions (Lecomte, 2008). They measure how much smearing an image can have due to a given acquisition setup.

A target-oriented truncated Hessian is obtained by computing the Hessian for \mathbf{x} 's that are within the target zone and a small number of \mathbf{x}' 's that are close to each \mathbf{x} (Valenciano et al., 2006; Valenciano, 2008). The reason that the Hessian can be approximated using a truncated version is because for conventional point-source acquisition geometry, the energy in each row of the Hessian is mostly concentrated around its diagonal ($H(\mathbf{x}, \mathbf{x})$), see Figure 1.2 in Chapter 1 for example. Therefore, the majority of the spreading effect can be captured by a limited number of \mathbf{x}' 's that are very close to \mathbf{x} . In general, the weaker the amplitudes in the diagonal of the Hessian, more points surrounding the diagonal are required to make an accurate approximation in the truncated Hessian. However, the truncated Hessian approximation breaks down for the case of blended-source acquisition geometry (Beasley et al., 1998; Beasley, 2008; Berkhout, 2008; Hampson et al., 2008), where energy of the Hessian is no

longer concentrated around the diagonal points, but spreads everywhere in the model domain (Tang and Biondi, 2009). In these situations, a data-domain implementation of the linearized inversion is preferred (Tang and Biondi, 2009).

Hereafter, I call $H(\mathbf{x}, \mathbf{x}')$ in equation 2.7 the exact Hessian, since it is derived strictly from the least-squares functional $F(\mathbf{m})$ in the shot-profile domain. However, direct implementation of equation 2.7 requires saving Green's functions, which may bring considerable computational issues, because the Green's functions can be huge for practical applications, especially in 3-D. To reduce the computational burden, in the subsequent sections, I introduce an alternative method based on phase encoding to compute the Hessian operator. As I will demonstrate, by using this approach, we do not need to save any Green's functions, and the cost is also significantly reduced.

PHASE-ENCODED HESSIAN

Encoding of the receiver-side Green's functions

Suppose we have a new operator $\tilde{H}(\mathbf{x}, \mathbf{x}', \mathbf{p}_r)$ defined as follows:

$$\begin{aligned} \tilde{H}(\mathbf{x}, \mathbf{x}', \mathbf{p}_r) = & \sum_{\omega} \omega^4 \sum_{\mathbf{x}_s} |f_s(\omega)|^2 G(\mathbf{x}, \mathbf{x}_s, \omega) G^*(\mathbf{x}', \mathbf{x}_s, \omega) \\ & \times \sum_{\mathbf{x}_r} W(\mathbf{x}_r, \mathbf{x}_s) G(\mathbf{x}, \mathbf{x}_r, \omega) \alpha(\mathbf{x}_r, \mathbf{p}_r, \omega) \\ & \times \sum_{\mathbf{x}'_r} W(\mathbf{x}'_r, \mathbf{x}_s) G^*(\mathbf{x}', \mathbf{x}'_r, \omega) \alpha^*(\mathbf{x}'_r, \mathbf{p}_r, \omega), \end{aligned} \quad (2.8)$$

where we introduce an extra summation $\sum_{\mathbf{x}'_r}$ for the receiver-side Green's functions, and $\alpha(\mathbf{x}_r, \mathbf{p}_r, \omega)$ is some weighting function, or more specifically, encoding function, to be specified later. Hereafter, $\tilde{H}(\mathbf{x}, \mathbf{x}', \mathbf{p}_r)$ is referred as the receiver-side phase-encoded Hessian. Though $\tilde{H}(\mathbf{x}, \mathbf{x}', \mathbf{p}_r)$ can be computed in a way similar to the direct implementation of the exact Hessian as defined by equation 2.7, it offers more flexibility and can be efficiently computed without explicitly saving the Green's functions.

Because of the linearity of wave equation with respect to sources, the summation term $\sum_{\mathbf{x}_r} W(\mathbf{x}_r, \mathbf{x}_s)G(\mathbf{x}, \mathbf{x}_r, \omega)\alpha(\mathbf{x}_r, \mathbf{p}_r, \omega)$ now becomes the extrapolated wavefield at image point \mathbf{x} . It corresponds to a composite source $f_c(x, y, \mathbf{x}_s, \mathbf{p}_r, \omega)$ on the surface that can be defined as follows:

$$f_c(x, y, \mathbf{x}_s, \mathbf{p}_r, \omega) = \sum_{\mathbf{x}_r} W(\mathbf{x}_r, \mathbf{x}_s)\delta(x - x_r, y - y_r)\alpha(\mathbf{x}_r, \mathbf{p}_r, \omega), \quad (2.9)$$

where $\delta(x - x_r, y - y_r)$ is the Dirac delta function centered at $\mathbf{x}_r = (x_r, y_r, 0)$ and can be considered as a point source on the surface. Hence, the composite source is obtained by linearly combining point sources at all receiver locations for a specific shot located at \mathbf{x}_s . The function $\alpha(\mathbf{x}_r, \mathbf{p}_r, \omega)$ serves as a weight when combining these point sources. The same thing holds for the other summation term, $\sum_{\mathbf{x}'_r} W(\mathbf{x}'_r, \mathbf{x}_s)G^*(\mathbf{x}'_r, \mathbf{x}', \omega)\alpha^*(\mathbf{x}'_r, \omega)$, except that it is the complex conjugate of the same extrapolated wavefield at a neighbor image point \mathbf{x}' . To make it clearer, we define a receiver wavefield $R(\mathbf{x}, \mathbf{x}_s, \mathbf{p}_r, \omega)$ corresponding to the receiver composite source $f_c(x, y, \mathbf{x}_s, \mathbf{p}_r, \omega)$ as

$$R(\mathbf{x}, \mathbf{x}_s, \mathbf{p}_r, \omega) = \sum_{\mathbf{x}_r} W(\mathbf{x}_r, \mathbf{x}_s)G(\mathbf{x}_r, \mathbf{x}, \omega)\alpha(\mathbf{x}_r, \mathbf{p}_r, \omega), \quad (2.10)$$

and a source wavefield corresponding to a point source located at \mathbf{x}_s on the surface as

$$S(\mathbf{x}, \mathbf{x}_s, \omega) = f_s(\omega)G(\mathbf{x}, \mathbf{x}_s, \omega). \quad (2.11)$$

If one-way wavefield extrapolation is used, wavefields S and R can be obtained by solving the following one-way wave equations:

$$\begin{cases} \left(\frac{\partial}{\partial z} - i\sqrt{\frac{\omega^2}{v^2(\mathbf{x})} + \nabla^2} \right) S(\mathbf{x}, \mathbf{x}_s, \omega) = 0 \\ S(x, y, z = 0, \mathbf{x}_s, \omega) = \sum_{\mathbf{x}_s} \delta(x - x_s, y - y_s)f_s(\omega) \end{cases}, \quad (2.12)$$

and

$$\begin{cases} \left(\frac{\partial}{\partial z} - i\sqrt{\frac{\omega^2}{v^2(\mathbf{x})} + \nabla^2} \right) R(\mathbf{x}, \mathbf{x}_s, \mathbf{p}_r, \omega) = 0 \\ R(x, y, z = 0, \mathbf{x}_s, \mathbf{p}_r, \omega) = \sum_{\mathbf{x}_r} W_r(\mathbf{x}_r, \mathbf{x}_s) \delta(x - x_r, y - y_r) \alpha(\mathbf{x}_r, \mathbf{p}_r, \omega) \end{cases}, \quad (2.13)$$

where $\nabla^2 = \frac{\partial^2}{\partial x^2} + \frac{\partial^2}{\partial y^2}$ is the Laplacian operator, and $v(\mathbf{x})$ is the velocity at image point \mathbf{x} .

Substituting equations 2.10 and 2.11 into equation 2.8 leads to

$$\begin{aligned} \tilde{H}(\mathbf{x}, \mathbf{x}', \mathbf{p}_r) = & \sum_{\omega} \omega^4 \sum_{\mathbf{x}_s} S(\mathbf{x}, \mathbf{x}_s, \omega) S^*(\mathbf{x}', \mathbf{x}_s, \omega) \\ & \times R(\mathbf{x}, \mathbf{x}_s, \mathbf{p}_r, \omega) R^*(\mathbf{x}', \mathbf{x}_s, \mathbf{p}_r, \omega), \end{aligned} \quad (2.14)$$

which means $\tilde{H}(\mathbf{x}, \mathbf{x}', \mathbf{p}_r)$ can be computed by crosscorrelating the source and receiver wavefields with their shifted complex conjugates (\mathbf{x}' is a neighborhood point around \mathbf{x}). Therefore, the algorithm for computing the receiver-side phase-encoded Hessian is similar to the wave-equation shot-profile migration algorithm, except that the boundary condition for the receiver wavefield and the imaging condition are slightly modified. In the shot-profile migration, the boundary condition for the receiver wavefield is the recorded data, and we crosscorrelate the source wavefield and the receiver wavefield to produce the image; here, in contrast, we use the composite source as the boundary condition for the receiver wavefield, and then invoke the imaging condition defined by equation 2.14 to produce the new operator $\tilde{H}(\mathbf{x}, \mathbf{x}', \mathbf{p}_r)$. In other words, we do not have to save the Green's functions at all. Computing $\tilde{H}(\mathbf{x}, \mathbf{x}', \mathbf{p}_r)$ is also efficient because multiple Green's functions are computed at the same time during wavefield extrapolation.

We can stack $\tilde{H}(\mathbf{x}, \mathbf{x}', \mathbf{p}_r)$ over \mathbf{p}_r and after some simple algebraic manipulation,

we obtain:

$$\begin{aligned}
\tilde{H}(\mathbf{x}, \mathbf{x}') &= \sum_{\mathbf{p}_r} \tilde{H}(\mathbf{x}, \mathbf{x}', \mathbf{p}_r) \\
&= \sum_{\omega} \omega^4 \sum_{\mathbf{x}_s} |f_s(\omega)|^2 G(\mathbf{x}, \mathbf{x}_s, \omega) G^*(\mathbf{x}', \mathbf{x}_s, \omega) \\
&\quad \times \sum_{\mathbf{x}_r} W(\mathbf{x}_r, \mathbf{x}_s) G(\mathbf{x}, \mathbf{x}_r, \omega) G^*(\mathbf{x}', \mathbf{x}_r, \omega) \sum_{\mathbf{p}_r} |\alpha(\mathbf{x}_r, \mathbf{p}_r, \omega)|^2 \\
&\quad + \sum_{\omega} \omega^4 \sum_{\mathbf{x}_s} |f_s(\omega)|^2 G(\mathbf{x}, \mathbf{x}_s, \omega) G^*(\mathbf{x}', \mathbf{x}_s, \omega) \\
&\quad \times \sum_{\mathbf{x}_r} \sum_{\mathbf{x}'_r \neq \mathbf{x}_r} W(\mathbf{x}_r, \mathbf{x}_s) G(\mathbf{x}, \mathbf{x}_r, \omega) W(\mathbf{x}'_r, \mathbf{x}_s) G^*(\mathbf{x}', \mathbf{x}'_r, \omega) \\
&\quad \times \sum_{\mathbf{p}_r} \alpha(\mathbf{x}_r, \mathbf{p}_r, \omega) \alpha^*(\mathbf{x}'_r, \mathbf{p}_r, \omega). \tag{2.15}
\end{aligned}$$

If we let the weighting function satisfy $\sum_{\mathbf{p}_r} |\alpha(\mathbf{x}_r, \mathbf{p}_r, \omega)|^2 = 1$, the first term in equation 2.15 becomes the exact Hessian $H(\mathbf{x}, \mathbf{x}')$ (equation 2.7); however, if the second term cannot be removed, it becomes undesired crosstalk from the crosscorrelations among different receiver-side Green's functions and we obtain:

$$\tilde{H}(\mathbf{x}, \mathbf{x}') = H(\mathbf{x}, \mathbf{x}') + \text{Crosstalk}. \tag{2.16}$$

Simultaneous encoding of the source- and receiver-side Green's functions

We can further encode the source-side Green's function by synthesizing composite sources from the source locations. For simplicity, we assume OBS or land acquisition geometries, where all shots have the same receiver spread. Therefore, we have the following relation:

$$W(\mathbf{x}_r, \mathbf{x}_s) = W_r(\mathbf{x}_r) W_s(\mathbf{x}_s), \tag{2.17}$$

where $W_r(\mathbf{x}_r)$ and $W_s(\mathbf{x}_s)$ define the ranges of receivers and sources for a given acquisition geometry. With the above assumption, we can construct a simultaneously phase-encoded Hessian as follows:

$$\begin{aligned} \tilde{H}(\mathbf{x}, \mathbf{x}', \mathbf{p}_s, \mathbf{p}_r) = & \sum_{\omega} \omega^4 \sum_{\mathbf{x}_s} W_s(\mathbf{x}_s) f_s(\omega) G(\mathbf{x}, \mathbf{x}_s, \omega) \beta(\mathbf{x}_s, \mathbf{p}_s, \omega) \\ & \times \sum_{\mathbf{x}'_s} W_s(\mathbf{x}'_s) f_s^*(\omega) G^*(\mathbf{x}', \mathbf{x}'_s, \omega) \beta^*(\mathbf{x}'_s, \mathbf{p}_s, \omega) \\ & \times \sum_{\mathbf{x}_r} W_r(\mathbf{x}_r) G(\mathbf{x}, \mathbf{x}_r, \omega) \alpha(\mathbf{x}_r, \mathbf{p}_r, \omega) \\ & \times \sum_{\mathbf{x}'_r} W_r(\mathbf{x}'_r) G^*(\mathbf{x}', \mathbf{x}'_r, \omega) \alpha^*(\mathbf{x}'_r, \mathbf{p}_r, \omega). \end{aligned} \quad (2.18)$$

where we introduce two extra summations: $\sum_{\mathbf{x}'_s}$ for the source-side Green's functions and $\sum_{\mathbf{x}'_r}$ for the receiver-side Green's functions. Similar to $\alpha(\mathbf{x}_r, \mathbf{p}_r, \omega)$, $\beta(\mathbf{x}_s, \mathbf{p}_s, \omega)$ is also a weighting function and will be specified later. Let us once again define the composite source wavefield $S(\mathbf{x}, \mathbf{p}_s, \omega)$ and composite receiver wavefield $R(\mathbf{x}, \mathbf{p}_r, \omega)$ as follows:

$$S(\mathbf{x}, \mathbf{p}_s, \omega) = \sum_{\mathbf{x}_s} W_s(\mathbf{x}_s) f_s(\omega) G(\mathbf{x}, \mathbf{x}_s, \omega) \beta(\mathbf{x}_s, \mathbf{p}_s, \omega), \quad (2.19)$$

and

$$R(\mathbf{x}, \mathbf{p}_r, \omega) = \sum_{\mathbf{x}_r} W_r(\mathbf{x}_r) G(\mathbf{x}, \mathbf{x}_r, \omega) \alpha(\mathbf{x}_r, \mathbf{p}_r, \omega), \quad (2.20)$$

which satisfy the following one-way wave equations, if one-way propagators are used:

$$\begin{cases} \left(\frac{\partial}{\partial z} - i\sqrt{\frac{\omega^2}{v^2(\mathbf{x})} + \nabla^2} \right) S(\mathbf{x}, \mathbf{p}_s, \omega) = 0 \\ S(x, y, z = 0, \mathbf{p}_s, \omega) = \sum_{\mathbf{x}_s} \delta(x - x_s, y - y_s) W_s(\mathbf{x}_s) f_s(\omega) \beta(\mathbf{x}_s, \mathbf{p}_s, \omega) \end{cases}, \quad (2.21)$$

and

$$\begin{cases} \left(\frac{\partial}{\partial z} - i\sqrt{\frac{\omega^2}{v^2(\mathbf{x})} + \nabla^2} \right) R(\mathbf{x}, \mathbf{p}_r, \omega) = 0 \\ R(x, y, z = 0, \mathbf{p}_r, \omega) = \sum_{\mathbf{x}_r} \delta(x - x_r, y - y_r) W_r(\mathbf{x}_r) \alpha(\mathbf{x}_r, \mathbf{p}_r, \omega) \end{cases}. \quad (2.22)$$

Substituting equations 2.19 and 2.20 into equation 2.18 leads to

$$\tilde{\tilde{H}}(\mathbf{x}, \mathbf{x}', \mathbf{p}_s, \mathbf{p}_r) = \sum_{\omega} \omega^4 S(\mathbf{x}, \mathbf{p}_s, \omega) S^*(\mathbf{x}', \mathbf{p}_s, \omega) R(\mathbf{x}, \mathbf{p}_r, \omega) R^*(\mathbf{x}', \mathbf{p}_r, \omega). \quad (2.23)$$

Therefore, computing the simultaneously phase-encoded Hessian $\tilde{\tilde{H}}(\mathbf{x}, \mathbf{x}', \mathbf{p}_s, \mathbf{p}_r)$ requires only two wavefield propagations: one for the composite source wavefield defined by equation 2.19, and the other for the composite receiver wavefield defined by equation 2.20.

Similar to the case of the receiver-side phase-encoded Hessian, we can stack $\tilde{\tilde{H}}(\mathbf{x}, \mathbf{x}', \mathbf{p}_s, \mathbf{p}_r)$ over both \mathbf{p}_s and \mathbf{p}_r . If the weighting functions α and β satisfy $\sum_{\mathbf{p}_r} |\alpha(\mathbf{x}_r, \mathbf{p}_r, \omega)|^2 = 1$ and $\sum_{\mathbf{p}_s} |\beta(\mathbf{x}_s, \mathbf{p}_s, \omega)|^2 = 1$, the stacked result $\tilde{\tilde{H}}(\mathbf{x}, \mathbf{x}')$ becomes the sum of the exact Hessian and the crosstalk:

$$\begin{aligned} \tilde{\tilde{H}}(\mathbf{x}, \mathbf{x}') &= \sum_{\mathbf{p}_s} \sum_{\mathbf{p}_r} \tilde{\tilde{H}}(\mathbf{x}, \mathbf{x}', \mathbf{p}_s, \mathbf{p}_r) \\ &= H(\mathbf{x}, \mathbf{x}') + \text{Crosstalk}. \end{aligned} \quad (2.24)$$

Thus, by encoding the Green's functions for the Hessian computation, we face a situation similar to that encountered in phase-encoding migration (Romero et al., 2000; Liu et al., 2006), i.e., our exact Hessian is contaminated by crosstalk artifacts, so we seek to define weighting functions $\alpha(\mathbf{x}_r, \mathbf{p}_r, \omega)$ and $\beta(\mathbf{x}_s, \mathbf{p}_s, \omega)$ that attenuate the crosstalk as much as possible. In the next two sections, I examine two different phase-encoding schemes to attenuate the crosstalk, namely, plane-wave-phase encoding and random-phase encoding.

Plane-wave-phase encoding

Suppose we choose the weighting functions to be

$$\alpha(\mathbf{x}_r, \mathbf{p}_r, \omega) = A_r(\omega)e^{i\omega\mathbf{p}_r\cdot\mathbf{x}_r}, \quad (2.25)$$

$$\beta(\mathbf{x}_s, \mathbf{p}_s, \omega) = A_s(\omega)e^{i\omega\mathbf{p}_s\cdot\mathbf{x}_s}, \quad (2.26)$$

which are the well known plane-wave or delayed-shot phase-encoding functions (Whitmore, 1995; Zhang et al., 2005; Liu et al., 2006), where $i = \sqrt{-1}$, $A_r(\omega)$ and $A_s(\omega)$ are real functions depending upon the angular frequency ω ; and $\mathbf{p}_r = (p_{rx}, p_{ry})$ and $\mathbf{p}_s = (p_{sx}, p_{sy})$ are the ray parameters for the receiver and source plane waves on the surface, respectively. As proved by Liu et al. (2006), in continuous case, integrating over plane waves completely attenuates the crosstalk in the plane-wave source migration, and the final migration result is exactly equivalent to the standard shot-profile migration result. The same property holds here in the scenario of Hessian computation, as proved in Appendix A: integrating over \mathbf{p}_r and \mathbf{p}_s , and choosing $A_r(\omega)$ and $A_s(\omega)$ to satisfy $A_r^2(\omega) = |\omega|$, $A_s^2(\omega) = |\omega|$ in 2-D and $A_r^2(\omega) = |\omega|^2$, $A_s^2(\omega) = |\omega|^2$ in 3-D, asymptotically, we have $\sum_{\mathbf{p}_r} \alpha(\mathbf{x}_r, \mathbf{p}_r, \omega)\alpha^*(\mathbf{x}'_r, \mathbf{p}_r, \omega)$ and $\sum_{\mathbf{p}_s} \beta(\mathbf{x}_s, \mathbf{p}_s, \omega)\beta^*(\mathbf{x}'_s, \mathbf{p}_s, \omega)$ equal 1 (if $\mathbf{x}_r = \mathbf{x}'_r$, $\mathbf{x}_s = \mathbf{x}'_s$) and 0 (if $\mathbf{x}_r \neq \mathbf{x}'_r$, $\mathbf{x}_s \neq \mathbf{x}'_s$). Hence the crosstalk in both equations 2.16 and 2.24 becomes zero, and the approximate Hessians $\tilde{H}(\mathbf{x}, \mathbf{x}')$ and $\tilde{\tilde{H}}(\mathbf{x}, \mathbf{x}')$ converge to the exact Hessian $H(\mathbf{x}, \mathbf{x}')$. In the discrete form used in practice, the number of \mathbf{p}_s and \mathbf{p}_r values can be chosen in a way similar to those discussed by Stork and Kapoor (2004); Zhang et al. (2005); Etgen (2005); Stork and Kapoor (2006); Zhang et al. (2006).

Random-phase encoding

Instead of using the plane-wave-phase encoding function, we can use random phases to disperse unwanted crossterms (Romero et al., 2000). The weighting functions can

be chosen as follows:

$$\alpha(\mathbf{x}_r, \mathbf{p}_r, \omega) = \frac{1}{\sqrt{N_{\text{realize}}}} e^{i\gamma(\mathbf{x}_r, \mathbf{p}_r, \omega)}, \quad (2.27)$$

$$\beta(\mathbf{x}_s, \mathbf{p}_s, \omega) = \frac{1}{\sqrt{N_{\text{realize}}}} e^{i\gamma(\mathbf{x}_s, \mathbf{p}_s, \omega)}, \quad (2.28)$$

where the phase functions $\gamma(\mathbf{x}_r, \mathbf{p}_r, \omega)$ and $\gamma(\mathbf{x}_s, \mathbf{p}_s, \omega)$ are sequences of random numbers between 0 and 2π , they are random functions of both space and frequency; the parameters \mathbf{p}_r and \mathbf{p}_s now define the indexes of different realizations of the random sequences; N_{realize} is the number of realizations. Obviously, the weighting functions satisfy $\sum_{\mathbf{p}_r} |\alpha(\mathbf{x}_r, \mathbf{p}_r, \omega)|^2 = 1$ and $\sum_{\mathbf{p}_s} |\beta(\mathbf{x}_s, \mathbf{p}_s, \omega)|^2 = 1$, therefore, the encoded Hessian has the same form as in equation 2.16 (receiver-side encoded Hessian) or 2.24 (simultaneously encoded Hessian).

Because the phases of the crosstalk are randomized, when we sum over frequencies, sources and receivers to generate the final result, the phases of the crosstalk will not agree with each other, and consequently, the crosstalk will be attenuated by stacking. To maximize the phase differences, a uniformly distributed random sequence could be used (Romero et al., 2000). As shown in Appendix B, with this choice of random sequence, the expectation of the crosstalk becomes zero. According to the law of large numbers—the ensemble average of a random sequence converges to its expectation (Gray and Davisson, 2003), the crosstalk therefore converges to zero in a statistical sense by stacking. To further attenuate the crosstalk, multiple realizations of the random sequences can be used ($N_{\text{realize}} > 1$): the randomly phase-encoded Hessian is computed multiple times with different realizations of the random-phase function and then stacked together to produce the final result. For a given acquisition geometry, i.e., for a fixed number of frequencies, shots and receivers, the number of realizations N_{realize} then controls the accuracy and cost of this approximation.

Cost comparison

In this section, I compare the cost for different methods to determine the savings generated by using the phase-encoding method. As discussed before, Hessian computation contains two main parts: wavefield propagation (Green’s functions) and crosscorrelation among different Green’s functions. Since the crosscorrelation parts are similar for methods with or without phase encoding, I will only compare the cost for the first part, i.e, wavefield propagation for Green’s functions. I consider general 3-D cases; for 2-D applications, the cost for each method can also be conveniently obtained by setting the corresponding crossline parameter(s) (with subscript y) to 1.

Let us assume a 3-D seismic survey that has N_s shots in total, covering a surface area that can be divided into $N_x \times N_y$ cells; and our target area for inversion is a 3-D cube with M_x , M_y and M_z samples in x , y and z directions. Table 2.1 illustrates the cost comparison for a marine acquisition geometry, while Table 2.2 compares the cost for an OBS or a land acquisition geometry. Since simultaneous phase encoding is derived under an OBS or a land acquisition geometry, Table 2.1 only compares the cost of the receiver-side encoding method with that of the direct method. In both tables, N_ω is the number of frequencies of the wavefield, $N_{p_{sx}}$ and $N_{p_{sy}}$ are the numbers of source ray parameters for the inline and crossline directions, and $N_{p_{rx}}$ and $N_{p_{ry}}$ are the numbers of receiver ray parameters for the inline and crossline directions, respectively. N_{realize} is the number of realizations of the random sequences, the same as that defined in the previous section.

Method	Number of wavefield propagations	Number of Green’s functions to store
Direct computation	$N_x N_y N_\omega$	$M_x M_y M_z N_x N_y N_\omega$
Plane-wave, receiver-side	$(1 + N_{p_{rx}} N_{p_{ry}}) N_s N_\omega$	0
Random, receiver-side	$(1 + N_{\text{realize}}) N_s N_\omega$	0

Table 2.1: Cost comparison for a marine acquisition geometry.

From both tables, we can find that the simultaneous random-phase encoding is the most efficient method for an OBS or a land acquisition geometry, which requires

Method	Number of wavefield propagations	Number of Green's functions to store
Direct computation	$N_x N_y N_\omega$	$M_x M_y M_z N_x N_y N_\omega$
Plane-wave, receiver-side	$(1 + N_{p_{rx}} N_{p_{ry}}) N_s N_\omega$	0
Plane-wave, simultaneous	$N_{p_{sx}} N_{p_{sy}} N_{p_{rx}} N_{p_{ry}} N_\omega$	0
Random, receiver-side	$(1 + N_{\text{realize}}) N_s N_\omega$	0
Random, simultaneous	$2 N_{\text{realize}} N_\omega$	0

Table 2.2: Cost comparison for an OBS or a land acquisition geometry.

only $2N_\omega$ wavefield propagations for one realization. If a marine acquisition geometry is used, it would be efficient to use the receiver-side random-phase encoding (if $N_s < N_x N_y$); the cost for one realization is comparable to that of a shot-profile migration. Plane-wave phase-encoding methods, however, may potentially need more wavefiled propagations than the direct method, depending on how many plane waves are used for computing the Hessian. Also note that the phase-encoding methods do not require storage of any Green's functions, which is a crucial benefit for large-scale applications, since the size of the Green's functions ($M_x M_y M_z N_x N_y N_\omega$) can easily reach an unaffordably large number. For example, for a target area with size $M_x = M_y = M_z = 100$ and survey area with size $N_x = N_y = 1000$, the Green's functions for a single frequency ($N_\omega = 1$) is about 8 terabytes (8 comes from the fact that the Green's function is a complex value).

SYNTHETIC-DATA EXAMPLES

In this section, I show several numerical examples for two different velocity models. The first is a simple constant-velocity model, which I use to verify the proposed algorithms for computing the Hessian; the second is the more complicated Sigsbee2A velocity model (Paffenholz et al., 2002), where the complex salt body prevents conventional wave-equation migration algorithms from producing reliable subsalt images. Therefore, it is useful to test if inversion by using the phase-encoded Hessian can improve the final image.

In the numerical examples, I compute Green’s functions by means of one-way wavefield extrapolation (Claerbout, 1985; Stoffa et al., 1990; Ristow and Rühl, 1994; Biondi, 2002). Since one-way wavefield propagation does not generate any back scatterings, the requirement of a smooth background velocity model can be relaxed. Although not discussed here, Green’s functions obtained using other methods, such as by solving two-way wave equation, can also be used under this framework.

Verification of the algorithm: A constant velocity model

I verify the proposed phase-encoding algorithms on a constant velocity model ($v = 2$ km/s) for several different acquisition geometries. Figure 2.1 shows the diagonal part of the Hessian (when $\mathbf{x} = \mathbf{x}'$) for an acquisition geometry containing one shot at -0.6 km and two receivers located at 0.6 km and 1.2 km on the surface. A ricker wavelet with a 20 Hz dominant frequency is used as the source function, and frequencies from 5 Hz to 35 Hz are used to generate the following results. Figure 2.1(a) is the exact diagonal of the Hessian, uncontaminated by any crosstalk artifacts. Figure 2.1(b) shows the Hessian with crosstalk, which is obtained using equation 2.8 with $\alpha(\mathbf{x}_r, \mathbf{p}_r, \omega) = 1$; the crosstalk can be easily identified as the vertical stripes on the right side of the image. Figure 2.1(c) is the receiver-side plane-wave phase-encoded Hessian with 31 plane waves stacked together. The crosstalk has been successfully removed, and Figure 2.1(c) looks very similar to Figure 2.1(a). Figure 2.1(d) shows the receiver-side randomly phase-encoded Hessian with one random realization; the crosstalk is dispersed throughout the image. Figures 2.1(e) and 2.1(f) show the results for 5 and 20 random realizations; as expected, the crosstalk is better attenuated by using more random realizations.

Figure 2.2 shows the Hessian with off-diagonals (with size 81×81) at image point $x = 0.5$ km, $z = 1.5$ km. The acquisition geometry is the same as that in Figure 2.1. The horizontal and vertical axes in Figure 2.2 denote the horizontal and vertical offsets away from the image point $x = 0.5$ km, $z = 1.5$ km. Figure 2.2(a) shows the exact Hessian. Since the illumination in the subsurface is very poor (only one source

and two receivers), we can observe two events intersecting at the origin (the diagonal element of the Hessian) and spreading out over the off-diagonals. When more sources and receivers are used, i.e., with better subsurface illumination, the energy in the local Hessian operator would be more focused at the origin (as illustrated in the subsequent examples). Figure 2.2(b) is the Hessian with crosstalk, where two extra undesired events are present in the operator; Figure 2.2(c) shows the receiver-side plane-wave phase-encoded Hessian, plane-wave-phase encoding successfully attenuates the crosstalk; Figures 2.2(d), 2.2(e) and 2.2(f) show the receiver-side randomly phase-encoded Hessian with different number of realizations.

In the next example, I change the acquisition geometry used in the previous example from two receivers to 401 receivers. The receivers range from -2 km to 2 km, with a spacing of 0.01 km. The source location is changed to -1 km. Once again, Figure 2.3 shows the diagonal part of the Hessian operator, while Figure 2.4 illustrates the off-diagonals at the image point $x = 0.5$ km, $z = 1.5$ km in the subsurface. Since the receiver spread is asymmetric with respect to the source location, the energy in the exact diagonal of Hessian (Figure 2.3(a)) is slightly tilted towards the right and the energy in the local Hessian operator shown in Figure 2.4(a) is well focused due to contributions from many receivers. However, when the Hessian is contaminated by crosstalk, the energy in the diagonal of the Hessian (Figure 2.3(b)) shows wrong orientation and the illumination pattern is very different from the correct one (Figure 2.3(a)); the local Hessian operator shown in Figure 2.4(b) is also far from focusing. The crosstalk is successfully attenuated by the proposed phase-encoding techniques, as shown in Figure 2.3(c) and Figure 2.4(c) for the receiver-side plane-wave-phase encoding (31 receiver-side plane waves are used), and Figure 2.3(d) and Figure 2.4(d) for the receiver-side random-phase encoding with one realization. Although the crosstalk is greatly suppressed in Figure 2.3(d) and Figure 2.4(d), some random noise appears in the background, which is caused by the random nature of the phase-encoding function. The random noise can be further suppressed by using more random realizations. Figure 2.3(e), Figure 2.4(e) and Figure 2.3(f), Figure 2.4(f) show the results with 5 and 20 random realizations, respectively. The crosstalk is greatly attenuated.

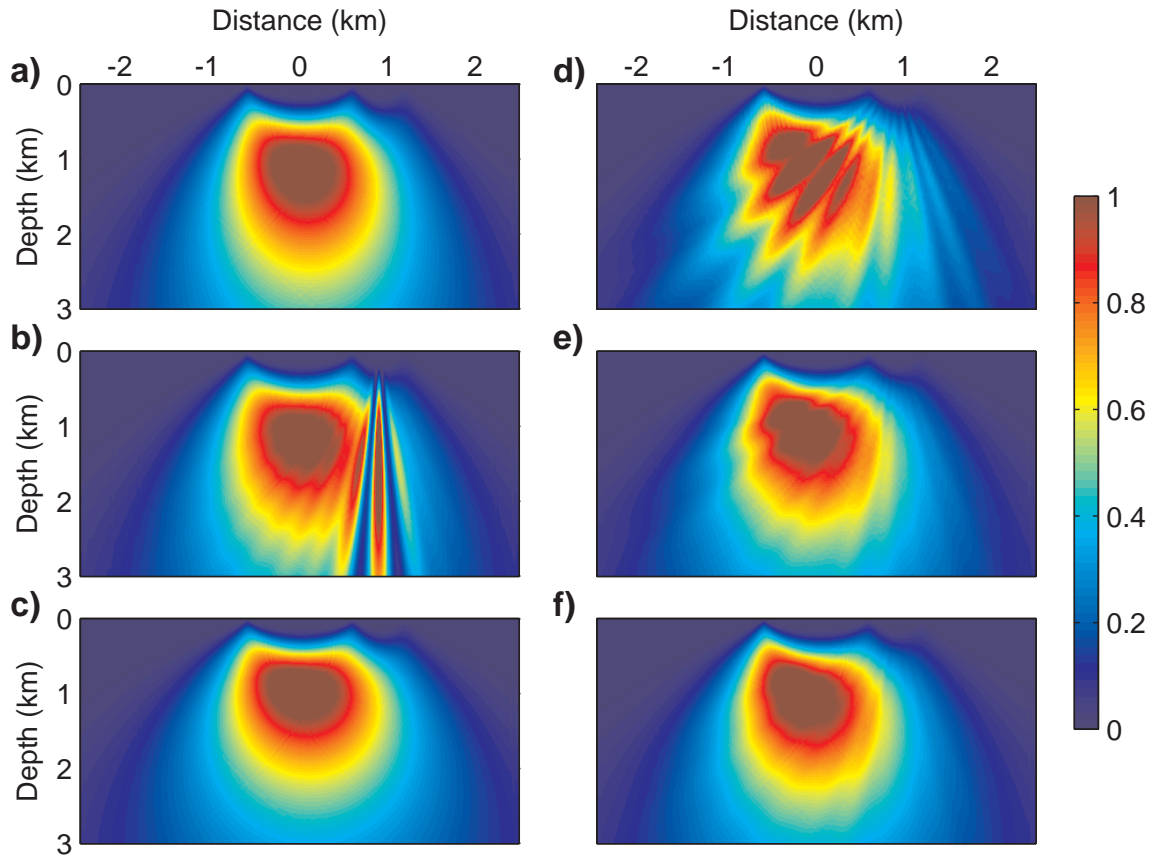


Figure 2.1: Diagonal of the Hessian for a constant-velocity model with one shot and two receivers. (a) The exact diagonal of the Hessian (equation 2.7); (b) the Hessian contaminated by crosstalk (equation 2.8 with $\alpha(\mathbf{x}_r, \mathbf{p}_r, \omega) = 1$); (c) the receiver-side plane-wave phase-encoded Hessian; (d), (e) and (f) are the receiver-side randomly phase-encoded Hessians obtained with 1, 5 and 20 random realizations, respectively.

[CR] chap2/. Figure1

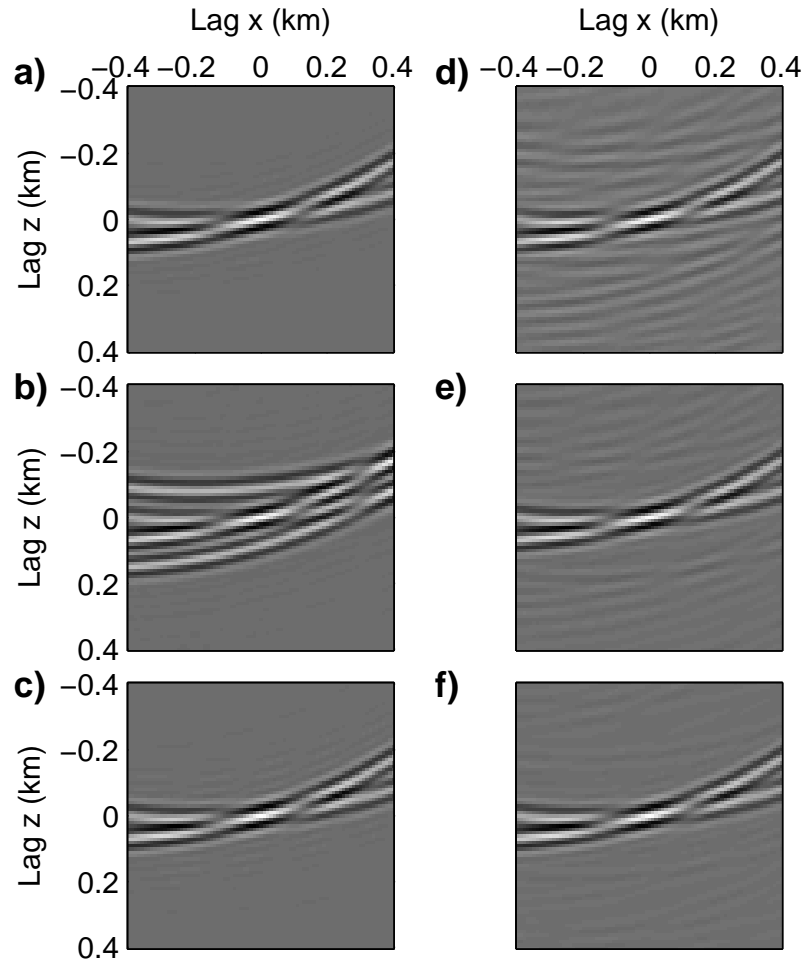


Figure 2.2: The local Hessian operator for image point $x = 0.5$ km, $z = 1.5$ km (a row of the Hessian matrix). The acquisition geometry is the same as that in Figure 2.1. The size of the Hessian operator is 81 samples in both x and z directions. (a) The exact Hessian; (b) The Hessian contaminated by crosstalk; (c) the receiver-side plane-wave phase-encoded Hessian; (d), (e) and (f) are the receiver-side randomly phase-encoded Hessian obtained with 1, 5 and 20 random realizations, respectively.

[CR] chap2/. Figure2

Instead of computing more random realizations, which may substantially increase the cost, we can use the fact that the randomized crosstalk can be well attenuated when many sources are used (this is almost always true in practice, where thousands of shots are often fired in acquiring field seismic data). Because the phase function is random both in space and frequency, stacking over more sources makes the phases of the crosstalk more inconsistent with each other, hence better suppresses these artifacts. Figure 2.5 and Figure 2.6 show examples when many sources are used for the same constant velocity model. In this case, a land acquisition geometry is used, where the receiver locations are fixed for all shots. The receiver location is the same as in the previous example, but now we have 401 shots from -2 km to 2 km with a 0.01 km spacing. Figure 2.5a shows the exact diagonal of the Hessian, while Figure 2.5(b) shows the diagonal of the receiver-side randomly phase-encoded Hessian with only one realization. As apposed to the previous example (Figure 2.3(d)), the crosstalk is greatly attenuated even with one random realization. Figure 2.6 compares the off-diagonals of the Hessian for the image point located at $x = 0.5$ km and $z = 1.5$ km; as we can see from the comparison, even with only one realization, the encoded Hessian is almost identical to the exact Hessian.

Application of the phase-encoded Hessian: Sigsbee2A model

To demonstrate an application of the explicit Hessian operator, I apply the image-domain inversion approach to the Sigsbee2A model (Paffenholz et al., 2002). Figure 2.7 shows the stratigraphic velocity model, which has been used for migration and Hessian computation. The original data is modeled using two-way wave equation with a marine-type acquisition geometry, where the receiver spread is moving along with the source (Paffenholz et al., 2002). There are 500 shots in total and the maximum offset for each shot is about 8 km. Though the data is modeled with two-way wave equation, in the following examples, one-way wave-equation-based Fourier finite-difference (FFD) (Ristow and Rühl, 1994) propagator is used for both migration and phase-encoded Hessian computation. The explicit Hessian operator is computed using the receiver-side random-phase encoding method with the frequency band from

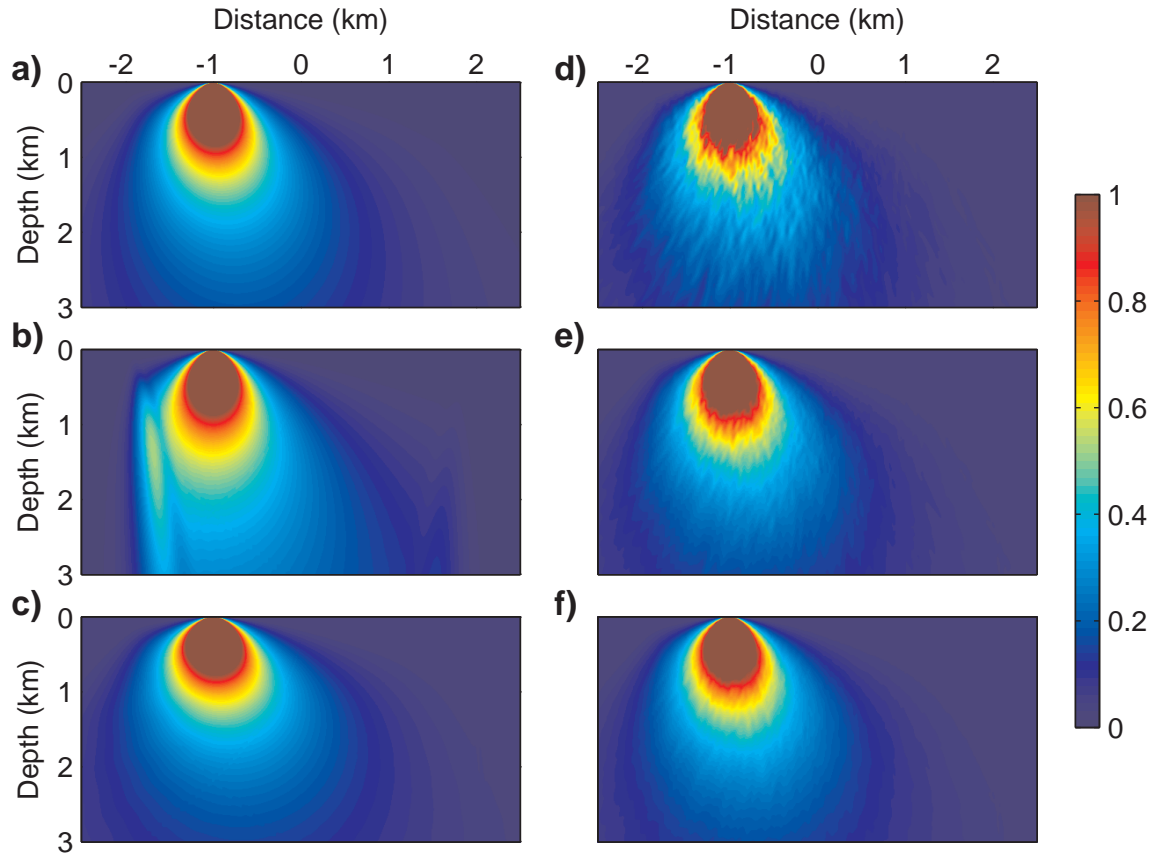


Figure 2.3: Diagonal of the Hessian for a constant-velocity model with one shot and 401 receivers. (a) The exact diagonal of the Hessian; (b) the Hessian contaminated by crosstalk; (c) the receiver-side plane-wave phase-encoded Hessian; (d), (e) and (f) are the receiver-side randomly phase-encoded Hessians obtained with 1, 5 and 20 random realizations, respectively. [CR] chap2/. Figure3

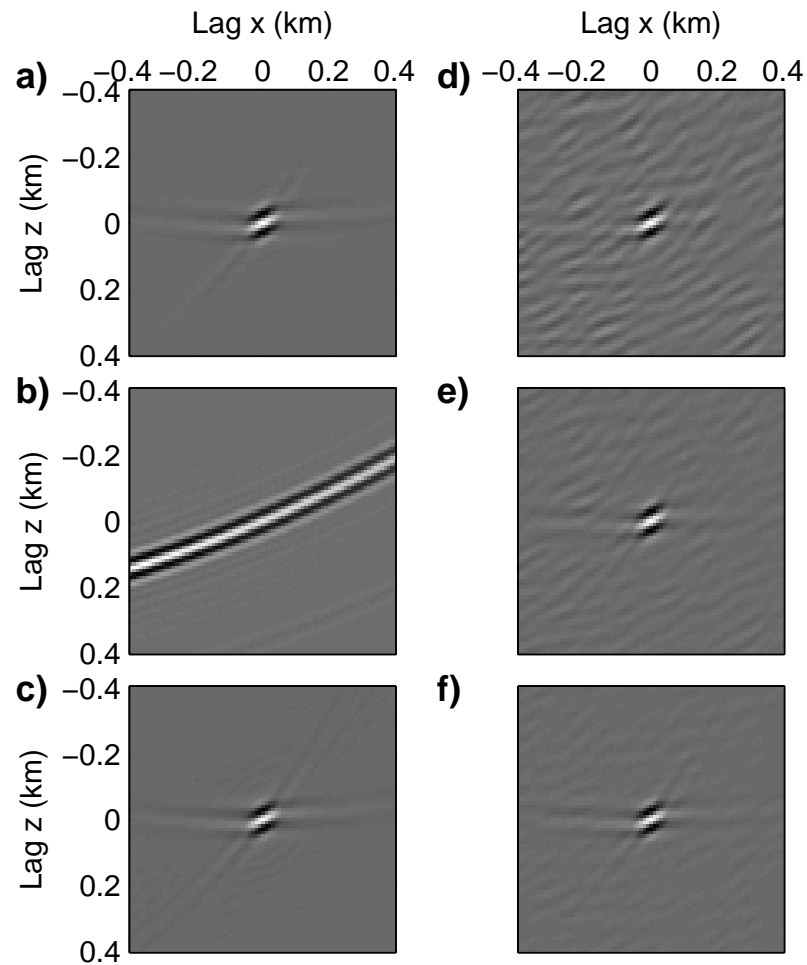


Figure 2.4: The local Hessian operator for image point $x = 0.5$ km, $z = 1.5$ km. The acquisition geometry is the same as that in Figure 2.3. (a) The exact Hessian; (b) The Hessian contaminated by crosstalk; (c) the receiver-side plane-wave phase-encoded Hessian; (d), (e) and (f) are the receiver-side randomly phase-encoded Hessian obtained with 1, 5 and 20 random realizations, respectively. [CR] chap2/. Figure4

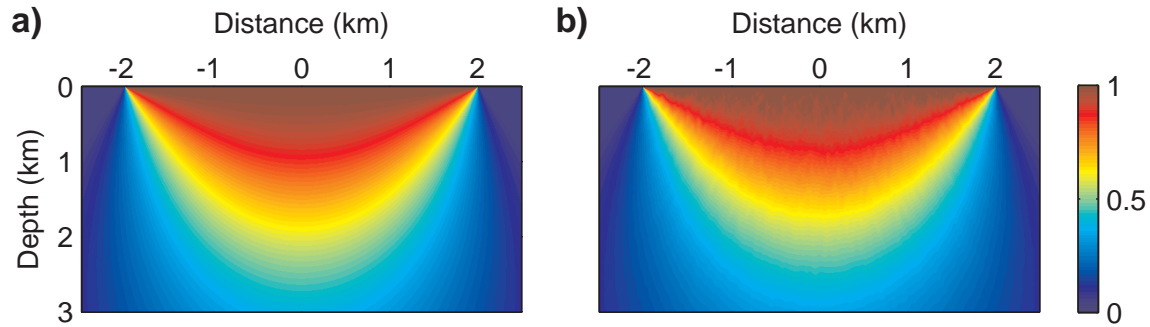


Figure 2.5: Diagonal of the Hessian with 401 shots and 401 receivers. (a) The exact diagonal of the Hessian; (b) the receiver-side randomly phase encoded Hessian with only one random realization. [CR] chap2/. Figure5

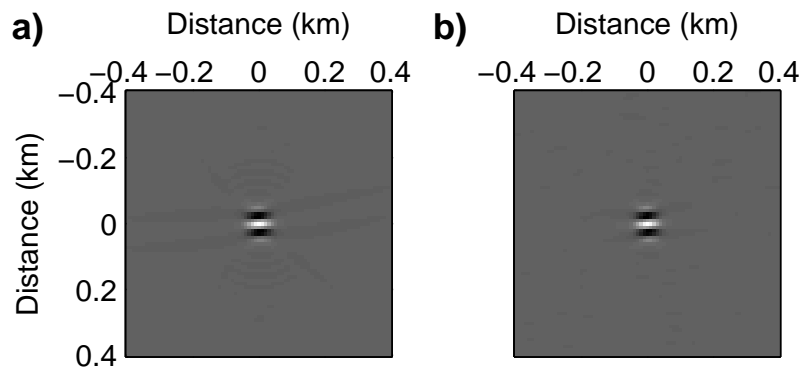


Figure 2.6: The local Hessian operator for image point at $x = 0.5$ km and $z = 1.5$ km. (a) The exact diagonal of the Hessian; (b) the receiver-side randomly phase encoded Hessian with only one random realization. [CR] chap2/. Figure6

5 Hz to 35 Hz, equivalent to that of the migrated image \mathbf{m}_{mig} . Only one realization has been used; because the number of shots is big, one realization is sufficient to provide reasonably good suppression of the crosstalk.

I use two different strategies of applying the explicit Hessian operator: the first is to compute only the diagonal of the Hessian operator and use it as a weight to normalize the migrated image; this is often known as the normalized migration (Rickett, 2003) or amplitude-preserving migration (Plessix and Mulder, 2004). The other strategy is to compute a limited number of Hessian off-diagonals, and then iteratively minimize the image-domain objective function $J(\mathbf{m})$ (equation 2.6) to find an optimum reconstruction of the reflectivity \mathbf{m} . In this example, the number of the off-diagonal elements is chosen by trial and error and each local Hessian filter has 21×21 elements, the size of which seems to be big enough to capture most of the energy even for poorly illuminated areas. A linear conjugate-gradient solver and a simple damping regularization that minimizes the energy of the model parameters are used for the image-domain iterative inversion.

Normalized migration

Figure 2.8 shows the diagonal of the receiver-side randomly phase-encoded Hessian. Note the uneven illumination below the salt caused by the complex salt body and limited acquisition geometry. For comparison, Figure 2.9 shows the source-wavefield intensity, computed using $H_{SI}(\mathbf{x}, \mathbf{x}) = \sum_{\omega} \omega^4 \sum_{\mathbf{x}_s} |f_s(\omega)G(\mathbf{x}, \mathbf{x}_s, \omega)|^2$. $H_{SI}(\mathbf{x}, \mathbf{x})$ is a crude approximation to the exact diagonal of Hessian, because it assumes the constant receiver-side Green's functions and ignores the effects of the limited receiver aperture. It over-estimates the total energy that enters the earth and returns to be recorded by the receivers. This is why Figure 2.9 shows stronger, but less accurate, illumination below the salt. The overall pattern in Figure 2.9 is also quite different from that in Figure 2.8.

Figure 2.10 shows the conventional one-way wave-equation shot-profile migrated image, where the unbalanced amplitudes caused by uneven illumination below the salt

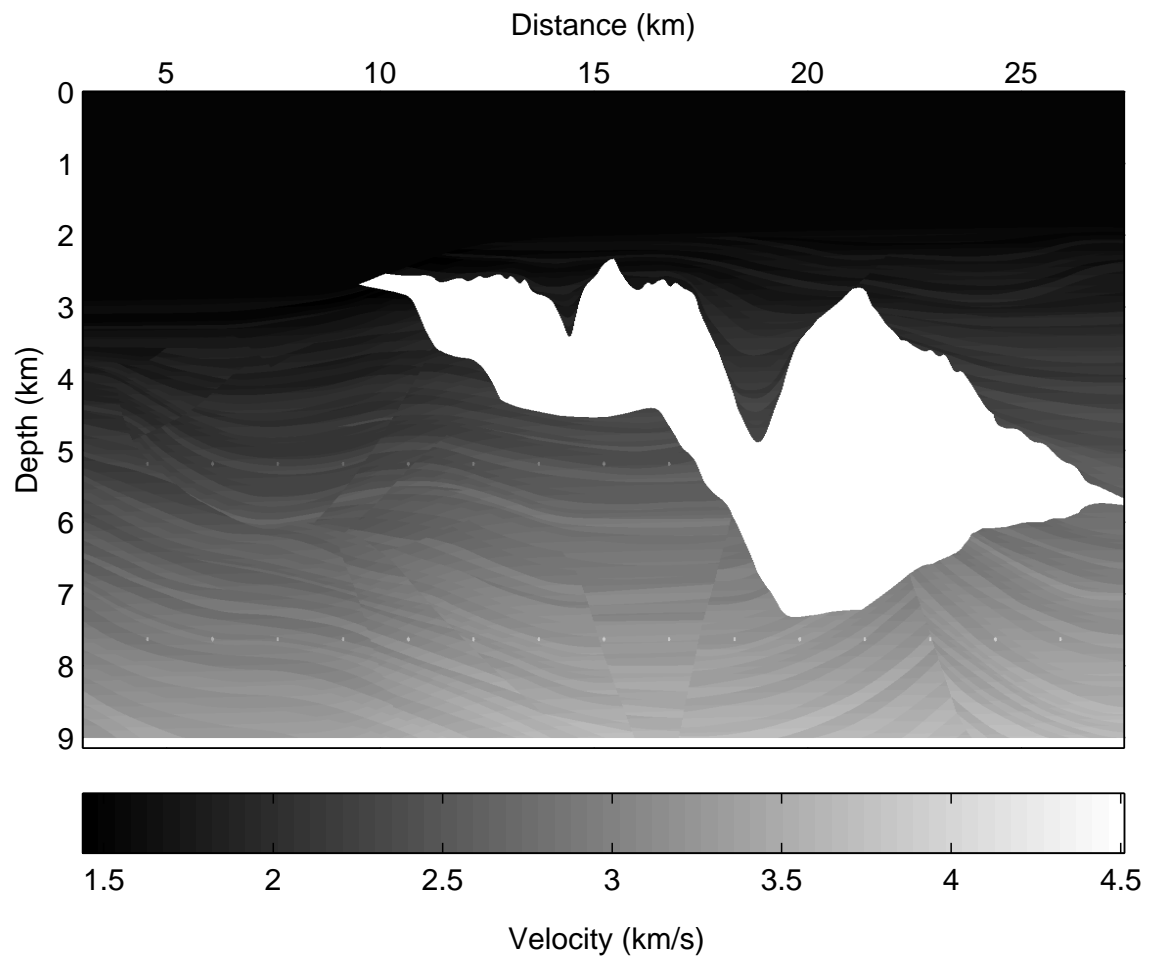


Figure 2.7: Sigsbee2A stratigraphic velocity model. [ER] chap2/. Figure7

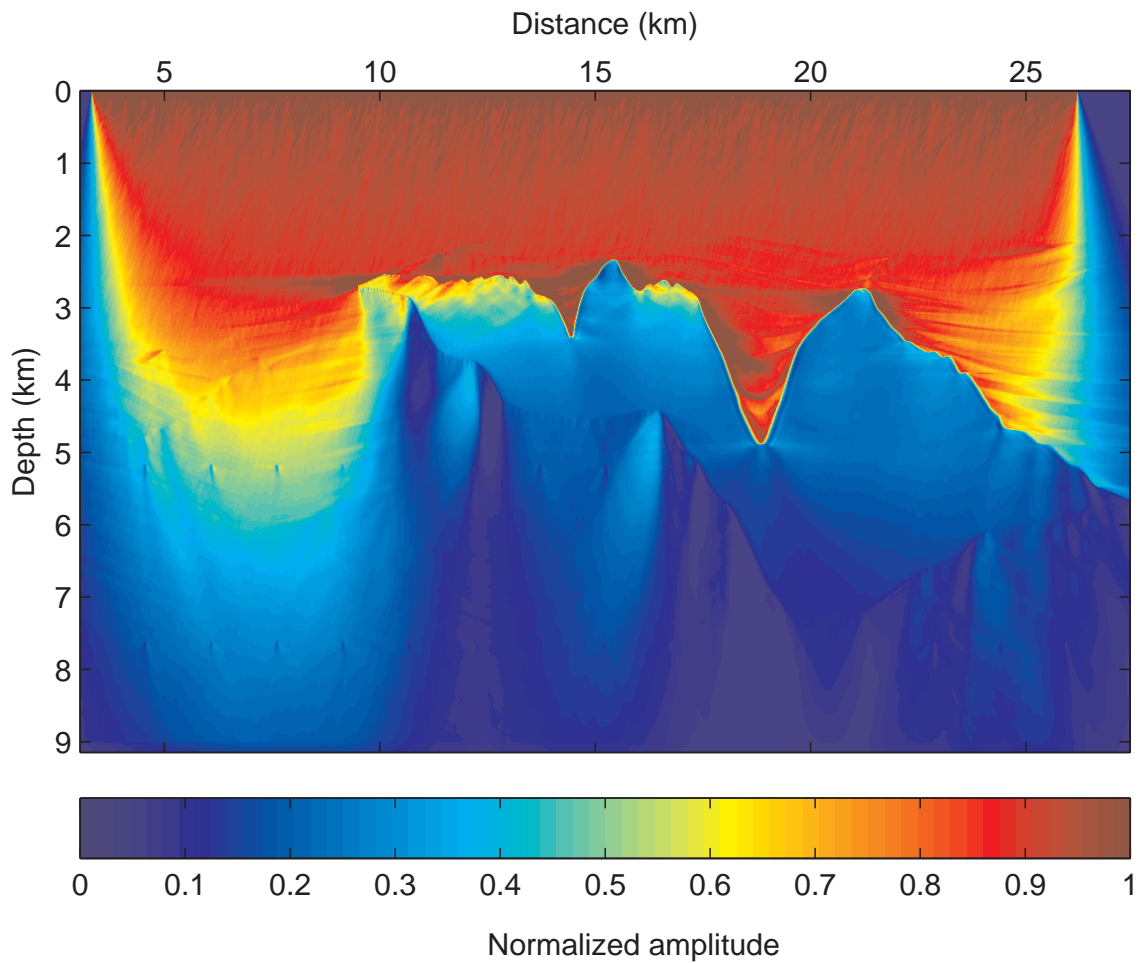


Figure 2.8: Diagonal of the Hessian for the Sigsbee2A model. The Hessian is obtained by using receiver-side random-phase encoding, which takes the limited receiver array into consideration. The result shows the Hessian for a frequency band from 5 Hz to 35 Hz. [CR] chap2/. Figure8

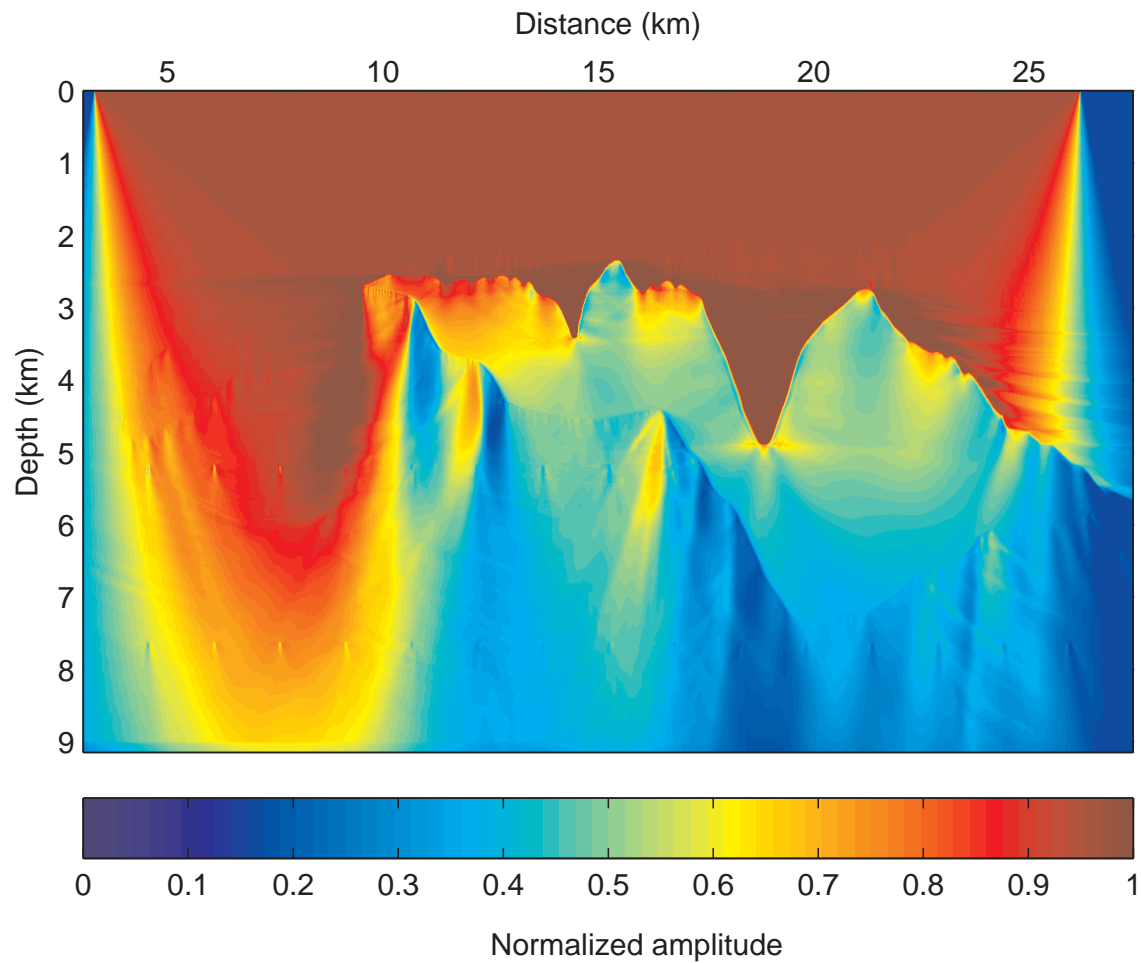


Figure 2.9: Source-wavefield intensity for the Sigsbee2A model, which assumes the receiver-side Green's functions to be constant; it ignores the effects of the limited receiver aperture and over-estimates the total energy that enters the earth and returns to be recorded by the receivers. [CR] [chap2/. Figure9](#)

are easily identified. Figure 2.11 and Figure 2.12 show the migrated image normalized with the diagonal of the phase-encoded Hessian (Figure 2.8) and the source-wavefield intensity (Figure 2.9), respectively. All three figures are plotted with the same scale. Figure 2.11 shows more balanced amplitudes across the section than Figure 2.12, especially in areas below the salt. However, also note that normalized migration does not help improve the resolution of the image, this is because the diagonal of the Hessian only serves as a scaling factor, it has no deconvolution effects. The resolution can be improved by using the off-diagonal elements of the Hessian matrix as shown in the subsequent examples.

Target-oriented inversion

The image-domain target-oriented inversion is performed to a selected area below the salt. Figure 2.13 shows the receiver-side randomly phase-encoded Hessian operator for a particular region of interest: Figure 2.13(a) shows the diagonal part of the Hessian operator; Figure 2.13(b) is obtained by convolving the Hessian operator (21×21 in size) with a collection of point scatterers (impulse responses). It demonstrates the varying shapes and non-stationarities of the Hessian operators across the section. Note that in well-illuminated areas, the Hessian operator is compact, while in poorly illuminated areas, the Hessian operator is tilted and smeared and has a preferred dipping orientation, which means these image points are illuminated by only a few dip angles.

Figure 2.14 shows the comparison between migration and inversion: Figure 2.14(a) is the migrated image, and Figure 2.14(b) is the inverted image obtained using the randomly phase-encoded Hessian operator. The result is obtained after 20 iterations of the linear conjugate-gradient method. Figure 2.15 plots the normalized residual as a function of iteration number; the residual converges after about 12 iterations. In the inversion result, the effects of uneven illumination are corrected, the inverted image looks slightly sharper and crisper than the migrated image; the shadow zones that in the migrated image are now filled in with structures (circled areas), and the sediments (the area outlined by the top circle) and the dipping faults (indicated with arrows)

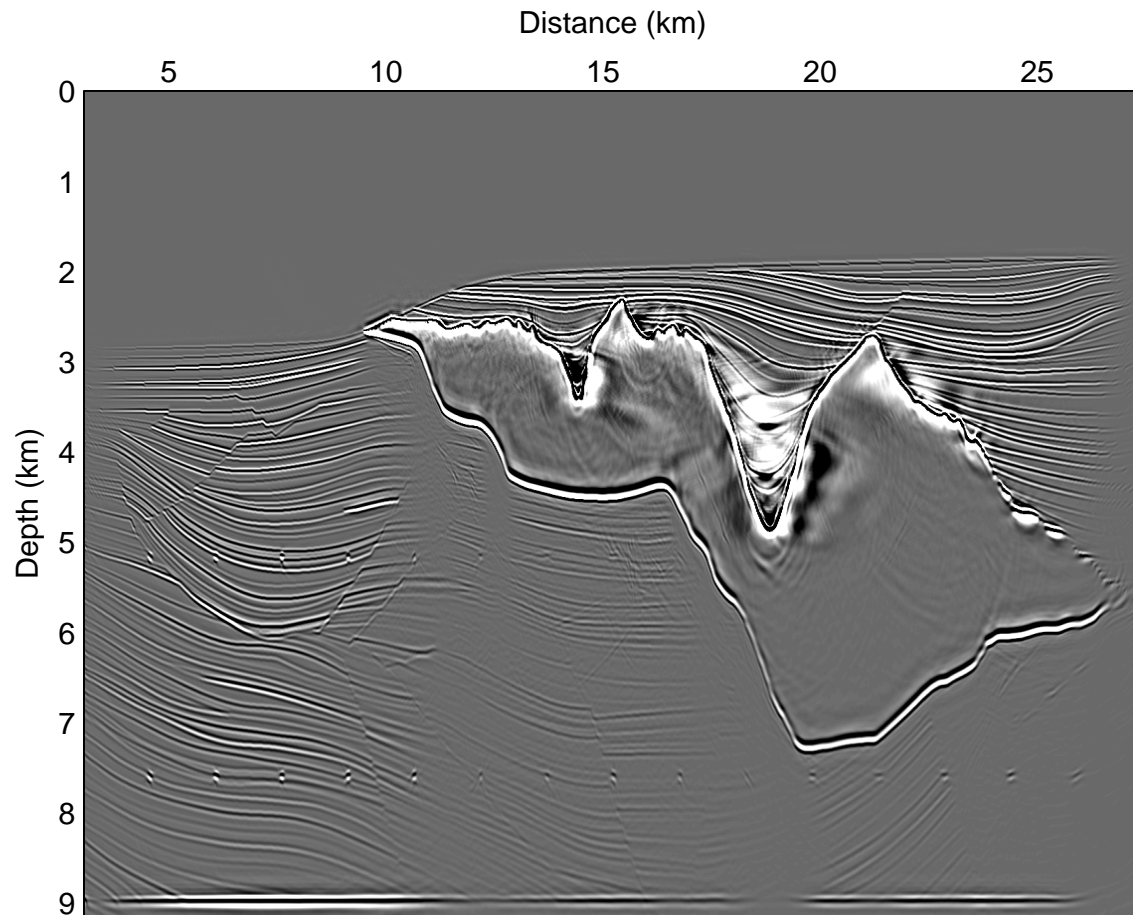


Figure 2.10: Conventional one-way wave-equation shot-profile migration result of the Sigsbee2A model. Note the uneven illumination below the salt. [CR] chap2/. Figure10

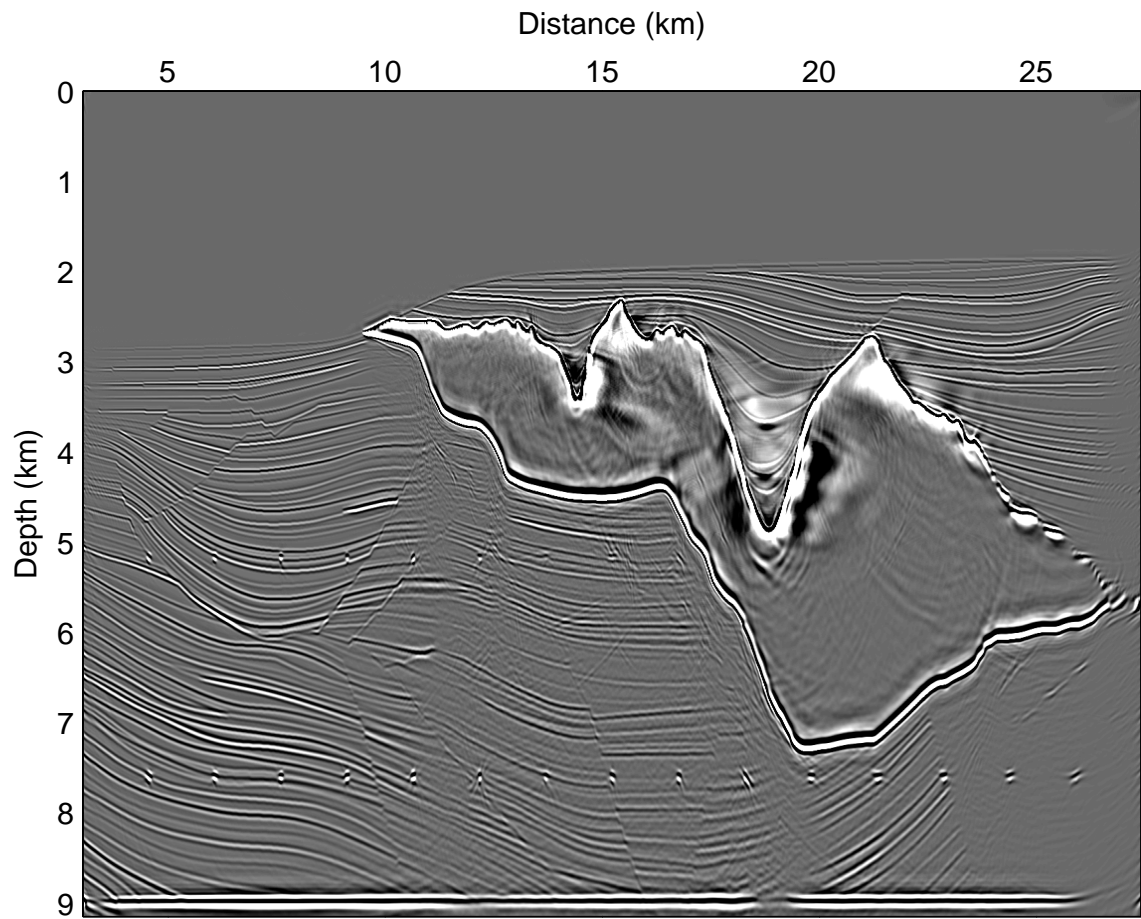


Figure 2.11: The migrated image (Figure 2.10) is normalized by the diagonal of the Hessian shown in Figure 2.8. [CR] chap2/. Figure11

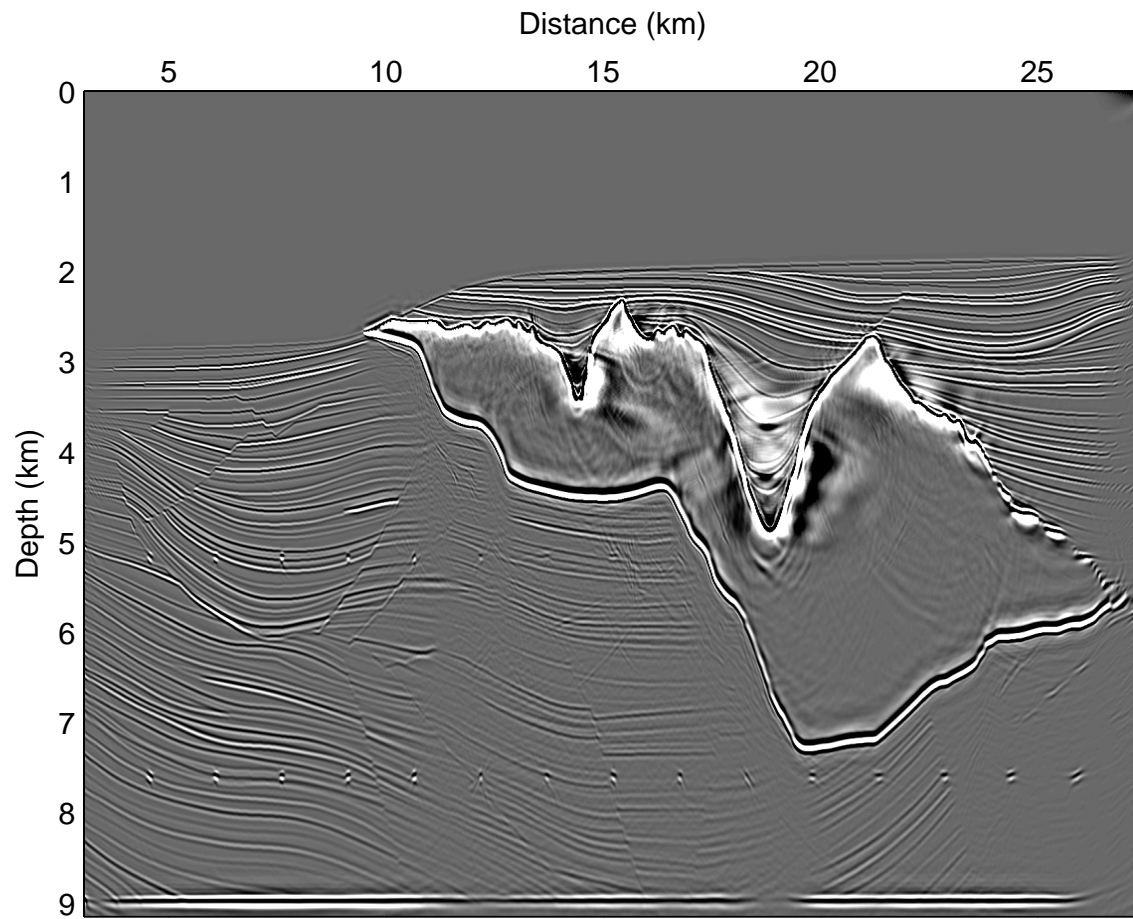


Figure 2.12: The migrated image (Figure 2.10) is normalized by the source-wavefield intensity shown in Figure 2.9. [CR] chap2/. Figure12

extend much closer to the salt body. The improved image helps locate sediment truncations against salt, which are important in finding subsalt structural traps. For comparison, Figure 2.14(c) shows the filtered true reflectivity.

A close-up comparison for areas around the point diffractors is shown in Figure 2.16. Figure 2.17 compares the amplitude spectrum of the migrated image (Figure 2.16(a)) and the inverted image (Figure 2.16(b)); the inverted image shows a broader range of spatial frequencies, suggesting improved spatial resolution. Figure 2.18 shows a horizontal trace located at depth level 5.2 km (slicing through the diffractors) extracted from different images shown in Figure 2.16. The inverted result (the dashed line) better predicts the true reflectivity (the dotted line) than the migrated result (the solid line).

DISCUSSION

The image-domain inversion approach, which requires building the Hessian operator $\mathbf{L}^*\mathbf{L}$, squares the condition number of the Born modeling operator \mathbf{L} . Generally speaking, the Hessian is often ill-conditioned, and inverting the Hessian is sensitive to roundoff errors. Hence, regularization should be used to stabilize the inversion process.

The inverted image, Figure 2.14(b), also shows increased noise, for example, at around horizontal distance 11 km and depth level 4 km, where the illumination is extremely poor. This is partially due to the null space of the Hessian operator. Another possible contribution might be the randomized crosstalk introduced in the randomly phase-encoded Hessian. This can be a concern, since the accuracy of the Hessian may affect the convergence of inversion. However, a small amount of random noise in the operator might also be useful if one considers it as a random regularization, hence, it may have the chance to improve the condition number of the Hessian operator, making it easier to invert. To suppress the noise, more sophisticated regularization that better predicts the inverse of the model covariance, such as roughening along reflection angles (Kühl and Sacchi, 2003; Clapp, 2005) or geological dips (Prucha and

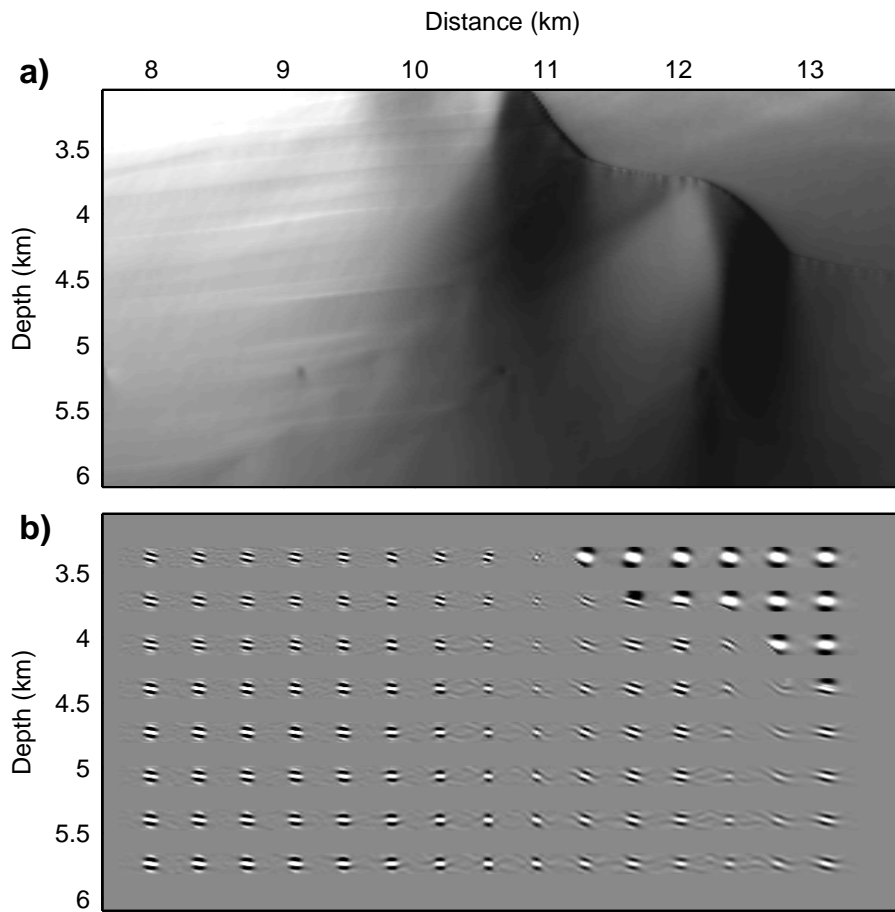


Figure 2.13: Receiver-side randomly phase-encoded Hessian operators for the Sigsbee2A model. Panel (a) shows the diagonal part for a particular region of interest under the salt. Note the uneven illumination due the complex salt body and limited acquisition geometry. Panel (b) shows the result obtained by convolving the Hessian operator (with a size 21×21) with a collection of point scatterers. Note the non-stationarities of the operators. [CR] chap2/. Figure13

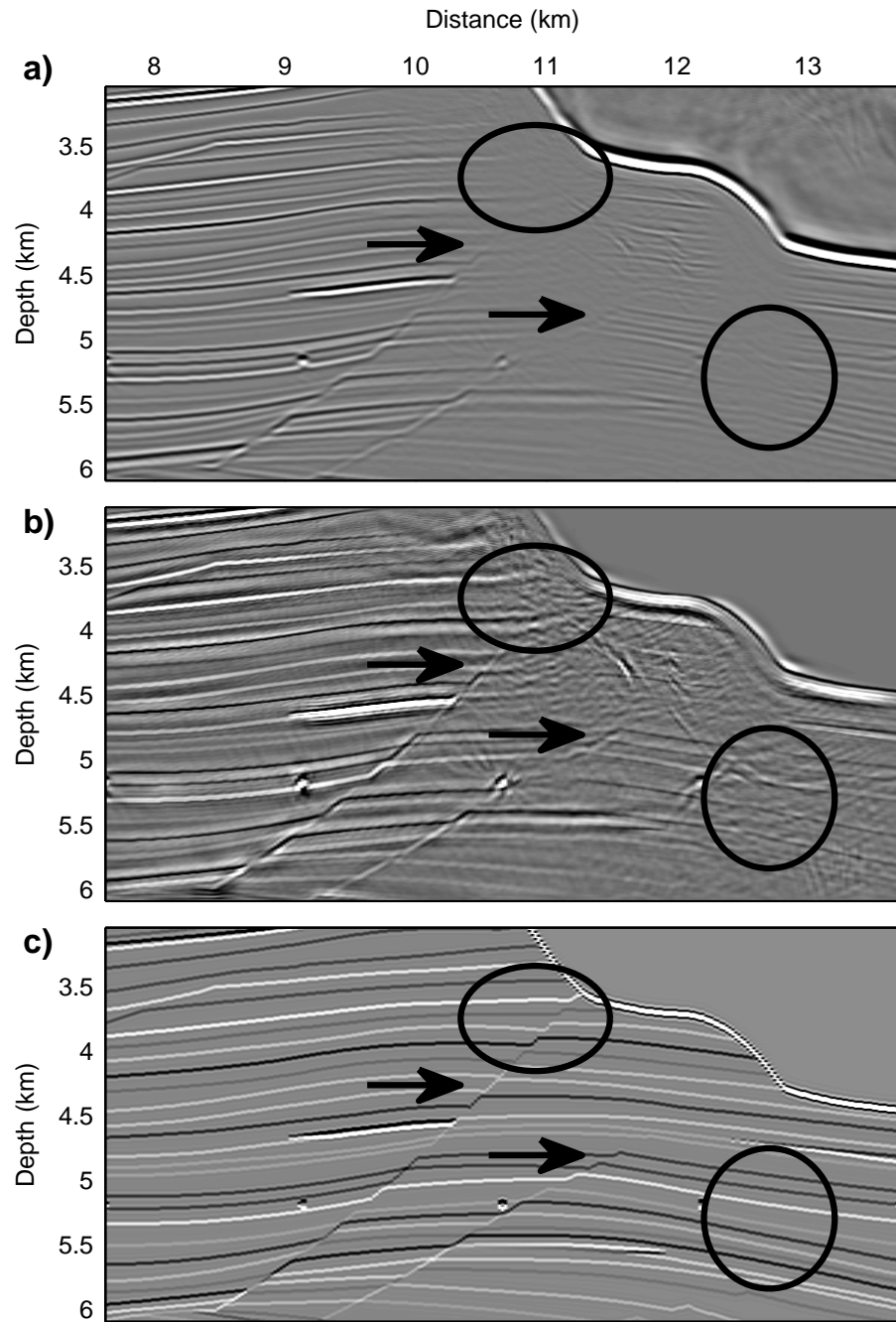


Figure 2.14: Comparison between migration and inversion. Panel (a) shows the migrated result, (b) shows the inversion result using the receiver-side randomly phase-encoded Hessian operator, and (c) is the filtered true reflectivity. All three panels are plotted with the same scale. [CR] chap2/. Figure14

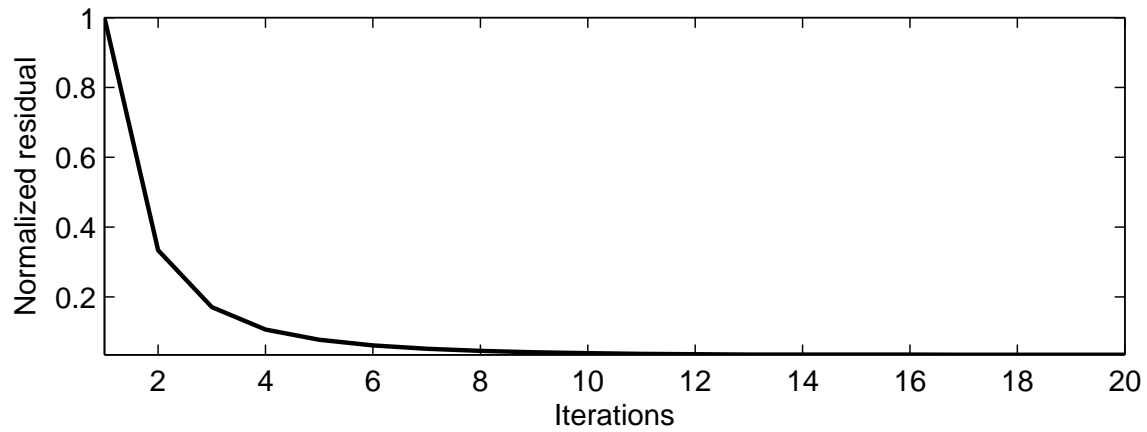


Figure 2.15: Normalized residual vs. number of iterations for the Sigsbee2A model; the inversion converges after about 12 iterations. [CR] chap2/. Figure15

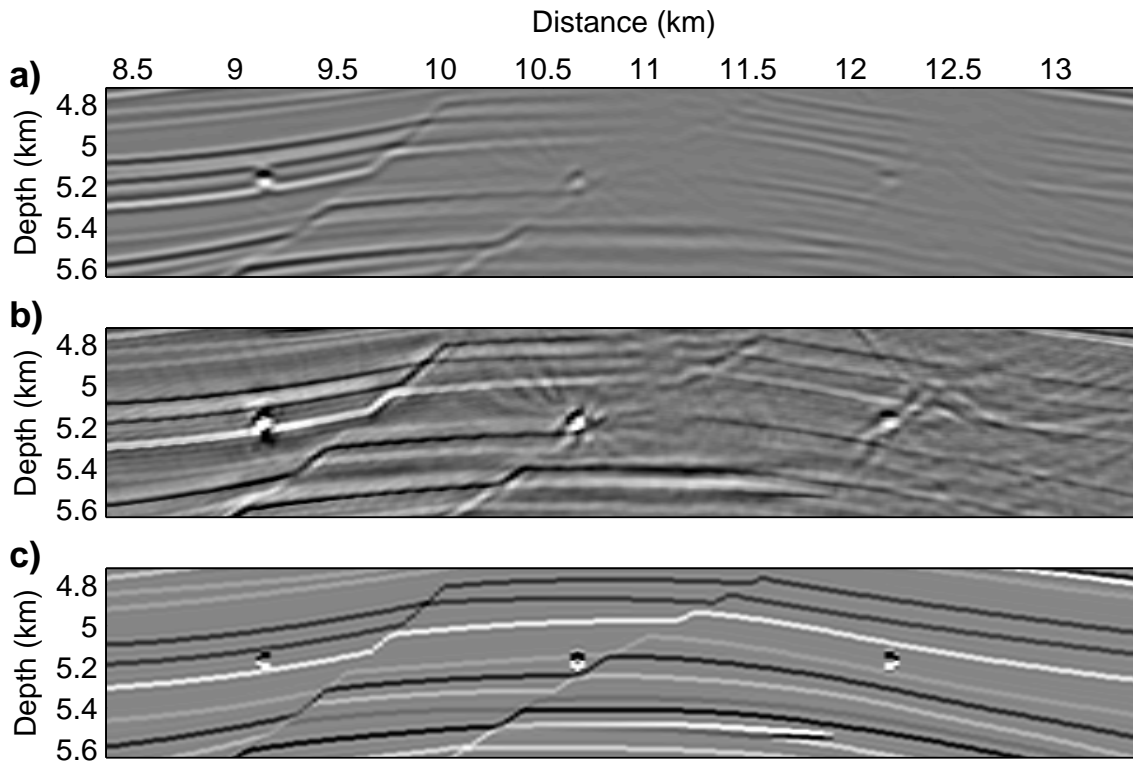


Figure 2.16: A close-up view of (a) the migrated image, (b) the inverted image and (c) the filtered true reflectivity model. [CR] chap2/. Figure16

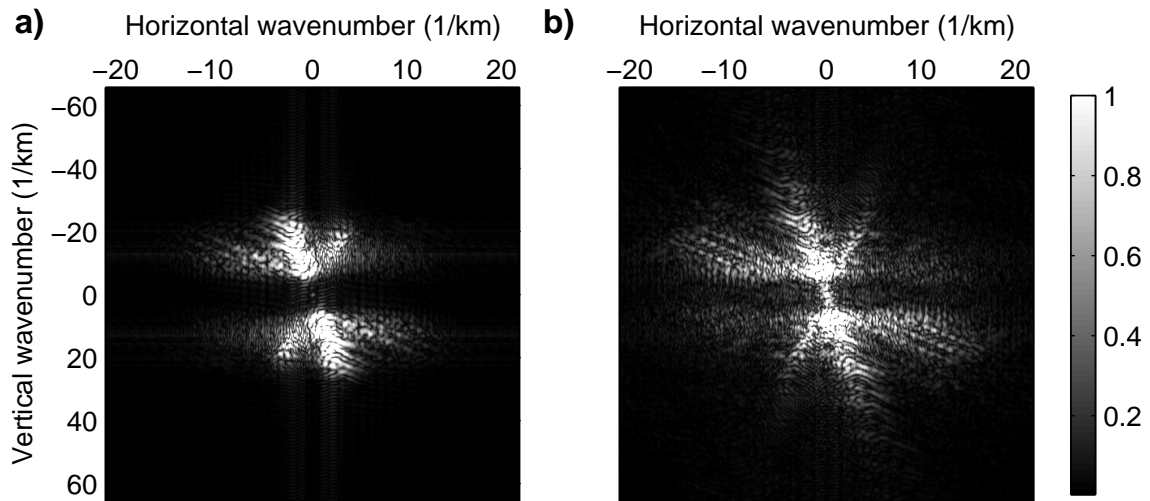


Figure 2.17: The amplitude spectrum of (a) the migrated image (Figure 2.16(a)) and (b) the inverted image (Figure 2.16(b)). Note the inverted image contains a broader range of spatial frequencies. [CR] chap2/. Figure17

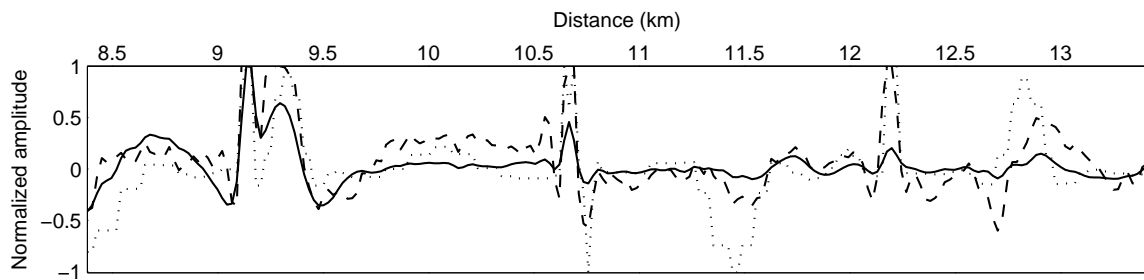


Figure 2.18: A horizontal trace at depth 5.2 km extracted from images shown in Figure 2.16. The dotted line, solid line and dashed line represent traces extracted from the true reflectivity model, the migrated image and the inverted image, respectively. [CR] chap2/. Figure18

Biondi, 2002; Clapp, 2005), can be introduced in the inversion process. I explore dip-regularized inversion in Chapter 4 and apply it to a 3-D field data set acquired from the Gulf of Mexico.

The least-squares migration approach assumes single scattering (Born approximation), other coherent energy, such as multiple, does not fit into this inversion framework. In the Sigsbee2A example, the internal multiple at around $x = 11.6$ km and $z = 4.2$ km in the migrated image (Figure 2.14(a)) becomes even more pronounced in the inverted image (Figure 2.14(b)). Hence, multiple suppression is suggested prior to inversion.

CONCLUSIONS

This chapter develops a method based on phase encoding to very efficiently and accurately compute the explicit Hessian operator, which is then used in image-domain least-squares migration to invert for the reflectivity in a target-oriented fashion. The proposed algorithm for computing the Hessian does not require storing Green's functions, which is often too big to be affordable in practice. Hence, the phase-encoded Hessian has the potential to be applied to large-scale problems at a lower cost. Although this chapter demonstrates examples with one-way wave equation, the theory for computing the phase-encoded Hessian is not limited to one-way wave equation. Two-way wave equation can also be used in a similar way to compute the phase-encoded Hessian, which may bring even more savings in computational cost. The phase-encoded Hessian using two-way wave equation may also be applied as a preconditioner for the full waveform inversion problem (Tang and Lee, 2010).

The target-oriented inversion examples on the Sigsbee2A model show that wave-equation least-squares migration/inversion can partially correct the effects of uneven illumination, and it can produce an image with more balanced amplitudes and higher spatial resolution than that produced by migration, especially in areas with low illumination and shadow zones. Thus it provides a good tool for imaging complex geologies.

ACKNOWLEDGMENTS

I thank Alejandro Valenciano and Biondo Biondi for enlightening discussions. I acknowledge SMAART JV for providing the Sigsbee2A data set.

Chapter 3

Target-oriented wavefield tomography

This chapter presents a method for estimating the background velocity in a target-oriented fashion using wavefield-based tomography. A target-oriented velocity inversion strategy is attractive, because it can significantly reduce the computational cost of wavefield-based velocity estimation, which is still high for industrial-scale applications. In addition, it can greatly increase the flexibility of wavefield-based methods, by making it possible to improve velocities only where necessary, such as in challenging subsalt regions, where conventional ray-based tomography often fails.

Target-oriented wavefield tomography is achieved by synthesizing a new data set specifically for velocity analysis. This new data set is generated from an initial unfocused image by a novel application of generalized Born wavefield modeling, extended from conventional Born modeling (Chapter 2) to include prestack parameters, such as the subsurface offset. The inclusion of the prestack parameters in the modeling process preserves the correct velocity information and is crucial to the success of this method. As will be shown in this chapter, the new data set can be synthesized for a specific target region where velocities are inaccurate. Therefore, the new data set can be much smaller than the original one while still containing the necessary velocity

information for successful velocity analysis. These features make this target data set suitable for fast, interactive velocity model-building. I demonstrate the performance of this method on both a 2-D synthetic data set and a 2-D field data set acquired from the Gulf of Mexico, where I update the subsalt velocity in a target-oriented fashion and obtain a subsalt image with improved continuity and signal-to-noise ratio and flattened angle-domain common-image gathers.

INTRODUCTION

Velocity estimation is always a challenging task in exploration seismology. In the past decade, ray-based tomography has been widely used in practice to derive velocity models. Although ray-based methods are efficient, the infinite-frequency approximation and the caustics inherent in ray theory prevent them from accurately modeling complicated wave phenomena (Hoffmann, 2001). As seismic exploration moves towards structurally more complex areas, ray-based methods become less reliable. In contrast, wave-equation-based tomography (Tarantola, 1984; Mora, 1989; Woodward, 1992; Pratt, 1999; Sava, 2004; Shen, 2004) uses wavefields as carriers of information. It more accurately describes the band-limited wave phenomena, and therefore is more suitable for complex geologies.

Wavefield tomography can be implemented in either the data domain or the image domain. In this chapter, I focus on image-domain wavefield tomography, which is also widely known as wave-equation migration-velocity analysis (Biondi and Sava, 1999; Sava, 2004; Shen, 2004). It optimizes the velocity model by minimizing the image inconsistency (or by maximizing the image coherence). Despite its advantages in modeling band-limited wavefields, practical applications of image-domain wavefield tomography are still rare and small in scale (Shen et al., 2005; Albertin et al., 2006; Fei et al., 2009). One impediment to more general use is its huge computational cost, which is due to the use of expensive wavefield modeling engines. Another is that it lacks flexibility, usually requiring use of the entire recorded data set for velocity estimation.

Several methods have been proposed to make image-domain wavefield tomography more cost-effective. The main idea is to reduce the size of the data set used for velocity estimation. One method is to assemble the originally recorded point-source gathers into a smaller number of areal-source gathers (Romero et al., 2000). The plane-wave source gather (Whitmore, 1995; Zhang et al., 2005; Shen and Symes, 2008; Tang et al., 2008) is the most popular choice for this because the plane-wave phase-encoding function is effective in attenuating crosstalk artifacts (Liu et al., 2006; Tang, 2008). But this strategy lacks flexibility, and full-domain wavefield propagation is still required at each velocity inversion iteration. Therefore, the cost reduction cannot be substantial.

Biondi (2006, 2007), Guerra et al. (2009) and Guerra (2010) approach this problem in a completely different way. They synthesize a new data set based on the initial image using the concept of prestack-exploding-reflector modeling. The new data set is then used specifically for velocity analysis. The advantage of this strategy is that it can model a new data set in a target-oriented fashion; therefore the wavefield propagation can be restricted to regions with velocity inaccuracies, substantially reducing the computational cost. However, the modeling generates crosstalk when multiple image events (reflectors) are modeled simultaneously. This limits the number of reflectors it can model. Manual picking and stochastic encoding methods, such as random-phase encoding, are required to mitigate the impact of the crosstalk (Guerra, 2010).

In this chapter, I present a new strategy to reduce the size of the data set used for image-domain wavefield tomography. The proposed strategy combines advantages of both prestack-exploding-reflector modeling and data-domain encoding. For example, not only can it model a new data set in a target-oriented fashion, but it also can use plane-wave sources to effectively attenuate the crosstalk. I start with initial subsurface-offset-domain common-image gathers (SODCIGs) obtained using a starting velocity model. The initial SODCIGs are further normalized using the diagonal of the imaging Hessian, efficiently computed using the phase-encoding method (Chapter 2), to optimally compensate for the uneven subsurface illumination and remove

the effects of the original acquisition geometry. Instead of using prestack-exploding-reflector modeling, I generalize the Born modeling method (Chapter 2) to include the SODCIGs in the modeling process and use it to simulate a new data set. As I demonstrate, the inclusion of the SODCIGs is crucial to correctly preserving the velocity information in the modeled new data set. When we do so, the corresponding image gathers obtained using this new data set are consistent in kinematics and amplitudes with those obtained using the original data set. Therefore, the new data set can be used for wavefield-based tomography.

I also show that the proposed modeling strategy is much more flexible than prestack-exploding-reflector modeling. Except for windowing out the target image from the initial image, no picking is necessary, but picking can also be introduced if desired. Human intervention can also be incorporated by carefully conditioning the initial image to be modeled.

The generalized Born modeling procedure is based on the single-scattering approximation to the full wave equation. The resulting data are obtained by convolving the source wavefield, computed using any type of source function (e.g. plane-wave sources), with the initial image gathers and then propagating the convolved wavefields to receiver locations, which can be located anywhere in the model. The target-oriented new data set is obtained by modeling image points only within a target zone or several key reflectors that carry important velocity information. This strategy can be related to datuming, but it is more general and more flexible than datuming, because it allows the computation to be localized not only in depth but also in lateral directions. This target-oriented strategy is useful, because it enables us to use wavefield-based velocity estimation to focus on improving velocities in the most challenging areas, e.g., subsalt regions, where conventional ray-based tomography often fails. The proposed strategy is also extremely efficient, because it uses a much smaller data set for velocity analysis and propagates wavefields only within the target region that has velocity inaccuracies. This important property makes the proposed strategy suitable for interactive wavefield-based velocity model-building, where it enables interpreters to test different geological scenarios in quasi-real time.

I use differential semblance optimization (DSO) (Symes and Carazzone, 1991; Shen, 2004) for velocity analysis, which has the advantage that it can be fully automated. But the synthesized Born data set is not limited to DSO; other criteria, such as maximizing image stack power (Soubaras and Gratacos, 2007), or differential residual migration fitting (Sava and Biondi, 2004a,b), could also be used to optimize the velocity.

In the next section, I introduce the theory of generalized Born modeling. In the subsequent sections, I apply the proposed target-oriented velocity-estimation method to both synthetic and field data sets to demonstrate the performance of this method.

TARGET-ORIENTED BORN WAVEFIELD MODELING

The proposed data-reduction method can be formulated under the framework of seismic data mapping (SDM) (Hubral et al., 1996; Bleistein and Jaramillo, 2000), where the approach is to transform the originally observed seismic data from one acquisition configuration to another with a designed mapping operator. SDM can be divided into two main steps, as illustrated in Figure 3.1: (1) apply the (pseudo-) inverse of the designed mapping operator to the original data set to generate a model, and (2) apply the forward mapping operator to the model to generate a new data set with a new acquisition configuration. This idea has been widely used in seismic data interpolation and regularization. For example, in Radon-based interpolation methods (Sacchi and Ulrych, 1995; Trad et al., 2002), the Radon operator is used as the mapping operator to regularize the data; azimuth moveout (AMO) (Biondi et al., 1998) uses dip moveout (DMO) as the mapping operator to transform the data from one azimuth to another.

I use wave-equation-based Born modeling (a.k.a. demigration) as the data-mapping operator. Instead of using the conventional Born modeling (Chapter 2), which models the reflection data from a stacked image (or reflectivity), I generalize the modeling operator to include prestack parameters, such as the subsurface offset (Rickett and

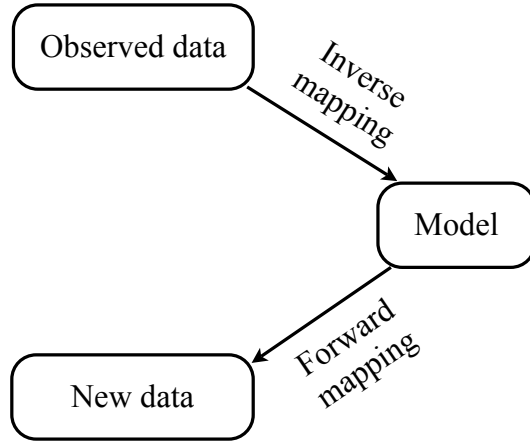


Figure 3.1: Flow diagrams of seismic data mapping. [NR]

chap3/. sdm

Sava, 2002; Sava and Fomel, 2003), as follows:

$$\begin{aligned}
 L(\mathbf{x}, \mathbf{h}, \mathbf{x}_r, \mathbf{x}_s, \omega) &= \omega^2 W(\mathbf{x}_r, \mathbf{x}_s) f_s(\omega) G(\mathbf{x} - \mathbf{h}, \mathbf{x}_s, \omega) \\
 &\quad \times G(\mathbf{x} + \mathbf{h}, \mathbf{x}_r, \omega),
 \end{aligned} \tag{3.1}$$

where $L(\mathbf{x}, \mathbf{h}, \mathbf{x}_r, \mathbf{x}_s, \omega)$ is one component of the generalized Born modeling operator; it is a function of the image point $\mathbf{x} = (x, y, z)$, the subsurface offset \mathbf{h} , the receiver coordinates $\mathbf{x}_r = (x_r, y_r, 0)$, the source coordinates $\mathbf{x}_s = (x_s, y_s, 0)$ and the angular frequency ω ; $f_s(\omega)$ is the source signature; $W(\mathbf{x}_r, \mathbf{x}_s)$ is the acquisition mask operator, which contains ones where we record data and zeros where we do not; and $G(\mathbf{x}, \mathbf{x}_s, \omega)$ and $G(\mathbf{x}, \mathbf{x}_r, \omega)$ are the Green's functions connecting the source and receiver, respectively, to the image point \mathbf{x} . Note that the generalized Born modeling operator defined in equation 3.1 not only models the zero-subsurface-offset image (when $\mathbf{h} = \mathbf{0}$), but also models the contribution of non-zero ones (when $\mathbf{h} \neq \mathbf{0}$). This is important, because when the initial image is obtained using an inaccurate velocity model, the events in the images will not focus at the zero subsurface offset (Biondi and Symes, 2004). Therefore, by including the nonzero-subsurface-offset images in the modeling process, we preserve important velocity information that will be used for later velocity analysis.

Following the SDM procedure, I first generate the initial SODCIGs by applying

the inverse of the generalized Born modeling operator, which uses an initial velocity model, to the observed data. Since the exact inverse of the generalized Born modeling operator is impossible to obtain in practice, I approximate it with its adjoint normalized by the diagonal of the Hessian matrix as follows:

$$\begin{aligned}
m(\mathbf{x}, \mathbf{h}) &= \frac{1}{H_0(\mathbf{x}, \mathbf{h}) + \epsilon} \sum_{\omega} \sum_{\mathbf{x}_s} \omega^2 f_s^*(\omega) G_0^*(\mathbf{x} - \mathbf{h}, \mathbf{x}_s, \omega) \\
&\quad \times \sum_{\mathbf{x}_r} W(\mathbf{x}_r, \mathbf{x}_s) G_0^*(\mathbf{x} + \mathbf{h}, \mathbf{x}_r, \omega) \\
&\quad \times d_{\text{obs}}(\mathbf{x}_r, \mathbf{x}_s, \omega),
\end{aligned} \tag{3.2}$$

where $*$ denotes the complex conjugate; $d_{\text{obs}}(\mathbf{x}_r, \mathbf{x}_s, \omega)$ is the frequency-domain recorded data at receiver position \mathbf{x}_r due to a source at \mathbf{x}_s ; and $m(\mathbf{x}, \mathbf{h})$ is the subsurface-offset-domain image. The Green's functions G_0 are computed using a starting velocity model \mathbf{v}_0 . $H_0(\mathbf{x}, \mathbf{h})$ is the diagonal component of the subsurface-offset-domain imaging Hessian defined as follows (Valenciano, 2008):

$$\begin{aligned}
H_0(\mathbf{x}, \mathbf{h}) &= \sum_{\omega} \sum_{\mathbf{x}_s} \sum_{\mathbf{x}_r} \omega^4 |f_s(\omega)|^2 W^2(\mathbf{x}_r, \mathbf{x}_s) \\
&\quad \times |G_0(\mathbf{x} - \mathbf{h}, \mathbf{x}_s, \omega)|^2 |G_0(\mathbf{x} + \mathbf{h}, \mathbf{x}_r, \omega)|^2,
\end{aligned} \tag{3.3}$$

the inverse of which partially compensates for the amplitude distortion in the image caused by uneven subsurface illumination and removes the effects of the original acquisition geometry (Rickett, 2003; Plessix and Mulder, 2004; Symes, 2008; Tang, 2009). This procedure yields an initial image $m(\mathbf{x}, \mathbf{h})$ that contains only the effects of the initial velocity used for migration and does not depend on how the original data are recorded. In equation 3.2, ϵ is a damping parameter to stabilize the division.

Computing the exact Hessian using equation 3.3 is challenging even with today's most powerful computers, because it requires either storing a large number of Green's functions, which can take up hundreds of terabytes of disk space, or computing many wavefield propagations (Each receiver-side Green's function has to be recomputed for each shot, resulting in a cost proportional to the product of the numbers of sources

and receivers.) To reduce the computational cost, I approximate the exact Hessian with the receiver-side random-phase-encoded Hessian (Chapter 2) as follows:

$$H_0(\mathbf{x}, \mathbf{h}) \approx \sum_{\omega} \sum_{\mathbf{x}_s} \omega^4 |f_s(\omega)|^2 |G_0(\mathbf{x} - \mathbf{h}, \mathbf{x}_s, \omega)|^2 |R_0(\mathbf{x} + \mathbf{h}, \mathbf{x}_s, \omega)|^2, \quad (3.4)$$

where R_0 is the encoded receiver-side Green's function,

$$R_0(\mathbf{x} + \mathbf{h}, \mathbf{x}_s, \omega) = \sum_{\mathbf{x}_r} W(\mathbf{x}_r, \mathbf{x}_s) G_0(\mathbf{x} + \mathbf{h}, \mathbf{x}_r, \omega) e^{i\gamma(\mathbf{x}_r, \mathbf{x}_s, \omega)}, \quad (3.5)$$

obtained using an areal source: $\sum_{\mathbf{x}_r} W(\mathbf{x}_r, \mathbf{x}_s) \delta(\mathbf{x} - \mathbf{x}_r) e^{i\gamma(\mathbf{x}_r, \mathbf{x}_s, \omega)}$, where $\delta(\cdot)$ is the Dirac delta function and $\gamma(\mathbf{x}_r, \mathbf{x}_s, \omega)$ is a uniformly distributed random sequence to attenuate the resulting crosstalk. Equation 3.5 converges to equation 3.3 statistically. Chapter 2 describes the phase-encoded Hessian in more detail. It is obvious that the computational cost of equation 3.5 is independent of the number of receivers, as opposed to the exact Hessian (equation 3.3), where the cost is proportional to the number of receivers.

I then use the generalized Born modeling operator to simulate a new data set based on the initial image. The modeling can be performed using arbitrary source functions and arbitrary acquisition geometries. Techniques in acquisition design (Maurer et al., 2010; Jin and Xu, 2010) can potentially be used to optimize the acquisition parameters. In this chapter, I focus on using blended acquisition (Romero et al., 2000; Berkhout, 2008; Tang and Biondi, 2009), where the encoded areal sources are propagated to simulate the data. The modeled data set reads (Tang, 2008)

$$\begin{aligned} \tilde{d}(\mathbf{p}_s, \tilde{\mathbf{x}}_r, \tilde{\omega}) &= \sum_{\tilde{\mathbf{x}}} \sum_{\mathbf{h}} \tilde{\omega}^2 \tilde{f}_s(\tilde{\omega}) G_0(\tilde{\mathbf{x}} - \mathbf{h}, \mathbf{p}_s, \tilde{\omega}) \\ &\quad \times G_0(\tilde{\mathbf{x}} + \mathbf{h}, \tilde{\mathbf{x}}_r, \tilde{\omega}) m(\tilde{\mathbf{x}}, \mathbf{h}), \end{aligned} \quad (3.6)$$

where $\tilde{\mathbf{x}} = (\tilde{x}, \tilde{y}, \tilde{z})$ is an image point within the selected target zone. Note that $\tilde{\mathbf{x}}_r = (\tilde{x}_r, \tilde{y}_r, \tilde{z}_r)$ is the receiver location used for collecting the data, which can differ substantially from the original receiver location $\mathbf{x}_r = (x_r, y_r, 0)$. The source signature

$\tilde{f}_s(\tilde{\omega})$ and frequency $\tilde{\omega}$ used for modeling can also be different from the ones used for initial migration (equation 3.2). $G_0(\tilde{\mathbf{x}}, \mathbf{p}_s, \tilde{\omega})$ is the Green's function obtained using the encoded areal source, which can be written as a weighted sum of point-source Green's functions as follows:

$$G_0(\tilde{\mathbf{x}}, \mathbf{p}_s, \tilde{\omega}) = \sum_{\tilde{\mathbf{x}}_s} G_0(\tilde{\mathbf{x}}, \tilde{\mathbf{x}}_s, \tilde{\omega}) \beta(\tilde{\mathbf{x}}_s, \mathbf{p}_s, \tilde{\omega}), \quad (3.7)$$

where $\beta(\tilde{\mathbf{x}}_s, \mathbf{p}_s, \tilde{\omega})$ and \mathbf{p}_s are the encoding function and encoding index, respectively, to be specified later. Like the new receiver location $\tilde{\mathbf{x}}_r$, the new source location $\tilde{\mathbf{x}}_s = (\tilde{x}_s, \tilde{y}_s, \tilde{z}_s)$ can also be substantially different from the original source location $\mathbf{x}_s = (x_s, y_s, 0)$. Note in particular that the Green's function used for modeling ($G_0(\tilde{\mathbf{x}}, \mathbf{p}_s, \tilde{\omega})$) is computed using the same velocity model (\mathbf{v}_0) used for migrating the original data (equation 3.2). Therefore, the modeling process undoes the effect of the starting velocity model \mathbf{v}_0 , resulting in a data set independent of the starting velocity.

The synthesized areal data can be imaged by using conventional migration of areal-source data (the adjoint equation of 3.6) as follows:

$$\begin{aligned} \hat{m}(\tilde{\mathbf{x}}, \mathbf{h}) &= \sum_{\omega} \sum_{\mathbf{p}_s} \tilde{\omega}^2 \tilde{f}_s^*(\tilde{\omega}) G^*(\tilde{\mathbf{x}} - \mathbf{h}, \mathbf{p}_s, \tilde{\omega}) \\ &\quad \times \sum_{\tilde{\mathbf{x}}_r} G^*(\tilde{\mathbf{x}} + \mathbf{h}, \tilde{\mathbf{x}}_r, \tilde{\omega}) \tilde{d}(\mathbf{p}_s, \tilde{\mathbf{x}}_r, \tilde{\omega}), \end{aligned} \quad (3.8)$$

where Green's functions G are obtained using the velocity model \mathbf{v} , which can be the same as or different from the starting velocity model \mathbf{v}_0 , as I discuss later. Imaging the areal-source data using equation 3.8, however, generates crosstalk artifacts (Romero et al., 2000; Liu et al., 2006; Tang, 2008). To attenuate the crosstalk, the encoding function β is chosen such that

$$\sum_{\mathbf{p}_s} \beta^*(\tilde{\mathbf{x}}_s, \mathbf{p}_s, \tilde{\omega}) \beta(\tilde{\mathbf{x}}'_s, \mathbf{p}_s, \tilde{\omega}) \approx \delta(\tilde{\mathbf{x}}_s - \tilde{\mathbf{x}}'_s). \quad (3.9)$$

In this chapter, I use plane-wave-phase encoding, and therefore,

$$\beta(\tilde{\mathbf{x}}_s, \mathbf{p}_s, \tilde{\omega}) = A(\tilde{\omega})e^{i\tilde{\omega}\mathbf{p}_s \cdot \tilde{\mathbf{x}}_s}, \quad (3.10)$$

with $A^2(\tilde{\omega}) = |\tilde{\omega}|$ in two dimensions and $A^2(\tilde{\omega}) = |\tilde{\omega}|^2$ in three dimensions. In addition, $\mathbf{p}_s = (p_{sx}, p_{sy}, 0)$ is the ray parameter for the source plane waves at depth level \tilde{z}_s .

Substituting equations 3.6 and 3.7 into equation 3.8 and using the relation in equation 3.9 yield

$$\hat{m}(\tilde{\mathbf{x}}, \mathbf{h}) = \sum_{\tilde{\mathbf{x}}'} \sum_{\mathbf{h}'} \Delta G(\tilde{\mathbf{x}}, \mathbf{h}, \tilde{\mathbf{x}}', \mathbf{h}') m(\tilde{\mathbf{x}}', \mathbf{h}'), \quad (3.11)$$

where

$$\begin{aligned} \Delta G(\tilde{\mathbf{x}}, \mathbf{h}, \tilde{\mathbf{x}}', \mathbf{h}') &= \sum_{\tilde{\omega}} \sum_{\tilde{\mathbf{x}}_s} \sum_{\tilde{\mathbf{x}}_r} \tilde{\omega}^4 |\tilde{f}_s(\tilde{\omega})|^2 \\ &\quad \times G^*(\tilde{\mathbf{x}} - \mathbf{h}, \tilde{\mathbf{x}}_s, \tilde{\omega}) G_0(\tilde{\mathbf{x}}' - \mathbf{h}', \tilde{\mathbf{x}}_s, \tilde{\omega}) \\ &\quad \times G^*(\tilde{\mathbf{x}} + \mathbf{h}, \tilde{\mathbf{x}}_r, \tilde{\omega}) G_0(\tilde{\mathbf{x}}' + \mathbf{h}', \tilde{\mathbf{x}}_r, \tilde{\omega}). \end{aligned} \quad (3.12)$$

When the same velocity model is used for Born modeling and migration ($\mathbf{v}_0 = \mathbf{v}$), $\Delta G(\tilde{\mathbf{x}}, \mathbf{h}, \tilde{\mathbf{x}}', \mathbf{h}')$ becomes the local Hessian operator or resolution function (Lecomte, 2008; Valenciano, 2008; Tang, 2009) under the new acquisition geometry. It has zero phase and is approximately centered at $\tilde{\mathbf{x}}' = \tilde{\mathbf{x}}$ and $\mathbf{h}' = \mathbf{h}$. Therefore, $\hat{m}(\tilde{\mathbf{x}}, \mathbf{h})$ is a filtered version of the original image $m(\tilde{\mathbf{x}}, \mathbf{h})$ and has exactly the same kinematics. When the migration velocity is different from the modeling velocity ($\mathbf{v}_0 \neq \mathbf{v}$), the two images may substantially differ.

Because we want to use migration results to estimate velocity, it is important to demonstrate that the velocity information contained in the prestack image, which was obtained from the data modeled using the proposed procedure, is consistent with the velocity information extracted from the prestack image, which was obtained

from migrating the originally recorded data set. I use the following simple numerical example to demonstrate that the synthesized new data set successfully preserves the correct velocity information. Since the one-way wavefield extrapolator has limited accuracy for large-angle propagation, I compute only the horizontal half subsurface offset, i.e., $\mathbf{h} = (h_x, 0)$ in two dimensions and $\mathbf{h} = (h_x, h_y, 0)$ in three dimensions. For steeply dipping reflectors, the vertical subsurface offset becomes necessary (Biondi and Symes, 2004); however, the additional cost is not justified when using angle-limited one-way propagators.

Figure 3.2 shows the initial image and SODCIGs obtained by migrating the original data set using a velocity that is 15% slower than the true velocity of 2000 m/s. The defocusing in the SODCIGs indicates the inaccuracy of the initial velocity model. I then synthesize two new data sets using different initial images. One is modeled using the entire image cube (Figure 3.2(a)), i.e., using the generalized Born modeling equation; the other is modeled using only the zero-subsurface-offset image (Figure 3.2(b)). In order to compare easily the modeled shots with the original shots, the new data sets are modeled using the same acquisition geometry as the original data set. Figure 3.3 compares the modeled data sets with the original data set. It is clear that shot gathers modeled using the SODCIGs (Figure 3.3(b)) show the same kinematics as the original data set (Figure 3.3(a)), and those modeled using only zero-subsurface offset image (Figure 3.3(c)) do not.

I then migrate both data sets and compare the obtained SODCIGs with the ones obtained using the original data set. Figures 3.4 and 3.5 show the SODCIGs extracted at CMP location $x = 0$ m, when migrating using a 15% slower and the true velocities, respectively. It is obvious that only when modeling the new data set with the SODCIGs, are the image gathers (Figure 3.4(b) and 3.5(b)) consistent with those obtained using the original data set (Figure 3.4(a) and 3.5(a)).

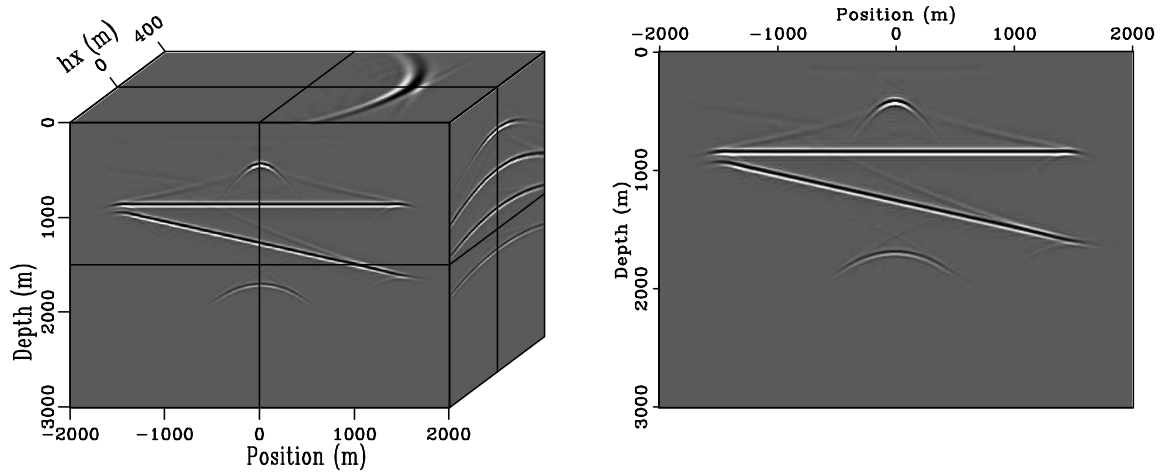


Figure 3.2: Initial images used for Born modeling. Panel (a) is the image cube with the third dimension being the subsurface offset, and (b) is the zero-subsurface-offset image. [ER] `chap3/. simple-orig-image-cube`

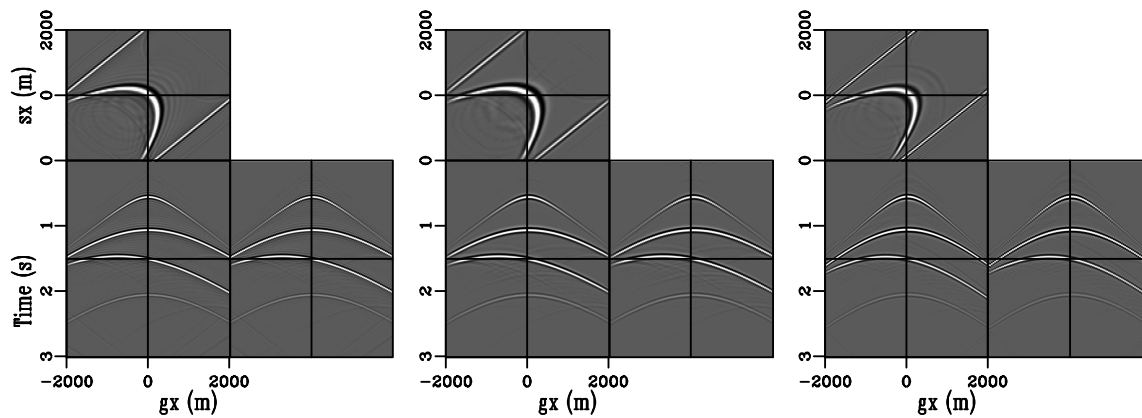


Figure 3.3: Comparison among (a) the original data set, (b) the new data set modeled using SODCIGs and (c) the new data set modeled using only zero-subsurface-offset image. [ER] `chap3/. simple-trec`

Figure 3.4: The extracted SOD-CIGs obtained using (a) the original data set, (b) the data set modeled using generalized Born modeling and (c) the data set modeled using conventional Born modeling. The three data sets are migrated using a velocity 15% slower than the true velocity. [ER]

chap3/. simple-odcig-slow

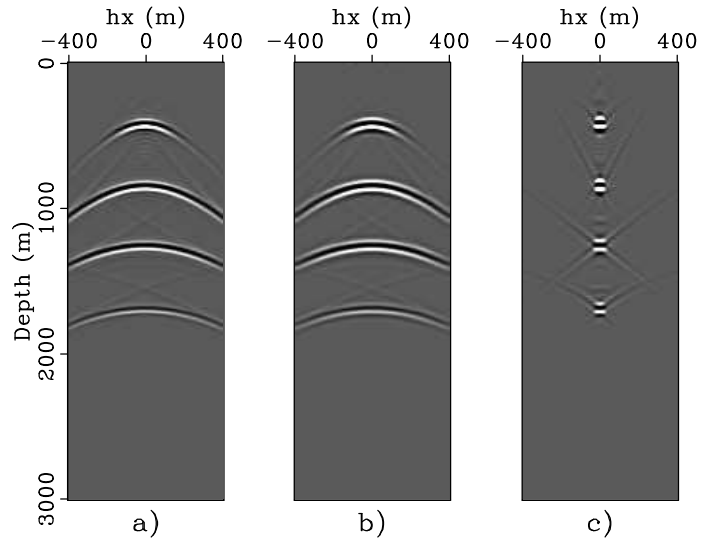
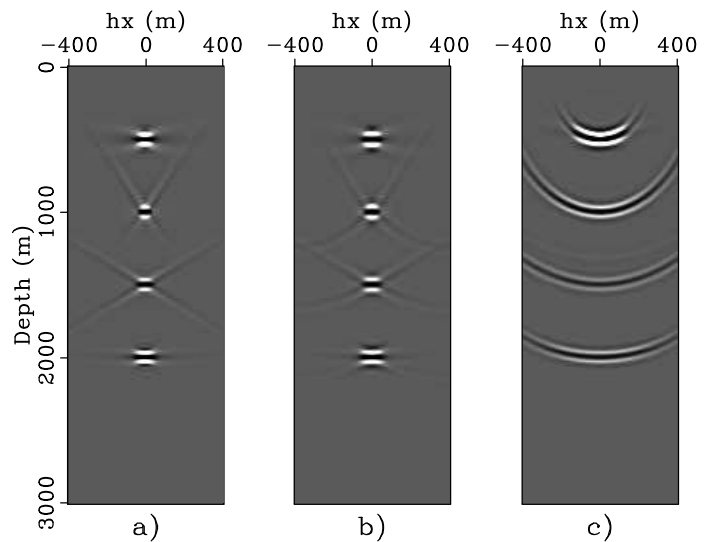


Figure 3.5: The extracted SOD-CIGs obtained using (a) the original data set, (b) the data set modeled using generalized Born modeling and (c) the data set modeled using conventional Born modeling. The three data sets are migrated using the true velocity. [ER]

chap3/. simple-odcig-true



TOMOGRAPHIC INVERSION USING THE SYNTHESIZED DATA

I pose the velocity estimation problem as an optimization problem that seeks an optimum velocity model by minimizing a user-defined image residual (or maximizing some measure of the image coherence). There are many ways of defining the objective functions. In this chapter, I use differential semblance optimization (DSO) (Symes and Carazzone, 1991) as the criterion to estimate the velocity. The DSO objective function in the subsurface-offset domain is (Shen, 2004; Shen and Symes, 2008)

$$F = \frac{1}{2} \sum_{\tilde{\mathbf{x}}} \sum_{\mathbf{h}} |\mathbf{h}|^2 \hat{m}^2(\tilde{\mathbf{x}}, \mathbf{h}). \quad (3.13)$$

The physical interpretation of the subsurface-offset-domain DSO is that it optimizes the velocity model by penalizing energy at non-zero subsurface offset, taking advantage of the fact that seismic events should focus at zero-subsurface offset if migrated using an accurate velocity model (Shen, 2004). However, the gradient of the objective function defined by equation 3.13 is sensitive to the amplitude variation of images due to uneven illumination (Vyas and Tang, 2010; Fei and Williamson, 2010). I propose to normalize the DSO objective function by the square of the root-mean-squared (RMS) image amplitudes to reduce the influence of image amplitude variations. The normalized DSO objective function is

$$J = \frac{1}{2} \sum_{\tilde{\mathbf{x}}, \tilde{\mathbf{y}}} \frac{\sum_{\tilde{\mathbf{z}}, \mathbf{h}} |\mathbf{h}|^2 |\hat{m}(\tilde{\mathbf{x}}, \mathbf{h})|^2}{\sum_{\tilde{\mathbf{z}}, \mathbf{h}} |\hat{m}(\tilde{\mathbf{x}}, \mathbf{h})|^2}. \quad (3.14)$$

The gradient of J with respect to velocity $v(\mathbf{y})$, where \mathbf{y} is the velocity coordinate vector, can be obtained as follows:

$$g(\mathbf{y}) = \frac{\partial J}{\partial v(\mathbf{y})} = \sum_{\tilde{\mathbf{x}}} \sum_{\mathbf{h}} \left[\frac{\partial \hat{m}(\tilde{\mathbf{x}}, \mathbf{h})}{\partial v(\mathbf{y})} \right]^* r(\tilde{\mathbf{x}}, \mathbf{h}), \quad (3.15)$$

where $\frac{\partial \widehat{m}(\tilde{\mathbf{x}}, \mathbf{h})}{\partial v(\mathbf{y})}$ is one component of the wave-equation tomographic operator (the Jacobian matrix) and $r(\tilde{\mathbf{x}}, \mathbf{h})$ is the image residual defined as follows:

$$r(\tilde{\mathbf{x}}, \mathbf{h}) = \frac{|\mathbf{h}|^2 \widehat{m}(\tilde{\mathbf{x}}, \mathbf{h}) w_m(\tilde{x}, \tilde{y}) - \widehat{m}(\tilde{\mathbf{x}}, \mathbf{h}) w_d(\tilde{x}, \tilde{y})}{w_m^2(\tilde{x}, \tilde{y})}, \quad (3.16)$$

where

$$w_m(\tilde{x}, \tilde{y}) = \sum_{\tilde{z}, \mathbf{h}} |\widehat{m}(\tilde{\mathbf{x}}, \mathbf{h})|^2, \quad (3.17)$$

$$w_d(\tilde{x}, \tilde{y}) = \sum_{\tilde{z}, \mathbf{h}} |\mathbf{h}|^2 |\widehat{m}(\tilde{\mathbf{x}}, \mathbf{h})|^2. \quad (3.18)$$

I use a gradient-based nonlinear conjugate gradient algorithm to minimize the objective function J , where the gradient (equation 3.15) is calculated using the adjoint-state method (with a one-way wave-equation formulation) without explicitly computing the Jacobian matrix (Shen and Symes, 2008; Sava and Vlad, 2008; Tang et al., 2008). Appendix C gives a detailed derivation of the one-way wave-equation-based tomographic operator.

To regularize the inversion, I smooth the gradient using a B-spline operator as follows:

$$\mathbf{g}_s = \mathbf{B}\mathbf{B}^* \mathbf{g}, \quad (3.19)$$

where \mathbf{g} and \mathbf{g}_s are the original and smoothed gradient vectors, respectively; \mathbf{B} is the B-spline projection operator. The spacing of the B-spline nodes then controls the smoothness of the velocity updates. The optimization algorithm is summarized in Algorithm 1.

SYNTHETIC DATA EXAMPLES

I first apply the proposed strategy to the synthetic Sigsbee2A data set introduced in Chapter 2. Figure 3.6 shows the true migration velocity. The complex salt geometry

Algorithm 1 Optimization algorithm

compute the migrated image: $\widehat{\mathbf{m}}_0$
 compute the residual field: \mathbf{r}_0
 compute the gradient: \mathbf{g}_0
 regularize the gradient: $\mathbf{g}_s^0 = \mathbf{B}\mathbf{B}^*\mathbf{g}_0$
 initialize the search direction: $\mathbf{p}_0 = -\mathbf{g}_s^0$
for $k = 1 \cdots N_k$ **do**
 perform a line search: optimize λ , $\operatorname{argmin}_{\lambda} J(\mathbf{v}_{k-1} + \lambda\mathbf{p}_{k-1})$
 update the velocity model: $\mathbf{v}_k = \mathbf{v}_{k-1} + \lambda\mathbf{p}_{k-1}$
 compute the migrated image: $\widehat{\mathbf{m}}_k$
 compute the residual field: \mathbf{r}_k
 compute the gradient: \mathbf{g}_k
 regularize the gradient: $\mathbf{g}_s^k = \mathbf{B}\mathbf{B}^*\mathbf{g}_k$
 find the search direction: $\mathbf{p}_k = -\mathbf{g}_k + \frac{(\mathbf{g}_s^k)^T(\mathbf{g}_s^k - \mathbf{g}_s^{k-1})}{(\mathbf{g}_s^{k-1})^T\mathbf{g}_s^{k-1}}$
end for

creates imaging and velocity-estimation challenges below the salt body. Figure 3.7 displays the initial velocity model, where the velocities in a local region below the salt body are about 10% slower than the true velocities (see Figure 3.14(b)). The black box delineates the region chosen for target-oriented velocity analysis.

The original data are modeled using a two-way wave equation with a marine acquisition geometry, where the receiver spread moves along with the source (Paffenholz et al., 2002). There are 500 shots, with the maximum offset being about 8 km. Each shot gather is 12 seconds long. The maximum frequency used for migration is 30 Hz. The SODCIGs and the target image, obtained using the initial velocity model and the original data set (Figure 3.8), show unbalanced amplitudes due to uneven subsurface illumination. After applying the diagonal of the Hessian matrix (Figure 3.9), efficiently computed using the phase-encoding method (Chapter 2), the normalized image (Figure 3.10) partially removes the illumination effects and the image amplitudes are more balanced.

I use the initial SODCIGs (Figure 3.10) and the generalized Born modeling described in the previous section to generate 31 plane-wave-source gathers at the top

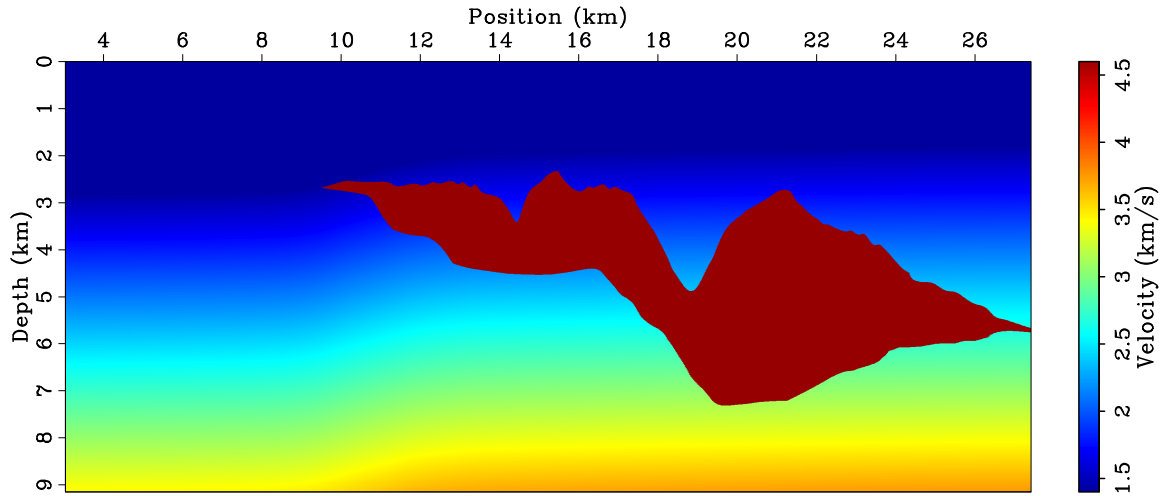


Figure 3.6: The true migration velocity of the Sigsbee2A model. [ER] chap3/. sigsb2a-vmod-full

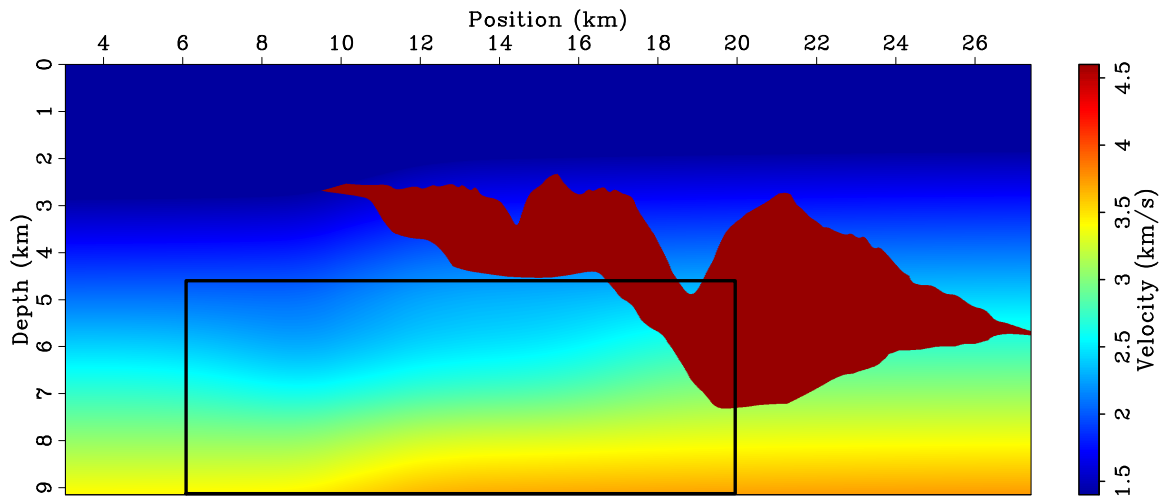


Figure 3.7: The initial velocity model for the Sigsbee2A example. The black box outlined area is the target region for velocity analysis. [ER] chap3/. sigsb2a-bvel-full

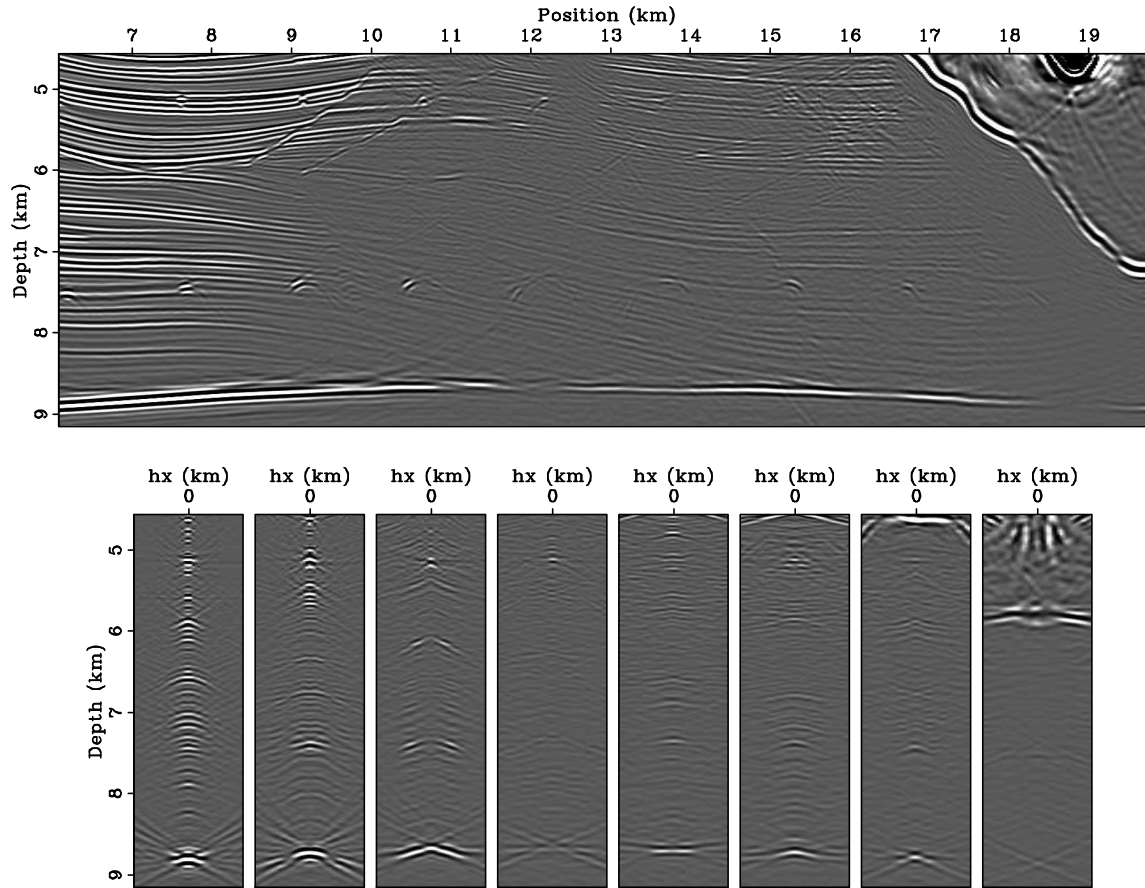


Figure 3.8: The zero-subsurface-offset image (top) and SODCIGs (bottom) for the target region, obtained by using the original data set and the initial velocity model. The SODCIGs are located at CMP location 7.62, 9.14, 10.67, 12.19, 13.72, 15.24, 16.76, 18.29 km, from left to right. [CR] [chap3/. sigsb2a-bimg-odcig-target](#)

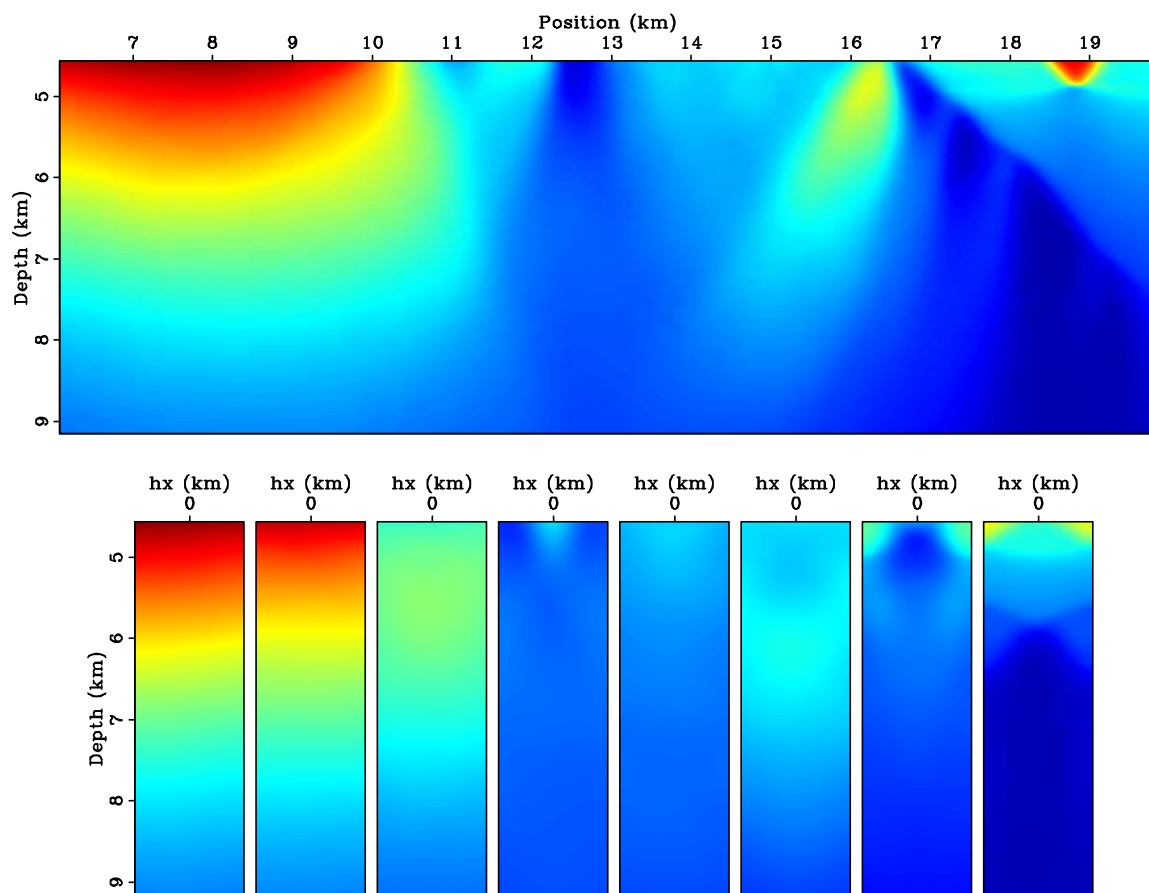


Figure 3.9: The diagonal of the Hessian computed using the initial velocity model and the original acquisition geometry. View descriptions are the same as in Figure 3.8. [CR] chap3/. sigsb2a-bhes-target-color

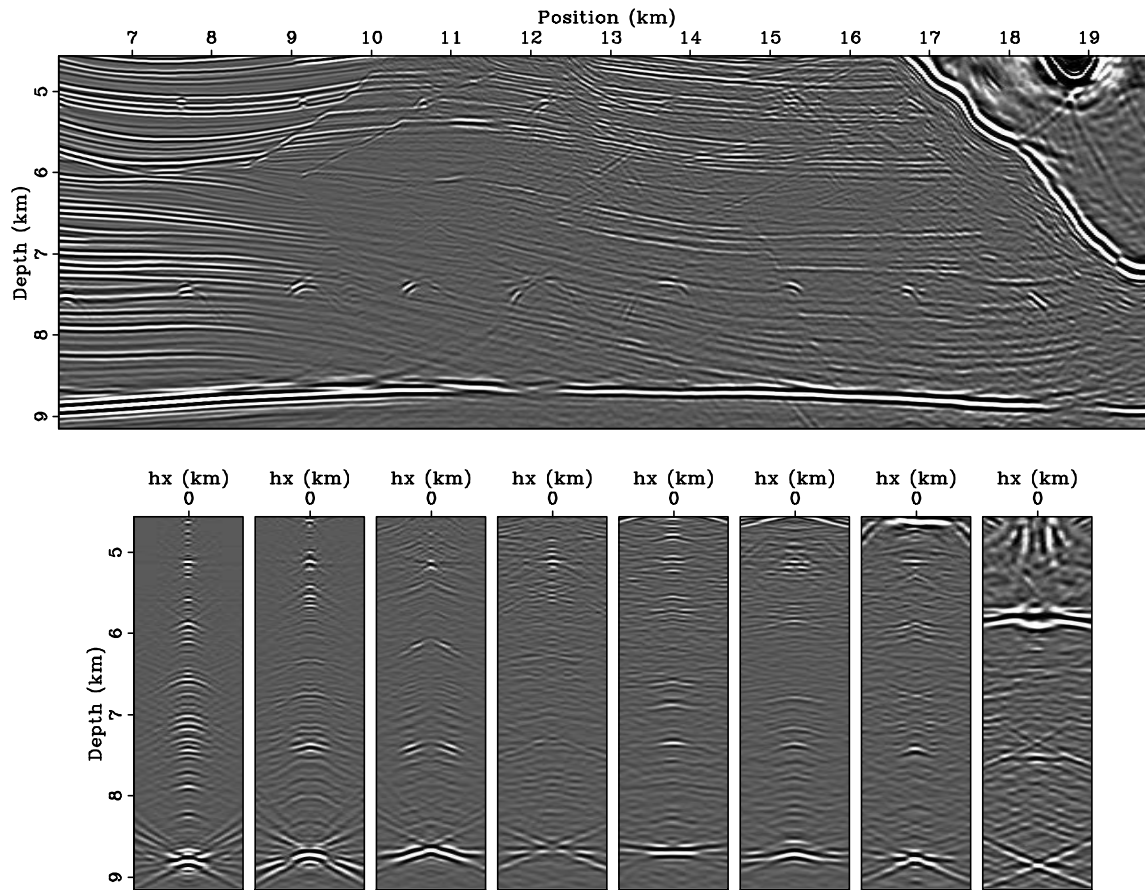


Figure 3.10: The initial target image and SODCIGs normalized by the diagonal of the Hessian shown in Figure 3.9. View descriptions are the same as in Figure 3.8.

[CR] chap3/. sigsb2a-bimg-odcig-target-cpst

of the target region ($z = 4.52$ km), where the take-off angle is from -40° to 40° . I model Born wavefields up to 25 Hz. Since the synthesized data is recorded in the subsurface, the record length can be much shorter than 12 seconds, or equivalently, the frequency domain sampling for one-way wave-equation-based modeling can be much coarser without introducing aliasing. Taking these factors into consideration, it is about 48 times faster to migrate the synthesized Born data set than the original data set.

Figure 3.11 shows the image and SODCIGs obtained by using the synthesized new data set and the initial velocity model. Figure 3.12 compares the corresponding angle-domain common-image gathers (ADCIGs). Note that the kinematics are the same in both images and the amplitudes are similar. This suggests that the velocity information has been successfully preserved using the new data set, which is substantially smaller than the original one.

The inverted velocity model obtained after 30 nonlinear iterations is shown in Figure 3.13(b), whereas Figures 3.13(a) and 3.13(c) show the initial and true velocity models, respectively. Figure 3.14 plots the velocity ratios for a better comparison. The anomaly below the salt body has been successfully recovered. But the inversion is not perfect, which might be a result of limited angular coverage below the salt. Nevertheless, the updated image and SODCIGs (Figure 3.15) show better focusing than the initial ones (Figure 3.8). The updated ADCIGs (Figure 3.17(b)) are also flatter than the initial ones (Figure 3.17(a)). For comparison, Figures 3.16 and 3.17(c) show the SODCIGs and ADCIGs obtained by using the true velocity model.

FIELD DATA EXAMPLES

I also apply the proposed strategy to a field data set acquired from the Gulf of Mexico (GOM). The data were collected using a narrow-azimuth towed-streamer (NATS) acquisition system, and further rotated using AMO (Biondi et al., 1998) into zero azimuth. I extracted one crossline from the 3-D data set and performed a 2-D target-oriented wavefield tomography to estimate the subsalt velocity. The extracted data

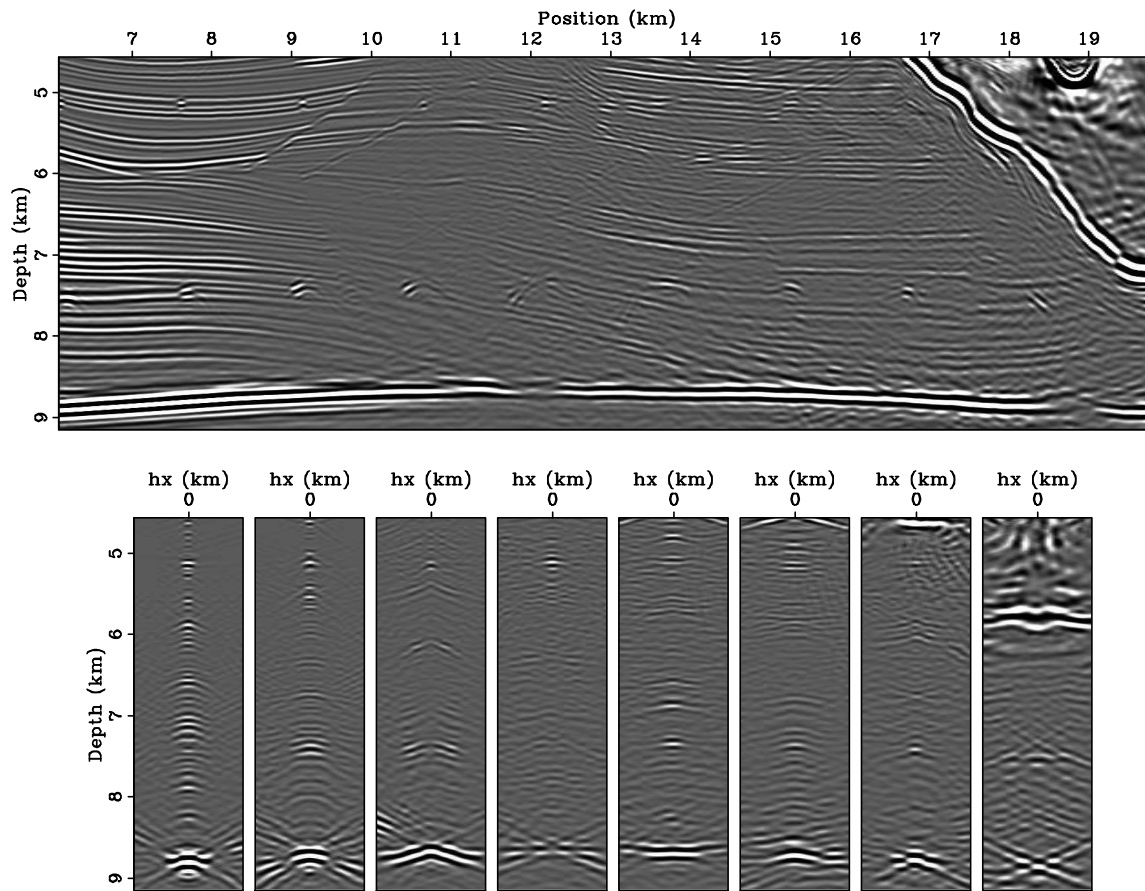
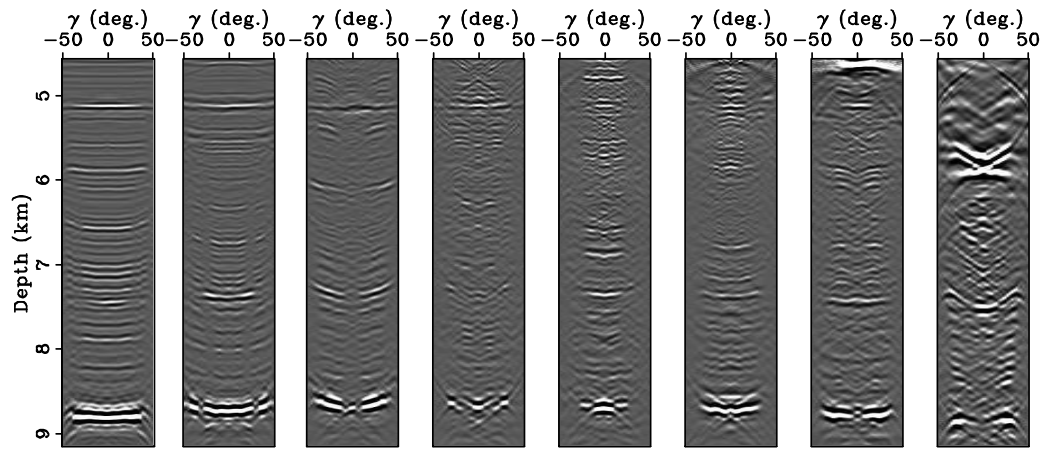
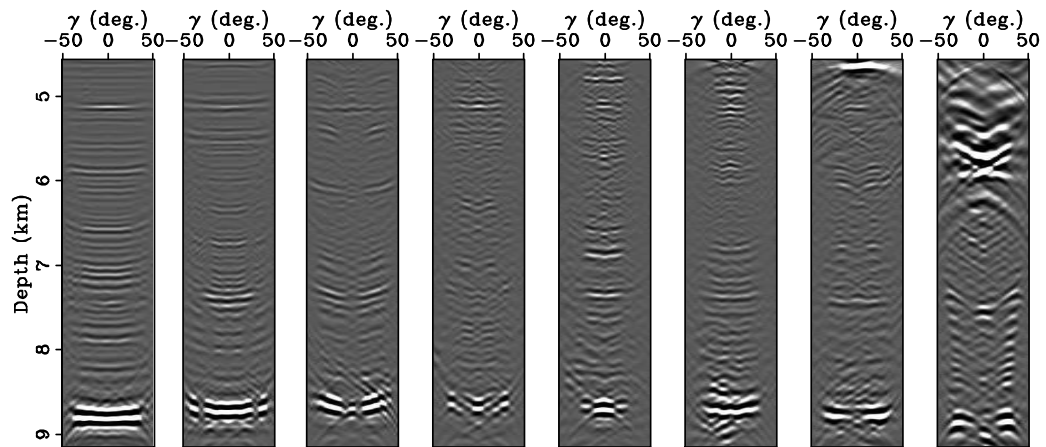


Figure 3.11: The target image and SODCIGs obtained by using the new data set (31 planewave-source gathers) and the initial velocity model. View descriptions are the same as in Figure 3.8. [CR] `chap3/. sigsb2a-bimg-odcig-target-born`



(a)



(b)

Figure 3.12: ADCIGs obtained using (a) the original data set and (b) the new data set. They are located at the same CMP location as the SODCIGs shown in Figure 3.8. [CR] chap3/. sigsb2a-bimg-adcig-target-cpst,sigsb2a-bimg-adcig-target-born

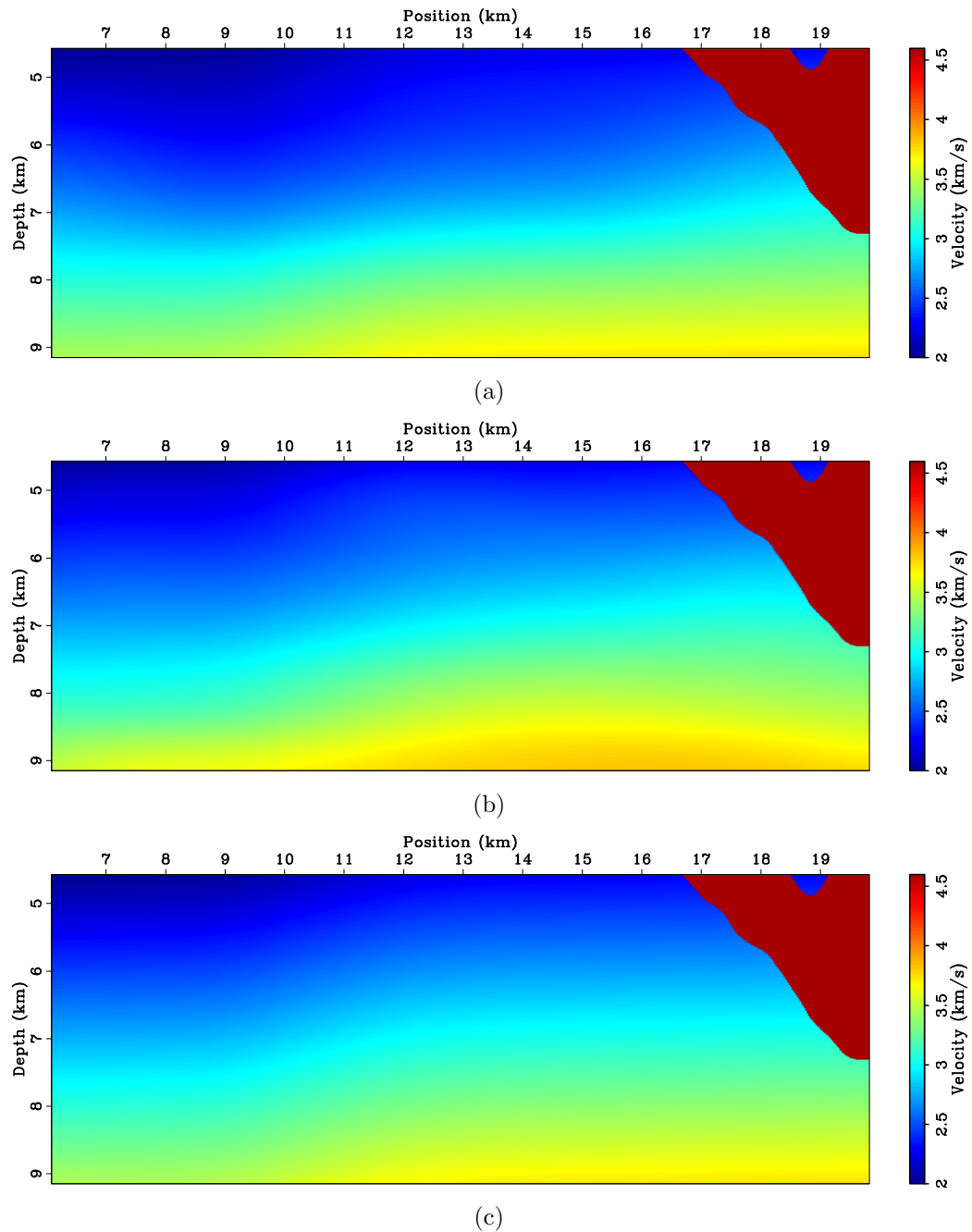


Figure 3.13: The initial velocity model for the target region (a), the inverted velocity model (b), and the true velocity model (c). [CR]

chap3/. sigsb2a-bvel-target,sigsb2a-invt-target,sigsb2a-vmod-target

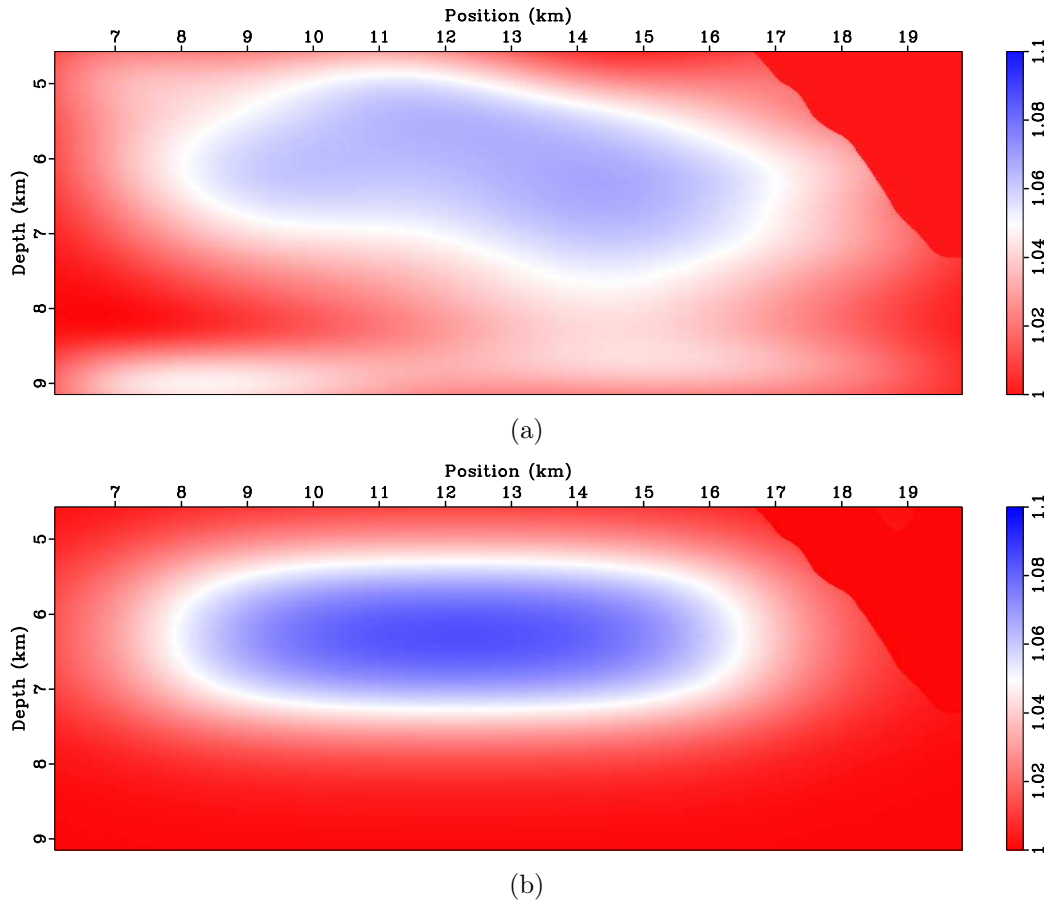


Figure 3.14: Panel (a) shows the ratio between the inverted velocity and the initial velocity, whereas panel (b) shows the ratio between the true velocity and the initial velocity. Notice the similarity of the estimated velocity anomaly to the one I introduced in the initial model. [CR] `chap3/. sigsb2a-vdif-invt,sigsb2a-vdif-true`

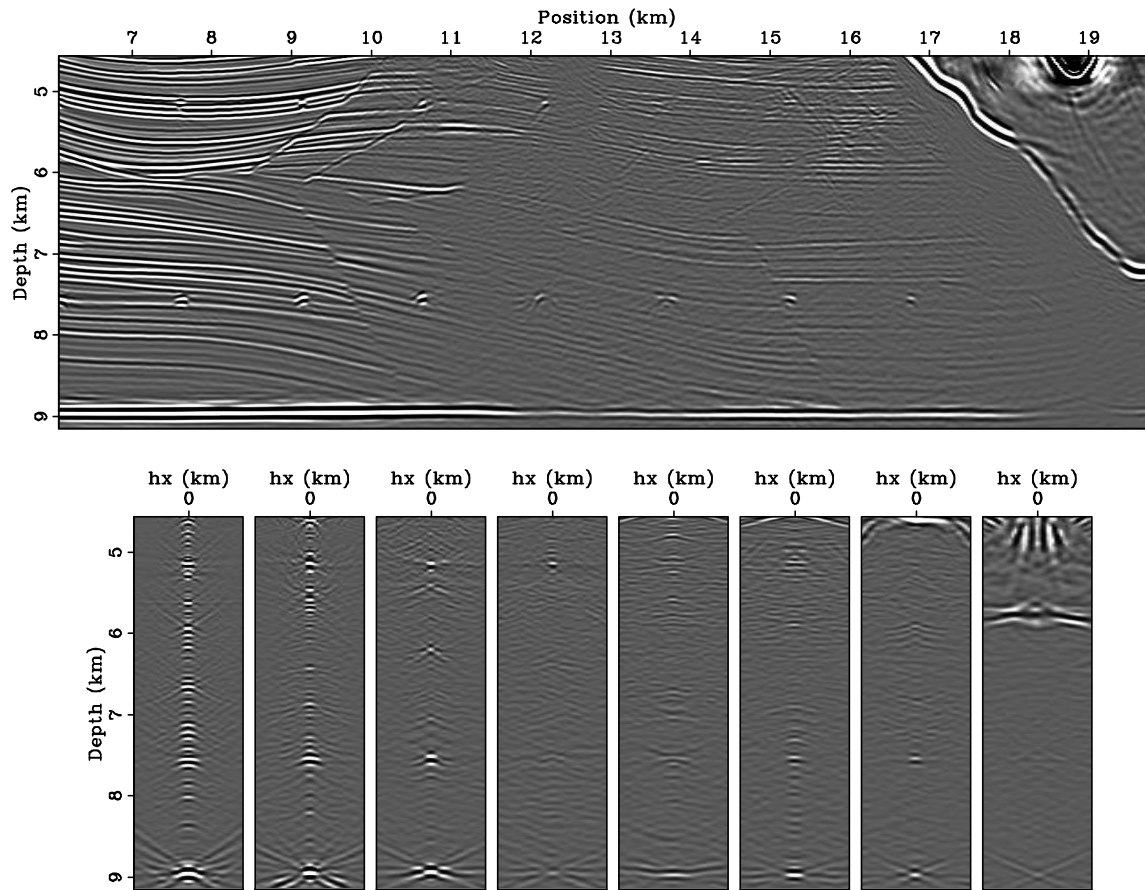


Figure 3.15: Zero-subsurface-offset image and SODCIGs obtained using the inverted velocity model and the original data set. View descriptions are the same as in Figure 3.8. [CR] chap3/. sigsb2a-invt-imag-odcig-target

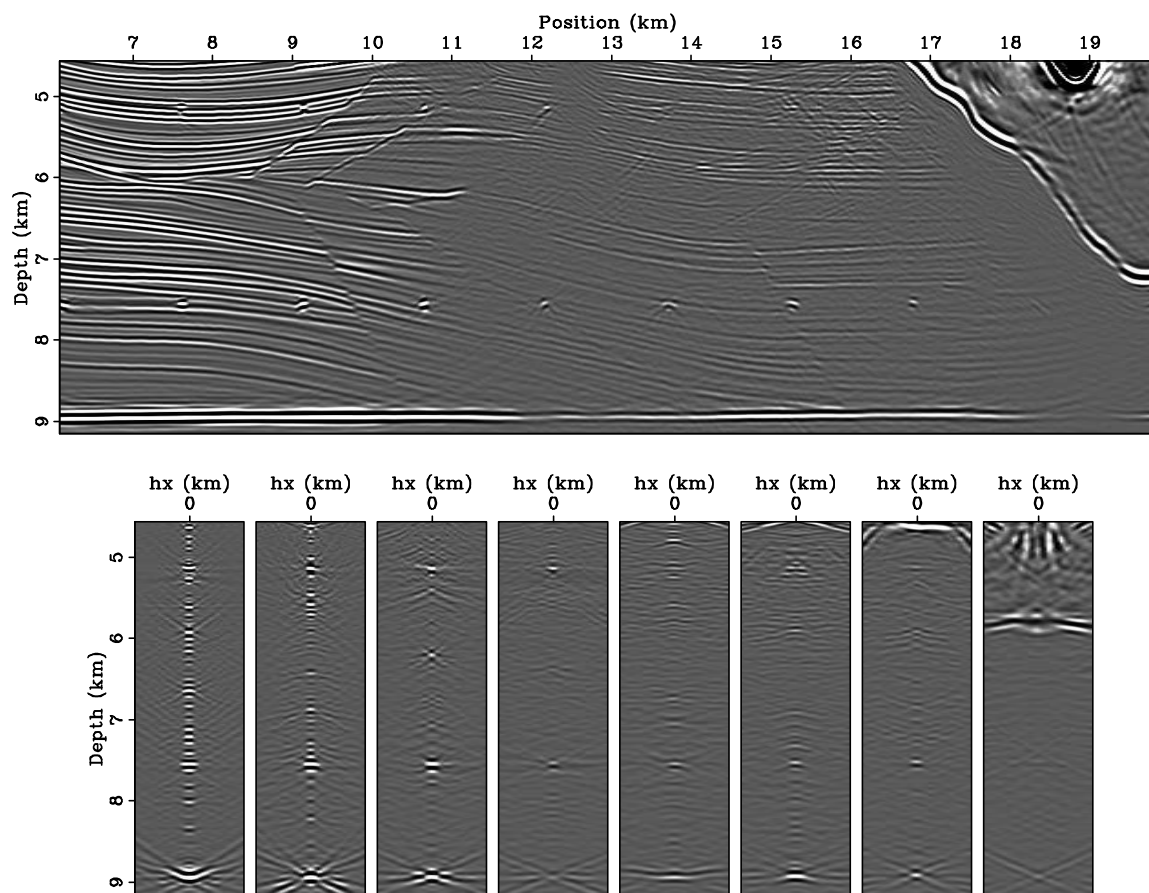
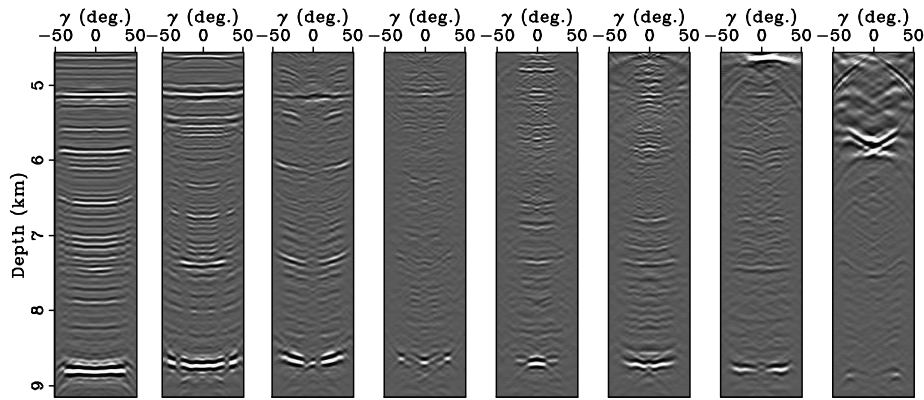
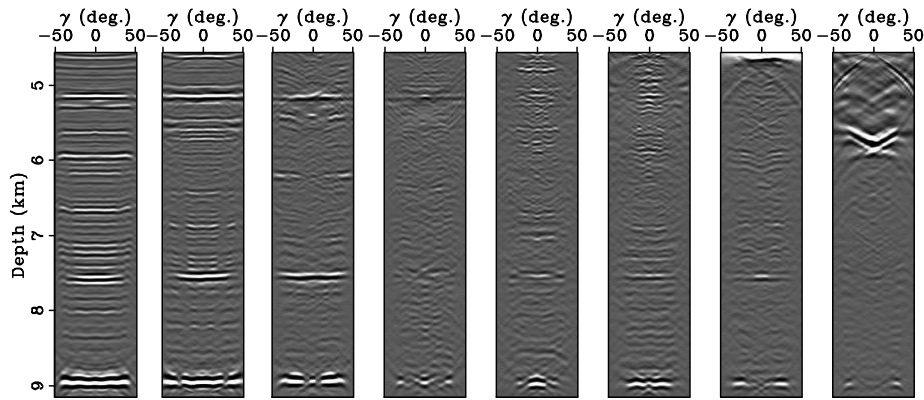


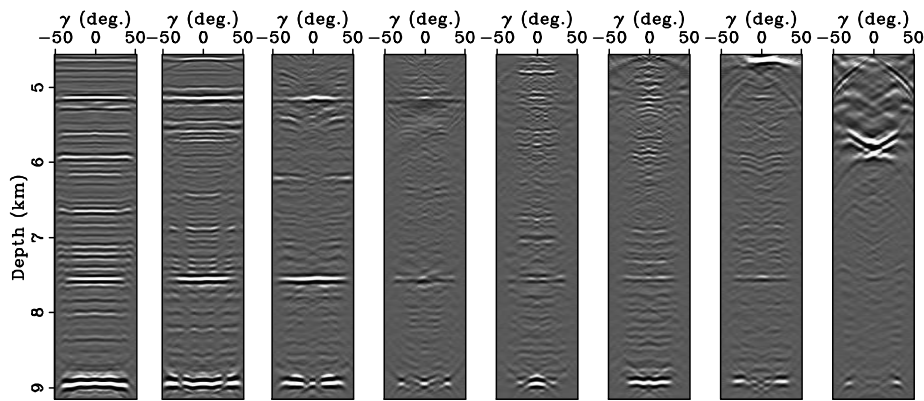
Figure 3.16: Zero-subsurface-offset image and SODCIGs obtained using the true velocity model and the original data set. View descriptions are the same as in Figure 3.8. [CR] chap3/. sigsb2a-imag-odcig-target



(a)



(b)



(c)

Figure 3.17: ADCIGs obtained using (a) the initial velocity model, (b) the inverted velocity model and (c) the true velocity model. The ADCIGs are located at CMP location 7.62, 9.14, 10.67, 12.19, 13.72, 15.24, 16.76, 18.29 km, respectively. [CR]

chap3/. sigsb2a-bimg-adcig-target,sigsb2a-invt-imag-adcig-target,sigsb2a-imag-adcig-target

contains 801 shots with the minimum and maximum inline offset equal to 0.3 km and 8.2 km, respectively. The frequency content ranges from 5 Hz to 35 Hz.

Figure 3.18 shows the initial velocity model for the extracted 2-D line. Velocities above the target (outlined by a black box) and the salt interpretation are assumed to be accurate. The goal is to invert for subsalt velocities inside the target region. The initial velocities inside the box are set to be $v(z)$. Figure 3.19 shows the initial image for the selected target region obtained using the initial velocity model and the original surface recorded data. The normalized image (Figure 3.21) obtained by applying the diagonal of the Hessian (Figure 3.20) optimally removes the uneven illumination effects caused by the complex overburden and limited acquisition geometry.

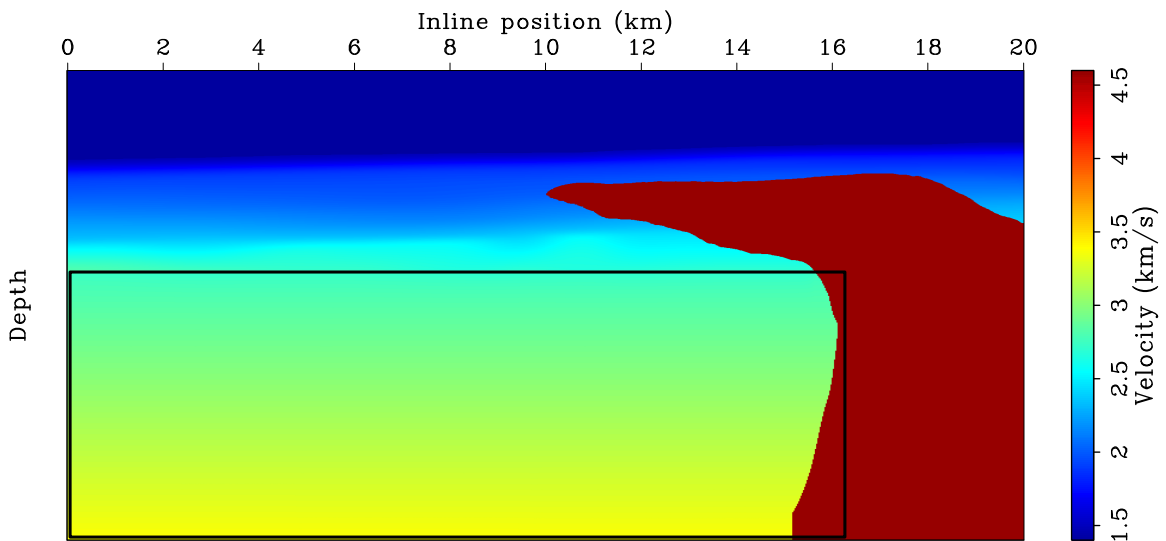


Figure 3.18: The initial velocity model for the selected 2-D line of the GOM data set. The area inside the black box is the target region for velocity analysis. Velocities outside the region are assumed to be accurate. [ER] chap3/. bpgom2d-bvel

Using the SDM procedure, I synthesize 31 planewave-source gathers at the top of the target region, where the take-off angle is from -30° to 30° . The new data set is collected just above the target region. I only model Born wavefields up to 25 Hz. For this particular example, I obtain a speedup by a factor of about 160 by switching from the original data set to the synthesized new data set for velocity analysis. Figure 3.22 shows the migrated image using the synthesized new data set and the initial velocity

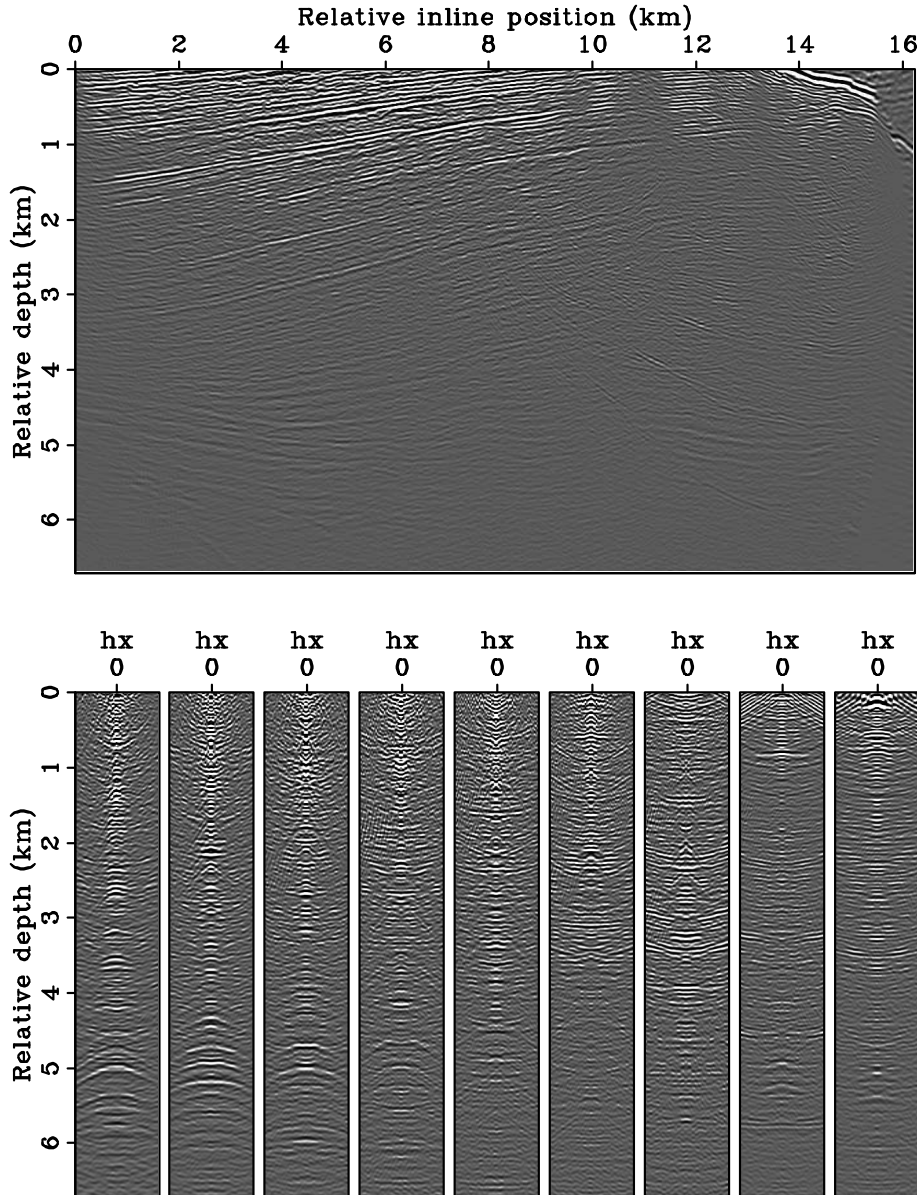


Figure 3.19: The zero-subsurface-offset image (top) and SODCIGs (bottom) obtained using the original data set and the initial velocity model. The SODCIGs are extracted at CMP locations 2.21, 3.74, 5.27, 6.79, 8.31, 9.84, 11.36, 12.89, 14.41 km, from left to right. The minimum and maximum subsurface offsets in the bottom panel are -0.75 km and 0.75 km, respectively. [CR] `chap3/. bpgom2d-bimg-target-odcig-raw`

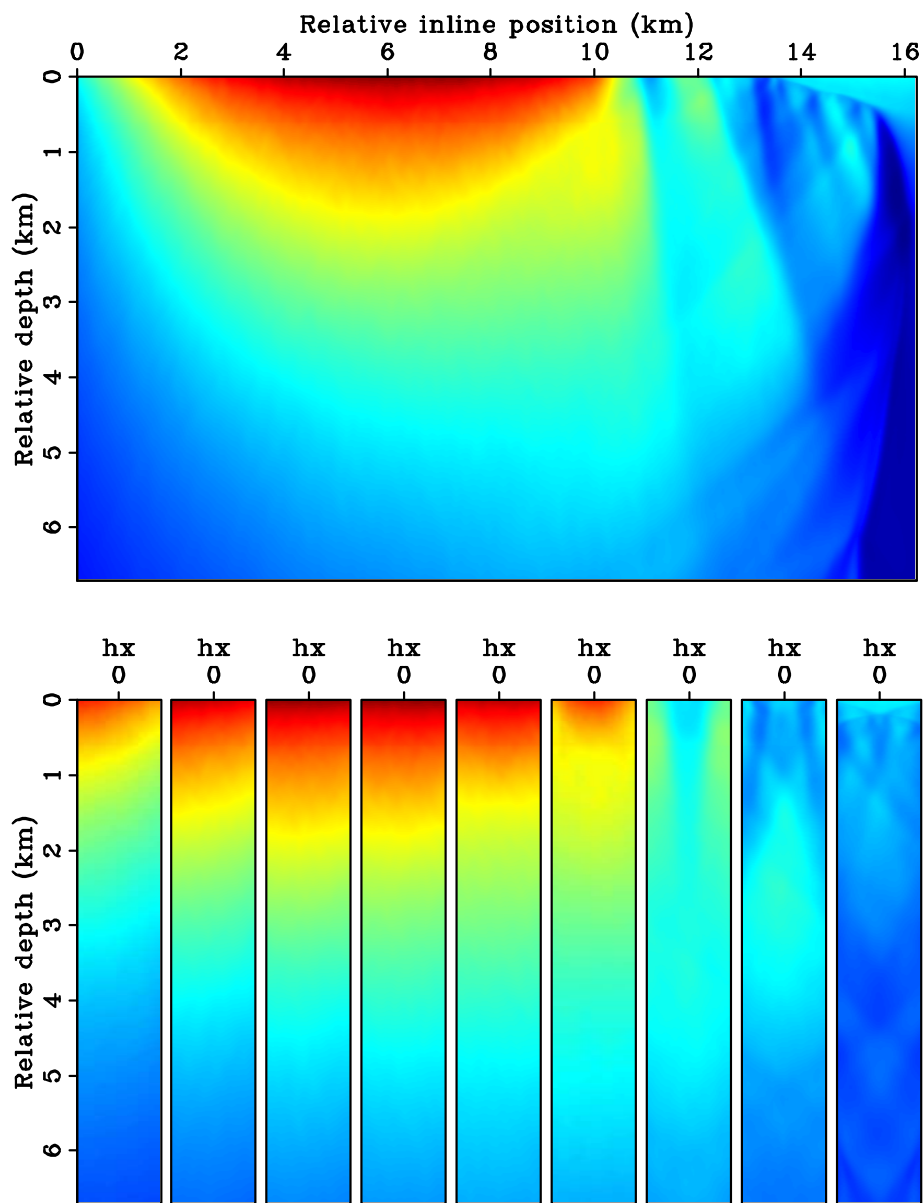


Figure 3.20: The diagonal of Hessian computed using the initial velocity model and the original acquisition geometry. View descriptions are the same as in Figure 3.19. [CR] chap3/. bpgom2d-bhes-target-odcig-color

model. The same kinematics and similarities in amplitudes in Figures 3.22 and 3.21 suggest the velocity has been successfully preserved using the new data set.

Figure 3.23 shows the inverted velocity model after 30 iterations. I then migrate the original data set using the inverted velocity model and compare the result with that obtained using the initial velocity model. Figures 3.24, 3.25 and 3.26 compare the stacked section (zero-subsurface-offset image) using the initial and updated velocities. The image obtained using the inverted velocity model shows improved continuities, better focusing and a higher signal-to-noise ratio. The SODCIGs migrated using the inverted velocity model (Figure 3.27(b)) are more focused than those obtained using the initial velocity model (Figure 3.27(a)). The updated ADCIGs (Figure 3.28(b)) are also flatter than the initial ones (Figure 3.28(a)).

DISCUSSION

The key ingredient of the proposed target-oriented velocity analysis strategy is that the synthesized Born data set preserves the correct velocity information. In this chapter, I have demonstrated that the modeling of subsurface-offset gathers can successfully achieve this goal. Although not discussed here, other kinds of prestack gathers, such as the angle gathers (Sava and Fomel, 2003) and time-shift gathers (Sava and Fomel, 2006) could also be potentially used for modeling without compromising any important velocity information.

However, both the generalized Born modeling and the subsequent differential semblance velocity analysis are based on the single-scattering approximation; other coherent energy, such as multiples, do not fit into the modeling and inversion framework. If multiples are present in the initial images, the generalized Born approach would model them as if they were primary reflections, and consequently the synthesized new data set would contain incorrect velocity information. Therefore, preprocessing of the initial image, such as multiple suppression, is suggested before applying the generalized Born wavefield modeling. Multiple-prediction and suppression techniques in the image domain (Sava and Guitton, 2005; Artman et al., 2007) can be useful to

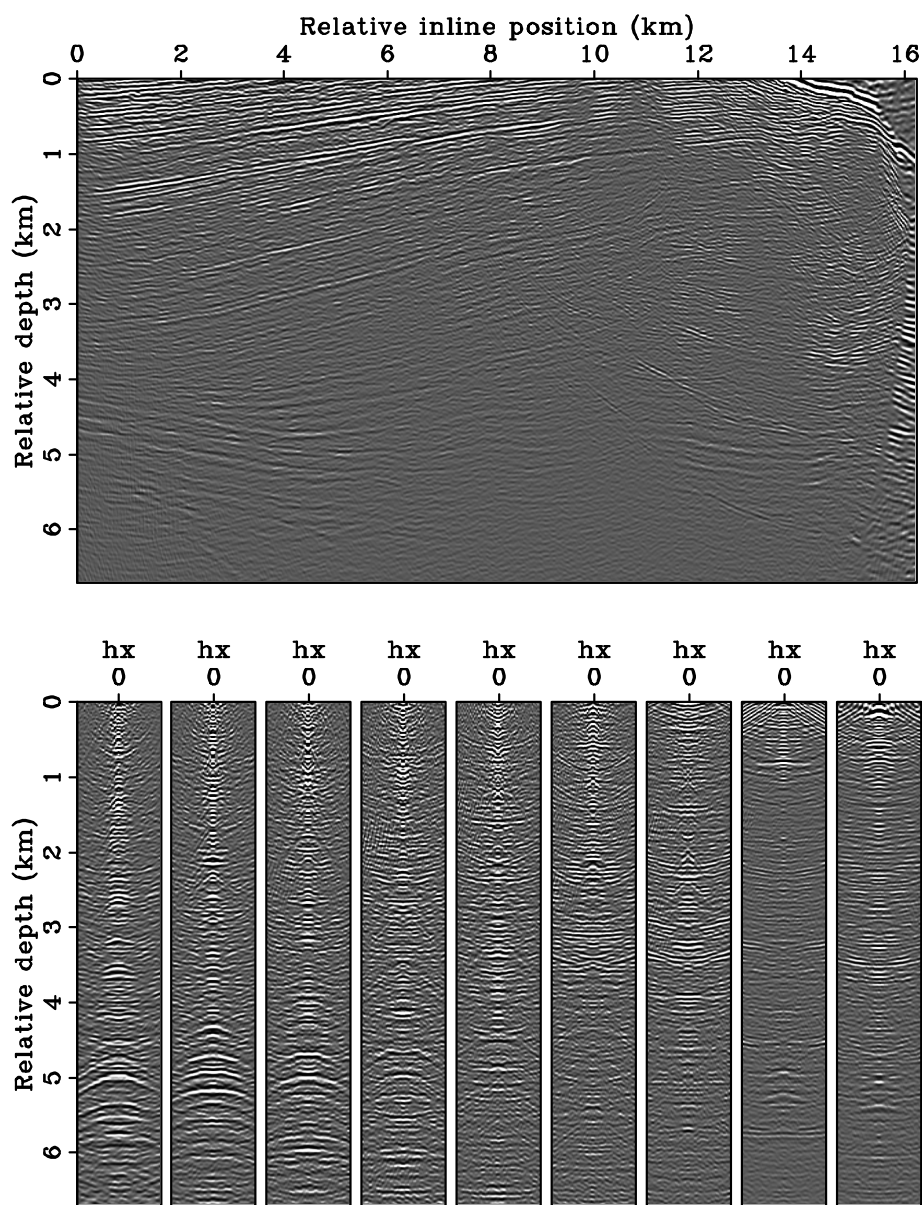


Figure 3.21: The initial target image and SODCIGs normalized by the diagonal of Hessian shown in Figure 3.20. View descriptions are the same as in Figure 3.19. [CR] [chap3/. bpgom2d-bimg-target-odcig-cpst](#)

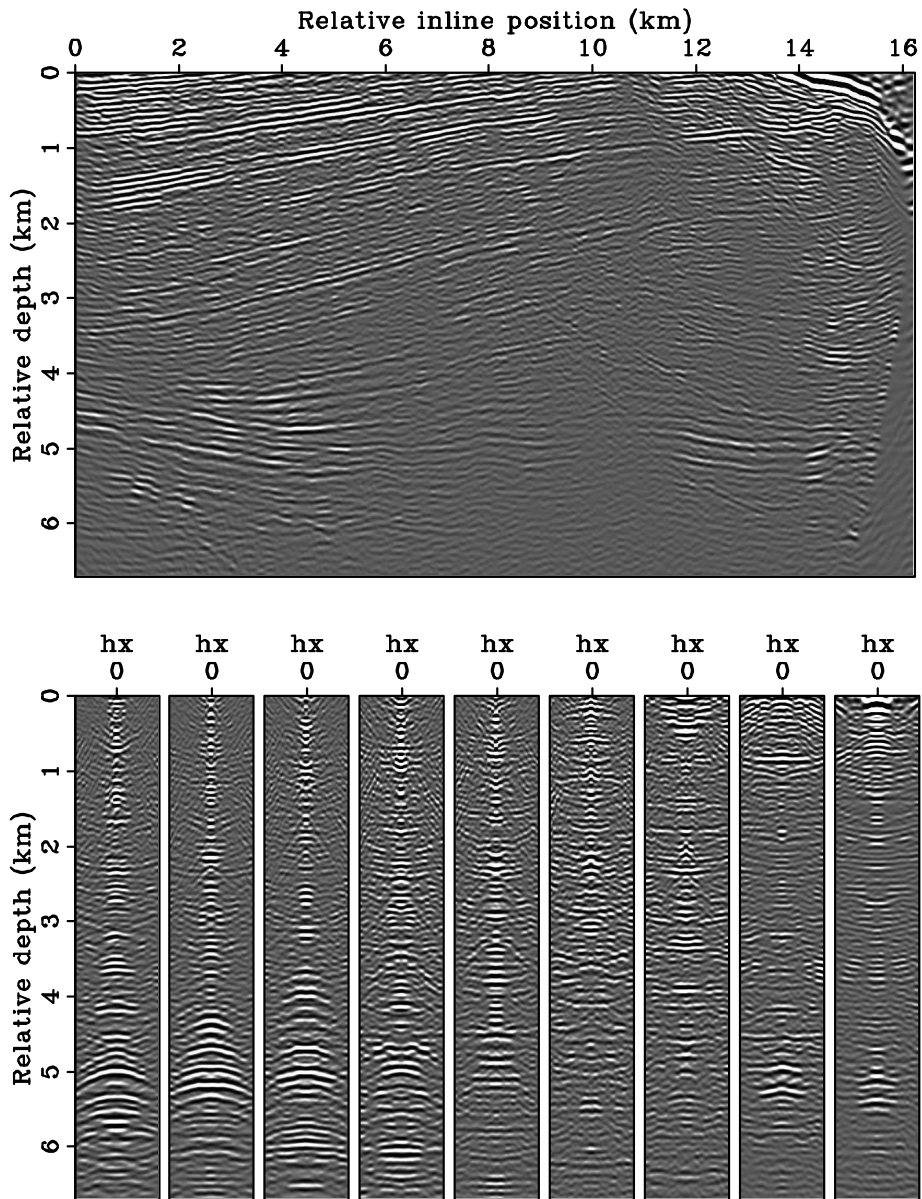


Figure 3.22: The target image and SODCIGs obtained by using the new data set and the initial velocity model. View descriptions are the same as in Figure 3.19. [CR] [chap3/. bpgom2d-bimg-odcig-born-planes](#)

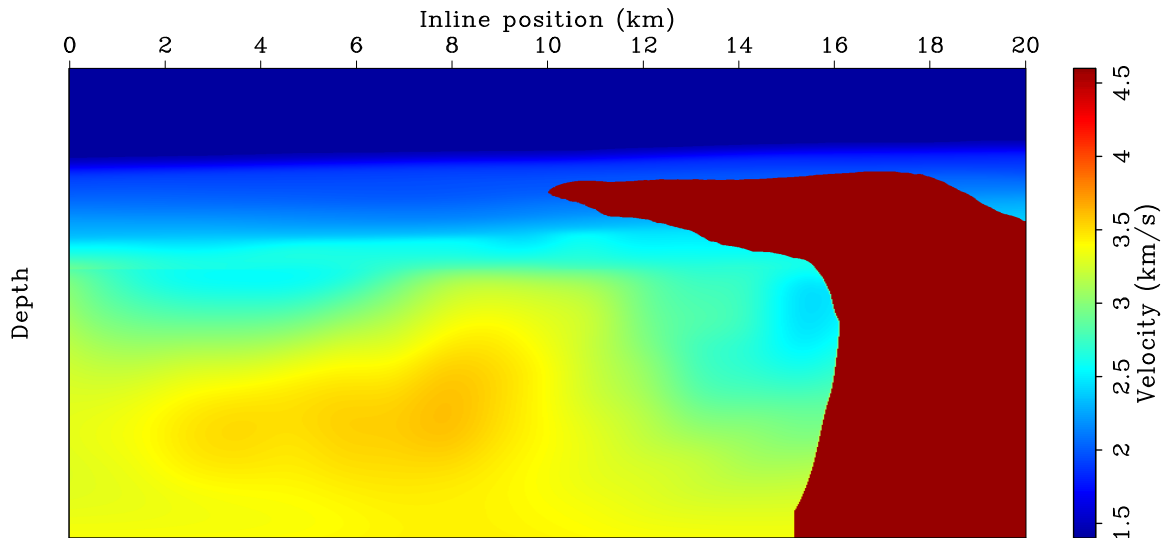
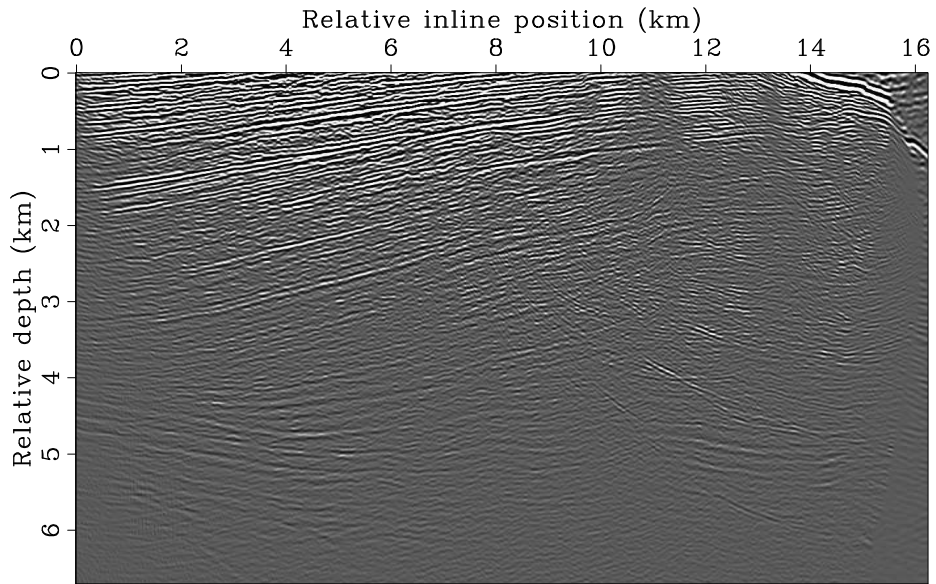


Figure 3.23: The inverted velocity model after 30 nonlinear iterations. [CR]
 chap3/. bpgom2d-invt-vmod

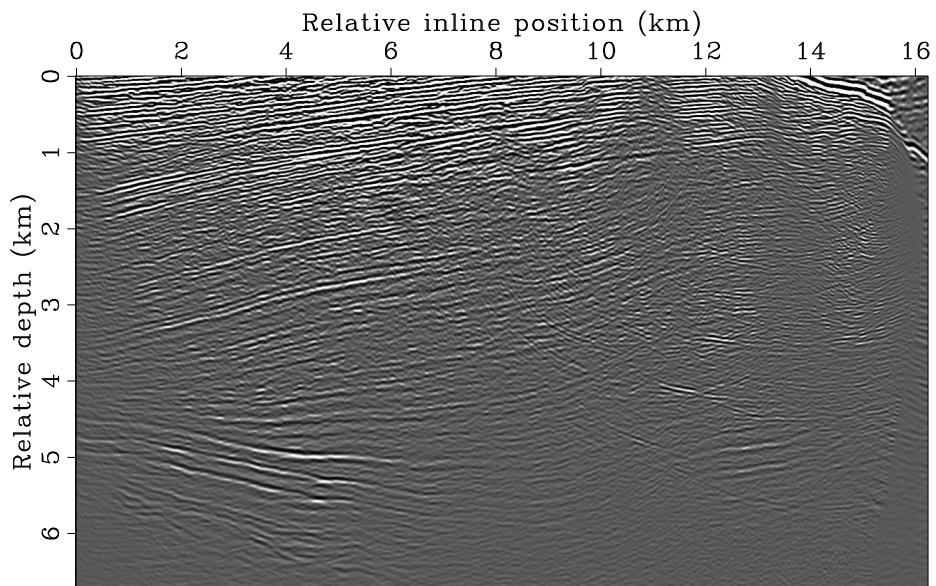
identify and remove multiples in the initial image and gathers.

Another interesting feature of the method is that, for a typical subsalt application, the migration operator used for imaging the synthesized Born data set can be much better behaved (or less singular) than the one used for imaging the original data set. This is because the former avoids propagating wavefields through the salt body, so that the complexities in the salt geometry have little influence on the operator itself. Figure 3.29 illustrates this point using the Sigsbee2A model. The operator under the new acquisition geometry (the planewave-source data synthesized at depth $z = 4.52$ km) is obviously much less singular than the one under the original acquisition geometry (the original point-source data recorded at the surface).

At a first glance, one might think that this process creates new information that is not present in the original data. However, this is not the case, because the modeling process involves non-stationary convolution between the modeling operator and the initial image (equation 3.6). Information that is not in the initial image will therefore not contribute to the modeling at all. For the Sigsbee2A example, the illumination

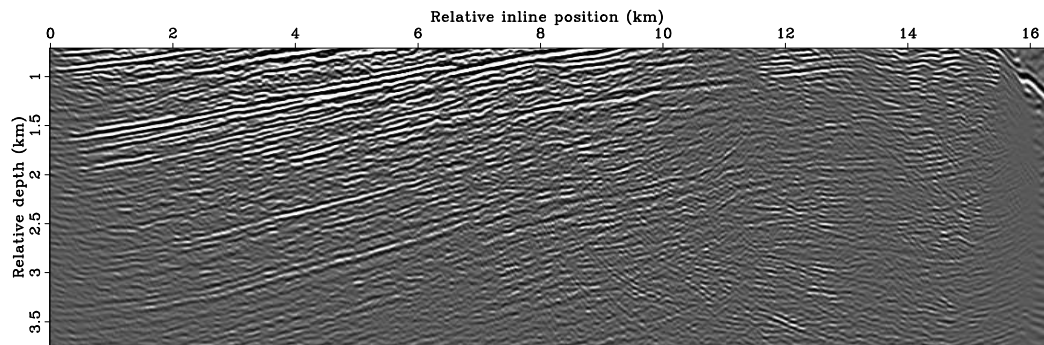


(a)

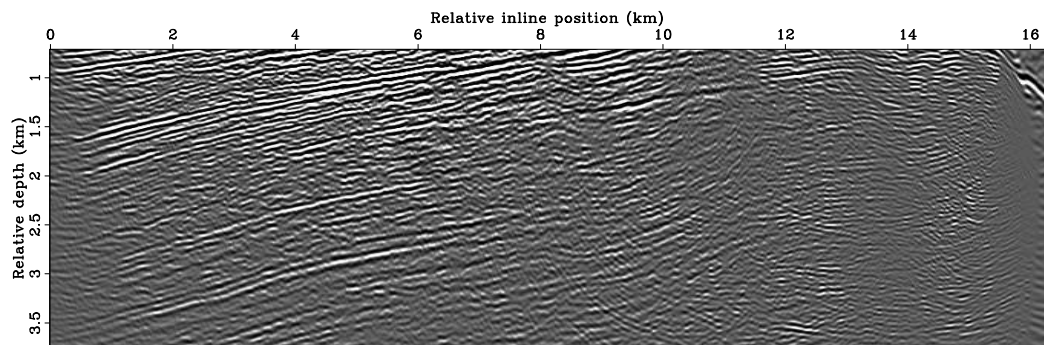


(b)

Figure 3.24: Zero-subsurface-offset images obtained using (a) the initial velocity model and (b) the inverted velocity model. The original data set is used for migration. [CR] `chap3/. bpgom2d-bimg-stack-raw,bpgom2d-imag-invt-stack-raw`



(a)



(b)

Figure 3.25: A close-up view of the upper section in Figure 3.24. Panels (a) and (b) are obtained using the initial and inverted velocity model, respectively. [CR] chap3/. bpgom2d-bimg-stack-raw-zoom1,bpgom2d-imag-invt-stack-raw-zoom1

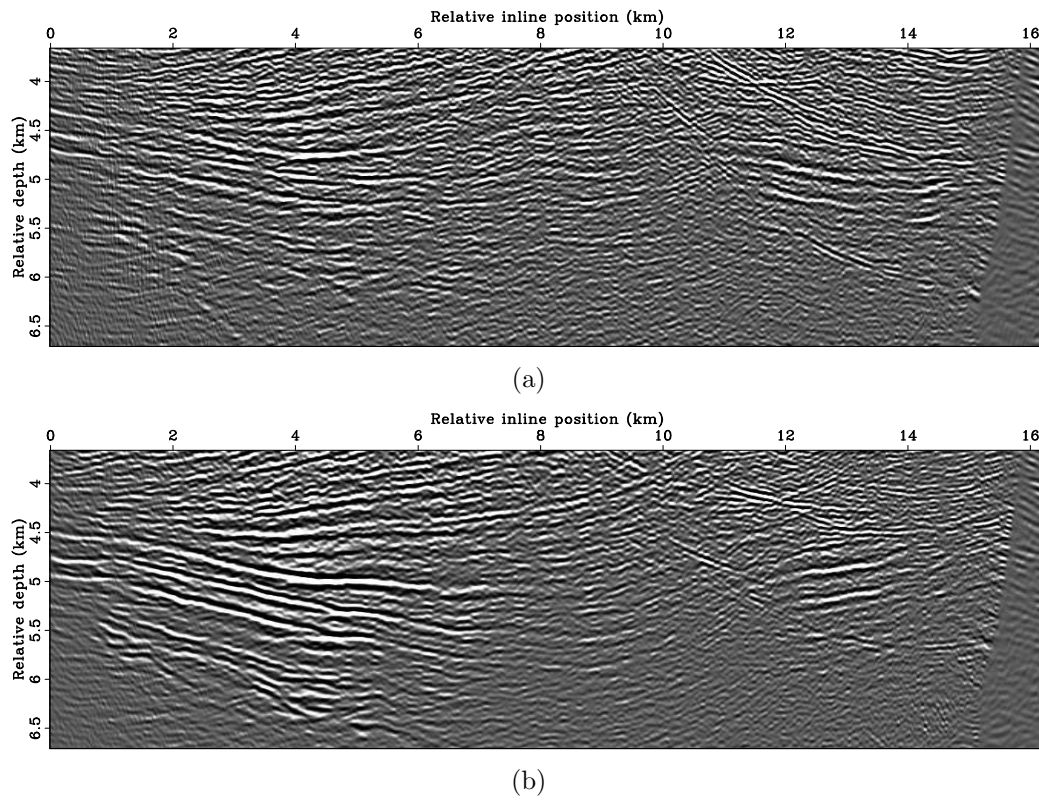


Figure 3.26: A close-up view of the lower section in Figure 3.24. Panels (a) and (b) are obtained using the initial and inverted velocity model, respectively. [CR] chap3/. bpgom2d-bimg-stack-raw-zoom2,bpgom2d-imag-invt-stack-raw-zoom2

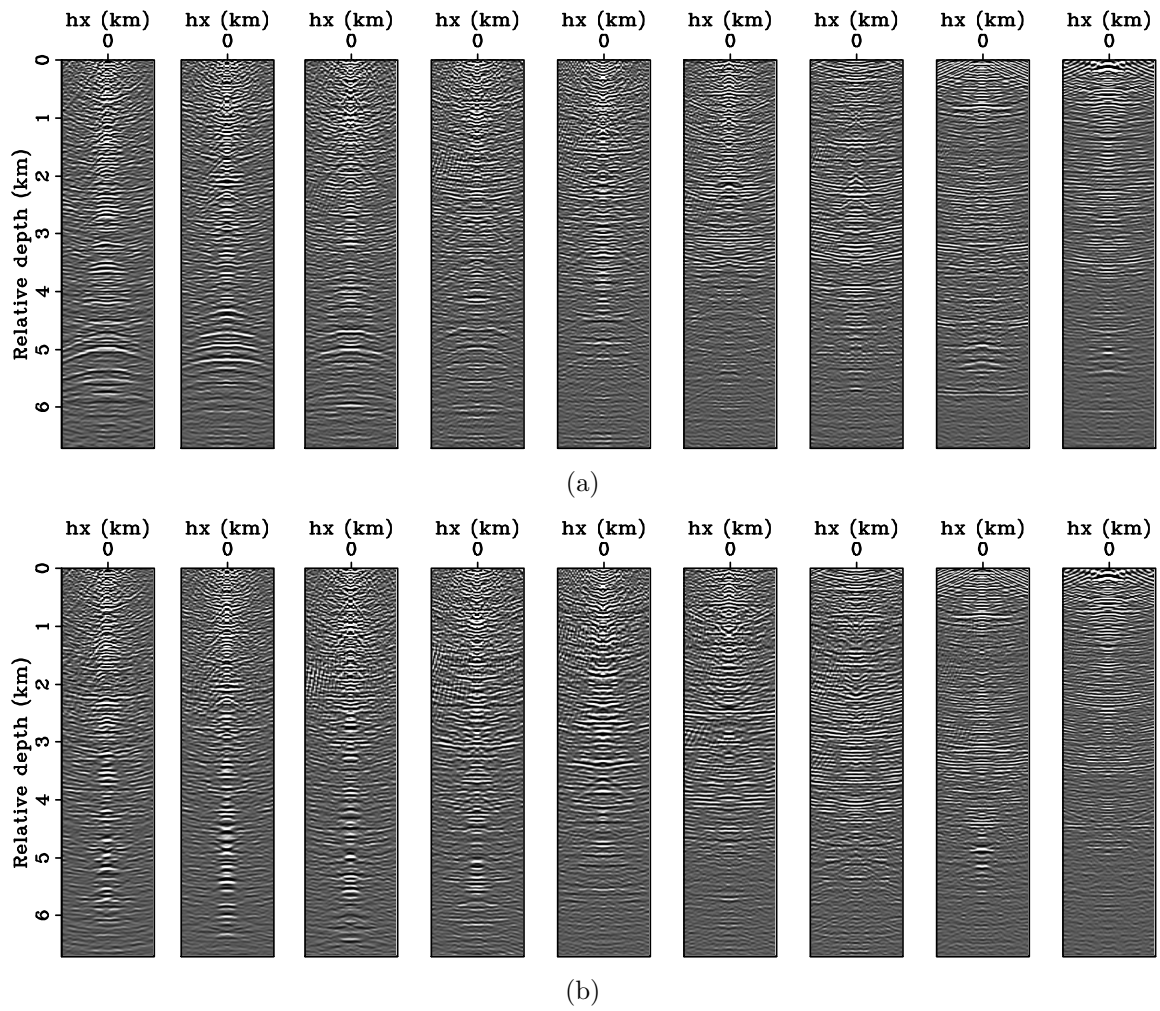


Figure 3.27: SODCIGs obtained using (a) the initial velocity model and (b) the inverted velocity model. The original data set is used for migration. The SODCIGs are extracted at the same CMP locations as those shown in Figure 3.19. [CR] chap3/. bpgom2d-bimg-offgath-raw,bpgom2d-imag-inv-offgath-raw

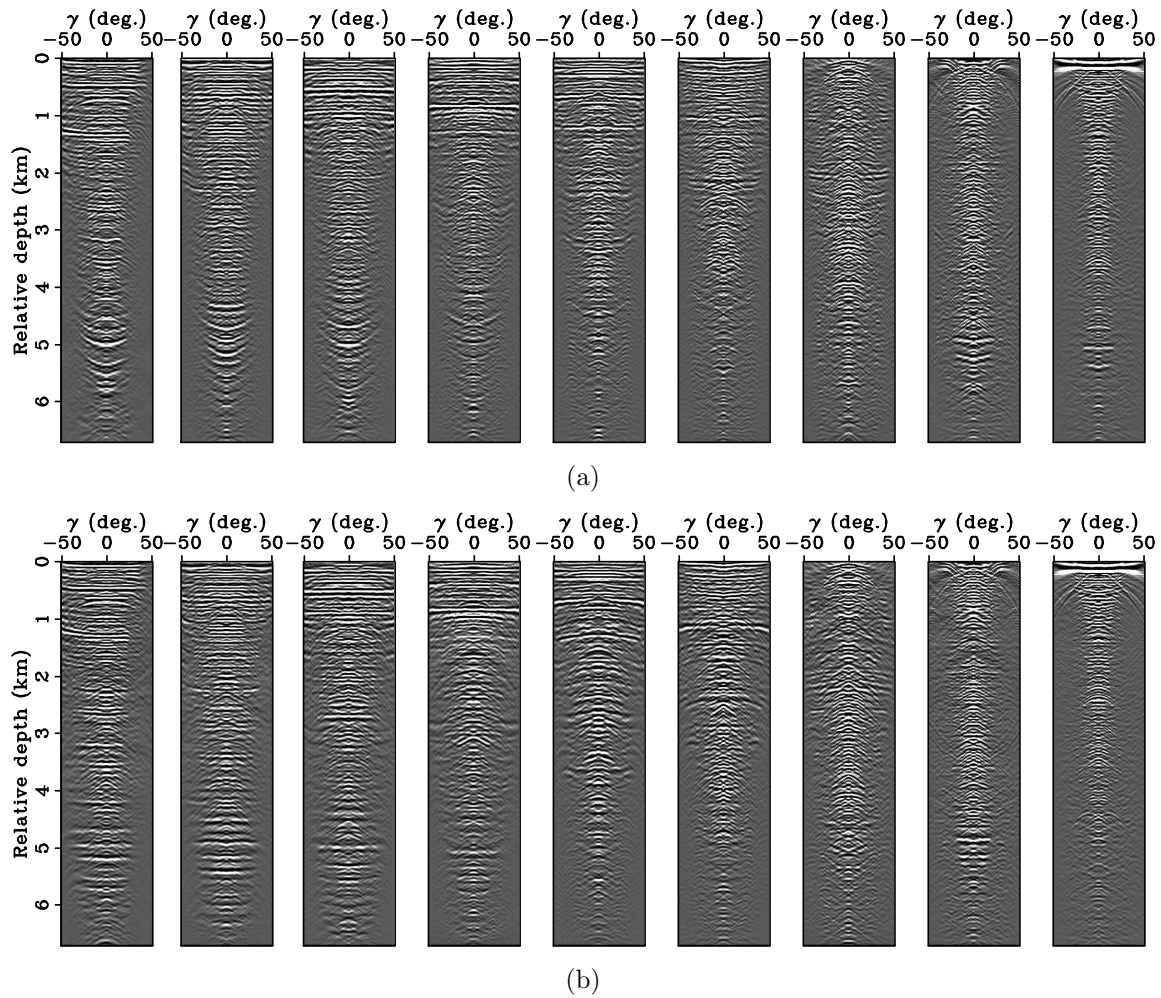


Figure 3.28: ADCIGs obtained using (a) the initial velocity model and (b) the inverted velocity model. The original data set is used for migration. The ADCIGs are extracted at the same CMP locations as those shown in Figure 3.27. [CR]

chap3/. bpgom2d-bimg-adcig,bpgom2d-imag-invt-adcig

holes in the ADCIGs obtained using the original data set (Figure 3.12(a)) are still present in the ADCIGs obtained using the new data set (Figure 3.12(b)).

Another important assumption of the proposed strategy is that the velocity outside the target region is sufficiently accurate. This is a relatively restrictive, but reasonable, assumption, because the proposed strategy aims at estimating velocities in the most challenging areas, such as the subsalt regions, whereas the velocities above the salt are usually very accurately determined even by ray-based tomography, thanks to the relatively simple geology.

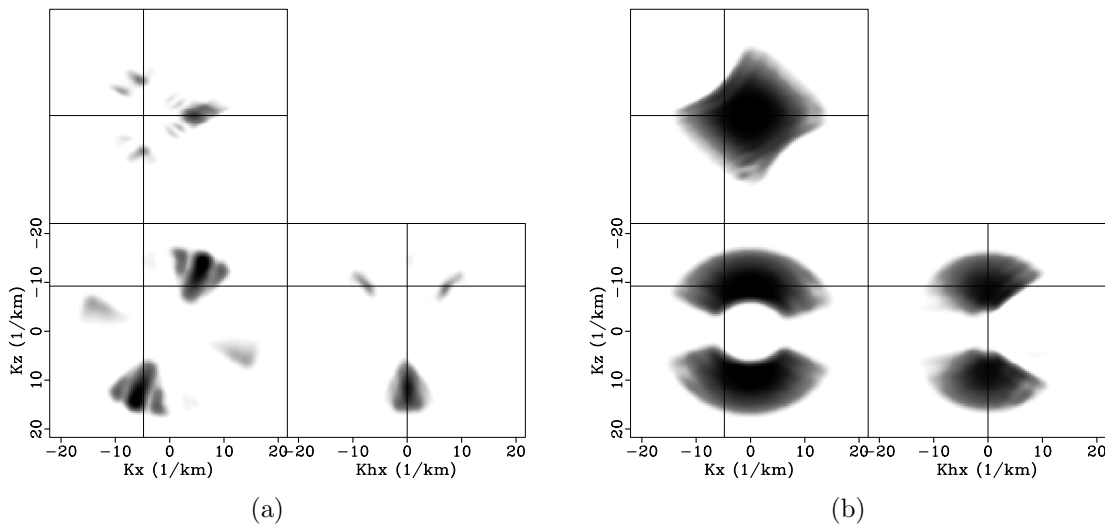


Figure 3.29: The amplitude spectrum of the prestack resolution functions (the Fourier transform of one row of the Hessian operator) at image point $x = 12.68$ km, $z = 5.49$ km for the Sigsbee2A model. Panel (a) is obtained using the original acquisition geometry, and (b) using the new acquisition geometry. Both resolution functions are computed using the velocity model shown in Figure 3.7. [CR] chap3/. sigsb2a-resolution-offs-fourier,sigsb2a-resolution-born-planes-offs-fourier

CONCLUSIONS

This chapter presents a methodology for performing target-oriented image-domain wavefield tomography. The proposed method is extremely efficient, because I formulate the velocity estimation problem in a target-oriented fashion, and use a synthesized

Born data set for velocity inversion. The synthesized Born data set can be an order of magnitude smaller than the originally recorded data set, but preserves all necessary velocity information for successful velocity analysis. The proposed method is wavefield-based; therefore it is suitable for estimating velocities in complex geologies. Numerical examples on 2-D synthetic and field data sets give satisfactory inversion results. The entire velocity analysis workflow can be fully automated, and no picking is necessary, although human interaction can be easily incorporated if it is desired. Thus this method provides a good tool for fast, accurate and flexible velocity model building in areas with complex geologies.

ACKNOWLEDGMENTS

I thank SMAART JV for providing the Sigsbee2A synthetic data set, and BP and ExxonMobil for providing the field data set. I also thank the Stanford Center for Computational Earth and Environmental Science for providing computing resources.

Chapter 4

3-D field-data examples

In this chapter, I extend the target-oriented wavefield inversion methodology (Chapters 2 and 3) to 3-D and apply it to a deep water 3-D field data set acquired from the Gulf of Mexico (GOM), provided by BP and ExxonMobil. Obtaining a clear and accurate subsalt image presents a challenge for this data set because of the presence of a complex salt body and the limited surface acquisition geometry. The velocities above the salt and the salt interpretation are given by the companies who provided the data and are known to be accurate. To image below the salt, I first estimate the subsalt velocities using target-oriented tomography (Chapter 3) and then use wavefield least-squares migration (Chapter 2) to invert a reflectivity image for a selected subsalt region. The 3-D inversion results illustrate that target-oriented wavefield tomography is a powerful tool for efficient and accurate velocity model-building in complex geologies, and that target-oriented wavefield least-squares migration optimally compensates for uneven subsurface illumination and produces subsalt reflectivity images easier to interpret than conventional migration alone.

This chapter starts with a review of 3-D conical-wave migration (Whitmore, 1995; Duquet et al., 2001; Zhang et al., 2005; Liu et al., 2006; Duquet and Lailly, 2006), which is used to generate the initial image gathers needed for extended Born wavefield modeling. I then demonstrate how the 3-D Hessian operator can be computed in the

3-D conical-wave domain. The 3-D Hessian operator is needed not only during the Born wavefield modeling step for subsalt velocity analysis, but also for the subsequent reflectivity imaging by target-oriented wavefield least-squares migration. Finally, I apply target-oriented wavefield inversion to the 3-D GOM field data set to sequentially invert subsalt velocities and reflectivities.

3-D CONICAL-WAVE MIGRATION

In general, a 3-D surface seismic data set can be represented by a 5-D object $d(\mathbf{x}_r, \mathbf{x}_s, \omega)$, with $\mathbf{x}_r = (x_r, y_r, z_r = 0)$ and $\mathbf{x}_s = (x_s, y_s, z_s = 0)$ being the receiver and source position, respectively, and ω being the angular frequency. Under the extended Born approximation (Chapter 3), the data can be modeled by a linear operator as follows:

$$d(\mathbf{x}_r, \mathbf{x}_s, \omega) = \sum_{\mathbf{x}} \sum_{\mathbf{h}} \omega^2 f_s(\omega) G(\mathbf{x} - \mathbf{h}, \mathbf{x}_s, \omega) G(\mathbf{x} + \mathbf{h}, \mathbf{x}_r, \omega) m(\mathbf{x}, \mathbf{h}), \quad (4.1)$$

where $f_s(\omega)$ is the source function; $G(\mathbf{x}, \mathbf{x}_s, \omega)$ and $G(\mathbf{x}, \mathbf{x}_r, \omega)$ are the Green's functions connecting the source and receiver position to the image point $\mathbf{x} = (x, y, z)$, respectively. We can transform data into the conical-wave domain by slant-stacking along the inline source axis x_s as follows:

$$d(\mathbf{x}_r, p_{s_x}, y_s, \omega) = \sum_{x_s} W(\mathbf{x}_r, x_s, y_s) d(\mathbf{x}_r, x_s, y_s, \omega) e^{i\omega p_{s_x} x_s}, \quad (4.2)$$

where $W(\mathbf{x}_r, x_s, y_s)$ is the acquisition mask operator, which contains ones where we record data, and zeros where we do not; p_{s_x} is the surface ray parameter in the inline direction. The inverse transform reads

$$W(\mathbf{x}_r, x_s, y_s) d(\mathbf{x}_r, x_s, y_s, \omega) = |\omega| \sum_{p_{s_x}} d(\mathbf{x}_r, p_{s_x}, y_s, \omega) e^{-i\omega p_{s_x} x_s}, \quad (4.3)$$

where $|\omega|$ on the right hand side of the equation is also known as the ‘‘rho’’ filter (Claerbout, 1985).

To find a reflectivity model \mathbf{m} that best fits the observed data for a given background velocity model, we can minimize a data-misfit function that measures the differences between the observed data and the synthesized data in a least-squares sense. In the point-source case, the data-misfit function reads

$$F(\mathbf{m}) = \frac{1}{2} \sum_{\omega} \sum_{\mathbf{x}_s} \sum_{\mathbf{x}_r} |W(\mathbf{x}_r, \mathbf{x}_s)[d(\mathbf{x}_r, \mathbf{x}_s, \omega) - d_{\text{obs}}(\mathbf{x}_r, \mathbf{x}_s, \omega)]|^2, \quad (4.4)$$

where d_{obs} is the observed data. Substituting equation 4.3 into 4.4 yields

$$\begin{aligned} F(\mathbf{m}) &= \frac{1}{2} \sum_{\omega} \sum_{y_s} \sum_{\mathbf{x}_r} \sum_{p_{s_x}} \sum_{p'_{s_x}} |\omega|^2 \\ &\quad \times [d(\mathbf{x}_r, p_{s_x}, y_s, \omega) - d_{\text{obs}}(\mathbf{x}_r, p_{s_x}, y_s, \omega)]^* \\ &\quad \times [d(\mathbf{x}_r, p'_{s_x}, y_s, \omega) - d_{\text{obs}}(\mathbf{x}_r, p'_{s_x}, y_s, \omega)] \sum_{x_s} e^{-i\omega(p'_{s_x} - p_{s_x})x_s}. \end{aligned} \quad (4.5)$$

If the inline source axis x_s is reasonably well sampled, we have $\sum_{x_s} e^{-i\omega(p'_{s_x} - p_{s_x})x_s} \approx \frac{1}{|\omega|} \delta(p'_{s_x} - p_{s_x})$, where $\delta(\cdot)$ is the Dirac delta function. Therefore, an objective function equivalent to equation 4.4 in the 3-D conical-wave domain takes the following form:

$$F(\mathbf{m}) \approx \frac{1}{2} \sum_{\omega} |\omega| \sum_{y_s} \sum_{p_{s_x}} \sum_{\mathbf{x}_r} |d(\mathbf{x}_r, p_{s_x}, y_s, \omega) - d_{\text{obs}}(\mathbf{x}_r, p_{s_x}, y_s, \omega)|^2 \quad (4.6)$$

Migration is known as the first iteration in the steepest-descent direction of the objective function defined by equation 4.6. It can be formally obtained as follows:

$$m(\mathbf{x}, \mathbf{h}) = \sum_{\omega} |\omega| \sum_{y_s} \sum_{p_{s_x}} \sum_{\mathbf{x}_r} \left(\frac{\partial d(\mathbf{x}_r, p_{s_x}, y_s, \omega)}{\partial m(\mathbf{x}, \mathbf{h})} \right)^* d_{\text{obs}}(\mathbf{x}_r, p_{s_x}, y_s, \omega). \quad (4.7)$$

With equations and 4.1 and 4.2, we obtain the expression of the derivative $\frac{\partial d(\mathbf{x}_r, p_{s_x}, y_s, \omega)}{\partial m(\mathbf{x}, \mathbf{h})}$

as follows:

$$\begin{aligned} \frac{\partial d(\mathbf{x}_r, p_{s_x}, y_s, \omega)}{\partial m(\mathbf{x}, \mathbf{h})} &= \sum_{x_s} \omega^2 W(\mathbf{x}_r, x_s, y_s) f_s(\omega) G(\mathbf{x} - \mathbf{h}, x_s, y_s, \omega) \\ &\quad \times G(\mathbf{x} + \mathbf{h}, \mathbf{x}_r, \omega) e^{i\omega p_{s_x} x_s}. \end{aligned} \quad (4.8)$$

Substituting equation 4.8 into 4.7 and rearranging the terms yield

$$\begin{aligned} m(\mathbf{x}, \mathbf{h}) &= \sum_{\omega} |\omega|^3 \sum_{y_s} \sum_{p_{s_x}} \sum_{\mathbf{x}_r} G^*(\mathbf{x} + \mathbf{h}, \mathbf{x}_r, \omega) d_{\text{obs}}(\mathbf{x}_r, p_{s_x}, y_s, \omega) \\ &\quad \sum_{x_s} W^*(\mathbf{x}_r, x_s, y_s) f_s^*(\omega) G^*(\mathbf{x} - \mathbf{h}, x_s, y_s, \omega) e^{-i\omega p_{s_x} x_s}. \end{aligned} \quad (4.9)$$

However, equation 4.9 is awkward and inefficient to implement because of the acquisition mask operator inside the summation loop. Fortunately, as shown in Appendix D, the acquisition mask operator can be ignored, if p_{s_x} is sufficiently well sampled. Therefore, equation 4.9 can be rewritten as follows:

$$m(\mathbf{x}, \mathbf{h}) = \sum_{\omega} |\omega|^3 \sum_{y_s} \sum_{p_{s_x}} U_s(\mathbf{x} - \mathbf{h}, p_{s_x}, y_s, \omega) U_r(\mathbf{x} + \mathbf{h}, p_{s_x}, y_s, \omega), \quad (4.10)$$

where U_s is the conjugate of the forward-propagated 3-D conical-wave source wavefield,

$$U_s(\mathbf{x}, p_{s_x}, y_s, \omega) = \sum_{x_s} f_s^*(\omega) G^*(\mathbf{x}, x_s, y_s, \omega) e^{-i\omega p_{s_x} x_s}, \quad (4.11)$$

and U_r is the backward-propagated 3-D conical-wave receiver wavefield,

$$U_r(\mathbf{x}, p_{s_x}, y_s, \omega) = \sum_{\mathbf{x}_r} G^*(\mathbf{x}, \mathbf{x}_r, \omega) d_{\text{obs}}(\mathbf{x}_r, p_{s_x}, y_s, \omega). \quad (4.12)$$

If we use one-way wavefield propagators, U_s and U_r satisfy the following one-way

wave equations:

$$\begin{cases} \left(\frac{\partial}{\partial z} + i\sqrt{\frac{\omega^2}{v^2(\mathbf{x})} + \nabla^2} \right) U_s(\mathbf{x}, p_{s_x}, y_s, \omega) = 0 \\ U_s(x, y, z = 0, p_{s_x}, y_s, \omega) = \sum_{x_s} \delta(x - x_s, y - y_s) f_s^*(\omega) e^{-i\omega p_{s_x} x_s} \end{cases}, \quad (4.13)$$

and

$$\begin{cases} \left(\frac{\partial}{\partial z} + i\sqrt{\frac{\omega^2}{v^2(\mathbf{x})} + \nabla^2} \right) U_r(\mathbf{x}, p_{s_x}, y_s, \omega) = 0 \\ U_r(x, y, z = 0, p_{s_x}, y_s, \omega) = \sum_{\mathbf{x}_r} \delta(x - x_r, y - y_r) d_{\text{obs}}(\mathbf{x}_r, p_{s_x}, y_s, \omega) \end{cases}. \quad (4.14)$$

In both equations 4.13 and 4.14, $v(\mathbf{x})$ is the velocity, $\nabla^2 = \frac{\partial^2}{\partial x^2} + \frac{\partial^2}{\partial y^2}$ is the Laplacian operator, and $\delta(\cdot)$ is the Dirac delta function.

Equations 4.10, 4.13 and 4.14 together define the 3-D conical-wave migration (Whitmore, 1995; Duquet et al., 2001; Zhang et al., 2005; Liu et al., 2006; Duquet and Lailly, 2006), which has been widely used to migrate marine streamer data.

3-D PHASE-ENCODED HESSIAN

The Hessian operator in the 3-D conical-wave domain can be obtained by taking the second-order derivatives of $F(\mathbf{m})$ (equation 4.6) with respect to the model parameters:

$$H(\mathbf{x}, \mathbf{x}', \mathbf{h}, \mathbf{h}') = \sum_{\omega} |\omega|^5 \sum_{y_s} \sum_{p_{s_x}} \sum_{\mathbf{x}_r} \left(\frac{\partial d(\mathbf{x}_r, p_{s_x}, y_s, \omega)}{\partial m(\mathbf{x}, \mathbf{h})} \right) \left(\frac{\partial d(\mathbf{x}_r, p_{s_x}, y_s, \omega)}{\partial m(\mathbf{x}', \mathbf{h}')} \right)^*. \quad (4.15)$$

When $\mathbf{x} = \mathbf{x}'$ and $\mathbf{h} = \mathbf{h}'$, we obtain the diagonal components of the Hessian, which are also known as subsurface illumination; otherwise, we obtain the off-diagonal components of the Hessian, which are also known as resolution functions for a given acquisition setup (Chapter 2).

Substituting equation 4.8 into equation 4.15 yields

$$\begin{aligned}
H(\mathbf{x}, \mathbf{x}', \mathbf{h}, \mathbf{h}') &= \sum_{\omega} |\omega|^5 \sum_{y_s} \sum_{p_{sx}} \sum_{\mathbf{x}_r} G(\mathbf{x} + \mathbf{h}, \mathbf{x}_r, \omega) G^*(\mathbf{x}' - \mathbf{h}', \mathbf{x}_r, \omega) \\
&\quad \sum_{x_s} W(\mathbf{x}_r, x_s, y_s) f_s(\omega) G(\mathbf{x} - \mathbf{h}, x_s, y_s, \omega) e^{i\omega p_{sx} x_s} \\
&\quad \sum_{x'_s} W(\mathbf{x}_r, x'_s, y_s) f_s^*(\omega) G^*(\mathbf{x}' - \mathbf{h}', x'_s, y_s, \omega) e^{-i\omega p_{sx} x'_s}. \quad (4.16)
\end{aligned}$$

Equation 4.16, however, is nontrivial and very expensive to implement as discussed in Chapter 2. In order to reduce the computational cost and make it affordable, I use the simultaneous phase-encoding technique developed in Chapter 2 to efficiently calculate an approximate version of equation 4.16.

As discussed in Chapter 2, simultaneous phase-encoding is only strictly valid when the acquisition mask operator is independent along the encoding axes. For example, in Chapter 2, when we encode Green's functions along both \mathbf{x}_s and \mathbf{x}_r , we require the acquisition mask operator to be separable along the the encoding axes, i.e., $W(\mathbf{x}_r, \mathbf{x}_r) = W_r(\mathbf{x}_r)W_s(\mathbf{x}_s)$. Ocean-bottom cable (OBC) or land acquisition geometry, where the receivers are fixed for all sources, obviously satisfies this condition. But marine streamer acquisition geometry, where the receiver cable moves with sources, apparently does not. For the 3-D conical-wave-domain Hessian, the encoding axes are the inline source axis x_s and the receiver axis $\mathbf{x}_r = (x_r, y_r)$, respectively. To make the theory applicable to the marine data case, I assume that the receiver location \mathbf{x}_r depends only on the crossline source position y_s , but is independent of the inline source position x_s . This implicitly assumes that for a fixed crossline y_s , all inline shots share the same receiver array. Therefore, we can express the acquisition mask operator as a product of two separate functions:

$$W(\mathbf{x}_r, x_s, y_s) \approx W_r(\mathbf{x}_r, y_s)W_s(x_s, y_s), \quad (4.17)$$

where W_r and W_s define the distributions of receiver position \mathbf{x}_r and the inline source position x_s , respectively, for a given crossline source position y_s .

Substituting equation 4.17 into equation 4.16 yields the expression of the exact Hessian in the 3-D conical-wave domain:

$$\begin{aligned}
H(\mathbf{x}, \mathbf{x}', \mathbf{h}, \mathbf{h}') &= \sum_{\omega} |\omega|^5 \sum_{y_s} \sum_{p_{sx}} \sum_{\mathbf{x}_r} W_r(\mathbf{x}_r, y_s) G(\mathbf{x} + \mathbf{h}, \mathbf{x}_r, \omega) G^*(\mathbf{x}' - \mathbf{h}', \mathbf{x}_r, \omega) \\
&\quad \sum_{x_s} W_s(x_s, y_s) f_s(\omega) G(\mathbf{x} - \mathbf{h}, x_s, y_s, \omega) e^{i\omega p_{sx} x_s} \\
&\quad \sum_{x'_s} W_s(x'_s, y_s) f_s^*(\omega) G^*(\mathbf{x}' - \mathbf{h}', x'_s, y_s, \omega) e^{-i\omega p_{sx} x'_s}. \tag{4.18}
\end{aligned}$$

With further encoding on the receiver-side Green's functions, we obtain the simultaneously phase-encoded Hessian as follows:

$$\begin{aligned}
\tilde{H}(\mathbf{x}, \mathbf{x}', \mathbf{h}, \mathbf{h}', \mathbf{p}_r) &= \sum_{\omega} |\omega|^5 \sum_{y_s} \sum_{p_{sx}} \\
&\quad \times \sum_{\mathbf{x}_r} W_r(\mathbf{x}_r, y_s) G(\mathbf{x} + \mathbf{h}, \mathbf{x}_r, \omega) \alpha(\mathbf{x}_r, \mathbf{p}_r, \omega) \\
&\quad \times \sum_{\mathbf{x}'_r} W_r(\mathbf{x}'_r, y_s) G^*(\mathbf{x}' - \mathbf{h}', \mathbf{x}'_r, \omega) \alpha^*(\mathbf{x}'_r, \mathbf{p}_r, \omega) \\
&\quad \times \sum_{x_s} W_s(x_s, y_s) f_s(\omega) G(\mathbf{x} - \mathbf{h}, x_s, y_s, \omega) e^{i\omega p_{sx} x_s} \\
&\quad \times \sum_{x'_s} W_s(x'_s, y_s) f_s^*(\omega) G^*(\mathbf{x}' - \mathbf{h}', x'_s, y_s, \omega) e^{-i\omega p_{sx} x'_s}, \tag{4.19}
\end{aligned}$$

where α is the receiver-side encoding function, defined similarly to the one defined in Chapter 2. Equation 4.19 can be greatly simplified as follows:

$$\begin{aligned}
\tilde{H}(\mathbf{x}, \mathbf{x}', \mathbf{h}, \mathbf{h}', \mathbf{p}_r) &= \sum_{\omega} |\omega|^5 \sum_{y_s} \sum_{p_{sx}} S(\mathbf{x} - \mathbf{h}, p_{sx}, y_s, \omega) S^*(\mathbf{x}' - \mathbf{h}', p_{sx}, y_s, \omega) \\
&\quad R(\mathbf{x} - \mathbf{h}, p_{sx}, y_s, \mathbf{p}_r, \omega) R^*(\mathbf{x}' - \mathbf{h}', p_{sx}, y_s, \mathbf{p}_r, \omega), \tag{4.20}
\end{aligned}$$

if we define

$$S(\mathbf{x}, p_{sx}, y_s, \omega) = \sum_{x_s} W_s(x_s, y_s) f_s(\omega) G(\mathbf{x}, x_s, y_s, \omega) e^{i\omega p_{sx} x_s}, \tag{4.21}$$

and

$$R(\mathbf{x}, p_{s_x}, y_s, \mathbf{p}_r, \omega) = \sum_{\mathbf{x}_r} W_r(\mathbf{x}_r, y_s) G(\mathbf{x}, \mathbf{x}_r, \omega) \alpha(\mathbf{x}_r, \mathbf{p}_r, \omega). \quad (4.22)$$

For one-way wave-equation-based application, S and R satisfy the following one-way wave equations:

$$\begin{cases} \left(\frac{\partial}{\partial z} - i \sqrt{\frac{\omega^2}{v^2(\mathbf{x})} + \nabla^2} \right) S(\mathbf{x}, p_{s_x}, y_s, \omega) = 0 \\ S(x, y, z = 0, p_{s_x}, y_s, \omega) = \sum_{x_s} W_s(x_s, y_s) \delta(x - x_s, y - y_s) f_s(\omega) e^{i\omega p_{s_x} x_s} \end{cases}. \quad (4.23)$$

and

$$\begin{cases} \left(\frac{\partial}{\partial z} - i \sqrt{\frac{\omega^2}{v^2(\mathbf{x})} + \nabla^2} \right) R(\mathbf{x}, p_{s_x}, y_s, \mathbf{p}_r, \omega) = 0 \\ R(x, y, z = 0, p_{s_x}, y_s, \mathbf{p}_r, \omega) = \sum_{\mathbf{x}_r} W_r(\mathbf{x}_r, y_s) \delta(x - x_r, y - y_r) \alpha(\mathbf{x}_r, \mathbf{p}_r, \omega) \end{cases}. \quad (4.24)$$

In the following numerical examples, I choose α to be a random phase encoding function; thus \mathbf{p}_r denotes the realization index of the random phase encoding function (Chapter 2). It would be very easy to verify that, with this choice of encoding functions, equation 4.19 converges to equation 4.18 by stacking over \mathbf{p}_r , according to the law of large numbers (Gray and Davisson, 2003):

$$\tilde{\tilde{H}}(\mathbf{x}, \mathbf{x}', \mathbf{h}, \mathbf{h}') = \sum_{\mathbf{p}_r} \tilde{\tilde{H}}(\mathbf{x}, \mathbf{x}', \mathbf{h}, \mathbf{h}', \mathbf{p}_r) \approx H(\mathbf{x}, \mathbf{x}', \mathbf{h}, \mathbf{h}'). \quad (4.25)$$

THE 3-D GOM FIELD-DATA EXAMPLES

The 3-D GOM data set spans an area of approximately 120 km², with 20 km inlines and 6 km crosslines. The data set does not have crossline offset, because it was acquired using a narrow-azimuth towed-streamer (NATS) acquisition system, and further rotated using azimuth moveout (AMO) (Biondi et al., 1998) into zero azimuth. The minimum and maximum inline offsets are 0.3 km and 8.2 km, respectively. The frequency content of the data set ranges between 5 Hz and 35 Hz.

The original data set is in the midpoint domain. I transform it into the shot-profile domain, and Figure 4.1 shows a typical shot gather. I also apply reciprocity during the coordinate transform, and therefore, the data set has both positive and negative offsets. As can be seen from Figure 4.1, the data set has been preprocessed to some degree, including muting, surface-related multiple removal, etc., by the companies who provide the data. Since the preprocessing steps cannot be reversed, I assume that the data set has been properly preprocessed, and that it is suitable for subsequent velocity analysis and imaging.

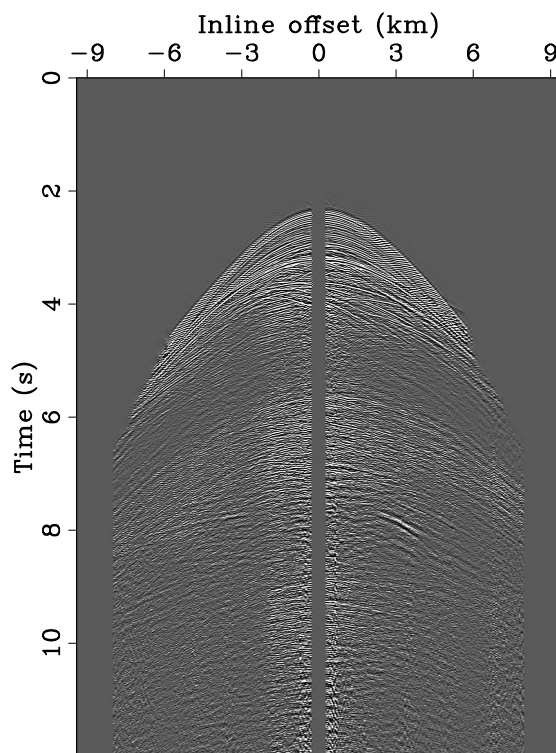


Figure 4.1: One typical shot gather for the GOM data set. The shot gather has only inline offset due to narrow azimuth acquisition and AMO transform. [CR]

chap4/. bpgom3d-shot

Subsalt velocity analysis

The initial 3-D velocity model corresponding to this data set is shown in Figure 4.2. Velocities above the target (outlined by a black box) and the salt interpretation are known to be accurate. The goal is to invert for subsalt velocities inside the target region. The initial velocities inside the box are set to be $v(z)$.

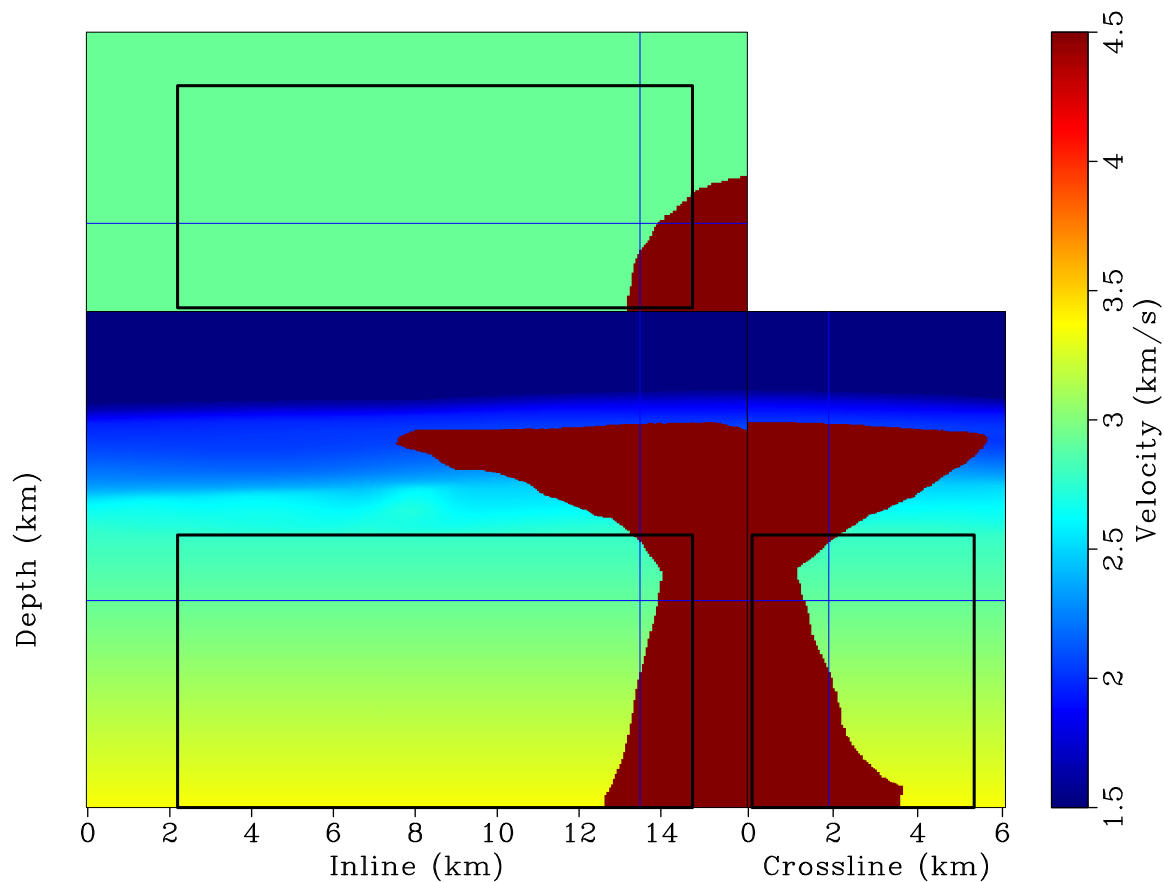


Figure 4.2: The initial 3-D velocity model. The area inside the black box is the target region for velocity analysis. Velocities above the target region and the salt interpretation are known to be accurate. [ER] `chap4/. bpgom3d-bvel-full`

Generating initial image gathers

The original data set contains 100125 point-source gathers in total, with 801 inline shots and 125 crossline shots. I perform 3-D conical-wave migration (equations 4.10, 4.13 and 4.14) to generate the initial image gathers, where I synthesize 101 conical waves for each crossline and migrate 12625 conical waves in total. The minimum and maximum inline take-off angles at the surface for the conical waves are -30° and 30° , respectively. The maximum frequency used for the initial migration is 20 Hz.

Figure 4.3 shows the zero-subsurface offset image for the target region obtained using the initial velocity model (Figure 4.2). To more accurately preserve the velocity information, I compute both inline and crossline subsurface offsets (Figure 4.4). The crossline subsurface offset is included because wavefields can travel out of plane during propagation, and therefore they may image the subsurface with different azimuths than that on the surface. The 3-D subsurface-offset-domain common-image gathers (SODCIGs) shown in Figure 4.4 confirm this: the events in the top panels of Figures 4.4(a) and 4.4(b) are tilted, suggesting that they are not imaged by zero subsurface azimuth. Also note that the 3-D SODCIGs are not well focused at the zero subsurface offset in either the inline or crossline directions. The defocusing in the inline subsurface offset (h_x) is mainly caused by velocity inaccuracies, whereas the defocusing in the crossline subsurface offset (h_y) is mainly due to insufficient crossline data coverage (single surface azimuth data) (Tang, 2007).

The diagonal of the subsurface-offset-domain phase-encoded Hessian computed using equation 4.20 is shown in Figures 4.5 and 4.6. The Hessian is obtained using one random realization. The uneven subsurface illumination is mainly caused by the complex salt shape and limited surface acquisition geometry. Note how energy can fail to penetrate the salt body, which has relatively high velocity. The normalized image and gathers (Figures 4.7 and 4.8) show more balanced amplitudes, suggesting that the Hessian does a good job of removing the effects of uneven illumination.

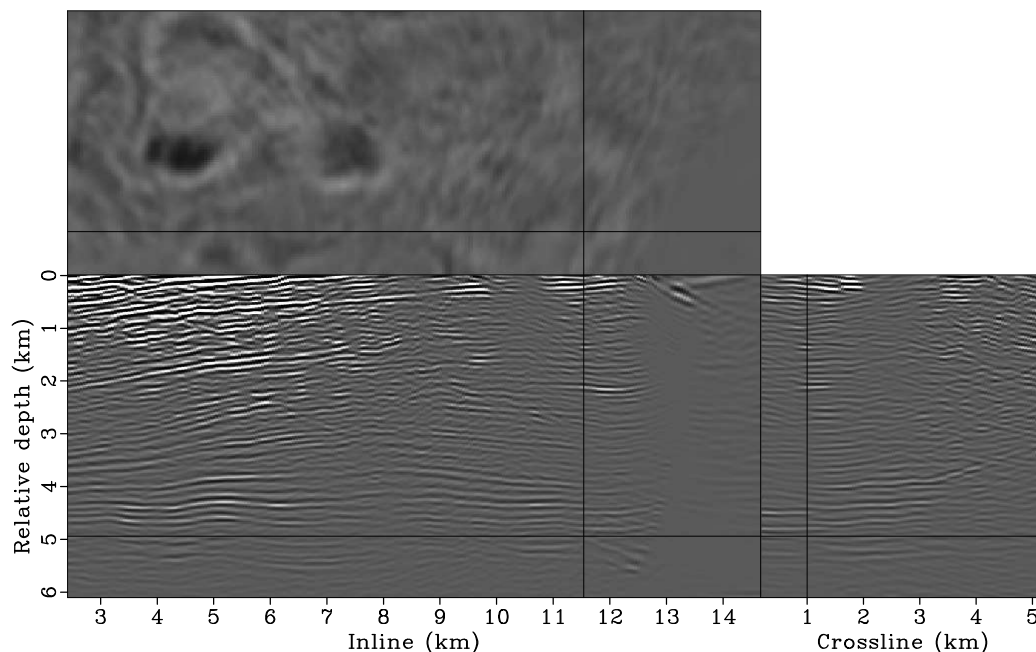


Figure 4.3: The zero-subsurface-offset image for the target region, obtained by migrating the original data set using the initial velocity model. [CR] chap4/. bpgom3d-bimg-orig1

3-D Born wavefield modeling

The next step is to model a new data set for velocity analysis. The initial image and gathers (Figures 4.7 and 4.8) have been preprocessed before the modeling step, where I simply mute events inside the salt body (Figure 4.9). More sophisticated preprocessing, such as noise attenuation, key reflection selection, etc., can also be applied. The preprocessing step allows human interaction in the velocity analysis workflow, adding desired flexibility and control to this method.

In Chapter 3, I use 2-D plane waves for generalized Born wavefield modeling for 2-D velocity analysis. In the 3-D case, I use 3-D plane-wave modeling to generate 3-D Born data at the top of the target region. To determine the optimum parameters for the 3-D modeling, I carried out seismic visibility analysis (Jin and Xu, 2010), which can provide us a quantitative estimate of which part of the data contributes most

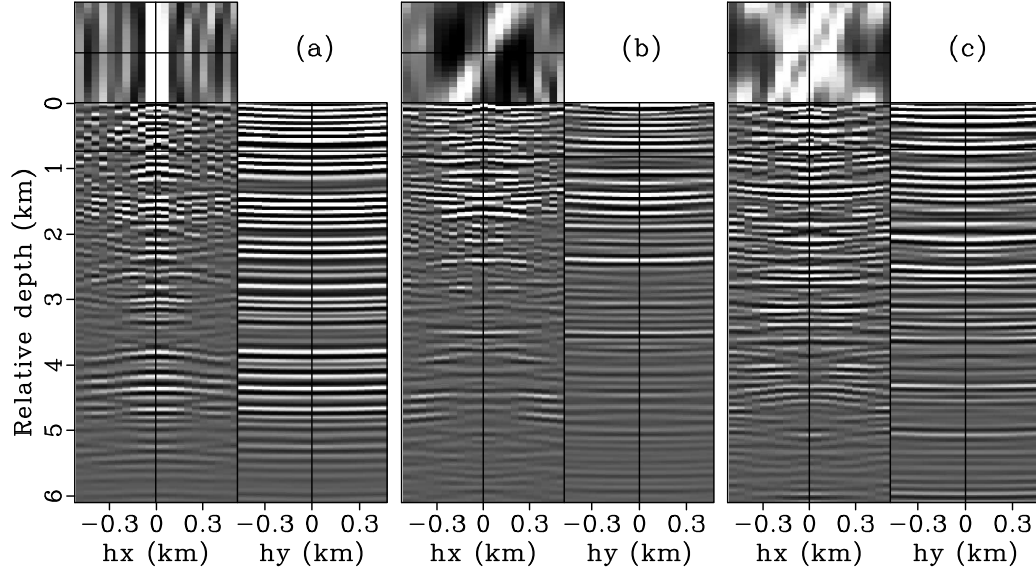


Figure 4.4: The 3-D SODCIGs obtained using the original data set and the initial velocity model. Panels (a), (b) and (c) are extracted at (3.04, 1.34) km, (6.09, 2.86) km and (9.13, 4.38) km, from left to right. [CR] chap4/. bpgom3d-cig3d-orig

to the target region for a given prestack acquisition geometry (see Appendix E for details). Figure 4.10 shows the average source visibility map for a single frequency of 10 Hz, as a function of both inline and crossline ray parameters. Note that most of the energy contributing to the target region falls within the range where $\tilde{p}_{s_x} \in (-213, 213)$ $\mu\text{s}/\text{m}$, and $\tilde{p}_{s_y} \in (-180, 180)$ $\mu\text{s}/\text{m}$.

Based on the result of visibility analysis, I model 315 plane waves in total at the top of the target region, with 21 plane waves inline and 15 plane waves crossline. The minimum and maximum values of ray parameters are -213 $\mu\text{s}/\text{m}$ and 213 $\mu\text{s}/\text{m}$ in the inline direction, and -180 $\mu\text{s}/\text{m}$ and 180 $\mu\text{s}/\text{m}$ in the crossline direction, respectively. If we convert these values into polar coordinates, the minimum and maximum angles of these plane waves are approximately -47.7° and 47.7° in dip, -40.2° and 40.2° in azimuth, respectively. I use a Ricker wavelet with a dominant frequency 10 Hz for the generalized Born wavefield modeling. The minimum and maximum frequencies of the Ricker wavelet are 3 Hz and 18 Hz, respectively. Figure 4.11 shows a 3-D

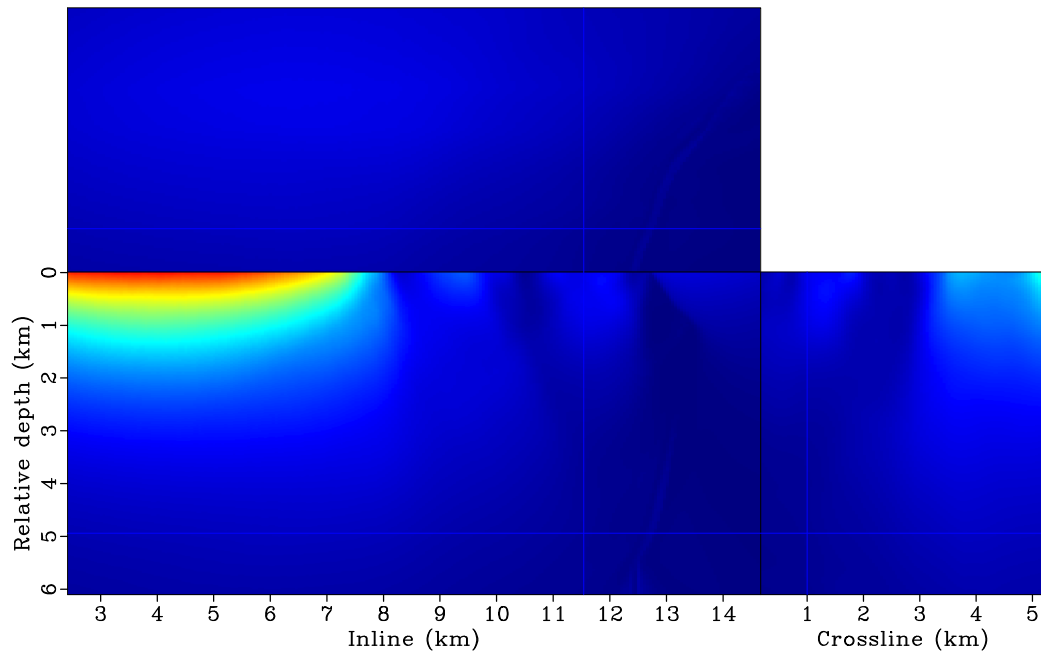


Figure 4.5: The diagonal components of the Hessian matrix for the target region obtained using the initial velocity model. Hot colors denote high illumination, whereas cold colors denote low illumination. [CR] `chap4/. bpgom3d-bhes1`

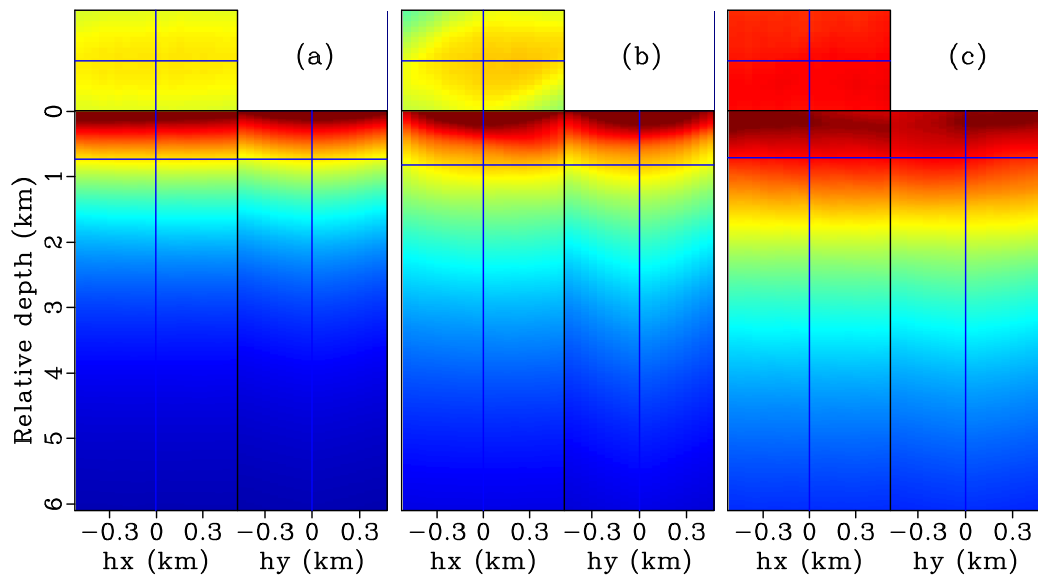


Figure 4.6: The subsurface-offset-domain illumination gathers. They are extracted at the same locations as those in Figure 4.4. [CR] `chap4/. bpgom3d-cig3d-bhes`

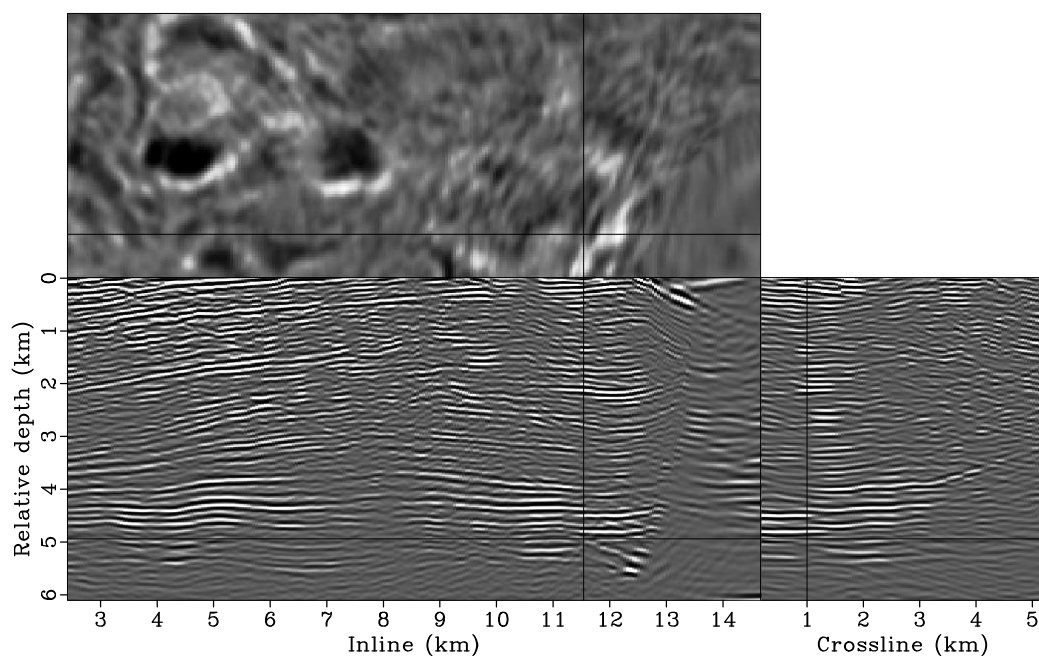


Figure 4.7: The zero-subsurface-offset image after illumination compensation. Compare the figure with Figure 4.3. [CR] `chap4/. bpgom3d-bimg-copy-cpst1`

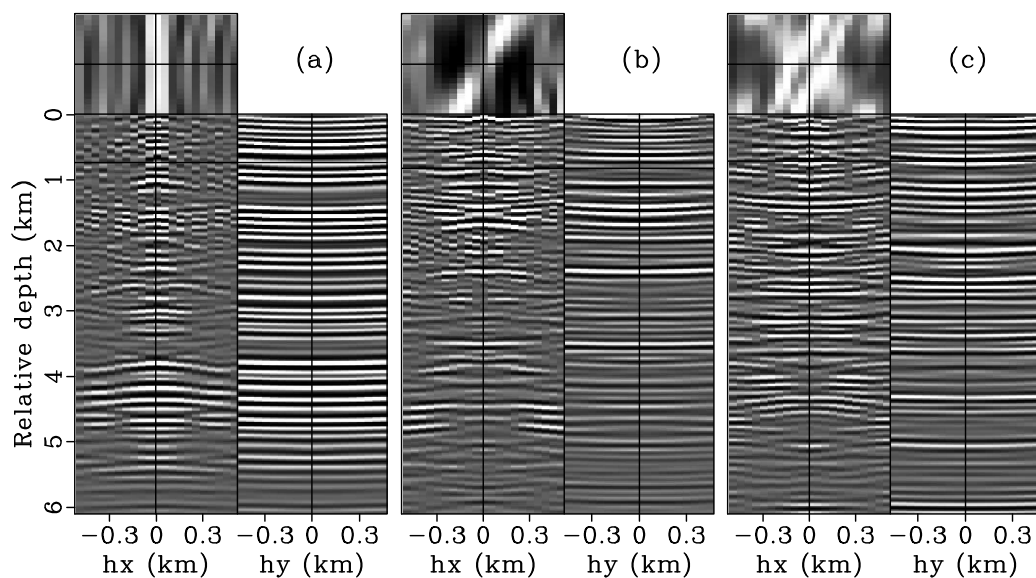


Figure 4.8: The 3-D SODCIGs after illumination compensation. Compare the figure with Figure 4.4. [CR] `chap4/. bpgom3d-cig3d-orig-cpst`

plane-wave source function with both incident dip and azimuth angles equal to 10° , shooting from the top of the target region (Figure 4.2), and the corresponding 3-D plane-wave gather collected at the top of the target region.

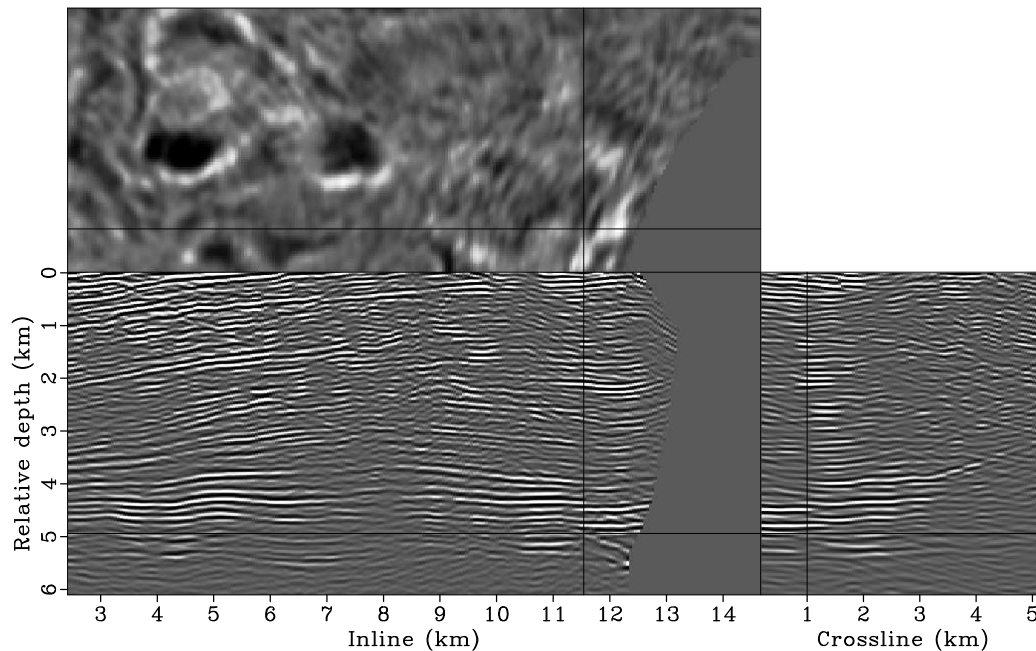
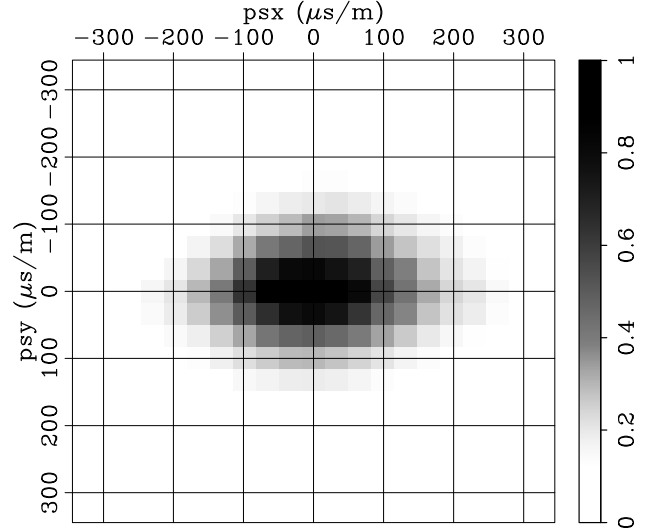


Figure 4.9: The initial zero-subsurface-offset image after muting the events in the salt body. The muted image and gathers are used for the generalized Born wavefield modeling. [CR] `chap4/. bpgom3d-bimg-cond1`

Figures 4.12 and 4.13 present the zero-subsurface-offset image and the corresponding 3-D SODCIGs obtained by migrating the synthesized Born data set. They show similar behaviors in both kinematics and amplitudes, when compared to the corresponding image and gathers in Figures 4.9 and 4.8, which are obtained using the original data set. Also note that images obtained using the synthesized Born data set have lower spatial resolution than those obtained using the original data set. This is partially because I use a lower dominant frequency to model the Born data. Another reason is the spatial filtering effect of the Hessian operator, which has been implicitly applied during the data mapping procedure (see Chapter 3 for details).

Figure 4.10: The average source visibility (data-domain illumination) for the target region using 3-D plane-wave acquisition geometry for the Born wavefield modeling. Note that most of the energy contributing to the target region falls within the range where $\tilde{p}_{s_x} \in (-213, 213)$, and $\tilde{p}_{s_y} \in (-180, 180)$. [CR]

chap4/. bpgom3d-born-visibility



Tomographic inversion

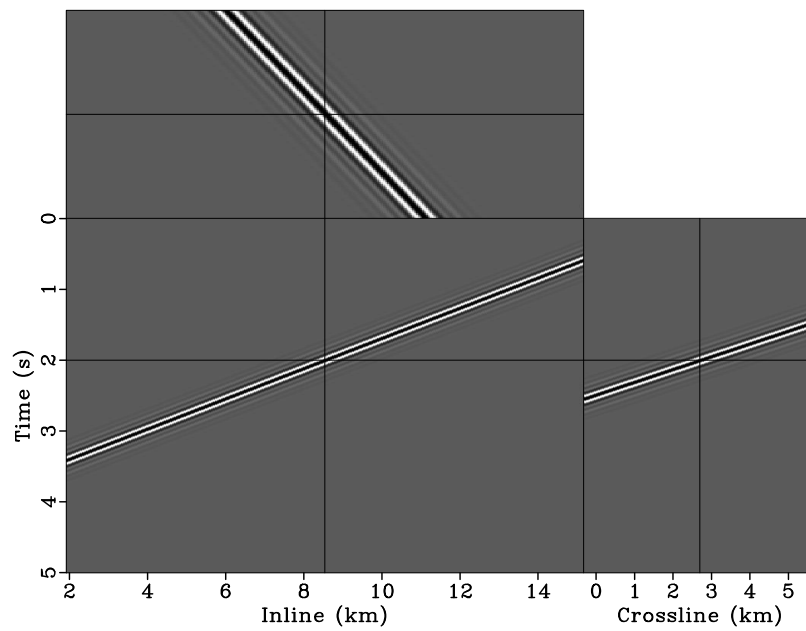
I use the normalized differential semblance optimization (NDSO), as discussed in Chapter 3, to optimize the subsalt velocity. Although the 3-D Born data are synthesized with both inline and crossline subsurface offsets, I use only the inline subsurface offsets (h_x) for velocity inversion because of the limited angular coverage in the crossline direction. The NDSO objective function to minimize then becomes

$$J = \frac{1}{2} \sum_{\tilde{x}, \tilde{y}} \frac{\sum_{\tilde{z}, h_x} h_x^2 |\hat{m}_{\text{target}}(\tilde{\mathbf{x}}, h_x)|^2}{\sum_{\tilde{z}, h_x} |\hat{m}_{\text{target}}(\tilde{\mathbf{x}}, h_x)|^2}, \quad (4.26)$$

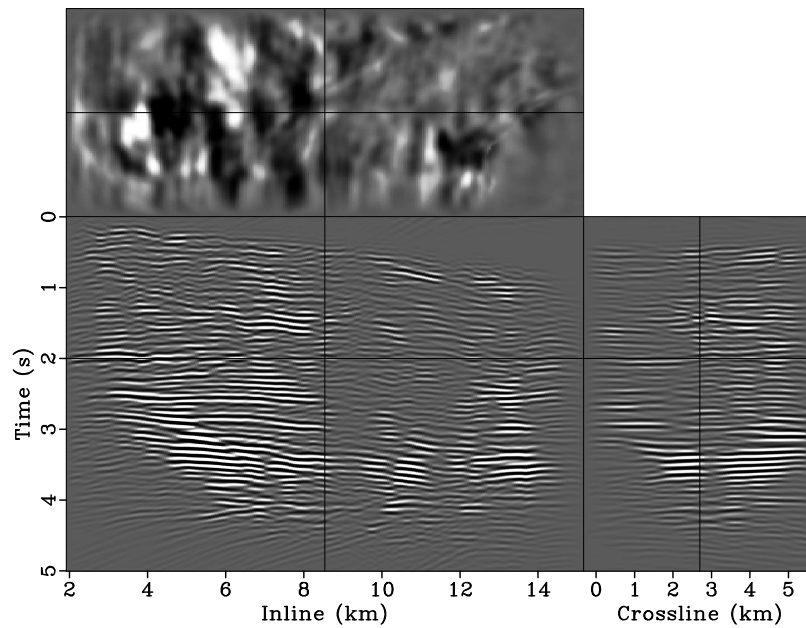
where \hat{m}_{target} is the image for the target region obtained by migrating the synthesized 3-D Born plane-wave data, and $\tilde{\mathbf{x}} = (\tilde{x}, \tilde{y}, \tilde{z})$ is the image point within the target region. I use the nonlinear conjugate-gradient method to optimize the velocity. The gradient is calculated using the adjoint-state method without explicitly computing the Jacobian matrix (see Appendix C for details).

To regularize the inversion, I use B-splines to smooth the gradient as follows:

$$\mathbf{g}_s = \mathbf{KBB}^* \mathbf{g}, \quad (4.27)$$



(a)



(b)

Figure 4.11: The synthesized 3-D plane-wave data. Panel (a) is the plane-wave source function with both incident dip and azimuth angles equal 10° at the top of the target region shown in Figure 4.2, and (b) is the corresponding plane-wave gather collected also at the top of the target region. [CR]

chap4/. bpgom3d-born-tsou,bpgom3d-born-trec

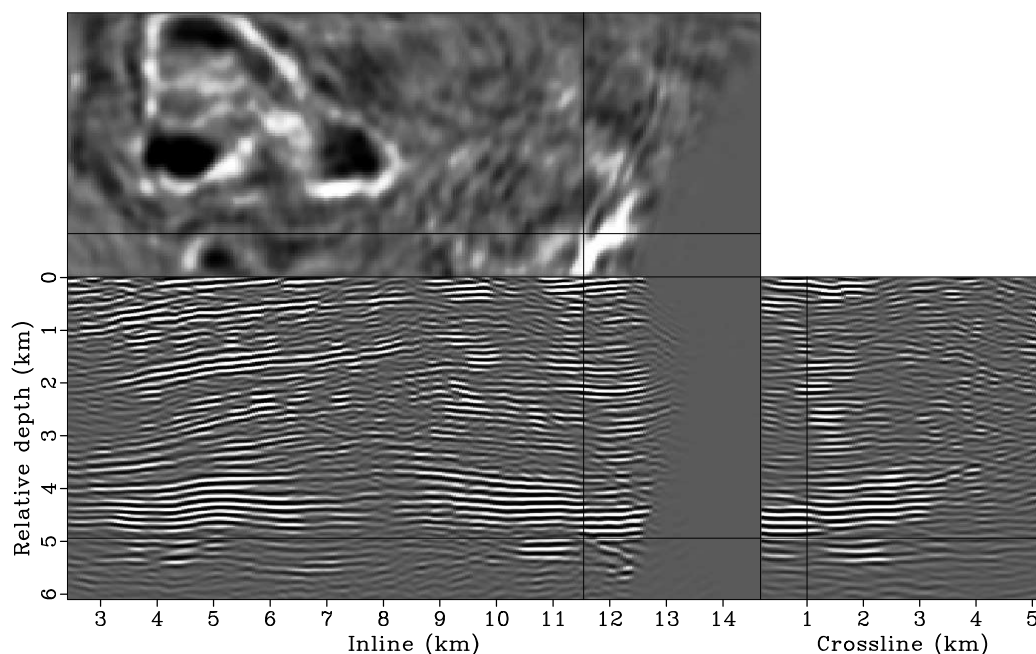


Figure 4.12: The zero-subsurface-offset image obtained using the synthesized Born data set. Compare the figure with Figure 4.9. [CR] [chap4/. bpgom3d-bimg-born1](#)

where \mathbf{g}_s and \mathbf{g} are the smoothed and raw gradient vectors, respectively; \mathbf{B} is the B-spline projection operator. The spacing of the B-spline nodes controls the smoothness of the velocity updates. A mask operator \mathbf{K} has been introduced to prevent updating the salt velocities (Figure 4.14).

Instead of using a fixed degree for gradient smoothing, I gradually decrease the smoothness of the gradient every few iterations by decreasing the spacing of the B-spline nodes (Biondi, 1990). I have found this strategy effective in finding an acceptable minimum, even when starting with a velocity model far from being accurate. Decreasing the smoothness of the gradient at later iterations also helps improve the resolution of the velocity model. This procedure is similar to the multi-scale inversion strategy, which has proven useful in practice (Bunks et al., 1995; Soubaras and Gratacos, 2007). Table 4.1 illustrates the spacings of the B-spline nodes for different iterations. Figures 4.15, 4.16, 4.17 and 4.18 present the normalized raw and smoothed gradients at iterations 1, 11, 21 and 31, respectively. The smoothed gradients are then

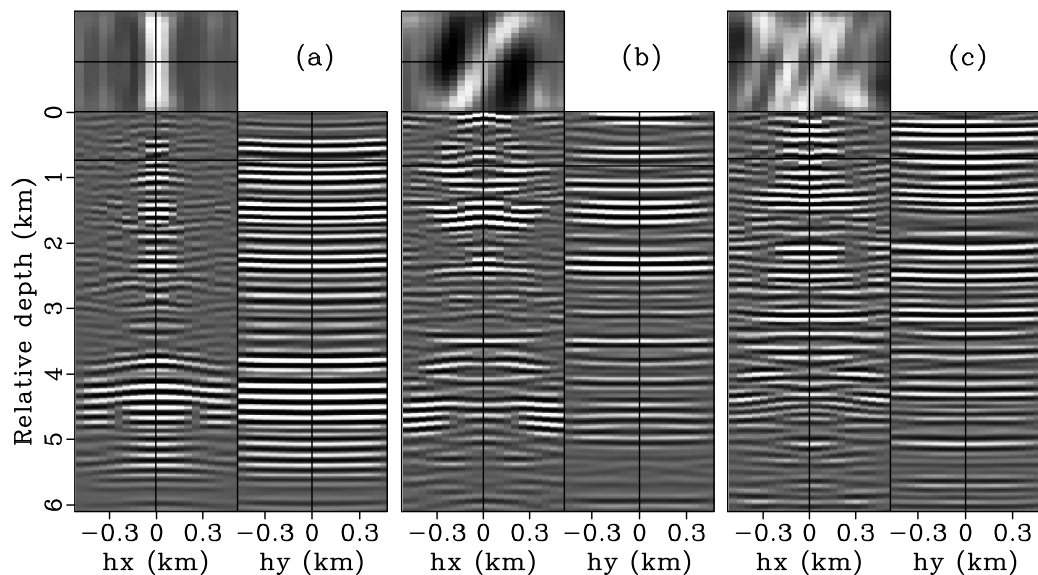


Figure 4.13: The 3-D SODCIGs obtained using the synthesized Born data set and the initial velocity model. Panels are extracted at (a) inline 3.04 km, crossline 1.34 km, (b) inline 6.09 km, crossline 2.86 km and (c) inline 9.13 km, crossline 4.38 km. Compare the figure with Figure 4.8. [CR] `chap4/. bpgom3d-cig3d-born`

used to calculate the search direction using the Polak-Ribière scheme (Nocedal and Wright, 2000). As it can be seen from these gradients, the node spacing in the B-splines determines the smoothness or roughness of the gradients, and consequently the velocity updates. As iteration proceeds, more details will be added into the inverted velocity model.

Iterations	Node spacing in x	Node spacing in y	Node spacing in z
1 to 10	2.0 km	2.0 km	0.6 km
11 to 20	1.8 km	1.8 km	0.4 km
21 to 30	1.2 km	1.2 km	0.3 km
31 to 40	0.7 km	0.7 km	0.2 km

Table 4.1: The spacings of B-spline nodes for different iterations.

I use a sliding-window line-search method to find a step length at each iteration. The method is similar to the one discussed by Krebs et al. (2009), which predicts trial

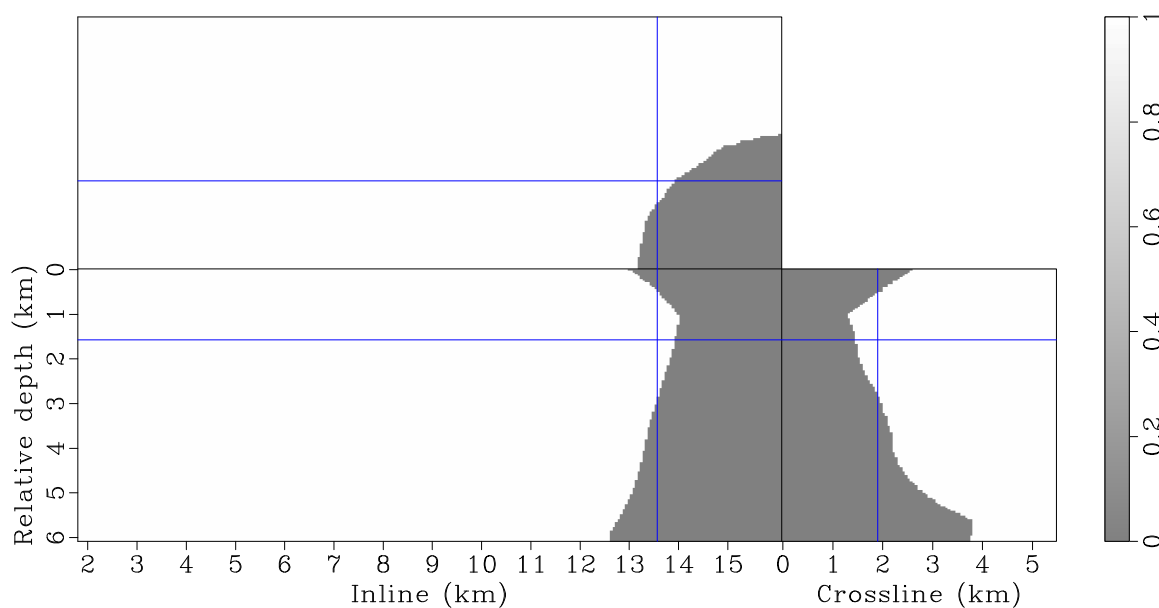


Figure 4.14: The mask operator applied to the gradient to prevent updating velocities inside the salt. [ER] `chap4/. bpgom3d-gmsk-target`

step lengths for the next iteration by using the step length at the current iteration. In my implementation, the line search evaluates the objective function for three models that are produced by adding uniformly scaled versions of the search direction to the current model. I then select the search model that gives the lowest objective-function value as the updated model of the current iteration. Finally, I adjust the line-search scale such that the picked model would have been in the center of the line search. This updated scale is used to perform the line search during the next iteration.

I restart the nonlinear conjugate gradient solver every 10 iterations, and I terminate the inversion after 40 iterations when the objective function does not decrease significantly. Figure 4.19 shows how the objective function evolves over the first 40 iterations, whereas Figure 4.20 plots the step lengths as a function of iterations. It seems that the objective function converges very fast at the first several iterations, then the convergence slows down quickly, and that the velocity model gets the most significant updates at the first several iterations.

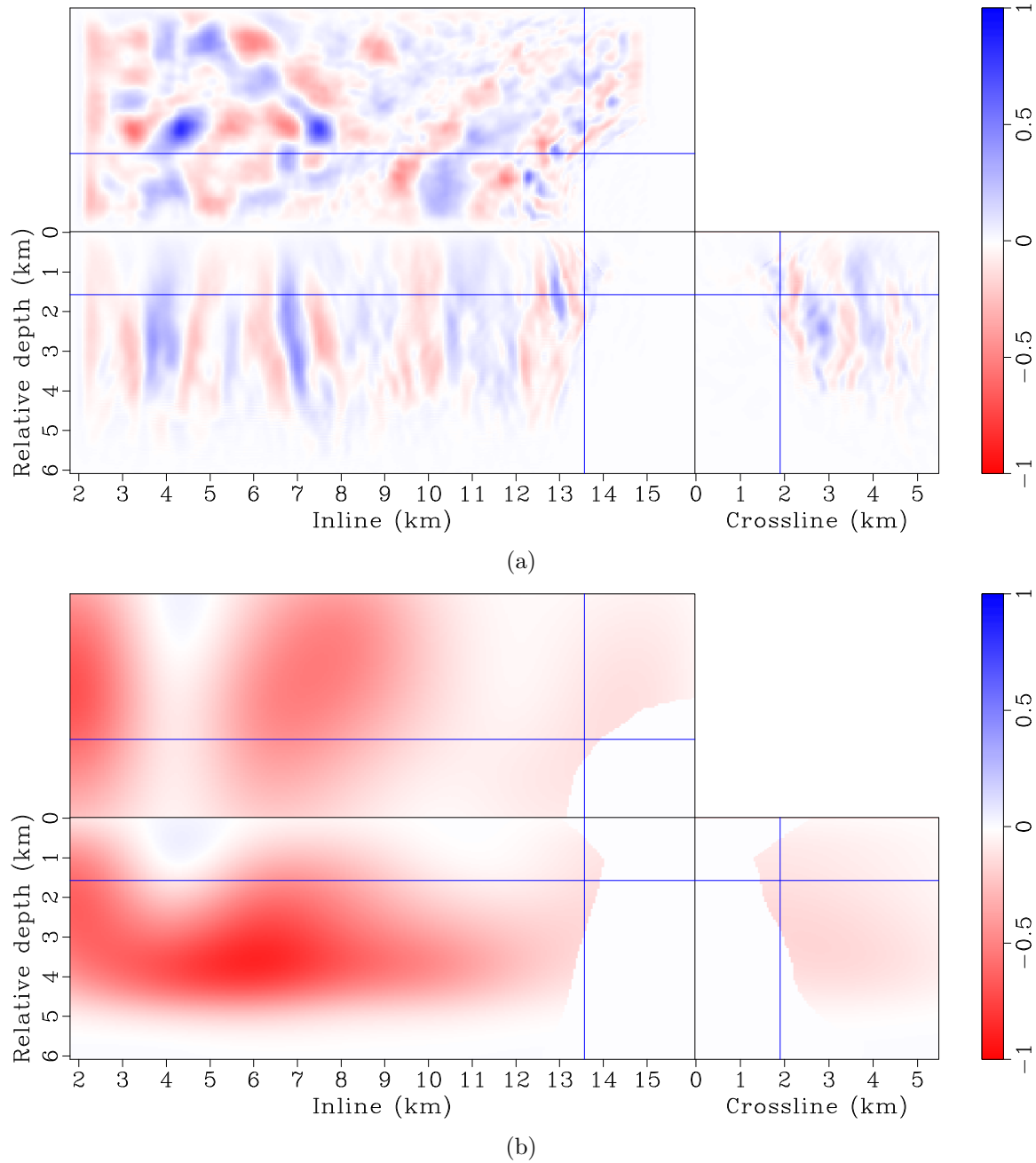
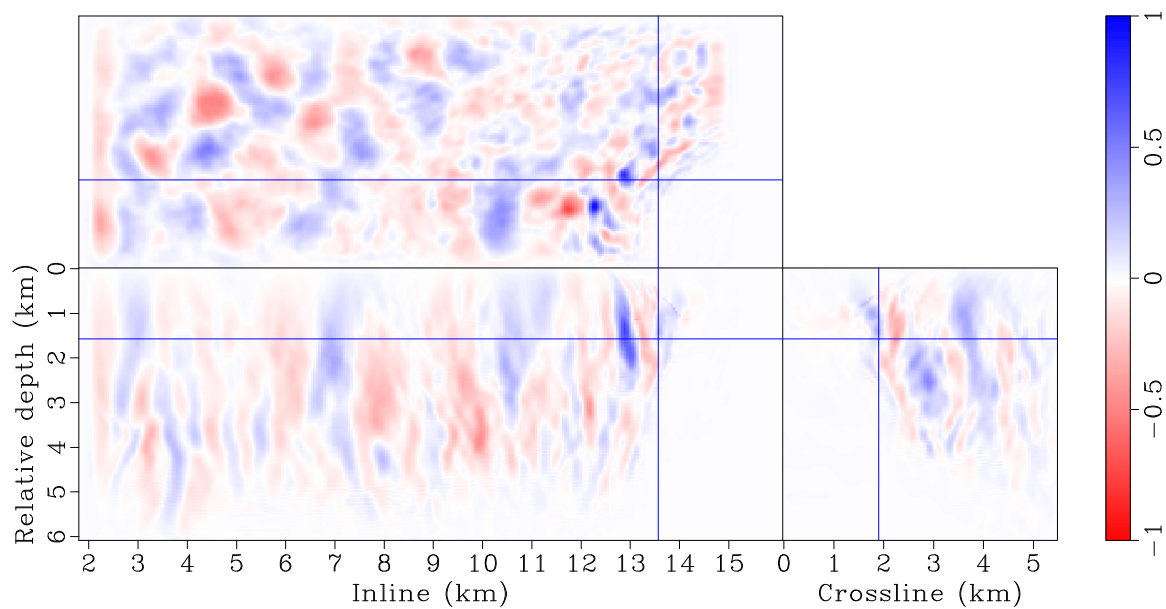
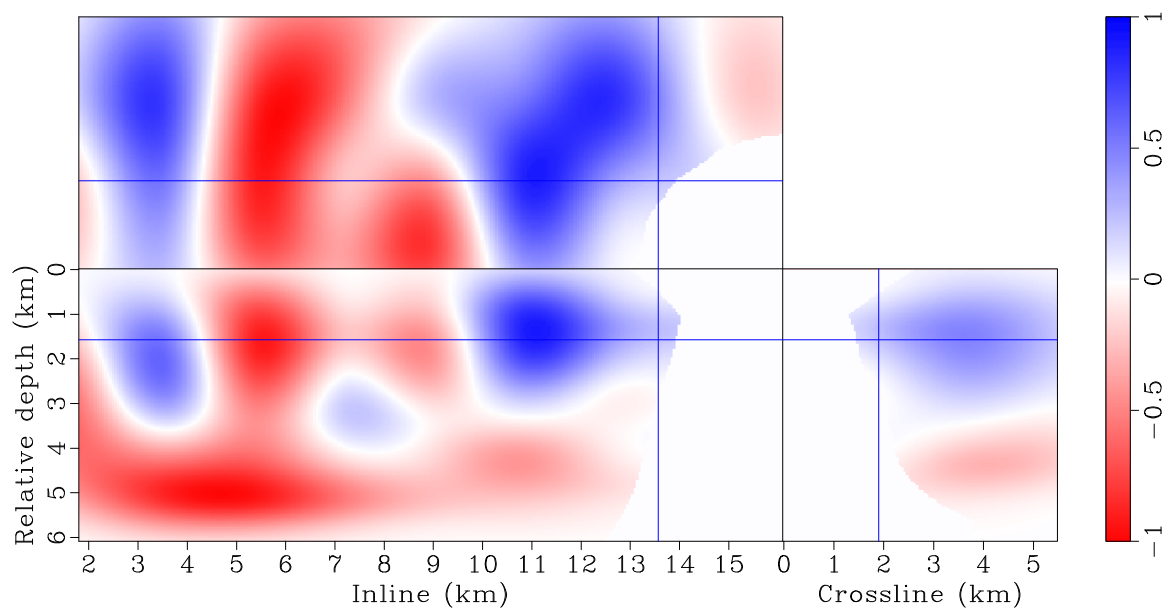


Figure 4.15: The normalized gradient at iteration one (a) before and (b) after applying the smoothing and mask operators. [CR]

chap4/. bpgom3d-grad-raw-target-iter1,bpgom3d-grad-smt-target-iter1



(a)



(b)

Figure 4.16: The normalized gradient at iteration 11 (a) before and (b) after applying the smoothing and mask operators. [CR]

chap4/. bpgom3d-grad-raw-target-iter11,bpgom3d-grad-smt-target-iter11

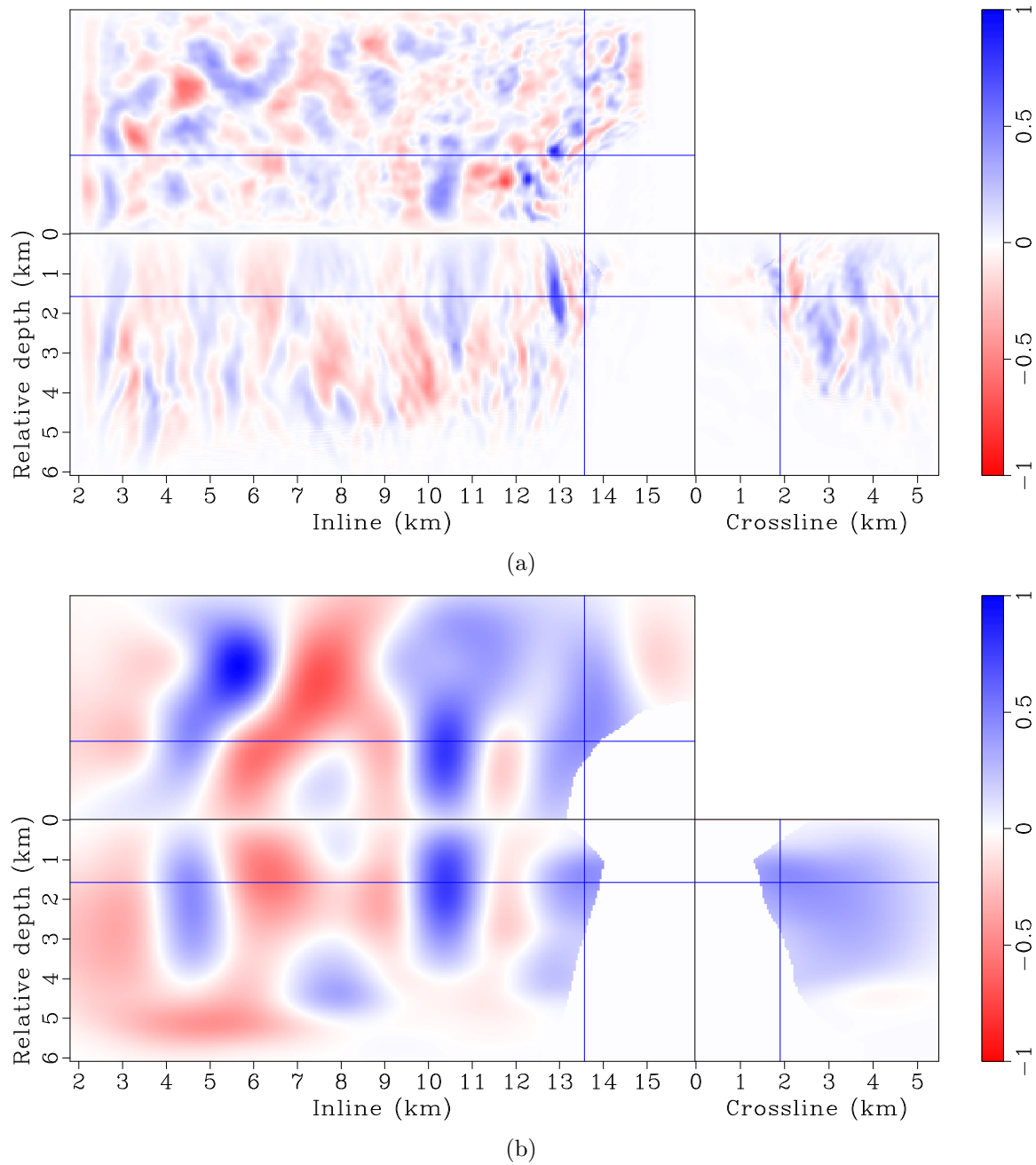
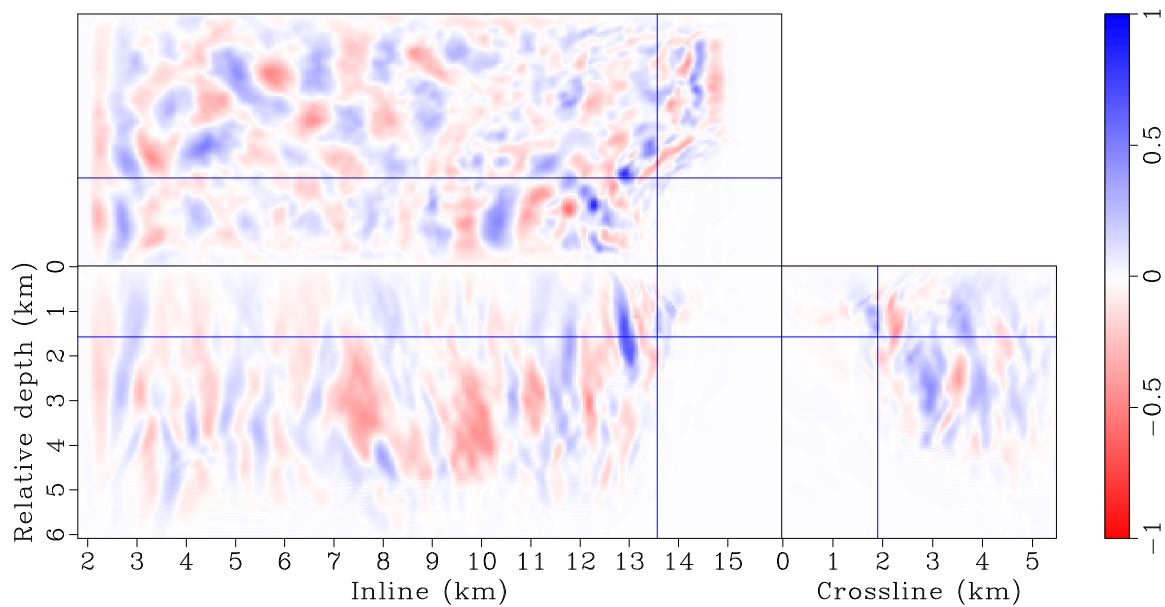
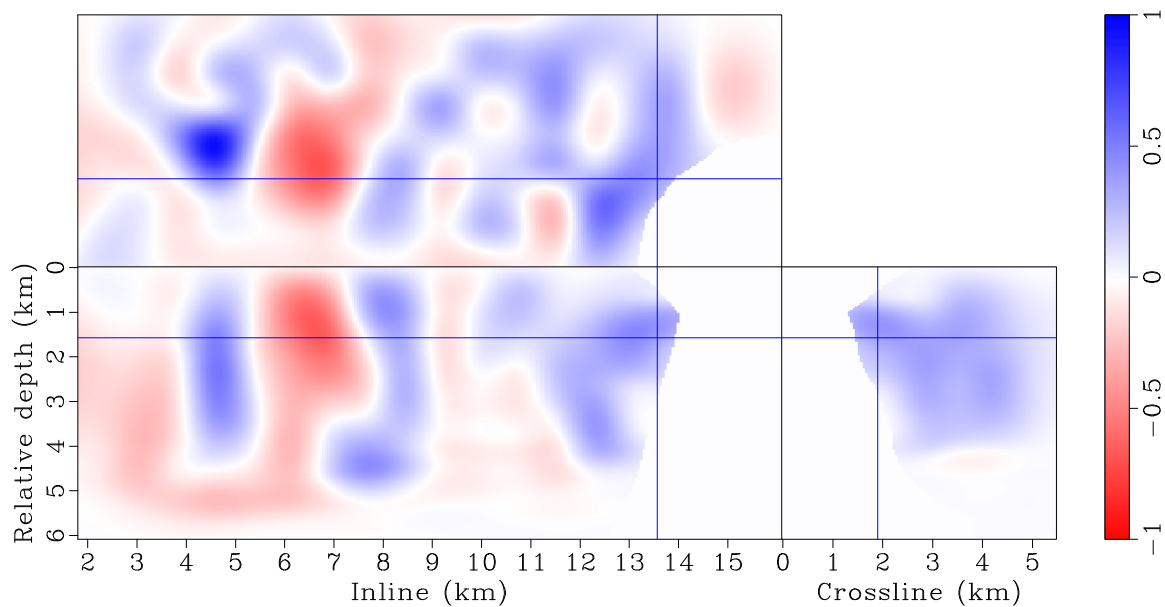


Figure 4.17: The normalized gradient at iteration 21 (a) before and (b) after applying the smoothing and mask operators. [CR]

chap4/. bpgom3d-grad-raw-target-iter21,bpgom3d-grad-smt-target-iter21



(a)



(b)

Figure 4.18: The normalized gradient at iteration 31 (a) before and (b) after applying the smoothing and mask operators. [CR]

chap4/. bpgom3d-grad-raw-target-iter31,bpgom3d-grad-smt-target-iter31

Figures 4.21(a), 4.21(b), 4.21(c) and 4.21(d) present the updated velocity model in the target region after 10, 20, 30 and 40 iterations, respectively. The final velocity model obtained by merging the inverted velocity model in the target region with the velocity model above the target is shown in Figure 4.22. It is interesting to note that the velocities beneath the salt body are slightly lower than the surrounding sediment velocities, and that the shape of the low velocities conforms well with the base of the salt body. The low velocities might indicate overpressure due to the compaction of the salt body.

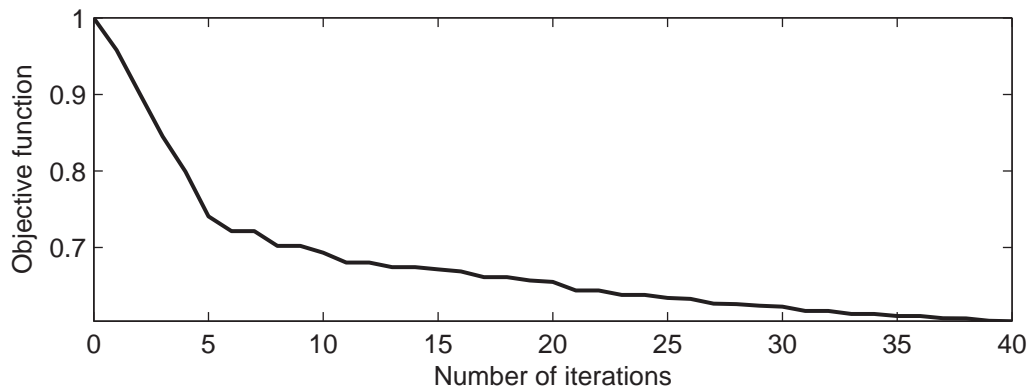


Figure 4.19: The evolution of the objective function over the first 40 DSO iterations. The objective function values have been normalized to 1. [CR] chap4/. fobj

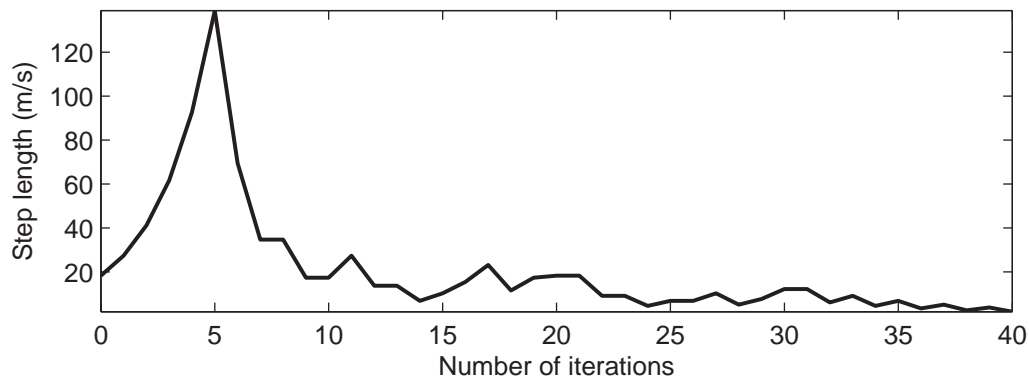


Figure 4.20: Step length versus the number of iterations. The initial step length is about 20 m/s. [CR] chap4/. step

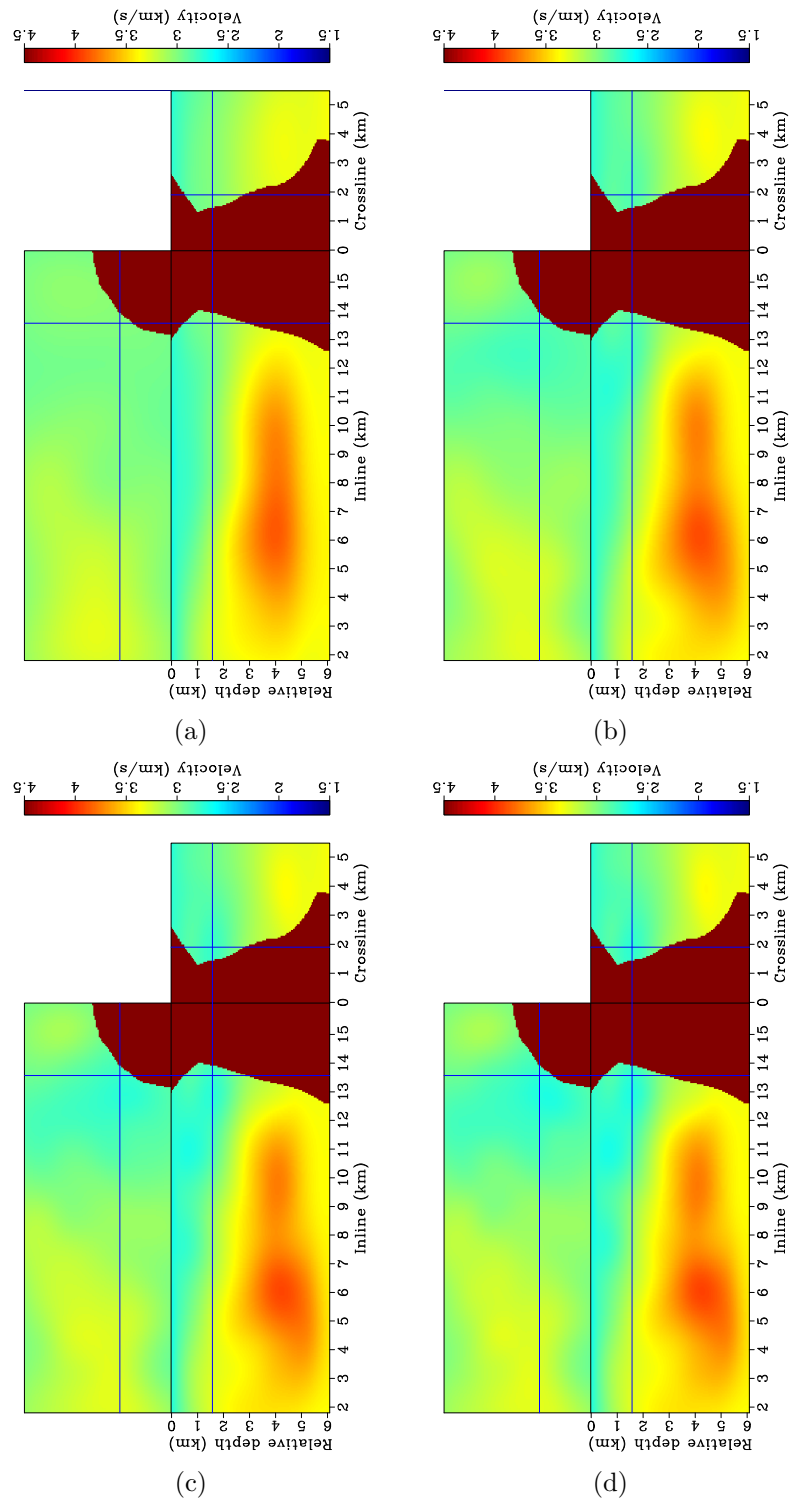


Figure 4.21: The inverted velocity model in the target region after (a) 10 iterations, (b) 20 iterations, (c) 30 iterations and (d) 40 iterations. [CR] chap4/. invt-stage1,invt-stage2,invt-stage3,invt-stage4

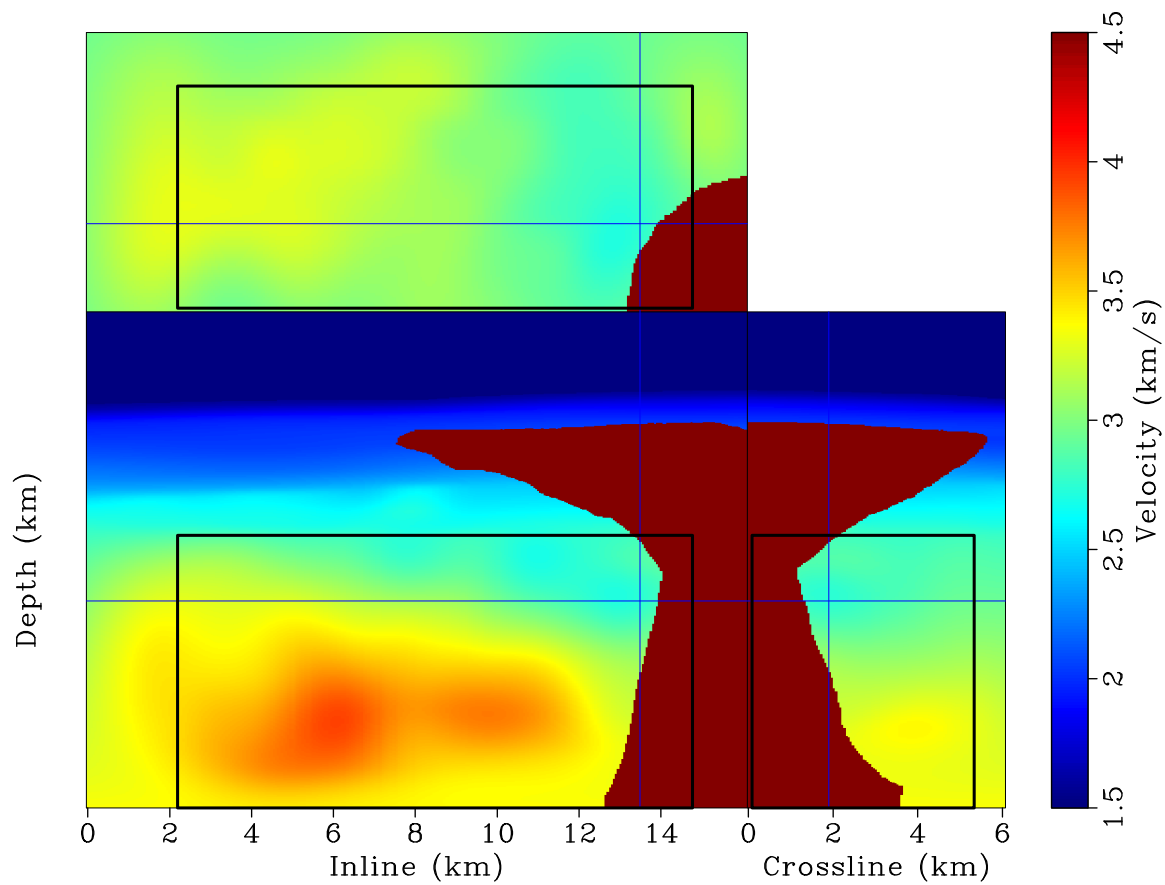


Figure 4.22: The final velocity model after merging the inverted velocity model in the target region (Figure 4.21(d)) with the velocity model above the target. [CR] chap4/. bpgom3d-vmod-full

The zero-subsurface-offset image obtained using the 3-D Born plane-wave data set and the inverted velocity model is shown in Figure 4.23, where the reflectors are more continuous than the ones in Figure 4.12, which is obtained using the initial velocity model. The updated SODCIGs (Figure 4.24(b)) are also more focused at the zero subsurface offset than the initial ones (Figure 4.24(a)), indicating that the updated velocity model is more accurate than the initial one.

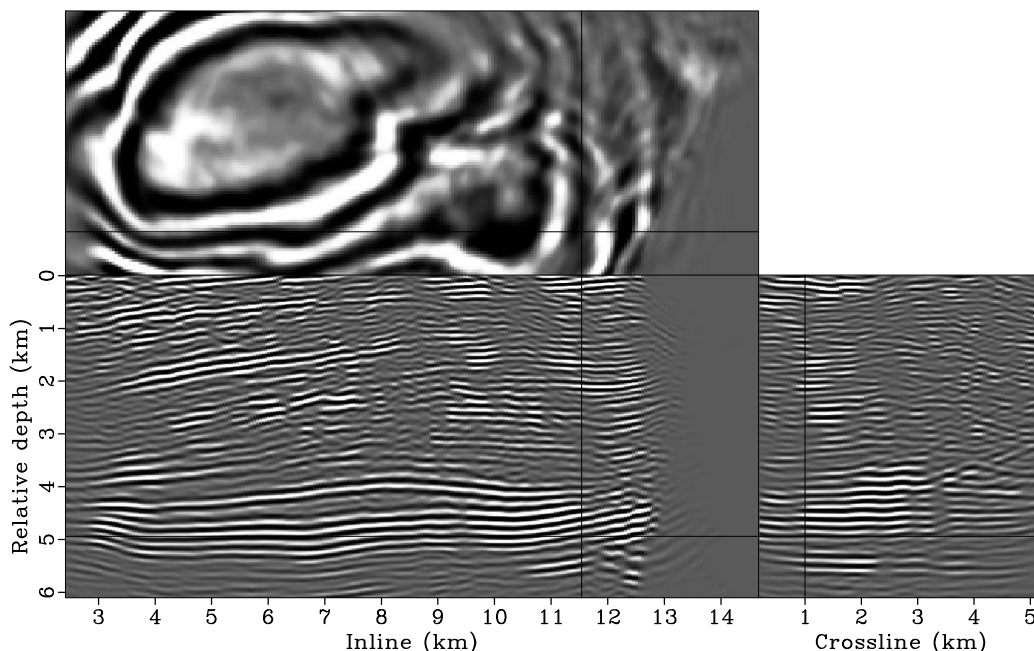


Figure 4.23: The zero-subsurface-offset image obtained using the synthesized Born data set and the updated velocity model. [CR] `chap4/. bpgom3d-imag-born1`

Migrating the original data set using the updated velocity model

After the tomographic inversion step, I migrate the original surface-recorded data set using the updated velocity model (Figure 4.22). Once again, I perform 3-D conical wave migration; the migrated image is shown in Figure 4.25. The image is further normalized using the diagonal of the Hessian (Figure 4.26), also computed using the updated velocity model, to compensate for uneven subsurface illumination. Note the differences between the diagonal of the Hessian before (Figure 4.5) and after updating

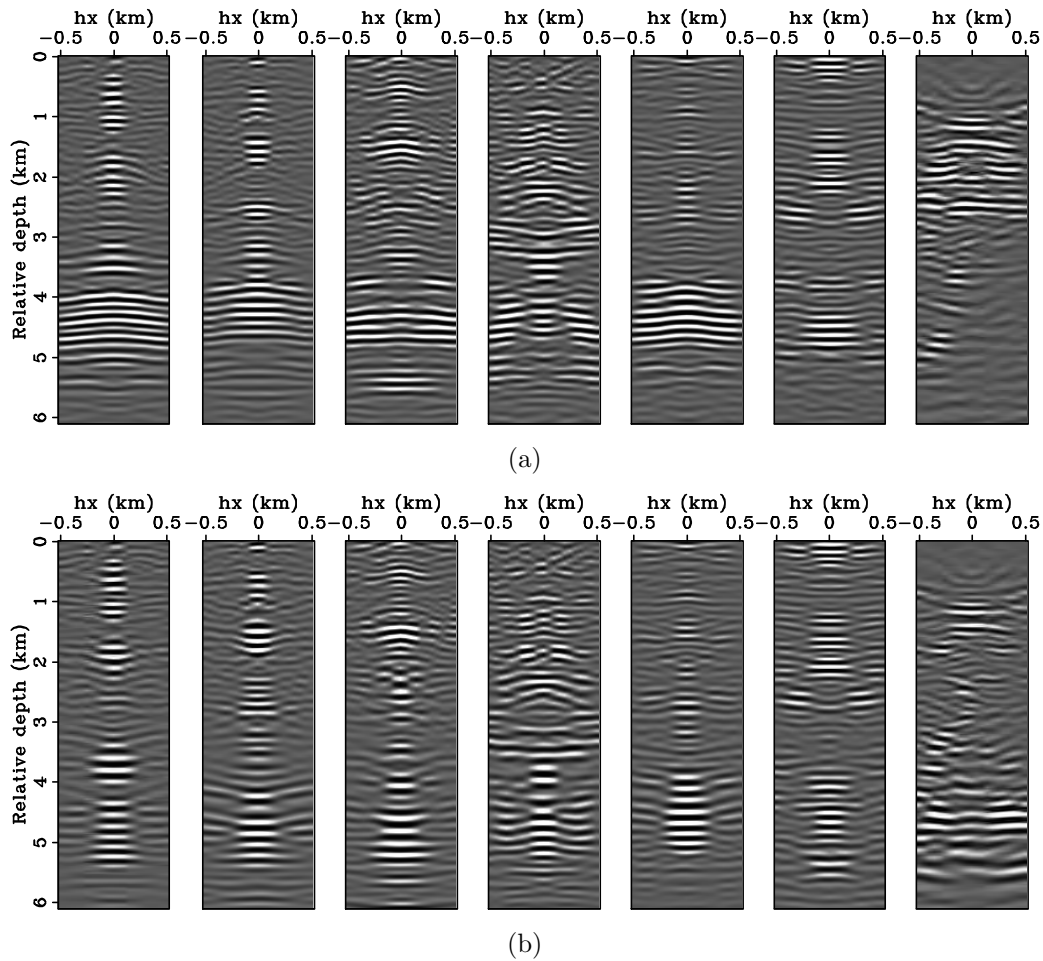


Figure 4.24: Comparison between the inline SODCIGs (a) before and (b) after updating the velocity. The results are obtained by migrating the synthesized Born data set. [CR] chap4/. cig2d-bvel-born1,cig2d-invt-born1

subsalt velocities (Figure 4.26). The updated velocity model creates a slightly more complicated illumination pattern than the original velocity model (simple $v(z)$ model).

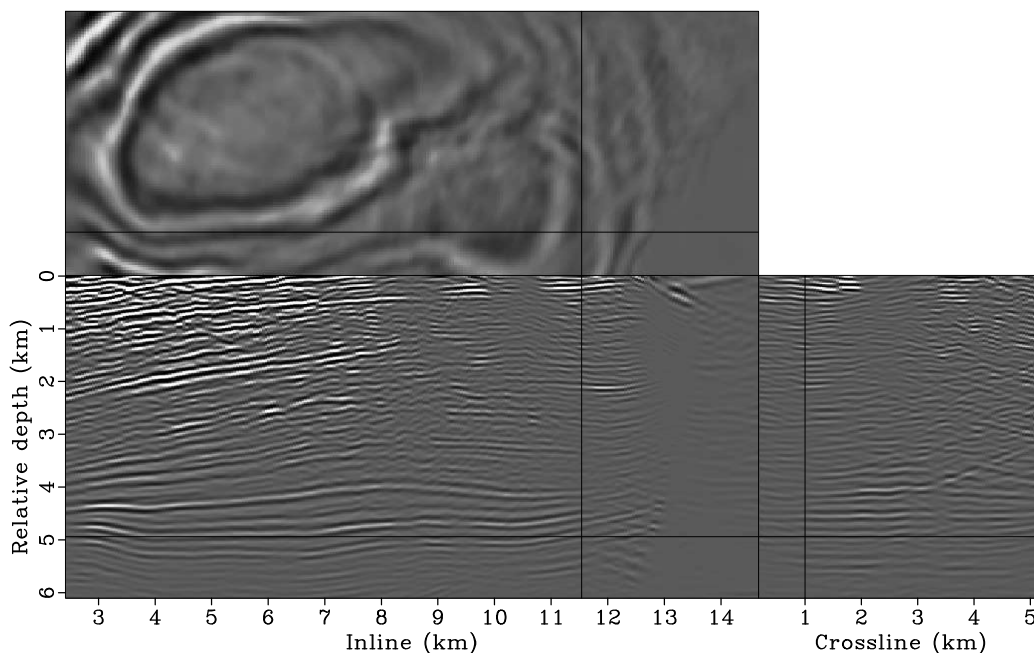


Figure 4.25: The zero-subsurface-offset image obtained by using the original data set and the updated velocity model. [CR] chap4/. bpgom3d-imag-orig1

Figures 4.27, 4.28 and 4.29 compare the normalized zero-subsurface-offset images with the ones obtained using the initial velocity model. The continuity and coherence of the reflectors in the updated images are significantly improved along both the inline and crossline directions. The anticline can be clearly interpreted after updating the velocity (Figure 4.27(b)), which gives good indication for oil reservoirs. The faults above the depth level 3 km in Figures 4.28(b) and 4.29(b) are more coherently imaged, and hence easier to interpret than the ones in the initial images (Figures 4.28(a) and 4.29(a)). The updated images are also more focused than the initial images.

The SODCIGs before and after updating the velocities are shown in Figures 4.30, 4.31 and 4.32, whereas Figures 4.33, 4.34 and 4.35 show the corresponding ADCIGs. The focus in SODCIGs and the flatness in ADCIGs have been improved considerably after updating the subsalt velocities. The ADCIGs are also much more coherent in

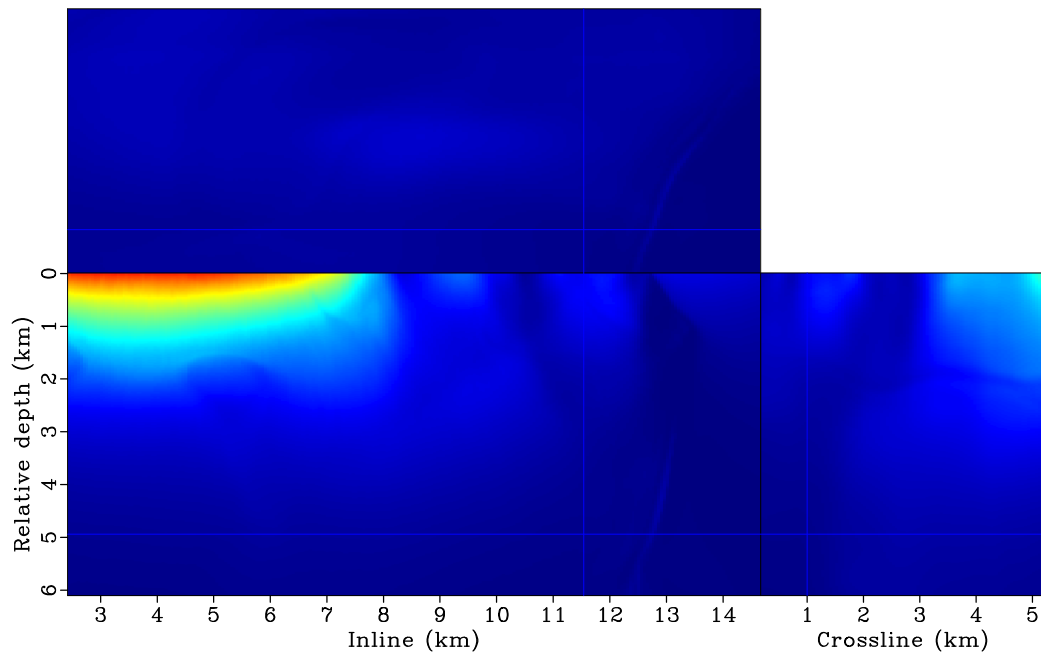
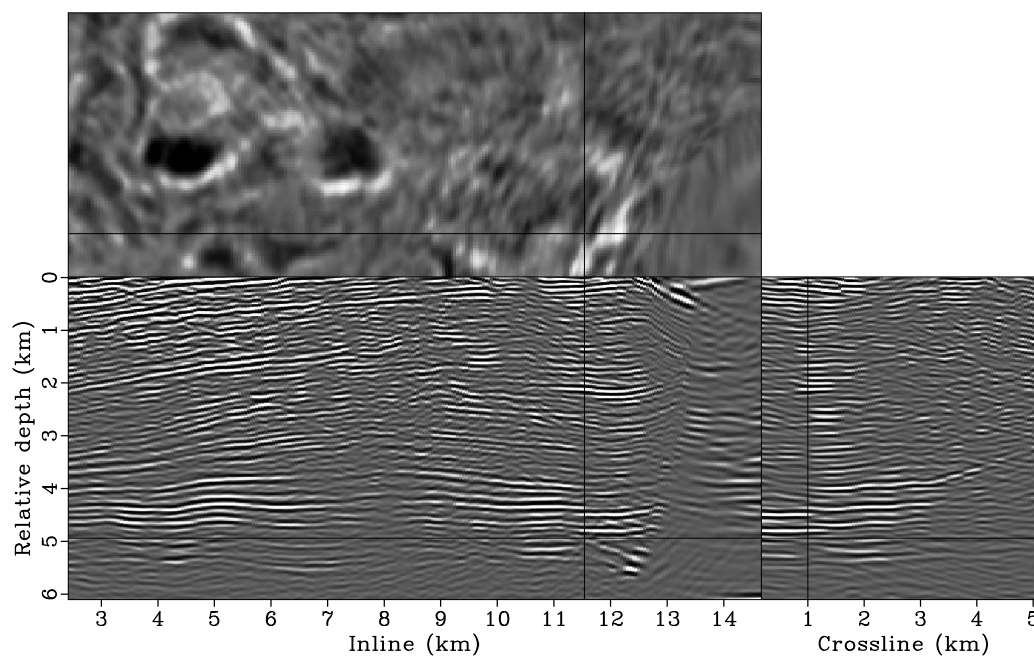
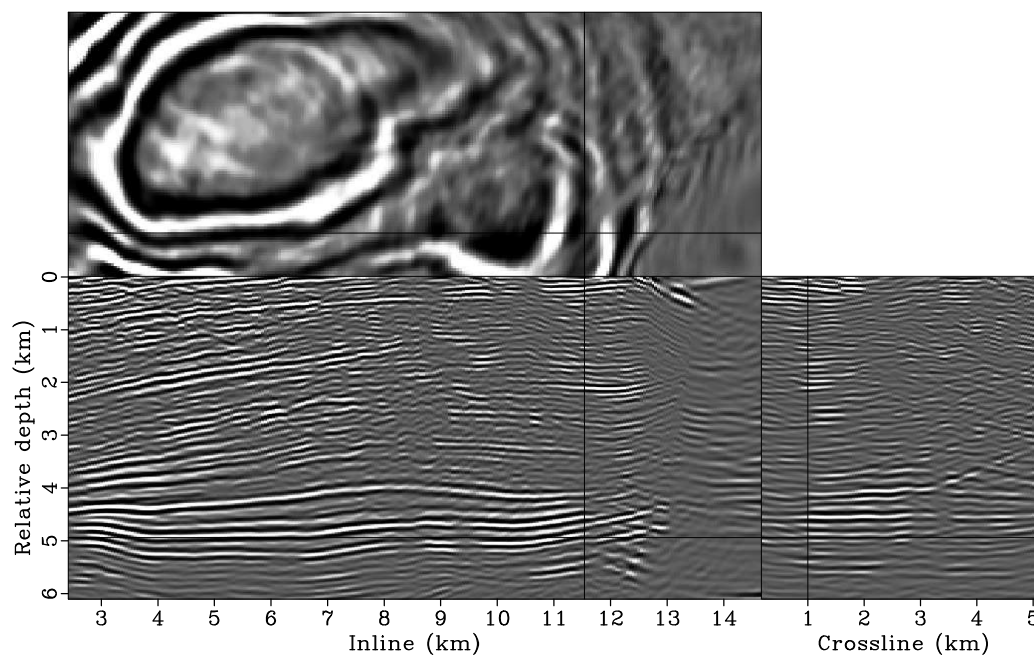


Figure 4.26: The diagonal components of the Hessian matrix obtained using the updated velocity model. [CR] `chap4/. bpgom3d-hess1`

the subsalt region. Overall, the updated images present much higher quality than do the initial images. Certainly, the updated image would help the interpretation and understanding of geological and structural history, adding more value to seismic information in an exploratory study.



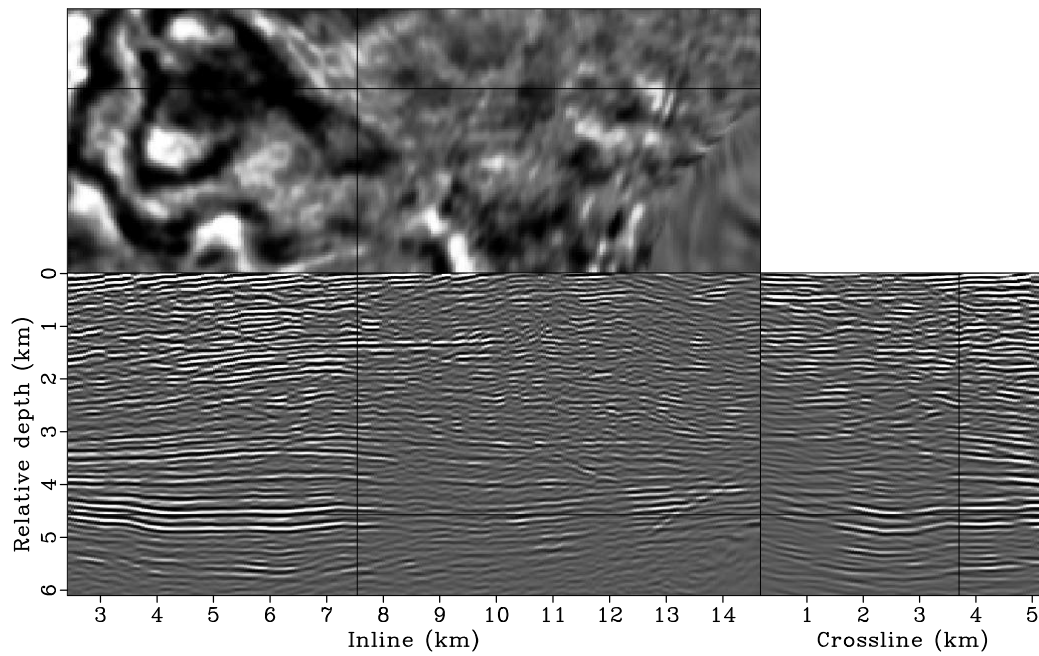
(a)



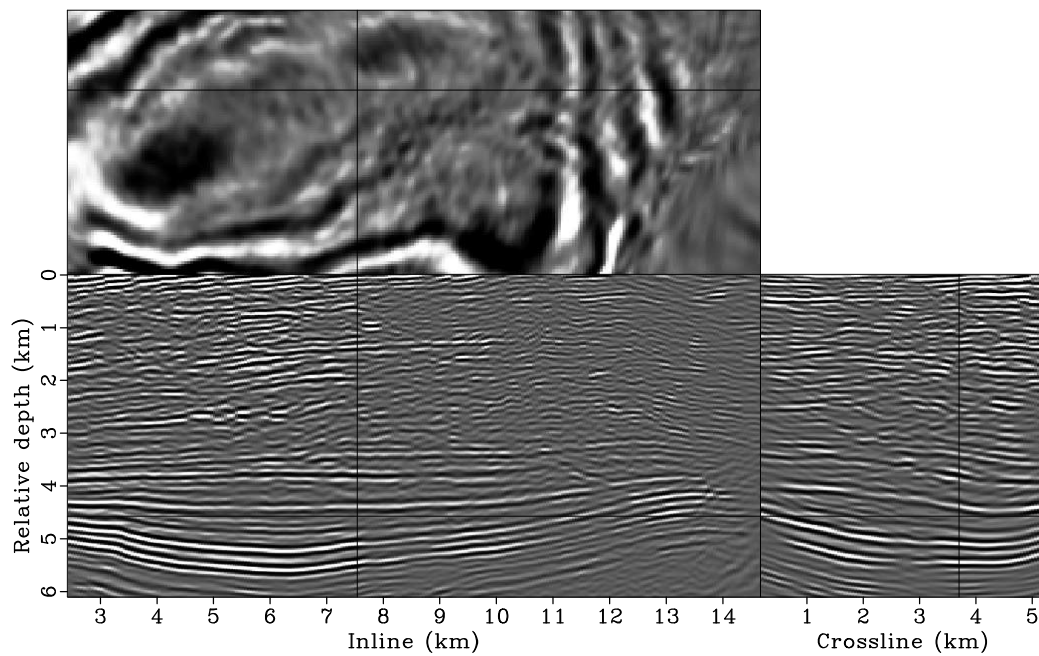
(b)

Figure 4.27: Comparison between the zero-subsurface-offset image (a) before and (b) after updating the velocities. Both results are obtained using the original surface-recorded data set. In both panels, the crosshair is taken at inline 11.55 km, crossline 1.00 km and relative depth 4.94 km. [CR]

chap4/. bpgom3d-bimg-cpst1,bpgom3d-imag-cpst1



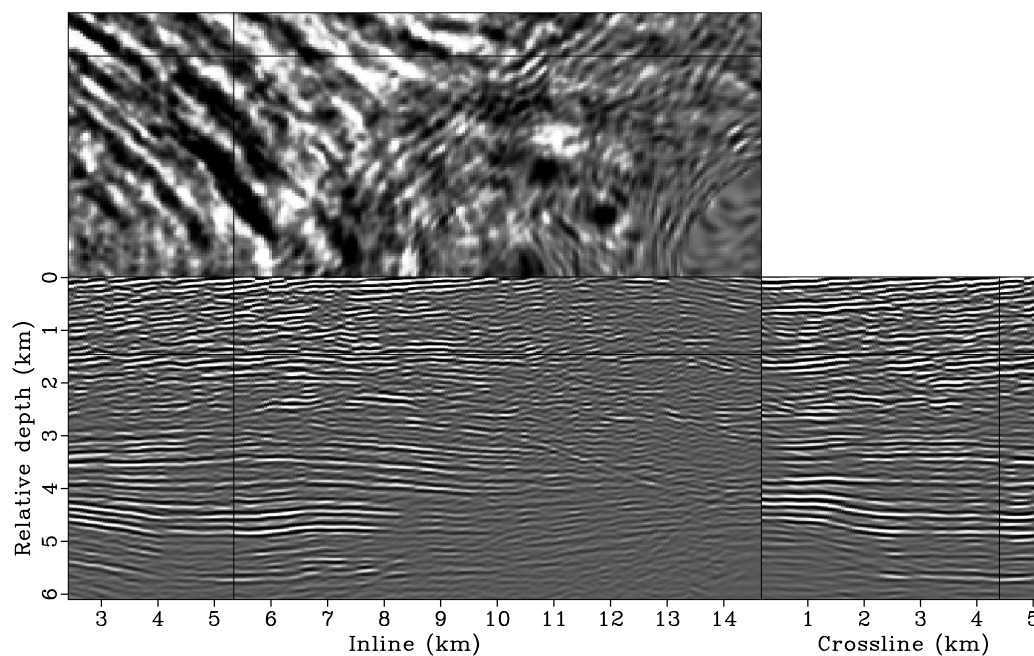
(a)



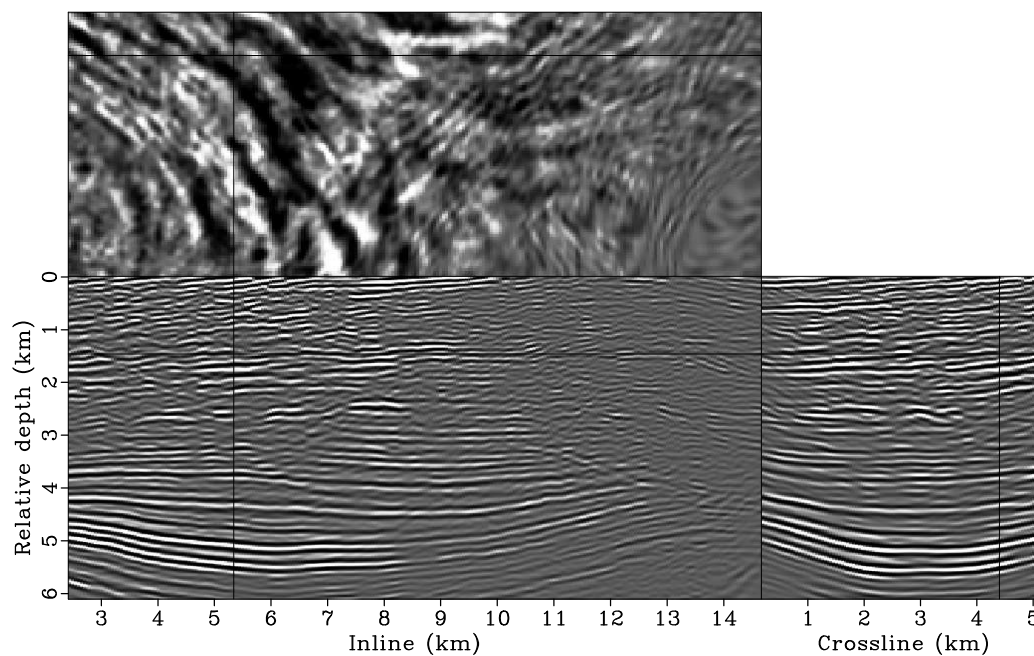
(b)

Figure 4.28: Comparison between the zero-subsurface-offset image (a) before and (b) after updating the velocities. Both results are obtained using the original surface-recorded data set. In both panels, the crosshair is taken at inline 7.55 km, crossline 3.70 km and relative depth 4.57 km. [CR]

chap4/. bpgom3d-bimg-cpst2,bpgom3d-imag-cpst2



(a)



(b)

Figure 4.29: Comparison between the zero-subsurface-offset image (a) before and (b) after updating the velocities. Both results are obtained using the original surface-recorded data set. In both panels, the crosshair is taken as inline 5.35 km, crossline 4.40 km and relative depth 1.46 km. [CR]

chap4/. bpgom3d-bimg-cpst3,bpgom3d-imag-cpst3

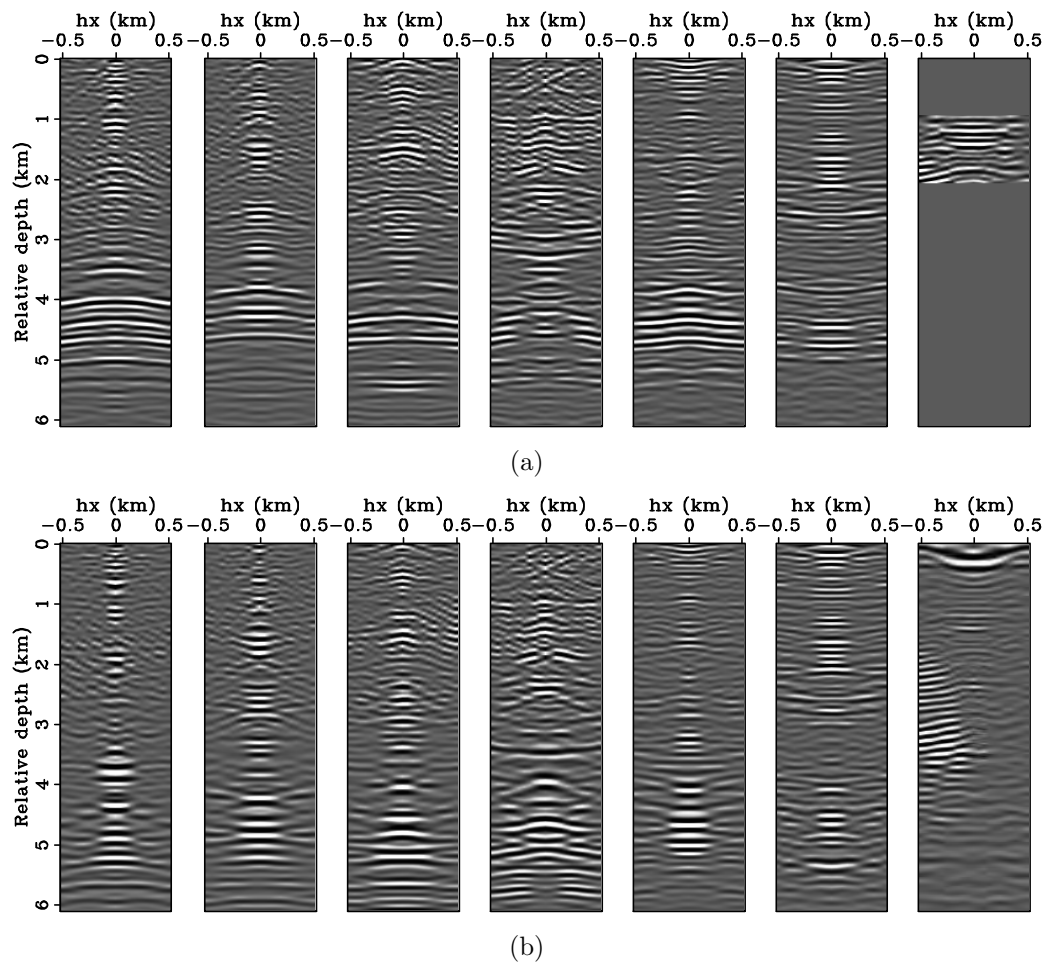
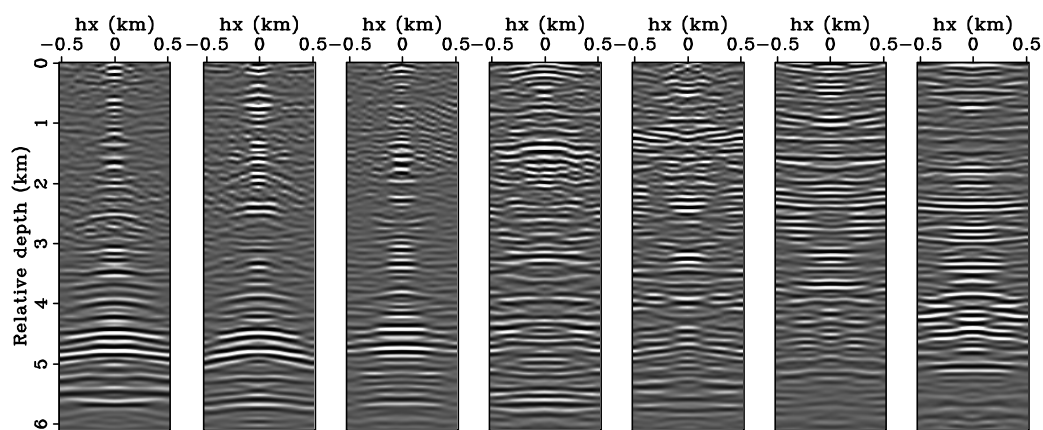
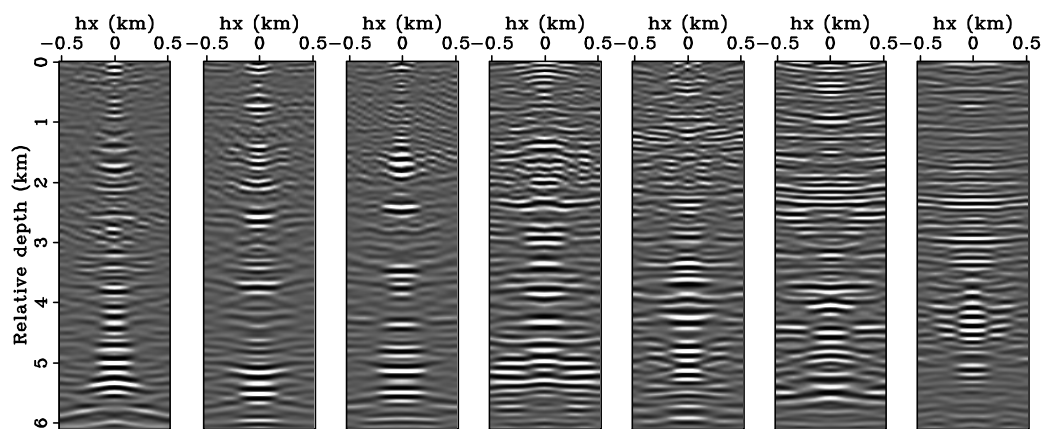


Figure 4.30: Comparisons between SODCIGs (a) before and (b) after updating the velocities. Both results are obtained using the original surface-recorded data set. All of the SODCIGs are extracted at the same crossline (1.00 km), but at inlines 1.52, 3.05, 4.57, 6.10, 7.62, 9.14 and 10.67 km, from left to right. [CR]

chap4/. cig2d-bvel-cpst1,cig2d-invt-cpst1



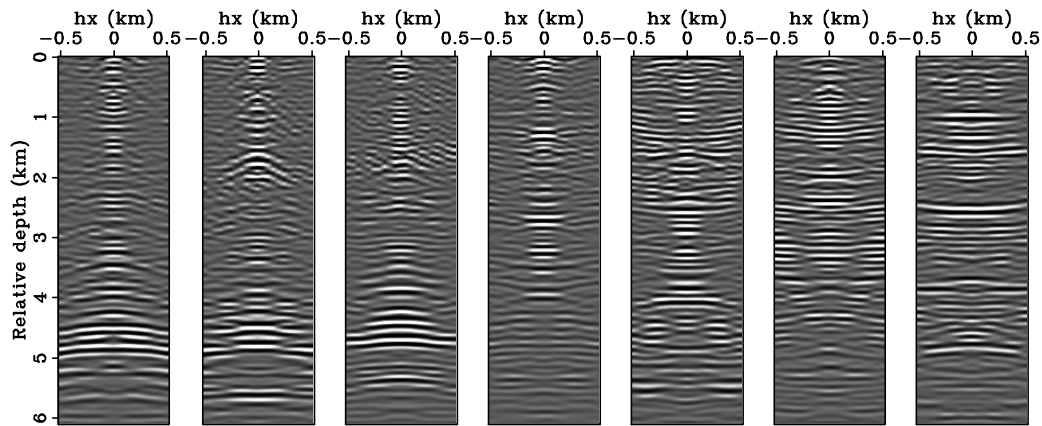
(a)



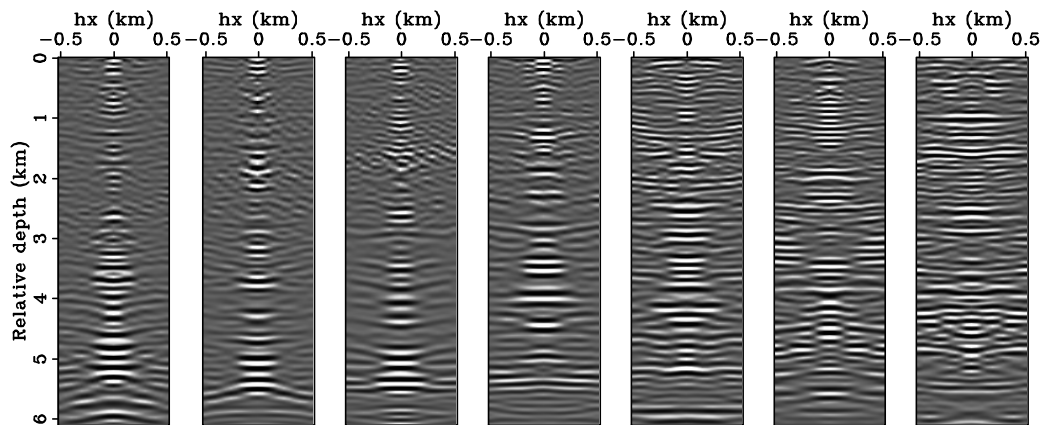
(b)

Figure 4.31: Comparisons between SODCIGs (a) before and (b) after updating the velocities. Both results are obtained using the original surface-recorded data set. All of the SODCIGs are extracted at the same crossline (3.70 km), but at inlines 1.52, 3.05, 4.57, 6.10, 7.62, 9.14 and 10.67 km, from left to right. [CR]

chap4/. cig2d-bvel-cpst2,cig2d-invt-cpst2



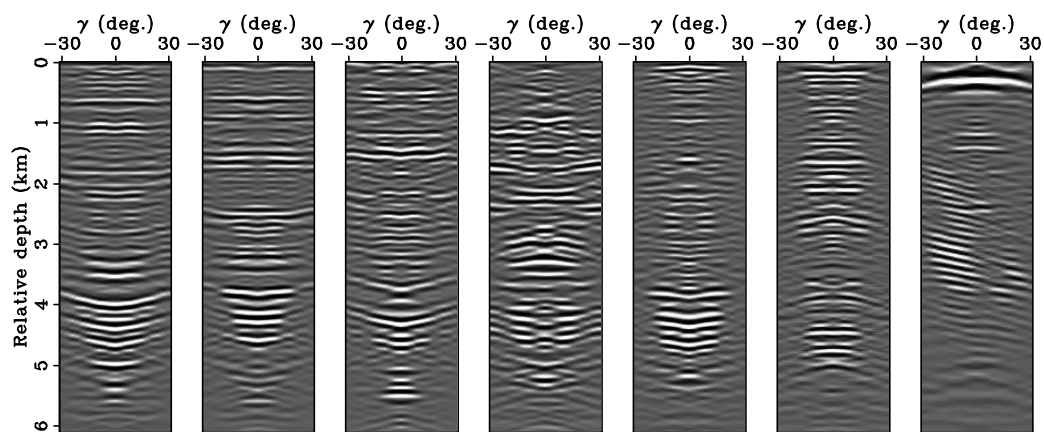
(a)



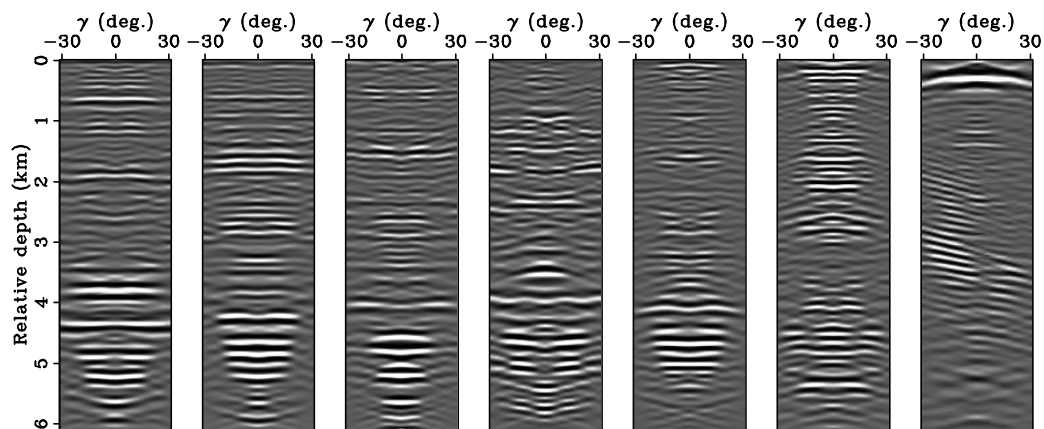
(b)

Figure 4.32: Comparisons between SODCIGs (a) before and (b) after updating the velocities. Both results are obtained using the original surface recorded data set. All of the SODCIGs are extracted at the same crossline (4.40 km), but at inlines 1.52, 3.05, 4.57, 6.10, 7.62, 9.14 and 10.67 km, from left to right. [CR]

chap4/. cig2d-bvel-cpst3,cig2d-invt-cpst3



(a)



(b)

Figure 4.33: Comparisons between ADCIGs (a) before and (b) after updating the velocities. Both results are obtained using the original surface-recorded data set. All of the ADCIGs are extracted at the same crossline (1.00 km), but at inlines 1.52, 3.05, 4.57, 6.10, 7.62, 9.14 and 10.67 km, from left to right. [CR]

chap4/.adcig2d-bvel-cpst1,adcig2d-invt-cpst1

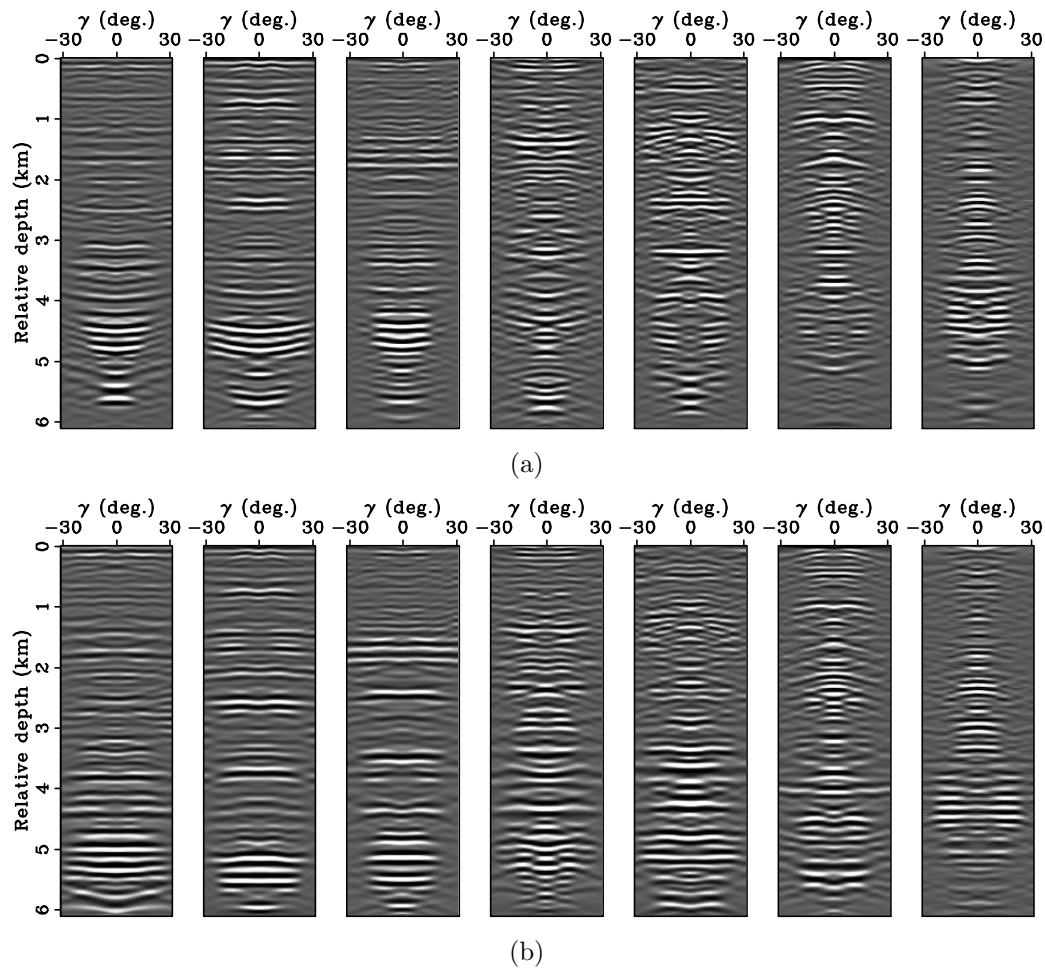
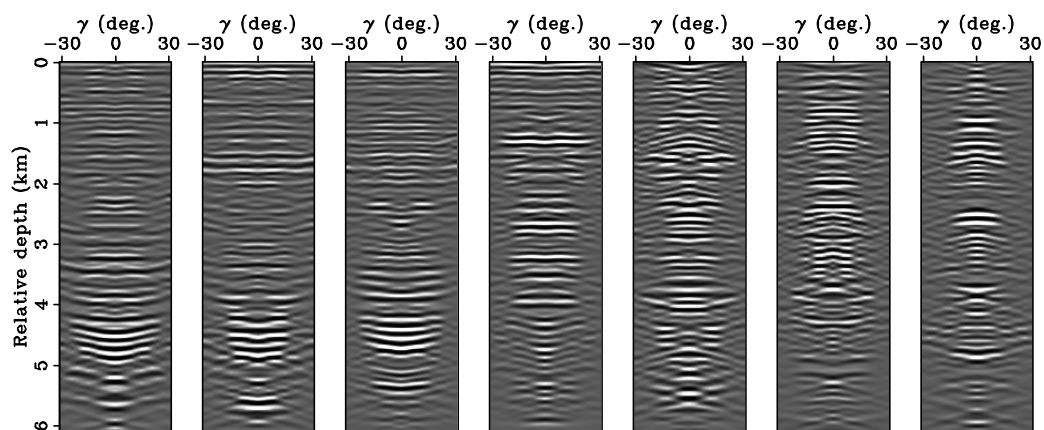
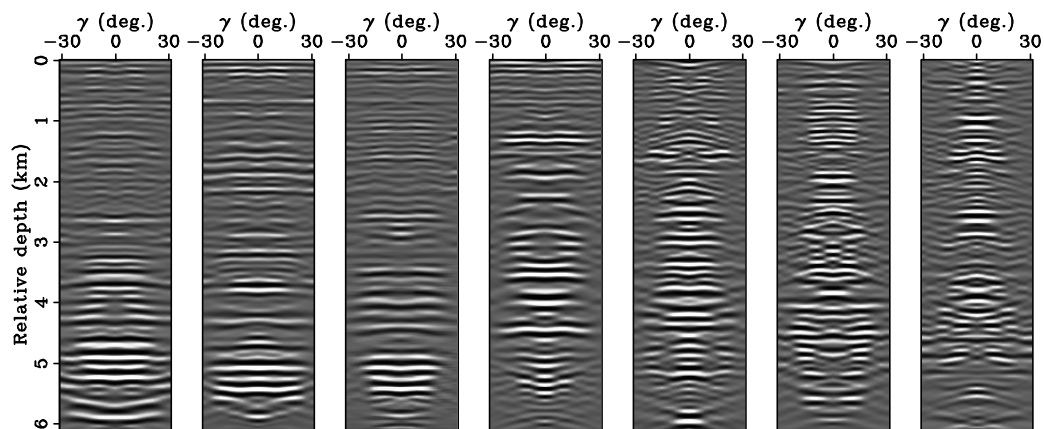


Figure 4.34: Comparisons between ADCIGs (a) before and (b) after updating the velocities. Both results are obtained using the original surface-recorded data set. All of the ADCIGs are extracted at the same crossline (3.70 km), but at inlines 1.52, 3.05, 4.57, 6.10, 7.62, 9.14 and 10.67 km, from left to right. [CR]

chap4/.adcig2d-bvel-cpst2,adcig2d-invt-cpst2



(a)



(b)

Figure 4.35: Comparisons between ADCIGs (a) before and (b) after updating the velocities. Both results are obtained using the original surface recorded data set. All of the ADCIGs are extracted at the same crossline (4.40 km), but at inlines 1.52, 3.05, 4.57, 6.10, 7.62, 9.14 and 10.67 km, from left to right. [CR]

chap4/.adcig2d-bvel-cpst3,adcig2d-invt-cpst3

Subsalt reflectivity imaging

After obtaining a more accurate subsalt velocity model, I proceed to recover the subsalt reflectivity using target-oriented wavefield least-squares migration (Chapter 2). The selected target region for the inversion test is shown in Figure 4.36. Figure 4.37 shows the prestack image obtained by using the migration operator (3-D conical-wave migration). Note the unbalanced amplitudes and the illumination shadows below the salt. The goal is to recover the reflectivities from the uneven illumination effects by using the target-oriented wavefield least-squares migration.

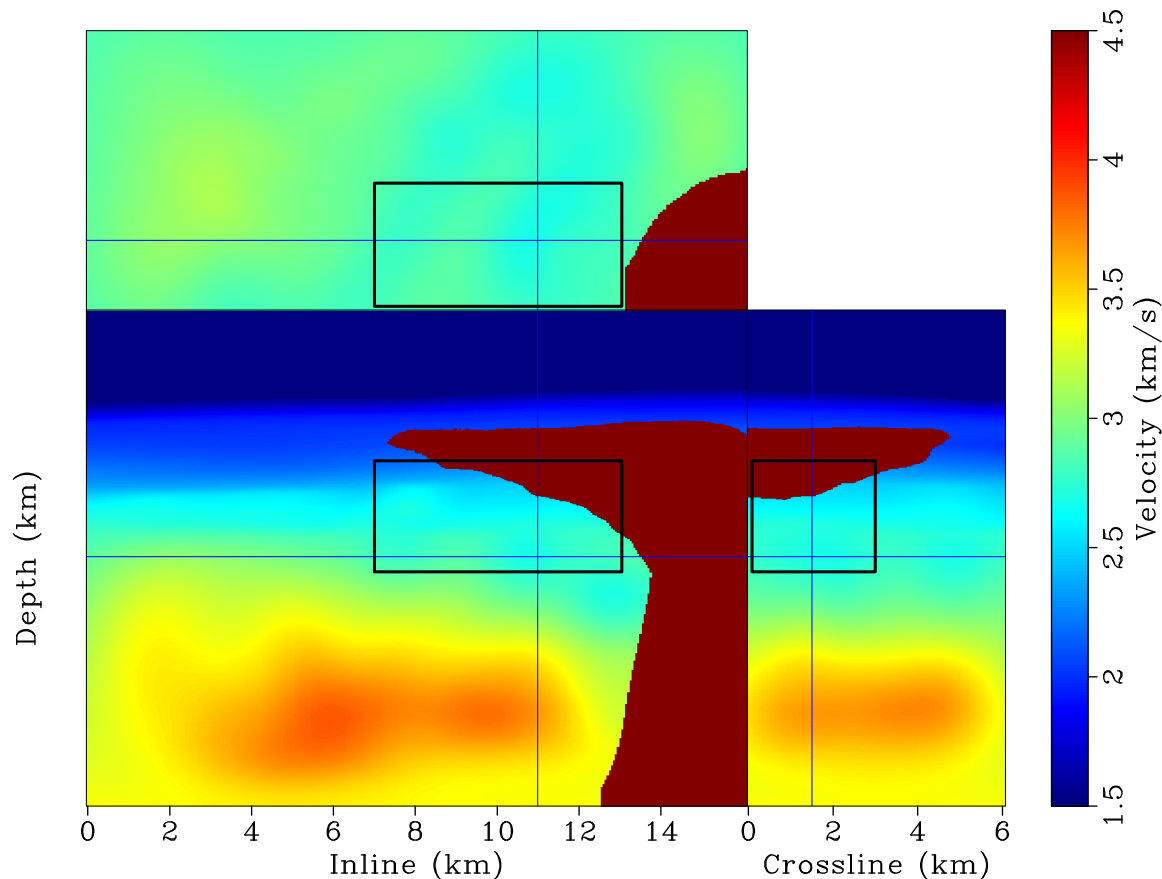


Figure 4.36: Target area selected (outlined by a box) for wavefield least-squares migration. [CR] chap4/. lsm3d-target

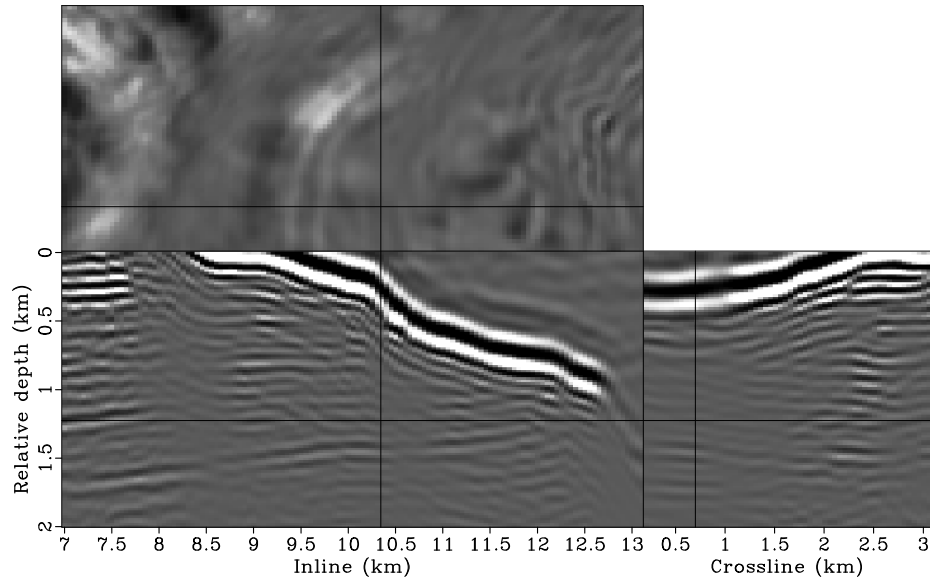


Figure 4.37: Migrated image for the selected target region. [CR]
 chap4/. lsm3d-imag

The 3-D phase-encoded Hessian with off-diagonal elements

I compute the phase-encoded Hessian in the 3-D conical-wave-domain (equations 4.19, 4.23 and 4.24) using the updated velocity model (Figure 4.22). Instead of computing only the diagonal components of the Hessian matrix, I compute also the off-diagonal components of the matrix. Due to the limited computing resources at hand, I compute the Hessian for only the zero-subsurface offset, i.e., $\tilde{\tilde{H}}(\mathbf{x}, \mathbf{x}', \mathbf{h} = \mathbf{0}, \mathbf{h}' = \mathbf{0})$.

The target region contains 784740 points, with 123 samples inline, 58 crossline and 110 in depth. The number of elements computed per row for the Hessian is 5155 (11 in x , 15 in y and 31 in z). Therefore, the widths of the local filter for each image point are 0.25 km, 0.35 km and 0.27 km in x , y and z directions, respectively. I calculate the filter with the widest length in y , because the data is acquired using a NATS acquisition system and further rotated into zero azimuth. The lack of data coverage in the crossline direction is likely to make the filter broader in the y direction.

The top panels in Figures 4.38 and 4.39 present the diagonal components of the

Hessian matrix at two different slices. Note that the values of the diagonal of the Hessian are far from uniform, and the left side values (not subsalt) are much higher than those elsewhere in the target region. This is not surprising, because the salt body that has relatively high velocities prevents most of the energy penetrating itself. The unevenness of the diagonal components also suggests that the Hessian matrix is highly nonstationary (each row is substantially different than the others). This is further illustrated by the bottom panels in Figures 4.38 and 4.39, which show one row of the Hessian matrix at two different image points. For an image point that is well illuminated (bottom panels in Figure 4.38), the off-diagonals have relatively wide spectrum coverage and are more focused around the diagonal. On the other hand, for an image point that is poorly illuminated (bottom panels in Figure 4.39), the off-diagonals have relatively narrow spectrum coverage and are broader in the space domain.

To further appreciate the nonstationarities of the 3-D Hessian matrix, I apply the Hessian to a reflectivity model containing a collection of point scatterers (Figure 4.40). The result can also be considered as the filter response (each row of Hessian can be seen as a filter) of the Hessian to point scatterers. Note how the shape and strength of the filters change across the space. Also note that the filter is more elongated in the crossline direction than in the inline direction. This is a result of the single-azimuth acquisition geometry. Figure 4.41 shows the Hessian filter response for four horizontal reflectors. Note the imprint of shadow zones on the reflectors. The characteristics of the shadow zones very closely match those in the migrated image (Figure 4.37), indicating that the computed Hessian matrix, albeit with some approximations, accurately captures the effects of uneven subsurface illumination due to limited acquisition geometry, band-limited wave phenomena and complex overburden. In the subsequent section, I demonstrate how the effects of uneven illumination can be optimally removed by inverting the Hessian matrix through regularized linear inversion.

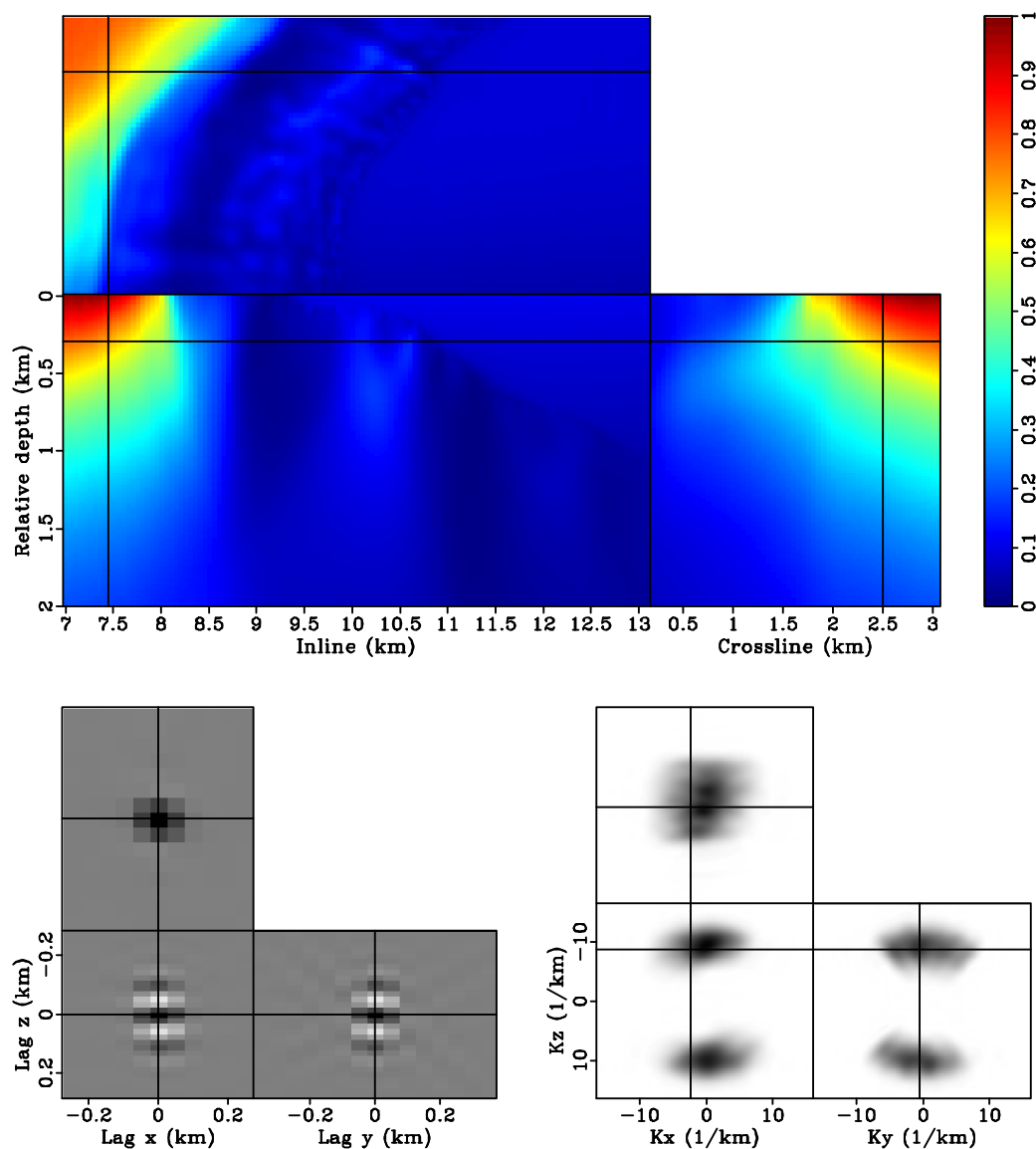


Figure 4.38: The Hessian matrix for the target region. The top panel shows the diagonal components of the matrix; the bottom left panel shows one row of the matrix taken from the image point at inline 7.45 km, crossline 2.50 km and relative depth 0.30 km (the intersection of the crosshairs in the top panel); the bottom right panel shows the amplitude spectrum of the bottom left panel. [CR] `chap4/.lsm3d-hess-filter1`

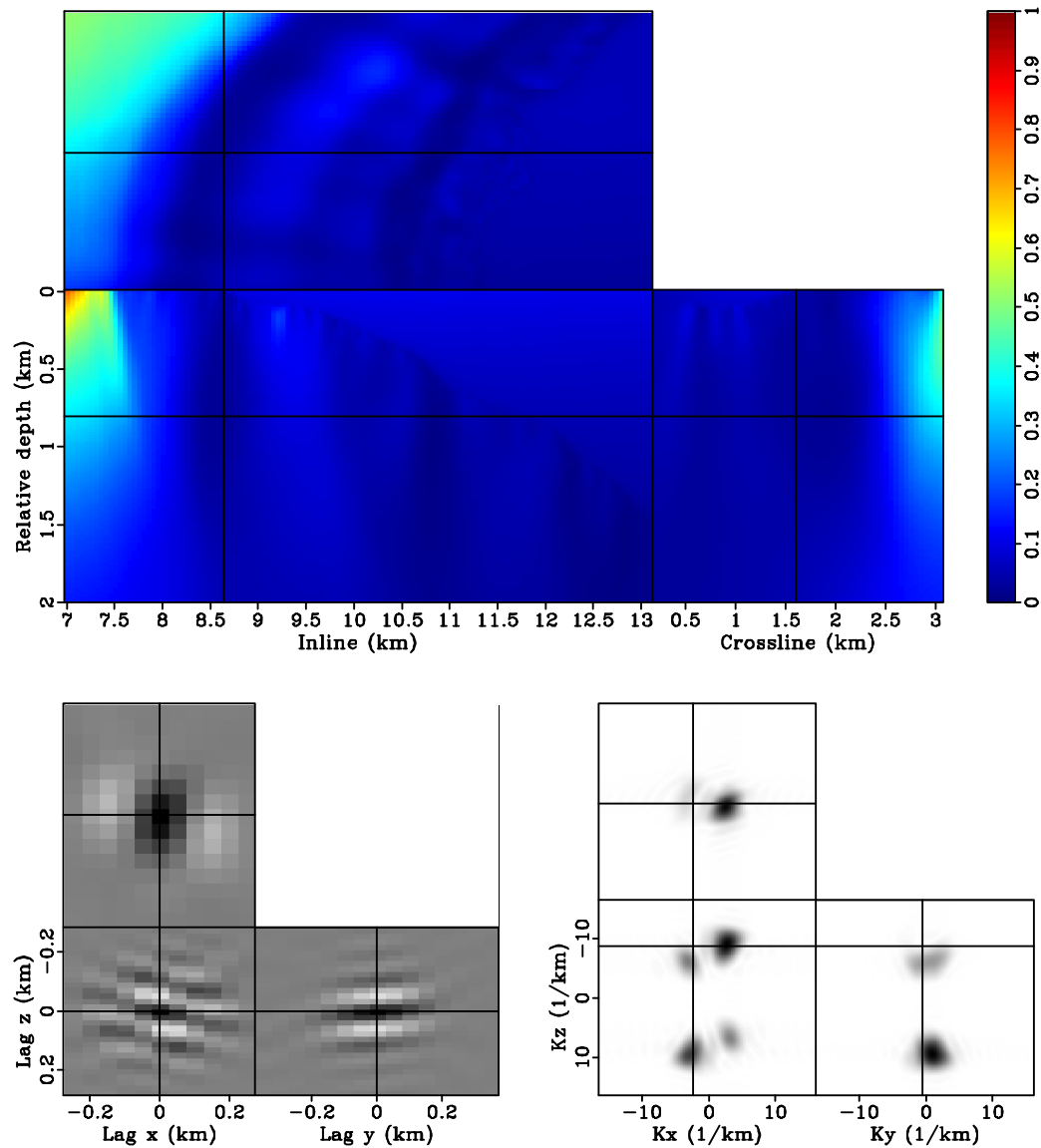
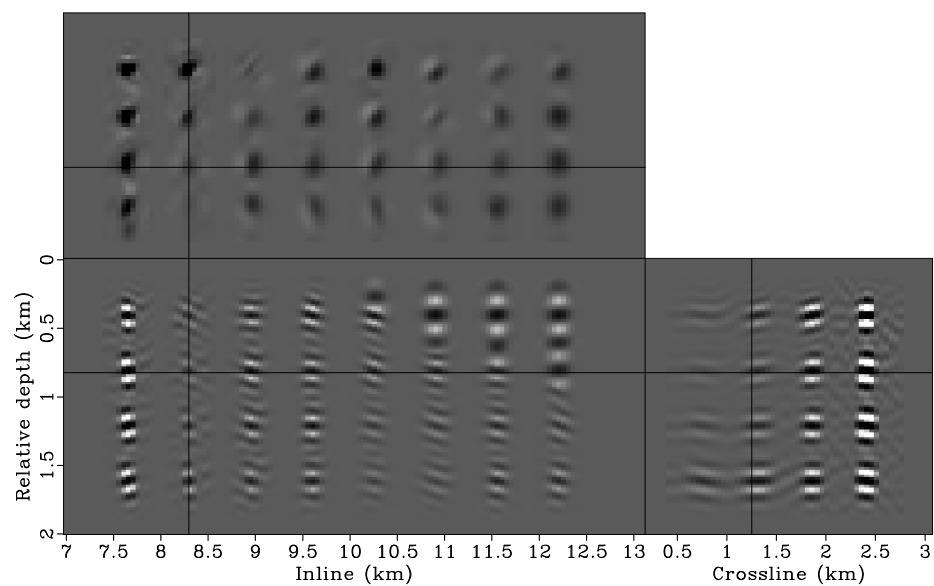
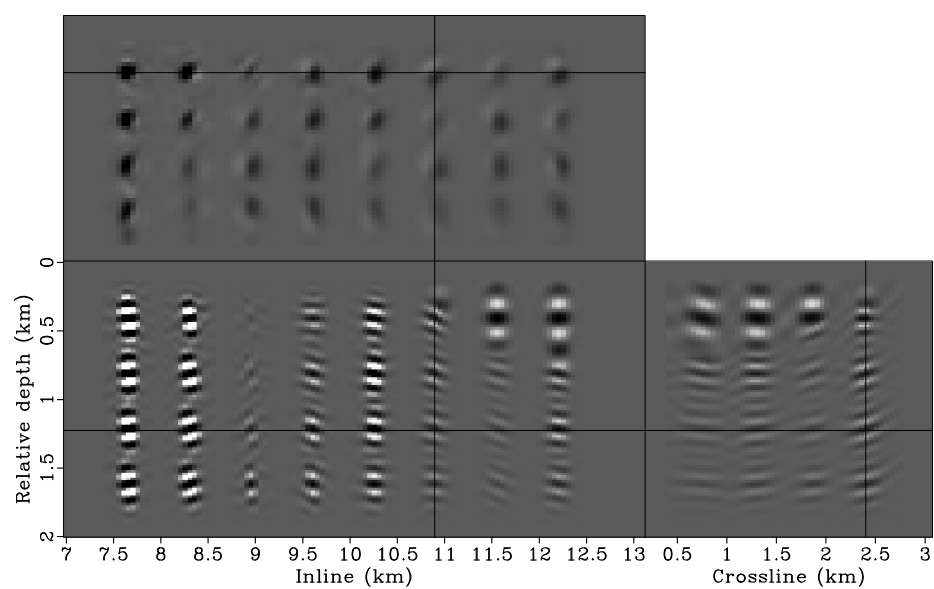


Figure 4.39: The Hessian matrix for the target region. The top panel shows the diagonal components of the matrix; the bottom left panel shows one row of the matrix taken from the image point at inline 8.65 km, crossline 1.60 km and relative depth 0.80 km (the intersection of the crosshairs in the top panel); the bottom right panel shows the amplitude spectrum of the bottom left panel. [CR] `chap4/.lsm3d-hess-filter2`

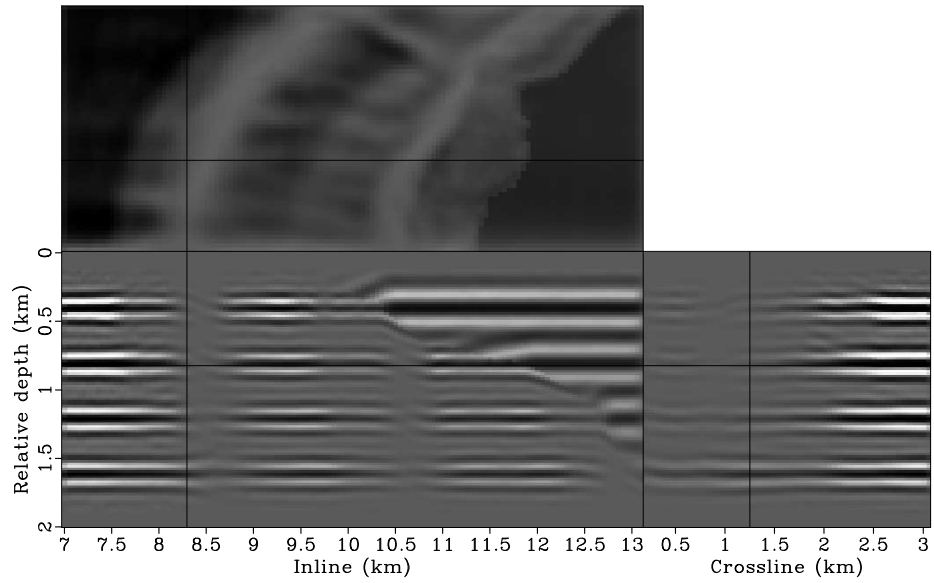


(a)

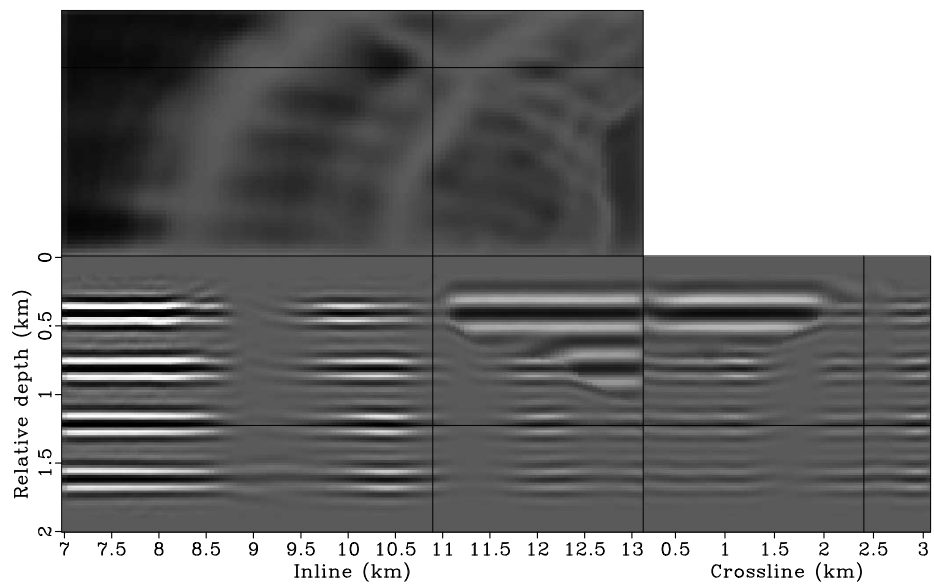


(b)

Figure 4.40: Hessian filter response for point scatterers. Panels (a) and (b) show different slices of the same 3-D cube. Note the nonstationarities of the filters. [CR] chap4/. lsm3d-imag-spike1,lsm3d-imag-spike2



(a)



(b)

Figure 4.41: Hessian filter response for horizontal reflectors. Panels (a) and (b) show different slices of the same 3-D cube. Note the imprint of shadow zones on the reflectors. [CR] chap4/. lsm3d-imag-flat1,lsm3d-imag-flat2

Regularized linear inversion

I optimize the reflectivity model by minimizing the following objective function as discussed in Chapter 2:

$$J(\mathbf{m}) = \frac{1}{2} \|\mathbf{H}\mathbf{m} - \mathbf{m}_{\text{mig}}\|^2 + \varepsilon \mathcal{R}(\mathbf{m}), \quad (4.28)$$

where \mathbf{m} and \mathbf{m}_{mig} are the reflectivity model and migrated image, respectively; \mathbf{H} is the Hessian operator computed using the phase-encoding method discussed in the previous section; $\mathcal{R}(\mathbf{m})$ is a regularization term that incorporates user-defined model covariance into the inversion; parameter ε controls the strength of regularization. In Chapter 2, a simple damping regularization

$$\mathcal{R}(\mathbf{m}) = \frac{1}{2} \|\mathbf{m}\|^2, \quad (4.29)$$

seems to be sufficient to produce a satisfactory inversion result for the Sigsbee2A synthetic example. In this section, I show examples that use different regularizations to produce different regularized inversion results.

To see the importance of regularization, I first invert the image containing horizontal reflectors (Figure 4.41). Figure 4.42 shows the inversion result after 100 iterations without applying any regularizations. The inversion improves the image considerably by showing more balanced amplitudes, narrower shadow zones and higher spatial resolution than those in Figure 4.41. However, the recovery from the shadow zones is slow, and the inverted image looks noisy due to the under-determined and ill-posed nature of the Hessian operator.

Regularization helps stabilize the inversion; it can shape the null space and remove unwanted features in the inverted result by introducing user-defined model-covariance operators. In the next example, I choose to use the following regularization term:

$$\mathcal{R}(\mathbf{m}) = \frac{1}{2} \|\mathbf{D}^* \mathbf{D}\mathbf{m}\|^2, \quad (4.30)$$

where operator \mathbf{D} contains wavekill filters (Claerbout, 2008), which annihilate local planar-events with given dips. The operator imposes continuity of reflectors along its dipping direction. This idea has also been explored by Clapp (2005) and Ayeni et al. (2009), who use similar filters (Clapp, 2003; Hale, 2007) to regularize the data-domain least-squares migration.

Instead of solving the inversion problem as a regularization problem, I solve it as a preconditioning problem by making change of variable as follows:

$$\mathbf{m} = \mathbf{S}\mathbf{n}, \quad (4.31)$$

where \mathbf{n} is the vector of preconditioned variables and \mathbf{S} is the preconditioning operator, which is defined to be an approximate inverse of the regularization operator $\mathbf{D}^*\mathbf{D}$. To find the inverse of $\mathbf{D}^*\mathbf{D}$, I factorize it into minimum-phase filters \mathbf{A} such that $\mathbf{D}^*\mathbf{D} \approx \mathbf{A}^*\mathbf{A}$. I use the Wilson-Burg factorization (Claerbout, 1992; Fomel et al., 2003) and apply it on the helix (Claerbout, 1998, 2008). Since minimum-phase filters have stable inverses, I can define the preconditioning operator as follows

$$\mathbf{S} = \mathbf{A}^{-1} (\mathbf{A}^*)^{-1}. \quad (4.32)$$

Contrary to $\mathbf{D}^*\mathbf{D}$, operator \mathbf{S} contains dip filters, which smooth along given dip directions. Substituting equations 4.30, 4.31 and 4.32 into 4.28 yields

$$J_p(\mathbf{n}) = \frac{1}{2} \|\mathbf{H}\mathbf{S}\mathbf{n} - \mathbf{m}_{\text{mig}}\|^2 + \frac{\varepsilon}{2} \|\mathbf{n}\|^2. \quad (4.33)$$

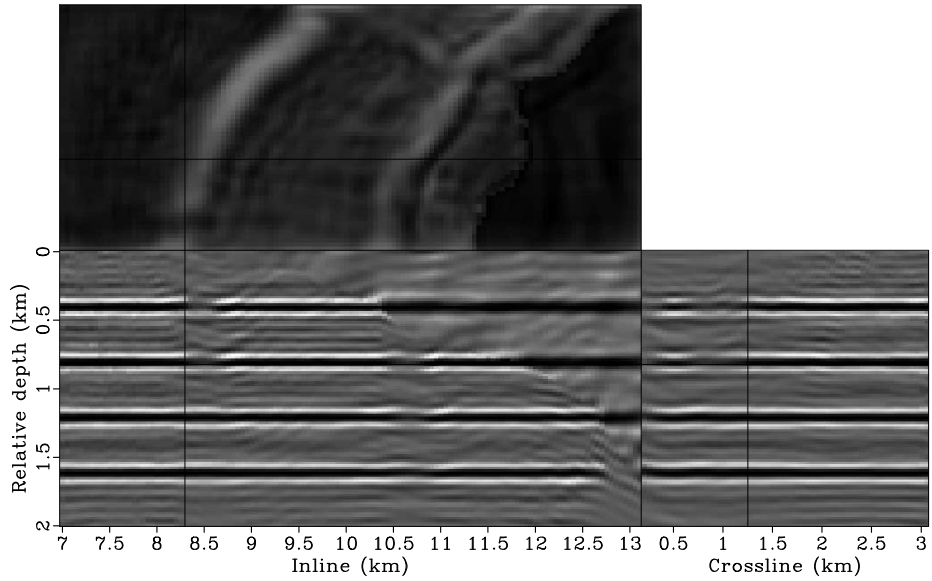
Objective function 4.33 is often solved by setting $\varepsilon = 0$ and iterating until an acceptable result is obtained (Claerbout, 2008). Solving it in this way implicitly assumes that we are starting with a model that has all the user-defined covariance, and that the more iteration we run, the more we honor the migrated image. Once a solution vector \mathbf{n}_{sol} has been found, the final model is obtained by computing $\mathbf{m}_{\text{sol}} = \mathbf{S}\mathbf{n}_{\text{sol}}$.

Figure 4.43 shows the inversion result after 100 iterations when preconditioned

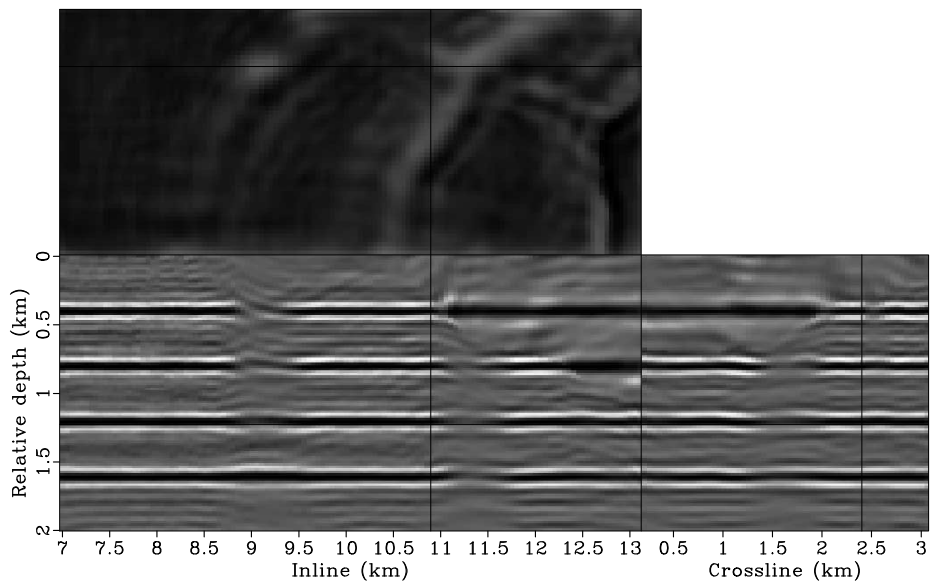
with dip filters that smooth horizontally. In this case, the dip filters correctly predict the model covariance. The inversion result looks much cleaner and recovers much better and faster from the effects of shadow zones than that obtained without any regularization (Figure 4.42). However, regularization can also be dangerous if the provided model-covariance differs greatly from the true one. Figure 4.44 shows the inversion result after 100 iterations when preconditioned with dip filters that smooth along a plane dipping -30° inline and 30° crossline. The inversion leads to a completely wrong solution, which is dominated by the dipping feature that the preconditioning operator imposes. These artifacts can be used as an indication that the wrong regularization has been used.

Next I invert the image obtained by migrating the 3-D GOM data set (Figure 4.37). Since the goal is to invert sediment reflectivities, I incorporate a mask operator (Figure 4.45) into the inversion to prevent updating the reflectivities of the salt boundary. I first run the inversion without applying any regularizations; the inverted image after 100 iterations is shown in Figure 4.47. Compared to migration (Figure 4.46), inversion significantly improves the spatial resolution of the image; the amplitudes are more balanced, and the illumination shadows are filled in. However, the inverted image is more noisy, and the continuity of the reflectors seems to be degraded. The increased noise level reveals the ill-posedness of the inversion problem due to the narrow bandwidth of the Hessian filter (bottom panels of Figures 4.38 and 4.39). Another reason might be the approximations used to compute the Green's function (acoustic one-way wave equation) and the migration do not fully match the way seismic waves propagate through the earth. The inconsistency of the operator and the data may further increase the ill-posedness of the inversion problem. Therefore, regularization becomes necessary.

I first regularize the inversion with a damping term (equation 4.29) and minimize the regularized objective function defined by equation 4.28. Figure 4.48 shows the inversion result after 100 iterations with the trade-off parameter $\varepsilon = 0.02$. The damping term stabilizes the inversion and the speckle noise present in Figure 4.47 is suppressed in Figure 4.48. The inverted image shows very good overall quality with

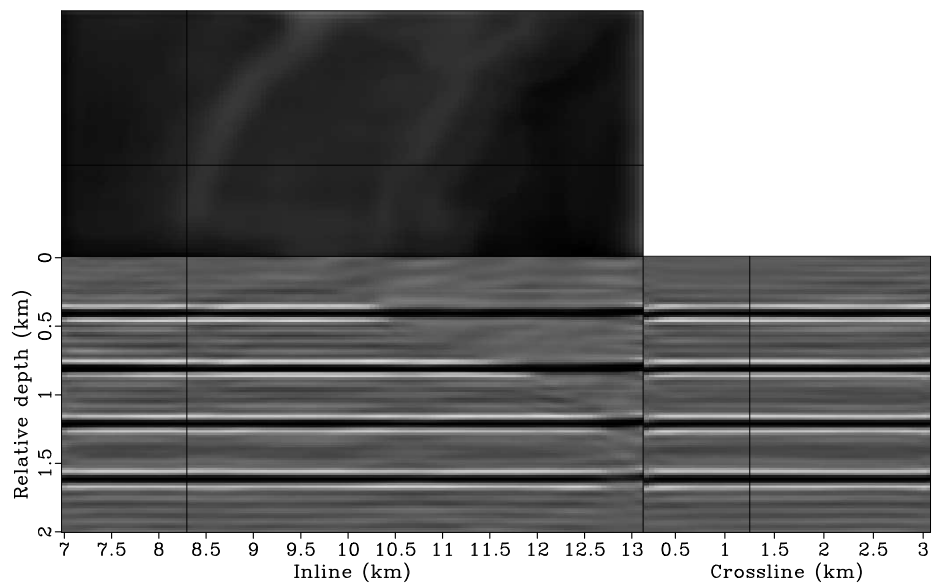


(a)

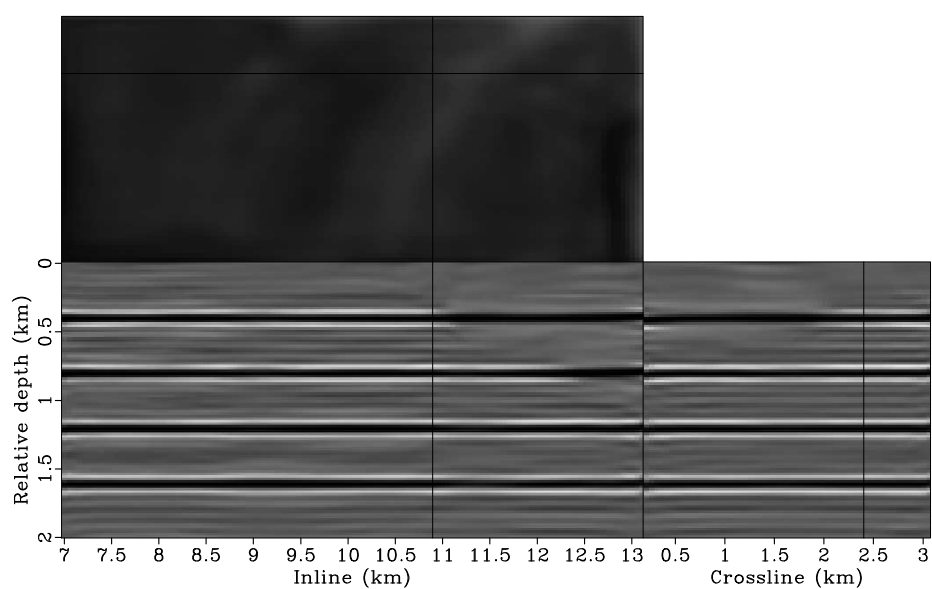


(b)

Figure 4.42: Inversion without any regularization for the horizontal-reflector model. Panels (a) and (b) show two different slices of the same 3-D cube. [CR] chap4/. lsm3d-invt-noreg-flat1,lsm3d-invt-noreg-flat2

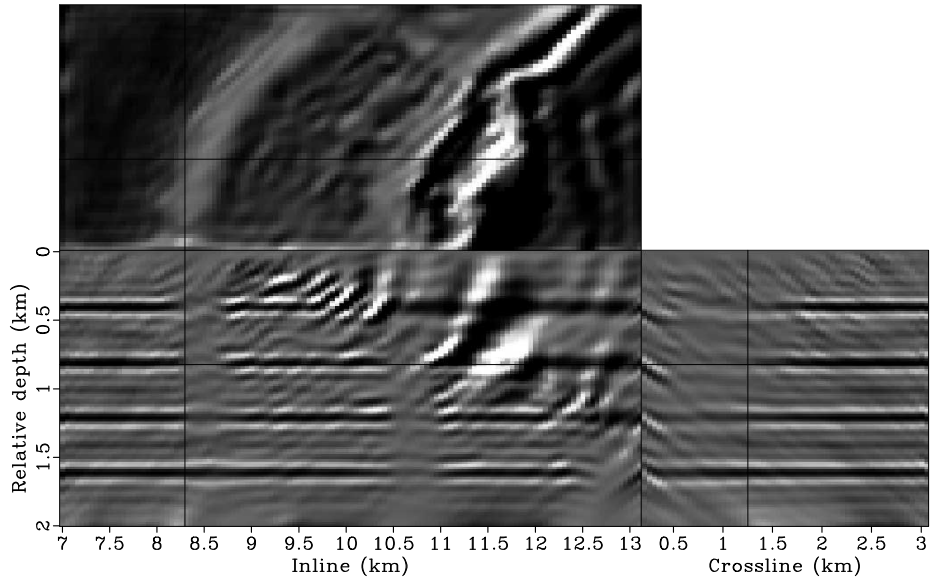


(a)

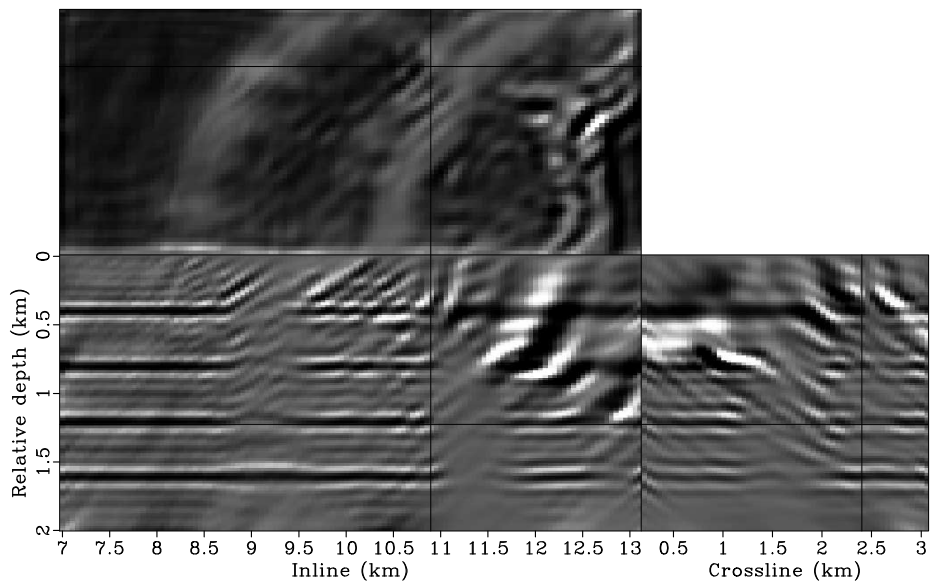


(b)

Figure 4.43: Inversion preconditioned by dip filters that smooth horizontally. Panels (a) and (b) show two different slices of the same 3-D cube. [CR] chap4/. lsm3d-invt-reg-flat1,lsm3d-invt-reg-flat2



(a)



(b)

Figure 4.44: Inversion preconditioned by dip filters that smooth along a plane dipping -30° inline and 30° crossline. Panels (a) and (b) show two different slices of the same 3-D cube. [CR] `chap4/.lsm3d-invt-reg30-flat1,lsm3d-invt-reg30-flat2`

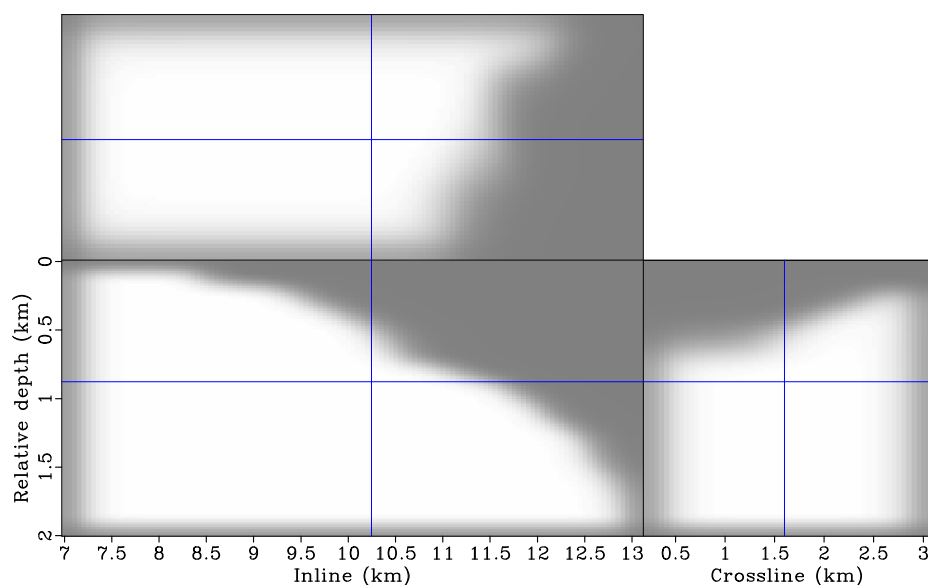
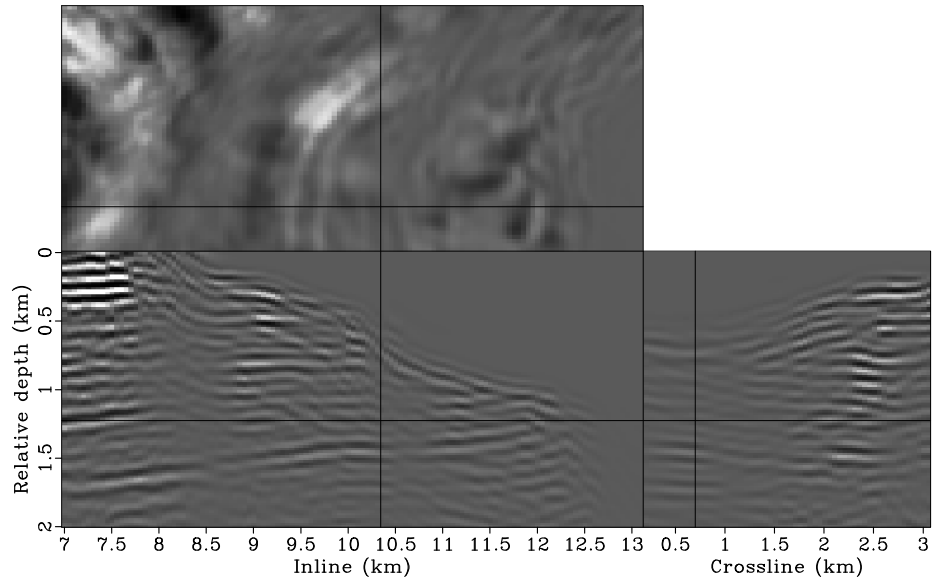


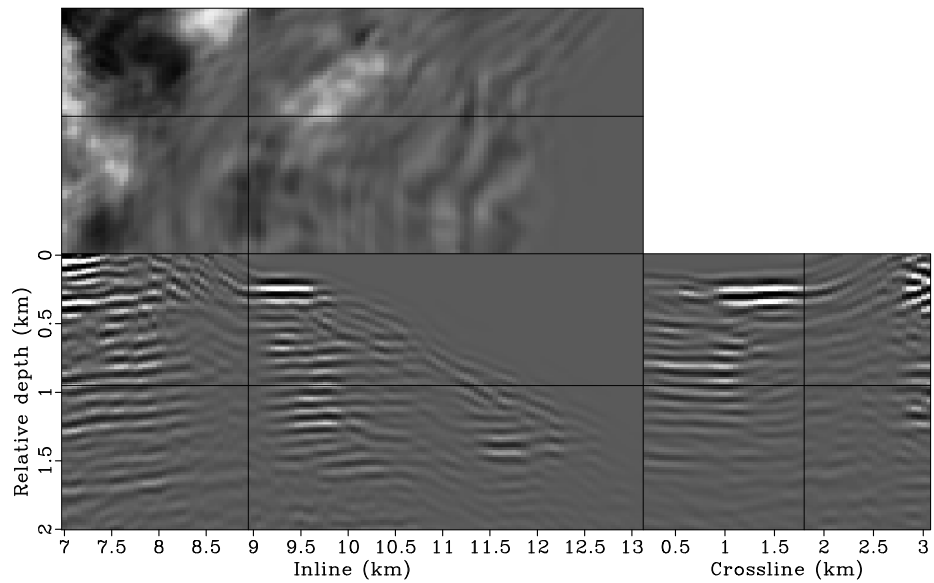
Figure 4.45: A mask operator used during inversion. [ER] `chap4/.lsm3d-mask`

more balanced amplitudes. But the illumination shadows are not filled in completely, and artifacts with conflicting dips, e.g., at inline 9.75 km and relative depth 1.25 km in Figure 4.48(a) are still present in the inverted image. Figure 4.49 shows the inversion result when I increase the trade-off parameter to $\varepsilon = 0.05$. The artifacts are further suppressed, but the effectiveness of inversion is also reduced. The illumination shadows are not well recovered.

Damping regularization assumes that the model is spatially uncorrelated. The reflectivities in the subsurface, however, are often spatially correlated and are continuous along their dip directions. In the subsequent examples, I precondition the inversion with dip filters and minimize the objective function defined by equation 4.33. In order to regularize the inversion with a reasonably accurate model covariance, I interpret the migrated image and manually pick several key reflectors (Figure 4.50). I estimate dip fields based on the interpreted reflectors using the structure tensor method (van Vliet and Verbeek, 1995; Hale, 2007). The estimated dips have been smoothed with a triangle filter and are shown in Figure 4.51. The dip field is then used to build a bank of dip filters for preconditioning. Figures 4.52, 4.53 and 4.54

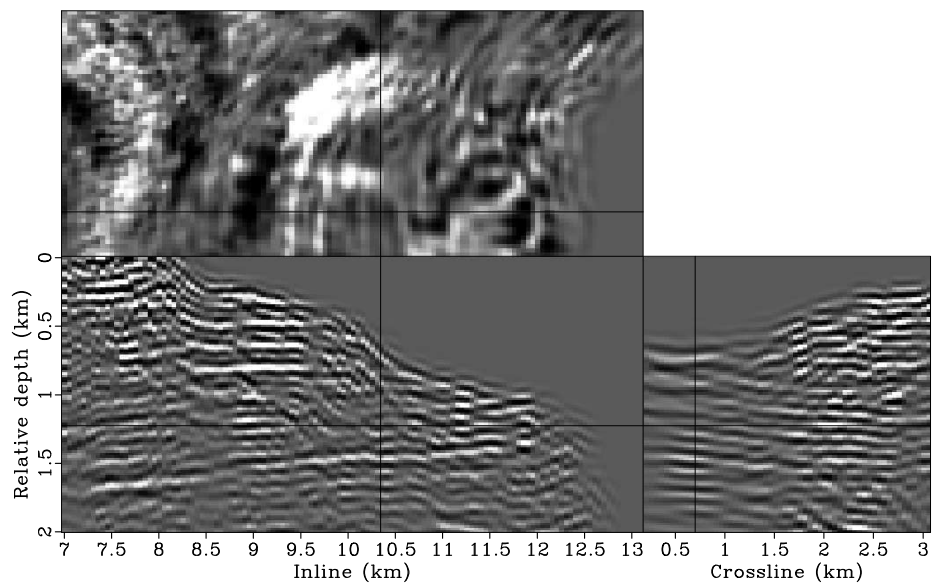


(a)

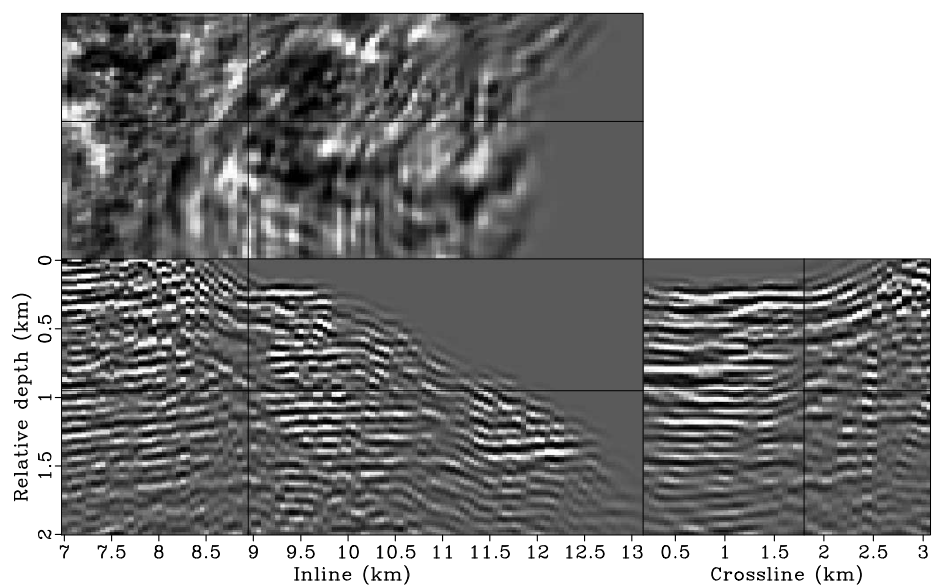


(b)

Figure 4.46: The migrated image of the 3-D GOM data set. Panels (a) and (b) show different slices of the same 3-D cube. The image has been masked using the mask operator shown in Figure 4.45 to focus on comparing sediment reflectivities. [CR] chap4/. lsm3d-imag-mask1,lsm3d-imag-mask2



(a)

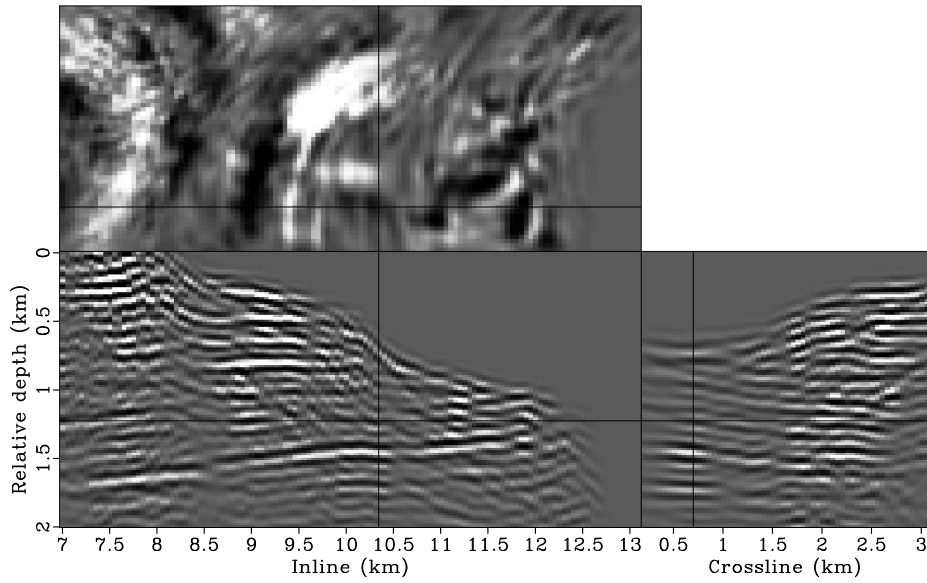


(b)

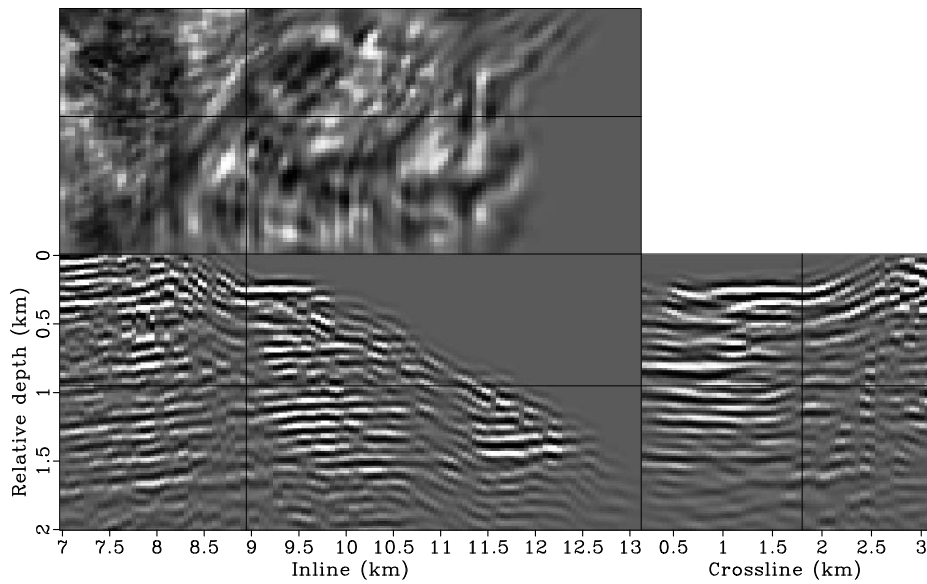
Figure 4.47: The inverted image without applying any regularization. Panels (a) and (b) show different slices of the same 3-D cube.

Pan-
[CR]

chap4/. lsm3d-noreg-invt1,lsm3d-noreg-invt2



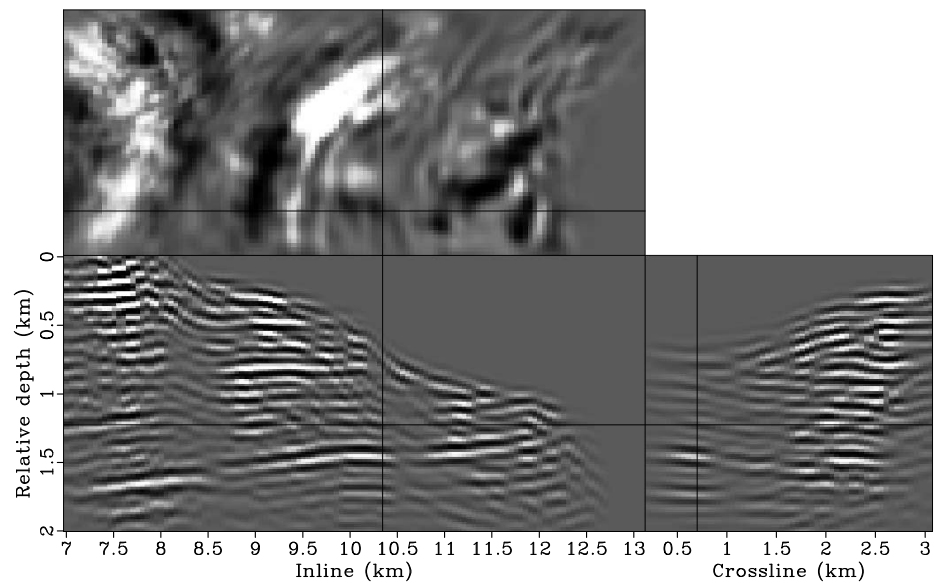
(a)



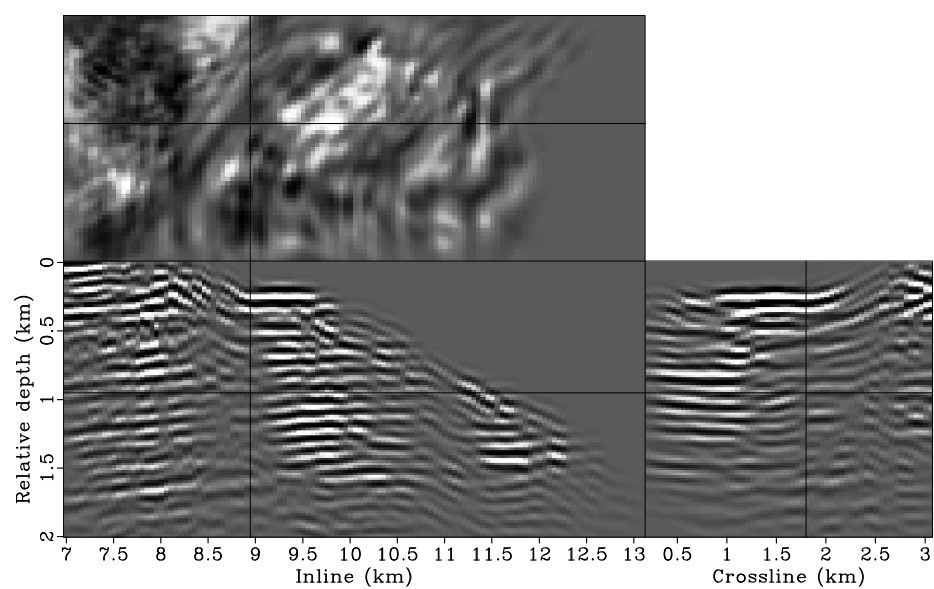
(b)

Figure 4.48: The inverted image with a damping regularization ($\varepsilon = 0.02$). Panels (a) and (b) show different slices of the same 3-D cube. [CR]

chap4/. lsm3d-damp4-invt1,lsm3d-damp4-invt2



(a)



(b)

Figure 4.49: The inverted image with a damping regularization ($\varepsilon = 0.05$). Panels (a) and (b) show different slices of the same 3-D cube. [CR]

chap4/.lsm3d-damp3-invt1,lsm3d-damp3-invt2

show impulse responses of the dip filters as smoothing strength increases. Note that the stronger the smoothing effect, the longer the filter response. These dip filters also vary spatially, and each dip filter smooths along a direction conformal to the corresponding dip value. Also note that the dip filters exhibit numerical anisotropies (the diamond shapes in the top panels of Figures 4.52, 4.53 and 4.54). The numerical anisotropy is caused by two-way splitting, where I approximate a 3-D dip filter with two cascading 2-D filters (Clapp, 2003).

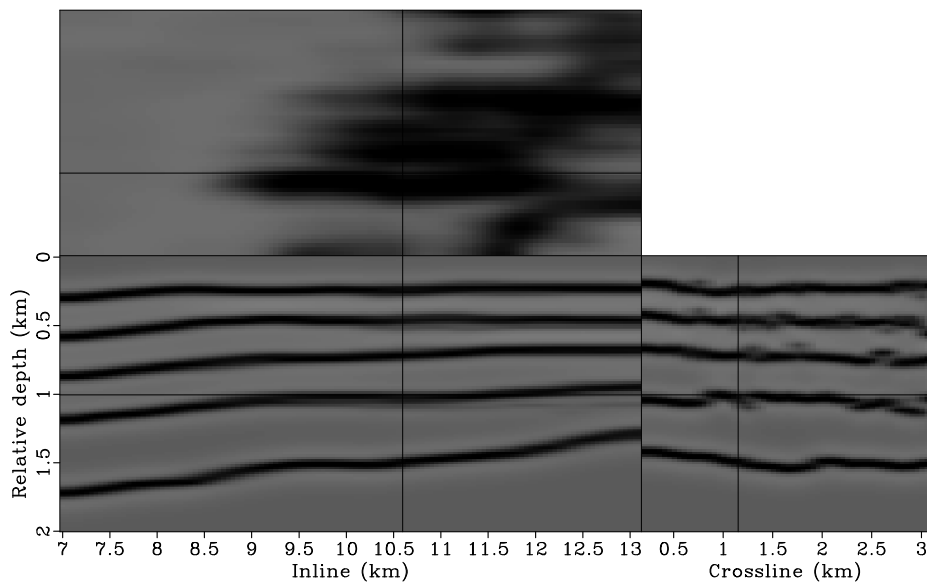
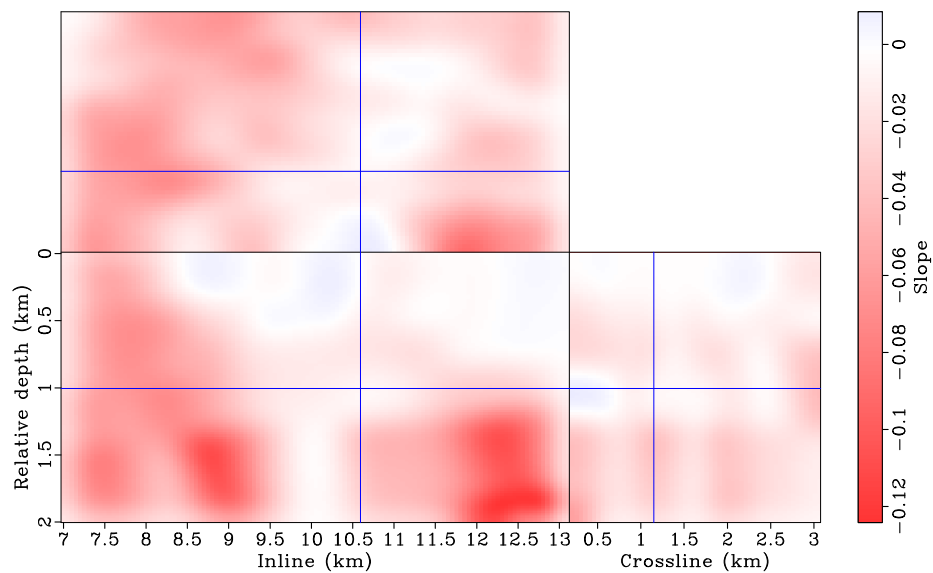


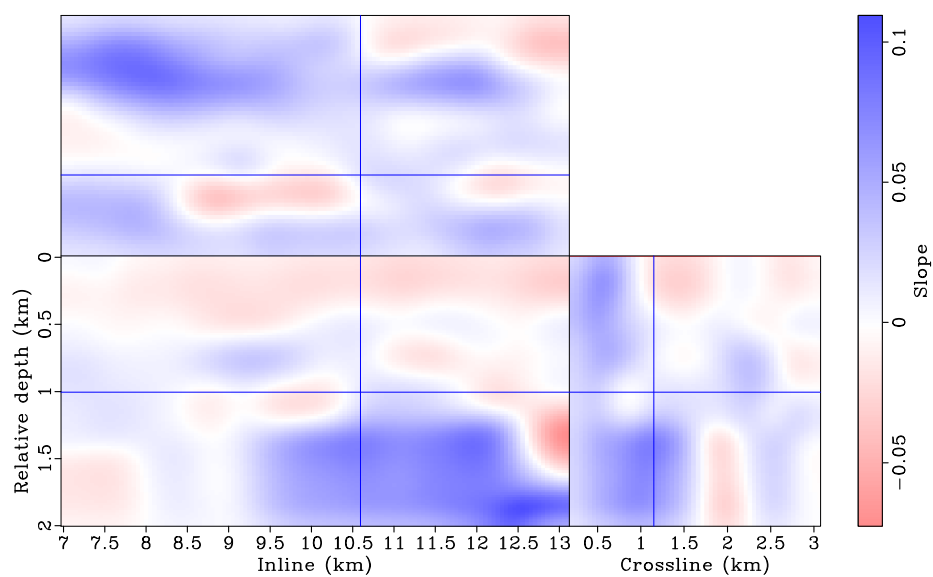
Figure 4.50: Interpreted horizons from the migrated image. The horizons are then used to build the dip field for dip filtering. [CR] chap4/. lsm3d-refl-pick

Figure 4.55 presents the inverted image after 100 iterations when preconditioned by the dip filter with weak smoothing (Figure 4.52). The result is significantly improved over the one obtained without any regularizations (Figure 4.47). The reflectors are much more coherent and they extend further into the shadow zone, filling in the illumination gap almost completely. The regularized image is much easier to interpret geologically.

To see the effects of regularization (or preconditioning), I increase the smoothing strength of the dip filters. Figure 4.56 shows the inversion result after 100 iterations when I use dip filters with moderate smoothing (Figure 4.53) for preconditioning.



(a)



(b)

Figure 4.51: The estimated dip field from the interpreted reflectors. Panels (a) and (b) are the slopes in the inline and crossline directions, respectively. [CR] chap4/. lsm3d-dipx-pick,lsm3d-dipy-pick

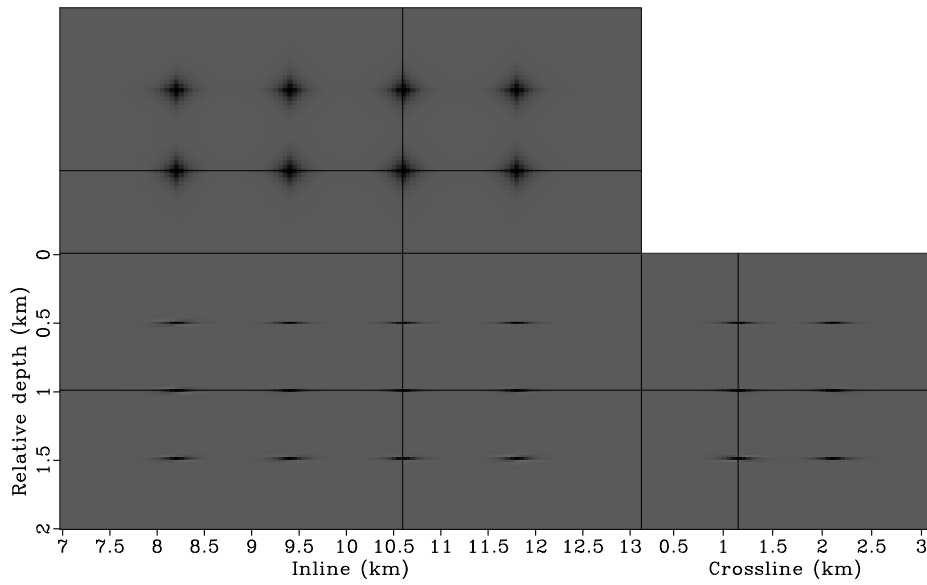


Figure 4.52: The impulse responses of dip filters with weak smoothing. [CR]
 chap4/.lsm3d-dipflt3

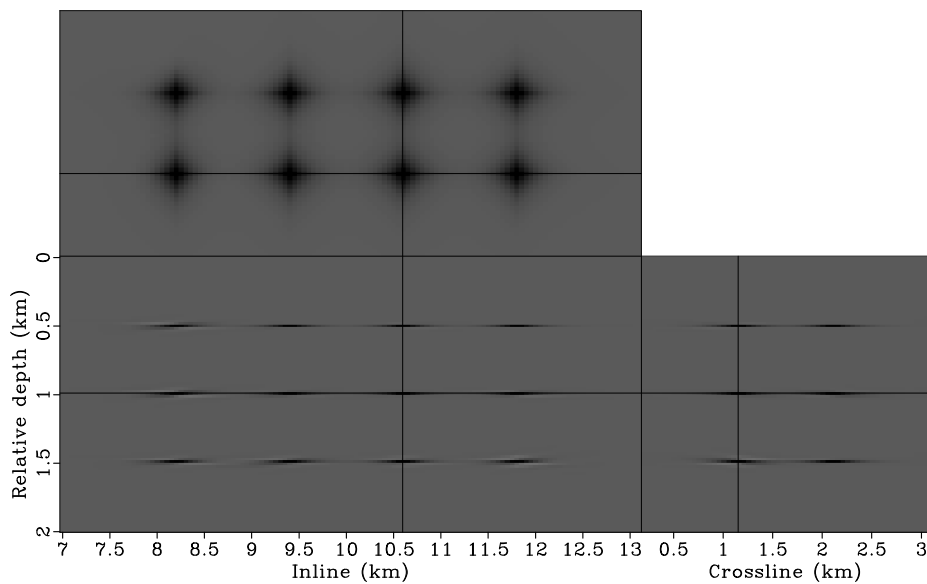


Figure 4.53: The impulse responses of dip filters with moderate smoothing. [CR]
 chap4/.lsm3d-dipflt1

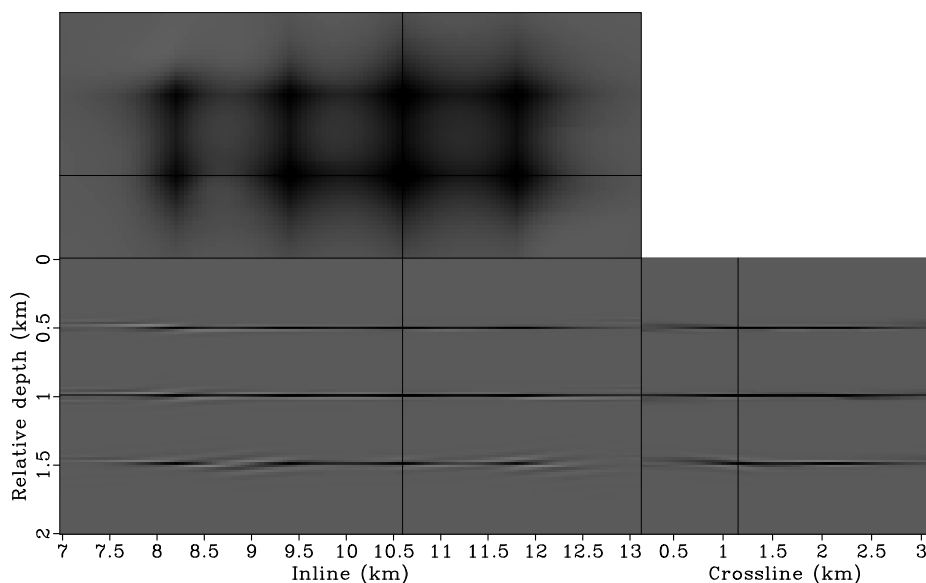
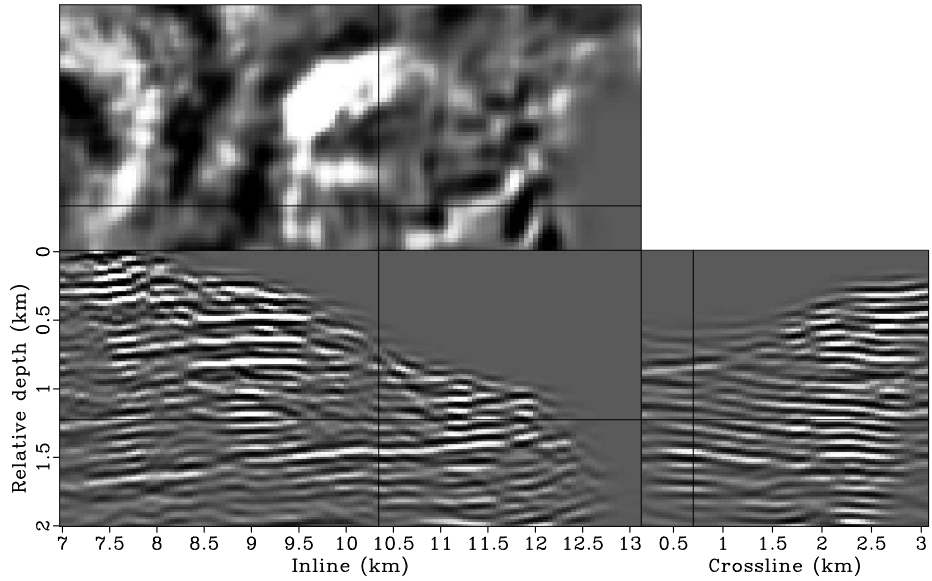


Figure 4.54: The impulse responses of dip filters with strong smoothing. [CR] chap4/. lsm3d-dipflt6

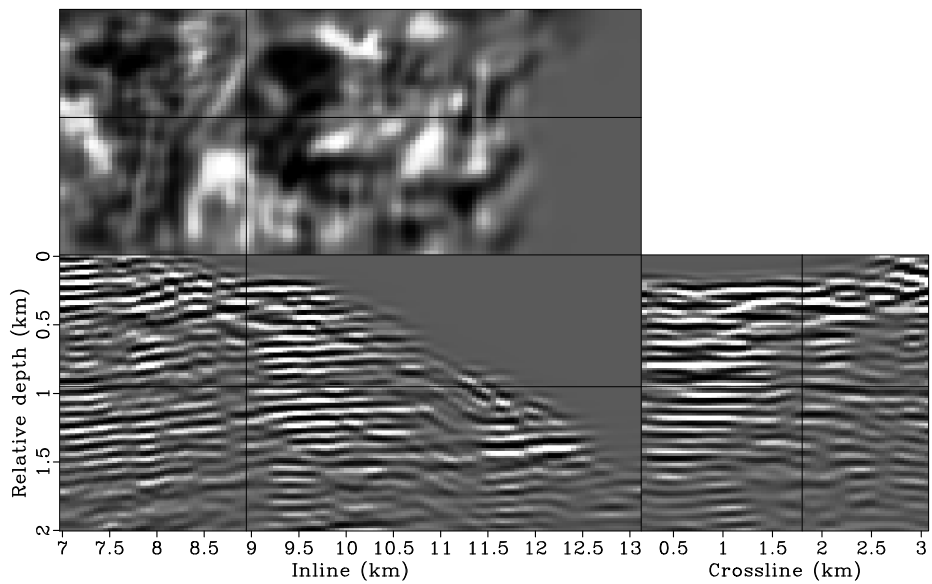
The result further enhances the coherence and continuity of the reflectors and the inverted image looks even cleaner. However, the spatial resolution of the image seems somewhat degraded by the smoothing effect of the preconditioner (This becomes clear by comparing the depth slices of Figures 4.47, 4.55 and 4.56).

Figure 4.57 shows the inversion result when I further increase the smoothing strength of the dip filters (Figure 4.54). In this extreme case, inversion is dominated by preconditioning. The inverted image honors the user-supplied model-covariance, but not necessarily the data. (The image fitting plays little role in this case.)

It is always instructive to look at inversion residuals. Figure 4.58 compares the image residuals, i.e., $\mathbf{H}\mathbf{m} - \mathbf{m}_{\text{mig}}$, obtained at the last iteration with different inversion methods. It is apparent that inversion without any regularizations yields the smallest image residual (Figure 4.58(a)). This phenomenon is caused by the fact that unconstrained inversion does not assume any prior information of the reflectivity model, and hence it tries to fit everything in the migrated image to minimize the residual under the ℓ_2 norm, which assumes the residual having an uncorrelated

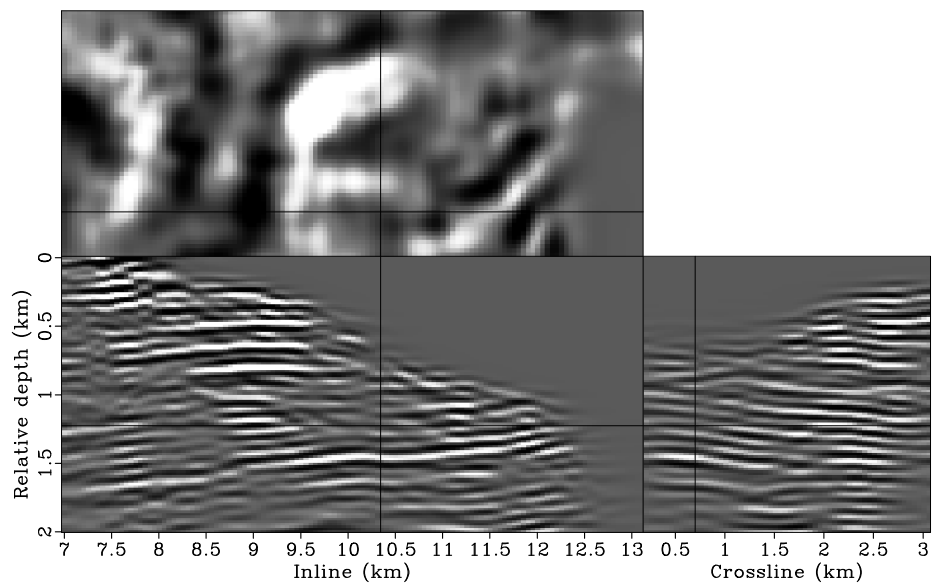


(a)

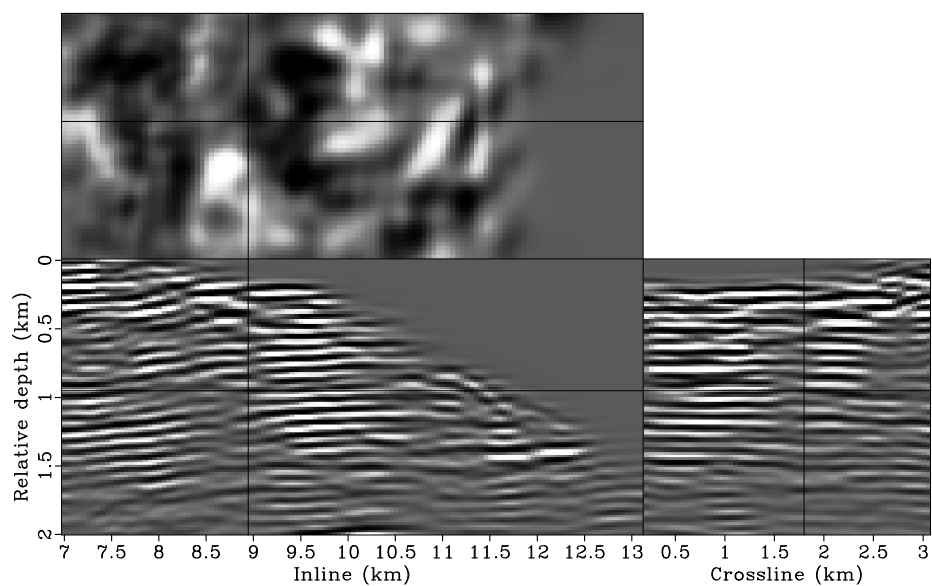


(b)

Figure 4.55: The inverted image when preconditioned using dip filters with weak smoothing (Figure 4.52). Panels (a) and (b) show different slices of the same 3-D cube. [CR] chap4/.lsm3d-a-invt1,lsm3d-a-invt2

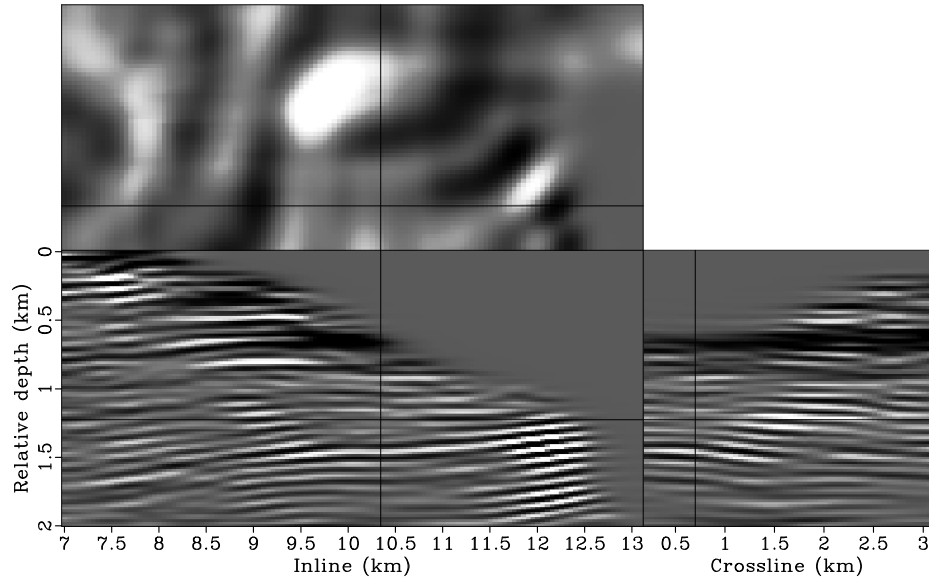


(a)

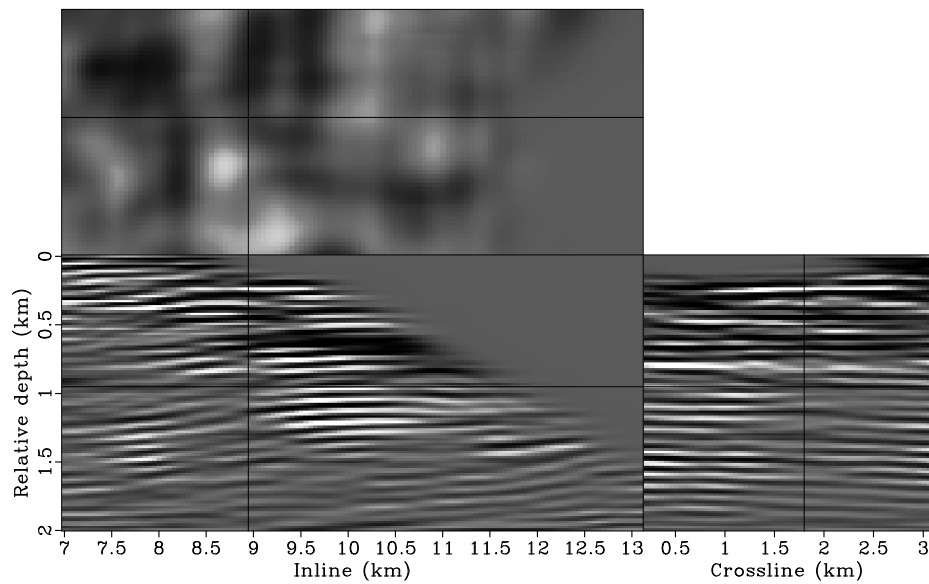


(b)

Figure 4.56: The inverted image when preconditioned using dip filters with moderate smoothing (Figure 4.53). Panels (a) and (b) show different slices of the same 3-D cube. [CR] chap4/. lsm3d-b-invt1,lsm3d-b-invt2



(a)



(b)

Figure 4.57: The inverted image when preconditioned using dip filters with strong smoothing (Figure 4.54). Panels (a) and (b) show different slices of the same 3-D cube. [CR] chap4/. lsm3d-c-invt1,lsm3d-c-invt2

Gaussian distribution. The “everything” here includes not only the signal obtained by migrating primaries that the Born modeling operator properly predicts, but also the coherent noise, such as internal multiples or converted waves, which the Born modeling operator does not model. As a consequence, the coherent noise remains in the inversion result, causing increased noise level in the inverted image (Figure 4.47).

Regularization with a damping term, on the other hand, constrains the inversion by penalizing the energy in the reflectivity model (\mathbf{m}). Damping regularization implicitly assumes that the reflectivity model is spatially uncorrelated. With this extra constraint, the inversion tries to find a model that both fits the migrated image (\mathbf{m}_{mig}) and the minimum-energy assumption. Therefore, coherent reflectors are left in the residual (Figure 4.58(b)), resulting in loss of important information in the inverted image (Figure 4.48). A bigger trade-off parameter ε results in more coherent reflectors being pushed into the residual (Figure 4.58(c)), further reducing the effectiveness of the image fitting (Figure 4.49).

In contrast, preconditioning with dip filters regularizes the inversion by smoothing the model along given dip directions. The model covariance imposed by the dip regularization is perhaps more accurate than that imposed by the damping regularization, because in practice reflectors do show spatial continuities along their dipping directions. By design, dip-constrained inversion pushes events that are not conformal to the smoothing directions of dip filters into the image residual. In this particular inversion example, I design dip filters using the interpreted dip fields (Figure 4.51). Events with conflicting dips, which are likely converted waves or internal multiples, are therefore left in the residual (Figure 4.58(d)), resulting in a cleaner and more interpretable inverted image (Figure 4.55). The interpreted dip fields, however, are not entirely accurate. That is why when I increase the strength of dip filtering, the image residual becomes bigger, and more coherent signal, which are likely primary reflections, is left in the residual (Figures 4.58(e) and 4.58(f)). As a result, the inverted images with excessive preconditioning (Figure 4.57) do not fit the migrated image very well.

It is worthwhile to point out that the dip filter used in this chapter smooths

along only one dominant dip direction at each spatial location. Therefore, if faults or unconformities are present to cause events having conflicting dips (in this particular example, however, events with conflicting dips are more likely to be artifacts instead of faults or unconformities), they may be attenuated after preconditioning, given that the interpreted dip fields do not conform to the faulting directions or the directions of unconformities. This limitation, however, can be overcome by preconditioning the gradient with two (or more) dip filters at each spatial location, which smooth along not only the dominant, but also the secondary, or even the third dip directions.

As a further comparison, Figure 4.59 plots the convergence curve of the image misfit (the first term in equation 4.28) for different inversion methods. As expected, inversion without any regularization, which fits the migrated image most closely, has the smallest image misfit, whereas inversion preconditioned with strong dip filters, which fits the image least closely, has the biggest image misfit.

As a final comparison, Figures 4.60 and 4.61 present the migration image (Figure 4.46) after applying automatic gain control (AGC) and the same migration image after both weak dip filtering and AGC, respectively, whereas Figures 4.62 and 4.63 show the damped inverse image (Figure 4.48) and the dip-constrained inverse image (Figure 4.55), both after applying the same AGC as in Figures 4.60 and 4.61. Apparently, AGC alone is able to balance the amplitudes in the migration image (Figure 4.60), but it also creates amplitude distortions, especially in areas of extremely low illumination (circled areas in Figure 4.60(b)). The continuities of reflectors are not improved by AGC. Dip-filtered migration image after AGC (Figure 4.61), on the other hand, shows significantly improved reflector continuities, but degraded spatial resolution. It is interesting to note that Figure 4.61 also shows enhanced discontinuities, e.g. at inline 8.5 km in Figure 4.61(a) and the circled areas in Figure 4.61(b). Interpreters would easily interpret these discontinuities as faults. However, if we compare Figures 4.61 and 4.46 carefully, we may realize that these discontinuities appear systematically in areas where the illumination is extremely poor. Therefore, they are more likely to be artifacts as a result of poor illumination, instead of faults.

In contrast, both inverse images (Figures 4.62 and 4.63) show improved spatial

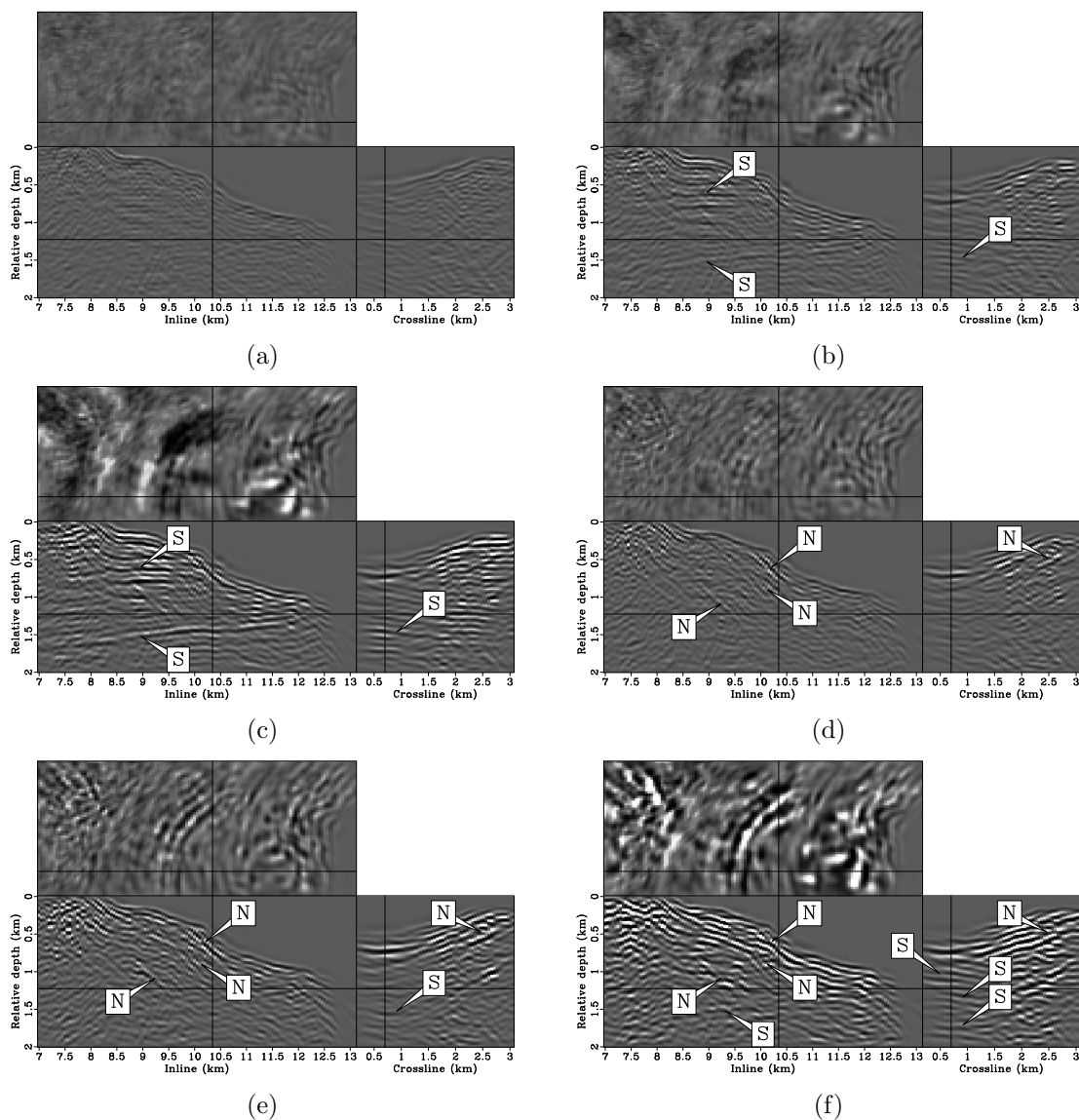


Figure 4.58: The image residual ($\mathbf{Hm} - \mathbf{m}_{\text{mig}}$) at the last iteration for different methods. Panel (a) is obtained using inversion without regularization. Panels (b) and (c) are obtained using inversion regularized by a damping term with $\varepsilon = 0.02$ and $\varepsilon = 0.05$, respectively. Panels (d), (e) and (f) are obtained using inversion preconditioned with weak, moderate and strong dip filtering, respectively. All panels are clipped to the same value. Symbol “S” denotes coherent signal, whereas “N” denotes coherent noise. [CR] chap4/. rd0,rd1,rd2,rd3,rd4,rd5

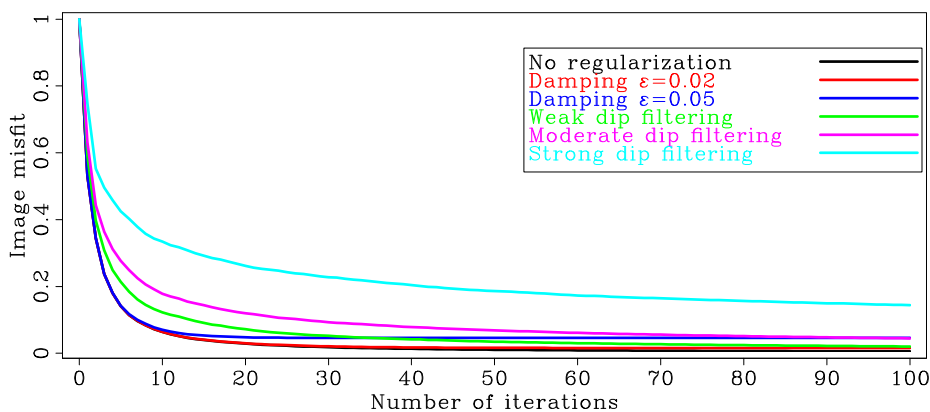
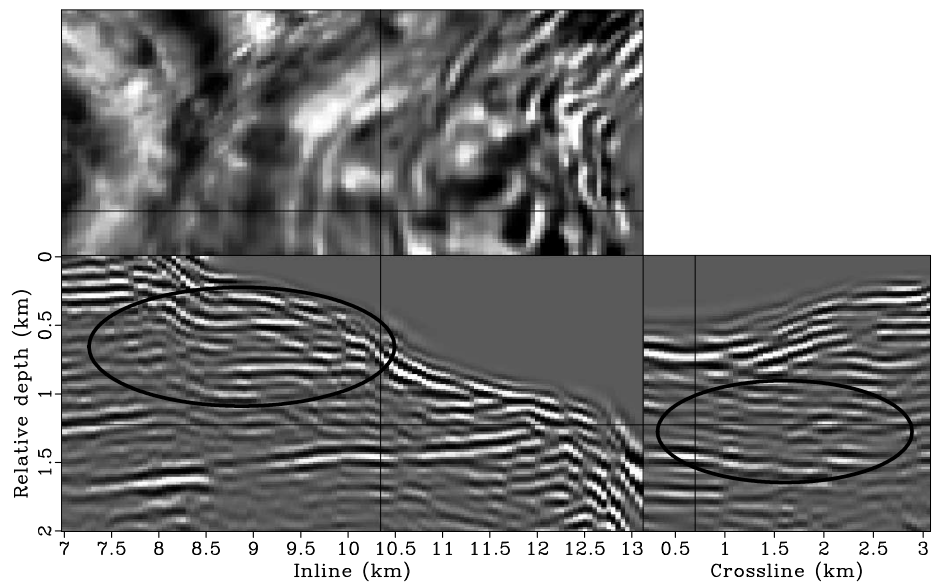


Figure 4.59: Evolution of the image misfit ($\frac{1}{2} \|\mathbf{H}\mathbf{m} - \mathbf{m}_{\text{mig}}\|^2$) for different inversion methods. [CR] chap4/. lsm3d-fobj

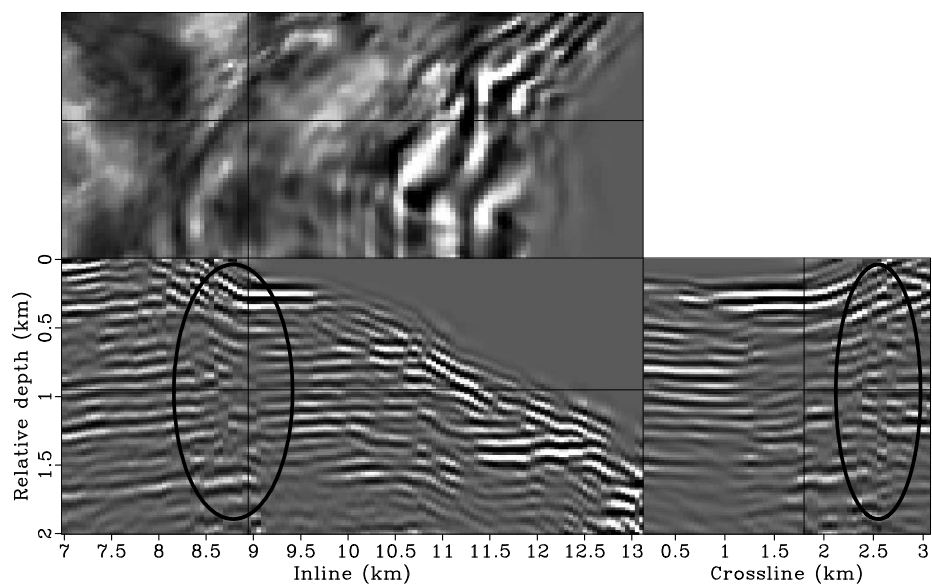
resolution; the amplitudes are more balanced than those in Figures 4.60 and 4.61. Apparently, AGC has little effects on inverse images if we compare Figures 4.62 and 4.63 with Figures 4.48 and 4.55. Note that both inversions do not produce the artificial discontinuities as seen in Figure 4.61. This suggests the importance of data fitting (really image fitting here). Therefore, the inverse image should have theoretically more accurate amplitudes comparing to migration image with AGC, which has less physical meaning. Comparing to damped inverse image (Figure 4.62), reflectors in the dip-constrained inverse image (Figure 4.63) are more continuous because of the dip regularization. Also note that the coherent reflector at around depth 0.75 km inside the circle in the inline section of Figures 4.62 and 4.63, which is not properly imaged by the migration operator (Figures 4.60 and 4.61), is now clearly and cleanly imaged by inversion, especially in Figure 4.63.

CONCLUSIONS

In this chapter, I extend the target-oriented inversion methodology to 3-D and apply it to a 3-D field data set for subsalt imaging. I first recover the subsalt velocities using target-oriented wavefield tomography and then recover the reflectivities using target-oriented wavefield least-squares migration.



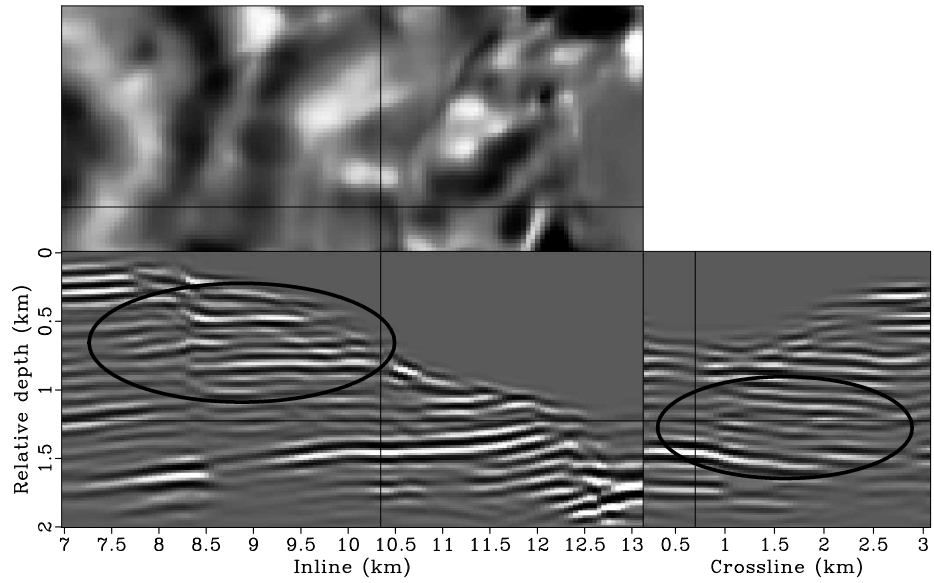
(a)



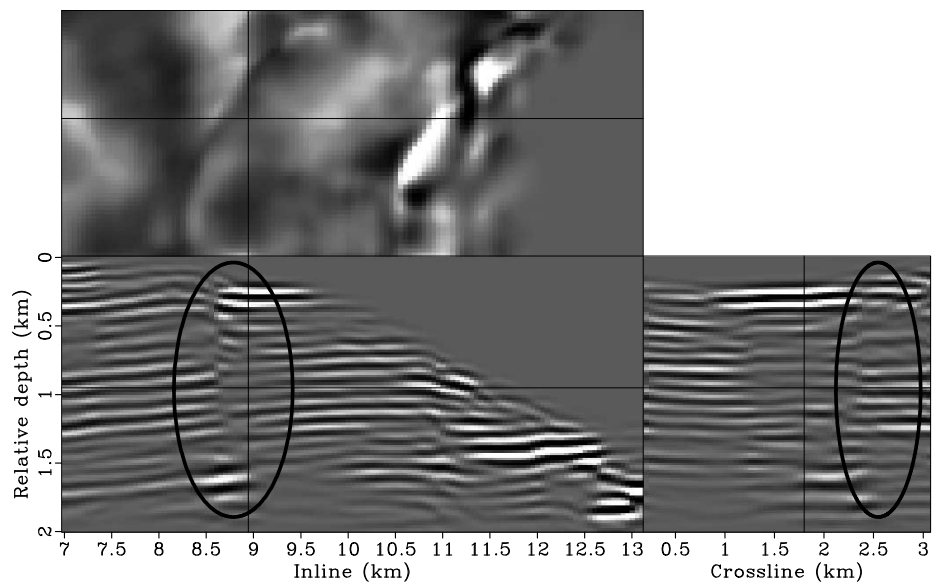
(b)

Figure 4.60: The migrated image (Figure 4.46) after applying AGC. Panels (a) and (b) show different slices of the same 3-D cube. [CR]

chap4/. lsm3d-agc-imgagc1,lsm3d-agc-imgagc2

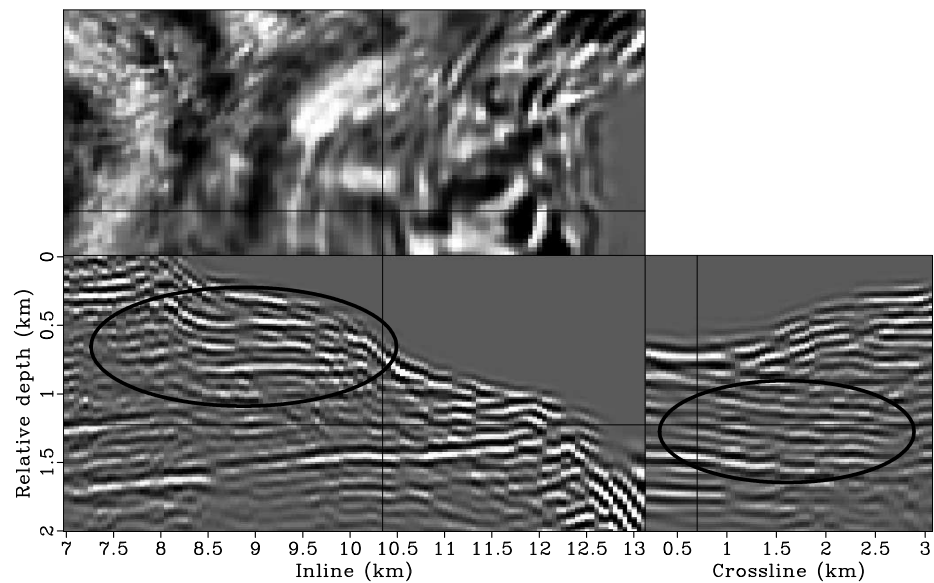


(a)

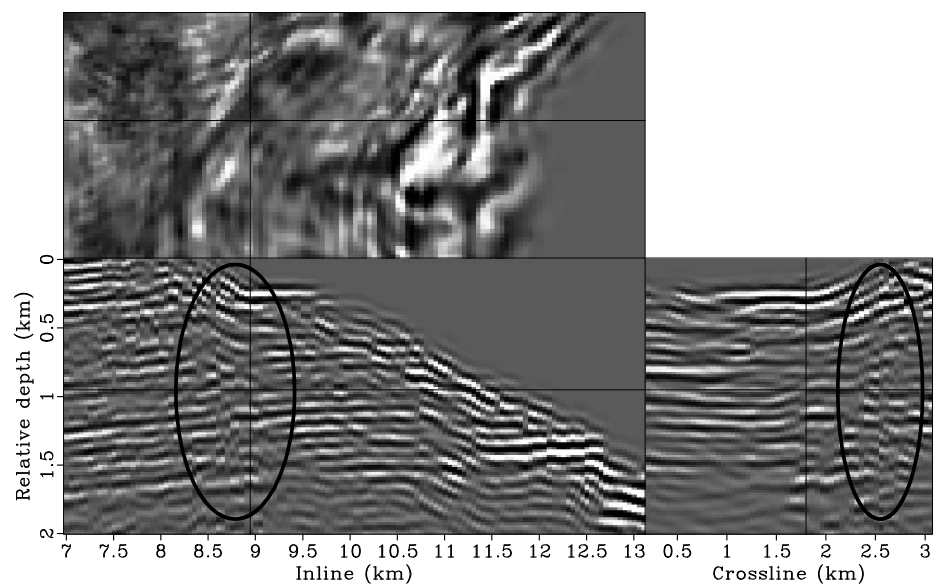


(b)

Figure 4.61: The migrated image (Figure 4.46) after applying both weak dip filtering and AGC. Panels (a) and (b) show different slices of the same 3-D cube. [CR] chap4/. lsm3d-agc-imgdip1,lsm3d-agc-imgdip2

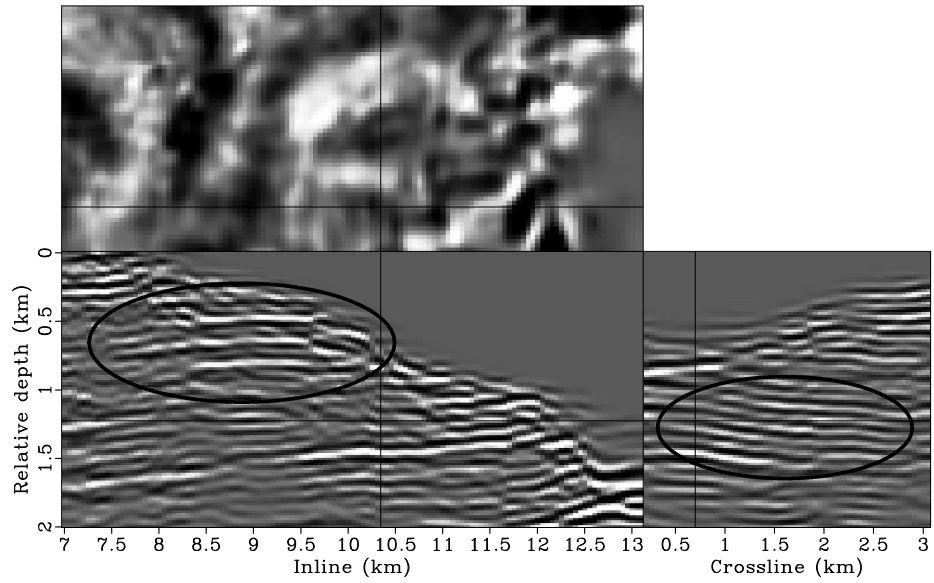


(a)

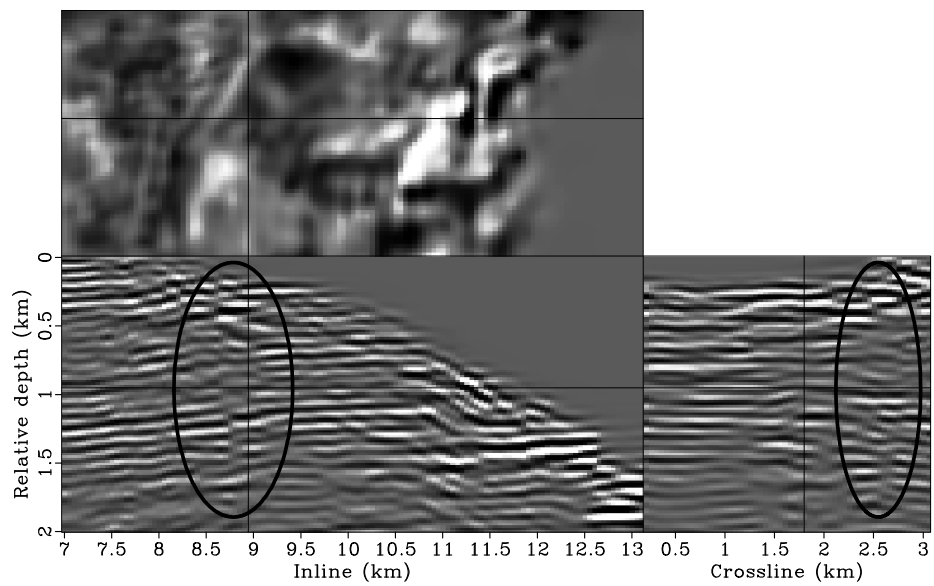


(b)

Figure 4.62: The inverted image with damping regularization (Figure 4.48) after applying AGC. Panels (a) and (b) show different slices of the same 3-D cube. [CR] chap4/. lsm3d-agc-invdam1,lsm3d-agc-invdam2



(a)



(b)

Figure 4.63: The inverted image with weak dip preconditioning (Figure 4.55) after applying AGC. Panels (a) and (b) show different slices of the same 3-D cube. [CR] chap4/. lsm3d-agc-invdp1,lsm3d-agc-invdp2

Target-oriented wavefield tomography is made possible by synthesizing a 3-D Born plane-wave data set for a specific target region. The synthesized new data set is much smaller than the surface-recorded data set, but it contains all the necessary velocity information. For the 3-D example shown in this chapter, this strategy reduces the data size for velocity analysis by about two orders of magnitude. With 280 CPUs (35 nodes with 8 cores on each), each iteration of velocity inversion takes about 2 hours, and I was able to obtain the inversion result in 4 days (40 iterations). Considering the computing resources available in the industry, it is possible to obtain the inversion result in real time and achieve the goal of interactive velocity model-building. Besides the computational gain, the excellent velocity inversion result of the 3-D field-data example demonstrates that target-oriented wavefield tomography can provide reliable velocity updates, even starting from a velocity model far from being accurate. The final migrated image obtained using the updated velocity model shows significant improvement over the initial image.

Solving wavefield least-squares migration in the image domain makes possible target-oriented application of this method, allowing reflectivity inversion at the reservoir level. The 3-D examples in the second half of this chapter demonstrate that simultaneous phase-encoding in the conical-wave domain drastically reduces the computational cost of the 3-D Hessian matrix. The phase-encoded Hessian, albeit with some approximations, accurately quantifies the illumination effects on the migrated image. Since inverting the Hessian is very fast, different regularization parameters or schemes can be tried at very low cost. For the 3-D example shown in this chapter, it takes only about 6 minutes to run 100 iterations using 34 CPUs (17 nodes with 2 cores on each). This is a very important advantage over the conventional data-domain implementation, which requires full-domain modeling and migration at each iteration. The high efficiency of this method also makes interactive reflectivity imaging possible, where we can repeat the inversion with regularizations that incorporate different geological scenarios and obtain the results in real time. The 3-D reflectivity inversion results illustrate that inversion preconditioned with dip filters successfully recovers the reflectivity from the effects of uneven illumination, yielding more balanced amplitudes and higher spatial resolution in the inverted image.

ACKNOWLEDGMENTS

I thank Gboyega Ayeni for insightful discussions about dip filtering. I thank BP and ExxonMobil for providing the field data set. I acknowledge the Stanford Center for Computational Earth and Environmental Science for providing computing resources.

Chapter 5

Conclusions

This thesis presents a target-oriented inversion framework that uses wavefields as carriers of information to image complex geological structures in the subsurface. Depth imaging consists of two components: reflectivity imaging and velocity estimation. No accurate imaging is possible without accurate, robust and efficient solutions to both components. I address the problem of reflectivity imaging with *target-oriented wavefield least-squares migration*, and the problem of velocity estimation with *target-oriented wavefield tomography*.

Chapter 2 tackles the uneven illumination problem in reflectivity imaging by least-squares migration. I formulate least-squares migration in the image domain and solve it in a target-oriented fashion. In the image-domain formulation, explicit computation of the Hessian operator is the most important and challenging step. I develop a novel method based on phase encoding to efficiently compute the target-oriented Hessian operator. I demonstrate that the phase-encoded Hessian converges to the exact Hessian either deterministically (for plane-wave phase encoding) or statistically (for random phase encoding), while having the important advantages that no Green's functions need to be stored during computation and that the number of wavefield propagations is also drastically reduced. I also demonstrate that the rows of the Hessian can be considered as resolution functions, which measure the illumination

deficiency of the imaging system and hence contain all necessary information for illumination correction. 2-D synthetic examples show that least-squares migration with phase-encoded Hessian can optimally recover reflectivities from the effects of uneven illumination.

Chapter 3 develops a novel strategy to improve the efficiency and flexibility of wavefield-based migration velocity analysis. In this method, I design new data sets specifically for velocity analysis. I describe all necessary steps to generate kinematically correct wavefields so that the synthesized new data sets maintain the same velocity information as in the original data. I show that the new data set can be much smaller than the original surface-recorded data set, because it can be synthesized in a target-oriented fashion by focusing on areas where velocities are inaccurate. I also show that the modeling is very flexible and no reflector-picking is necessary, but picking can be easily incorporated if it is desired. The reduction in data size and computational domain significantly increase the efficiency and flexibility of wavefield-based tomography. I show with 2-D synthetic and field-data examples that the computational cost of wavefield tomography can be reduced by one or two orders of magnitude.

Chapter 4 applies the theory developed in the previous chapters to a 3-D field data set acquired from the Gulf of Mexico (GOM). The complex salt body and limited acquisition geometry present challenges for accurate imaging below the salt. I update the subsalt velocity in a target-oriented fashion by synthesizing a 3-D Born plane-wave data set. The new data set is about two orders of magnitude smaller than the original data set. The excellent velocity inversion results prove the effectiveness of target-oriented wavefield tomography. In the subsequent reflectivity inversion, I precondition wavefield least-squares migration with dip filters, which naturally incorporate interpreted geological information. The 3-D examples show that imaging by regularized inversion can successfully recover reflectivities from the effects of uneven illumination, yielding images with more balanced amplitudes and higher spatial resolution.

Numerical examples presented in Chapter 4 also prove the efficiency of the proposed inversion methodology, which formulates wavefield inversion as a local problem, instead of a global problem. As demonstrated in this thesis, most of the computation in the target-oriented inversion framework, such as synthesizing a new data set for velocity estimation and computing the Hessian for reflectivity imaging, is done up front; the subsequent velocity and reflectivity inversion is actually very efficient and costs little. For a typical 3-D data set, such as the GOM data set used in Chapter 4, I am able to finish the velocity inversion for 40 iterations in only a few days in an academic-scale computing environment. The reflectivity inversion is even faster, where I am able to obtain the inversion result for 100 iterations in several minutes. With the computing resources available in industry, I project both velocity and reflectivity inversion can be finished in seconds, making interactive wavefield-based inversion possible.

Appendix A

Convergence property of plane-wave phase encoding

This appendix demonstrates that the plane-wave phase-encoded Hessians converge to the exact Hessian by integrating over the ray parameter(s). As in Chapter 2, the receiver-side plane-wave phase-encoded Hessian for a single receiver-ray parameter $\mathbf{p}_r = (p_{r_x}, p_{r_y})$ takes the form:

$$\begin{aligned} \tilde{H}(\mathbf{x}, \mathbf{x}', \mathbf{p}_r) = & \sum_{\omega} \omega^4 \sum_{\mathbf{x}_s} |f_s(\omega)|^2 A_r^2(\omega) G(\mathbf{x}, \mathbf{x}_s, \omega) G^*(\mathbf{x}', \mathbf{x}_s, \omega) \\ & \times \sum_{\mathbf{x}_r} W(\mathbf{x}_r, \mathbf{x}_s) G(\mathbf{x}, \mathbf{x}_r, \omega) e^{i\omega \mathbf{p}_r \cdot \mathbf{x}_r} \\ & \times \sum_{\mathbf{x}'_r} W(\mathbf{x}'_r, \mathbf{x}_s) G^*(\mathbf{x}', \mathbf{x}'_r, \omega) e^{-i\omega \mathbf{p}_r \cdot \mathbf{x}'_r}. \end{aligned} \quad (\text{A.1})$$

Integrating over \mathbf{p}_r from $-\infty$ to $+\infty$, and changing the order of integration and summation, we have

$$\begin{aligned}
\tilde{H}(\mathbf{x}, \mathbf{x}') &= \int_{-\infty}^{+\infty} \tilde{H}(\mathbf{x}, \mathbf{x}', \mathbf{p}_r) d\mathbf{p}_r \\
&= \sum_{\omega} \omega^4 \sum_{\mathbf{x}_s} |f_s(\omega)|^2 A_r^2(\omega) G(\mathbf{x}, \mathbf{x}_s, \omega) G^*(\mathbf{x}', \mathbf{x}_s, \omega) \\
&\quad \times \sum_{\mathbf{x}_r} W(\mathbf{x}_r, \mathbf{x}_s) G(\mathbf{x}, \mathbf{x}_r, \omega) \sum_{\mathbf{x}'_r} W(\mathbf{x}'_r, \mathbf{x}_s) G^*(\mathbf{x}', \mathbf{x}'_r, \omega) \\
&\quad \times \int_{-\infty}^{+\infty} e^{-i\omega \mathbf{p}_r \cdot (\mathbf{x}'_r - \mathbf{x}_r)} d\mathbf{p}_r. \tag{A.2}
\end{aligned}$$

Note that

$$\int_{-\infty}^{+\infty} e^{-i\omega \mathbf{p}_r \cdot (\mathbf{x}'_r - \mathbf{x}_r)} d\mathbf{p}_r = \frac{1}{|\omega|} \delta(\mathbf{x}'_r - \mathbf{x}_r) \tag{A.3}$$

in 2-D and

$$\int_{-\infty}^{+\infty} e^{-i\omega \mathbf{p}_r \cdot (\mathbf{x}'_r - \mathbf{x}_r)} d\mathbf{p}_r = \frac{1}{|\omega|^2} \delta(\mathbf{x}'_r - \mathbf{x}_r) \tag{A.4}$$

in 3-D. Thus, if we choose the real function $A_r(\omega)$ such that it satisfies $A_r^2(\omega) = |\omega|$ in 2-D and $A_r^2(\omega) = |\omega|^2$ in 3-D, then we get

$$\tilde{H}(\mathbf{x}, \mathbf{x}') = H(\mathbf{x}, \mathbf{x}'). \tag{A.5}$$

We can perform a similar analysis on the simultaneously plane-wave phase-encoded Hessian, which takes the form

$$\begin{aligned}
\tilde{\tilde{H}}(\mathbf{x}, \mathbf{x}', \mathbf{p}_s, \mathbf{p}_r) &= \sum_{\omega} \omega^4 |f_s(\omega)|^2 A_s^2(\omega) A_r^2(\omega) \\
&\quad \times \sum_{\mathbf{x}_s} W_s(\mathbf{x}_s) G(\mathbf{x}, \mathbf{x}_s, \omega) e^{i\omega \mathbf{p}_s \cdot \mathbf{x}_s} \sum_{\mathbf{x}'_s} W_s(\mathbf{x}'_s) G^*(\mathbf{x}', \mathbf{x}'_s, \omega) e^{-i\omega \mathbf{p}_s \cdot \mathbf{x}'_s} \\
&\quad \times \sum_{\mathbf{x}_r} W_r(\mathbf{x}_r) G(\mathbf{x}, \mathbf{x}_r, \omega) e^{i\omega \mathbf{p}_r \cdot \mathbf{x}_r} \sum_{\mathbf{x}'_r} W_r(\mathbf{x}'_r) G^*(\mathbf{x}', \mathbf{x}'_r, \omega) e^{-i\omega \mathbf{p}_r \cdot \mathbf{x}'_r}. \tag{A.6}
\end{aligned}$$

Integrating over $\mathbf{p}_s = (p_{s_x}, p_{s_y})$ and $\mathbf{p}_r = (p_{r_x}, p_{r_y})$, and changing the order of summation and integration, we get

$$\begin{aligned}
\tilde{H}(\mathbf{x}, \mathbf{x}') &= \int_{-\infty}^{+\infty} \int_{-\infty}^{+\infty} \tilde{H}(\mathbf{x}, \mathbf{x}', \mathbf{p}_s, \mathbf{p}_r) d\mathbf{p}_s d\mathbf{p}_r \\
&= \sum_{\omega} \omega^4 |f_s(\omega)|^2 A_s^2(\omega) A_r^2(\omega) \\
&\quad \times \sum_{\mathbf{x}_s} W_s(\mathbf{x}_s) G(\mathbf{x}, \mathbf{x}_s, \omega) \sum_{\mathbf{x}'_s} W_s(\mathbf{x}'_s) G^*(\mathbf{x}', \mathbf{x}'_s, \omega) \\
&\quad \times \int_{-\infty}^{+\infty} e^{-i\omega \mathbf{p}_s \cdot (\mathbf{x}'_s - \mathbf{x}_s)} d\mathbf{p}_s \\
&\quad \times \sum_{\mathbf{x}_r} W_r(\mathbf{x}_r) G(\mathbf{x}, \mathbf{x}_r, \omega) \sum_{\mathbf{x}'_r} W_r(\mathbf{x}'_r) G^*(\mathbf{x}', \mathbf{x}'_r, \omega) \\
&\quad \times \int_{-\infty}^{+\infty} e^{-i\omega \mathbf{p}_r \cdot (\mathbf{x}'_r - \mathbf{x}_r)} d\mathbf{p}_r. \tag{A.7}
\end{aligned}$$

Once again note that

$$\int_{-\infty}^{+\infty} e^{-i\omega \mathbf{p}_s \cdot (\mathbf{x}'_s - \mathbf{x}_s)} d\mathbf{p}_s = \frac{1}{|\omega|} \delta(\mathbf{x}'_s - \mathbf{x}_s), \tag{A.8}$$

$$\int_{-\infty}^{+\infty} e^{-i\omega \mathbf{p}_r \cdot (\mathbf{x}'_r - \mathbf{x}_r)} d\mathbf{p}_r = \frac{1}{|\omega|} \delta(\mathbf{x}'_r - \mathbf{x}_r), \tag{A.9}$$

in 2-D and

$$\int_{-\infty}^{+\infty} e^{-i\omega \mathbf{p}_s \cdot (\mathbf{x}'_s - \mathbf{x}_s)} d\mathbf{p}_s = \frac{1}{|\omega|^2} \delta(\mathbf{x}'_s - \mathbf{x}_s), \tag{A.10}$$

$$\int_{-\infty}^{+\infty} e^{-i\omega \mathbf{p}_r \cdot (\mathbf{x}'_r - \mathbf{x}_r)} d\mathbf{p}_r = \frac{1}{|\omega|^2} \delta(\mathbf{x}'_r - \mathbf{x}_r), \tag{A.11}$$

in 3-D. Thus, if we choose real functions $A_s(\omega)$ and $A_r(\omega)$ satisfying $A_s^2(\omega) = |\omega|$, $A_r^2(\omega) = |\omega|$ in 2-D and $A_s^2(\omega) = |\omega|^2$, $A_r^2(\omega) = |\omega|^2$ in 3-D, then we have

$$\tilde{H}(\mathbf{x}, \mathbf{x}') = H(\mathbf{x}, \mathbf{x}'). \tag{A.12}$$

Appendix B

Convergence property of random phase encoding

This appendix demonstrates that the crosstalk in the randomly phase-encoded Hessians statistically converges to zero when the random-phase encoding function(s) are properly chosen. From Chapter 2, the crosstalk in the receiver-side randomly phase-encoded Hessian takes the following form:

$$\begin{aligned} C_r(\mathbf{x}, \mathbf{x}') = & \sum_{\omega} \omega^4 \sum_{\mathbf{x}_s} |f_s(\omega)|^2 G(\mathbf{x}, \mathbf{x}_s, \omega) G^*(\mathbf{x}', \mathbf{x}_s, \omega) \\ & \times \sum_{\mathbf{x}_r} \sum_{\mathbf{x}'_r \neq \mathbf{x}_r} W(\mathbf{x}_r, \mathbf{x}_s) G(\mathbf{x}, \mathbf{x}_r, \omega) W(\mathbf{x}'_r, \mathbf{x}_s) G^*(\mathbf{x}', \mathbf{x}'_r, \omega) \\ & \times \sum_{\mathbf{p}_r} \alpha(\mathbf{x}_r, \mathbf{p}_r, \omega) \alpha^*(\mathbf{x}'_r, \mathbf{p}_r, \omega), \end{aligned} \quad (\text{B.1})$$

where α is the random-phase encoding function, defined as follows

$$\alpha(\mathbf{x}_r, \mathbf{p}_r, \omega) = \frac{1}{\sqrt{N_{\text{realize}}}} e^{i\gamma(\mathbf{x}_r, \mathbf{p}_r, \omega)}, \quad (\text{B.2})$$

where $\gamma(\mathbf{x}_r, \mathbf{p}_r, \omega)$ is a random sequence as a function of both receiver location \mathbf{x}_r and frequency ω , with \mathbf{p}_r as its realization index. If we generate $\gamma(\mathbf{x}_r, \mathbf{p}_r, \omega)$ such that

it is independent of $\gamma(\mathbf{x}'_r, \mathbf{p}_r, \omega)$ when $\mathbf{x}_r \neq \mathbf{x}'_r$, then $\alpha(\mathbf{x}_r, \mathbf{p}_r, \omega)$ is also independent of $\alpha(\mathbf{x}'_r, \mathbf{p}_r, \omega)$ when $\mathbf{x}_r \neq \mathbf{x}'_r$. Therefore, the expectation of $\alpha(\mathbf{x}_r, \mathbf{p}_r, \omega)\alpha^*(\mathbf{x}'_r, \mathbf{p}_r, \omega)$ can be written as follows:

$$E[\alpha(\mathbf{x}_r, \mathbf{p}_r, \omega)\alpha^*(\mathbf{x}'_r, \mathbf{p}_r, \omega)] = E[\alpha(\mathbf{x}_r, \mathbf{p}_r, \omega)]E^*[\alpha(\mathbf{x}'_r, \mathbf{p}_r, \omega)]. \quad (\text{B.3})$$

We choose γ to be an independent, uniformly distributed random sequence from 0 to 2π . In the discrete case, the sample space of γ is

$$\left\{ 0, \frac{2\pi}{N_r}, \frac{4\pi}{N_r}, \dots, \frac{2(N_r - 1)\pi}{N_r} \right\}, \quad (\text{B.4})$$

where N_r is the number of receivers. Since γ is uniformly distributed, the probability of γ taking each value in the sample space is $\frac{1}{N_r}$. Therefore, the expectation of $\alpha(\mathbf{x}_r, \mathbf{p}_r, \omega)$ can be calculated as follows (Gray and Davisson, 2003):

$$E[\alpha(\mathbf{x}_r, \mathbf{p}_r, \omega)] = \sum_{k=1}^{N_r} \frac{1}{N_r} e^{i\frac{2(k-1)\pi}{N_r}} = \frac{1}{N_r} \frac{1 - \left(e^{i\frac{2\pi}{N_r}}\right)^{N_r}}{1 - e^{i\frac{2\pi}{N_r}}} = 0. \quad (\text{B.5})$$

Substituting equation B.5 into equation B.3 yields

$$E[\alpha(\mathbf{x}_r, \mathbf{p}_r, \omega)\alpha^*(\mathbf{x}'_r, \mathbf{p}_r, \omega)] = 0 \quad (\text{B.6})$$

According to the law of large numbers—the ensemble average of a random sequence converges to its expectation (Gray and Davisson, 2003)—the crosstalk $C_r(\mathbf{x}, \mathbf{x}')$ in equation B.1, which is the average of the random variable $\alpha(\mathbf{x}_r, \mathbf{p}_r, \omega)\alpha^*(\mathbf{x}'_r, \mathbf{p}_r, \omega)$ over sources, receivers, frequencies and random realizations, converges to the expectation of $\alpha(\mathbf{x}_r, \mathbf{p}_r, \omega)\alpha^*(\mathbf{x}'_r, \mathbf{p}_r, \omega)$, which is zero.

For the simultaneously encoded Hessian, the crosstalk reads

$$\begin{aligned}
C_{sr}(\mathbf{x}, \mathbf{x}') &= \sum_{\omega} \omega^4 |f_s(\omega)|^2 \sum_{\mathbf{x}_s} \sum_{\mathbf{x}'_s \neq \mathbf{x}_s} W(\mathbf{x}_s) G(\mathbf{x}, \mathbf{x}_s, \omega) W(\mathbf{x}'_s) G^*(\mathbf{x}', \mathbf{x}'_s, \omega) \\
&\quad \times \sum_{\mathbf{p}_s} \beta(\mathbf{x}_s, \mathbf{p}_s, \omega) \beta^*(\mathbf{x}'_s, \mathbf{p}_s, \omega) \\
&\quad \times \sum_{\mathbf{x}_r} \sum_{\mathbf{x}'_r \neq \mathbf{x}_r} W(\mathbf{x}_r) G(\mathbf{x}, \mathbf{x}_r, \omega) W(\mathbf{x}'_r) G^*(\mathbf{x}', \mathbf{x}'_r, \omega) \\
&\quad \times \sum_{\mathbf{p}_r} \alpha(\mathbf{x}_r, \mathbf{p}_r, \omega) \alpha^*(\mathbf{x}'_r, \mathbf{p}_r, \omega), \tag{B.7}
\end{aligned}$$

where we have an additional source-side random-phase encoding function β defined by

$$\beta(\mathbf{x}_r, \mathbf{p}_r, \omega) = \frac{1}{\sqrt{N_{\text{realize}}}} e^{i\gamma(\mathbf{x}_s, \mathbf{p}_s, \omega)}, \tag{B.8}$$

where $\gamma(\mathbf{x}_s, \mathbf{p}_s, \omega)$ is chosen to be an independent, uniformly distributed random sequence from 0 to 2π , and \mathbf{p}_s is the realization index for the source-side encoding function. The same analysis that we have applied to the receiver-side encoding function can also be applied to the source-side encoding function. Consequently, we obtain

$$E[\beta(\mathbf{x}_s, \mathbf{p}_s, \omega)] = 0. \tag{B.9}$$

If we generate $\gamma(\mathbf{x}_s, \mathbf{p}_s, \omega)$ to be independent of $\gamma(\mathbf{x}_r, \mathbf{p}_r, \omega)$, then we have

$$\begin{aligned}
&E[\alpha(\mathbf{x}_r, \mathbf{p}_r, \omega) \alpha^*(\mathbf{x}'_r, \mathbf{p}_r, \omega) \beta(\mathbf{x}_s, \mathbf{p}_s, \omega) \beta^*(\mathbf{x}'_s, \mathbf{p}_s, \omega)] \\
&= E[\alpha(\mathbf{x}_r, \mathbf{p}_r, \omega)] E^*[\alpha(\mathbf{x}'_r, \mathbf{p}_r, \omega)] E[\beta(\mathbf{x}_s, \mathbf{p}_s, \omega)] E^*[\beta(\mathbf{x}'_s, \mathbf{p}_s, \omega)] \\
&= 0. \tag{B.10}
\end{aligned}$$

Therefore $C_{sr}(\mathbf{x}, \mathbf{x}')$ also converges to zero statistically, according to the law of large numbers. However, the convergence of $C_{sr}(\mathbf{x}, \mathbf{x}')$ can be slower than the convergence of $C_r(\mathbf{x}, \mathbf{x}')$, because it has more crosstalk terms generated by encoding the sources.

From the above analysis, we can also see that the crosstalk C_r and C_{sr} always converge to zero statistically as long as α and β have zero expectations. Therefore, the random phase function γ does not have to be uniformly distributed. It can take any distribution, as long as the expectations of α and β are zero.

Appendix C

Wave-equation tomographic operator

This appendix demonstrates how to evaluate the forward and adjoint tomographic operator based on the single-square-root (SSR) extrapolator. Derivation of the tomographic operator based on the double-square-root (DSR) extrapolator can be found in Sava (2004); Biondi (2006). I derive the tomographic operator using perturbation theory. An alternative derivation can be carried out through an augmented functional analysis (Shen, 2004; Plessix, 2006).

In SSR migration, the migrated image at each depth level can be obtained by correlating the forward-propagated source wavefield with the backward-propagated receiver wavefield as follows:

$$m_z(\mathbf{x}, \mathbf{h}) = \sum_{\text{shots}} \sum_{\omega} U_z^s(\mathbf{x} - \mathbf{h}) U_z^r(\mathbf{x} + \mathbf{h}), \quad (\text{C.1})$$

where $\mathbf{x} = (x, y)$ is the horizontal spatial location vector, $\mathbf{h} = (h_x, h_y)$ is the subsurface offset; and m_z is the image at depth z . U_z^s and U_z^r are the source and receiver wavefields at depth z , respectively. For conciseness, I omit the dependencies of both wavefields on frequency ω and shots.

The source and receiver wavefields satisfy the following depth recursion

$$\begin{cases} \mathbf{U}_{z+\Delta z}^s = \mathbf{E}_z \mathbf{U}_z^s \\ \mathbf{U}_{z=z_{\min}}^s = \overline{\mathbf{f}}_s \end{cases}, \quad (\text{C.2})$$

and

$$\begin{cases} \mathbf{U}_{z+\Delta z}^r = \mathbf{E}_z \mathbf{U}_z^r \\ \mathbf{U}_{z=z_{\min}}^r = \mathbf{d}_{\text{obs}} \end{cases}, \quad (\text{C.3})$$

where \mathbf{U}_z^s , $\mathbf{U}_{z+\Delta z}^s$ and \mathbf{U}_z^r , $\mathbf{U}_{z+\Delta z}^r$ are the source and receiver wavefields at depth z and $z + \Delta z$, respectively. They are vectors containing the wavefields at all horizontal locations for specific depth levels. In equation C.2, \mathbf{f}_s is the source vector serving as the boundary condition for extrapolating the source wavefield; the overline on \mathbf{f}_s in equation C.2 denotes taking complex conjugate. On the other hand, equation C.3 uses the observed data vector, \mathbf{d}_{obs} , as the boundary condition to extrapolate the receiver wavefield. For point-source migration, \mathbf{f}_s and \mathbf{d}_{obs} are the point sources and the corresponding point-source gathers; for plane-wave migration, \mathbf{f}_s and \mathbf{d}_{obs} become the plane-wave sources and the corresponding plane-wave source gathers. In both equations C.2 and C.3, \mathbf{E}_z is the SSR operator defined as follows:

$$\mathbf{E}_z = e^{-ik_z(\mathbf{v}_z)\Delta z} = e^{-i\sqrt{\omega^2/\mathbf{v}_z^2 + \nabla^2}}, \quad (\text{C.4})$$

where \mathbf{v}_z is the velocity at depth z , k_z is the vertical wavenumber, and $\nabla^2 = \frac{\partial^2}{\partial x^2} + \frac{\partial^2}{\partial y^2}$ is the Laplacian operator.

Application of the forward tomographic operator

We first examine how to evaluate the forward tomographic operator. The perturbed image as a result of velocity perturbation can be derived by a simple application of

the chain rule to equation C.1:

$$\Delta m_z(\mathbf{x}, \mathbf{h}) = \sum_{\text{shots}} \sum_{\omega} \left[\Delta U_z^s(\mathbf{x} - \mathbf{h}) \widehat{U}_z^r(\mathbf{x} + \mathbf{h}) + \widehat{U}_z^s(\mathbf{x} - \mathbf{h}) \Delta U_z^r(\mathbf{x} + \mathbf{h}) \right], \quad (\text{C.5})$$

where \widehat{U}_z^s and \widehat{U}_z^r are the background source and receiver wavefields computed with the background velocity; ΔU_z^s and ΔU_z^r are the perturbed source and receiver wavefields, respectively, the results of the velocity perturbation.

The perturbed source wavefield at some depth level can be derived by perturbing equation C.2:

$$\Delta \mathbf{U}_{z+\Delta z}^s = \widehat{\mathbf{E}}_z \Delta \mathbf{U}_z^s + \Delta \mathbf{E}_z \widehat{\mathbf{U}}_z^s, \quad (\text{C.6})$$

with $\Delta \mathbf{U}_{z=z_{\min}}^s = \mathbf{0}$ as the boundary condition. In equation C.6, $\widehat{\mathbf{U}}_z^s$ is the background source wavefield computed using equation C.2 with the background velocity; $\widehat{\mathbf{E}}_z$ is the extrapolator using the background velocity, and $\Delta \mathbf{E}_z$ represents the perturbed extrapolator, which can be obtained by a formal linearization of the extrapolator (equation C.4) with respect to velocity:

$$\begin{aligned} \mathbf{E}_z = e^{-ik_z(\mathbf{v}_z)\Delta z} &\approx e^{-i\Delta z \widehat{k}_z} + e^{-i\Delta z \widehat{k}_z} \left(-i\Delta z \left. \frac{dk_z}{d\mathbf{v}_z} \right|_{\mathbf{v}_z=\widehat{\mathbf{v}}_z} \right) \Delta \mathbf{v}_z \\ &= \widehat{\mathbf{E}}_z + \widehat{\mathbf{E}}_z \left(-i\Delta z \left. \frac{dk_z}{d\mathbf{v}_z} \right|_{\mathbf{v}_z=\widehat{\mathbf{v}}_z} \right) \Delta \mathbf{v}_z, \end{aligned} \quad (\text{C.7})$$

where $\widehat{k}_z = k_z(\widehat{\mathbf{v}}_z)$ and $\widehat{\mathbf{v}}_z$ is the background velocity at depth z . From equation C.7, the perturbed extrapolator reads as follows:

$$\Delta \mathbf{E}_z = \widehat{\mathbf{E}}_z \left(-i\Delta z \left. \frac{dk_z}{d\mathbf{v}_z} \right|_{\mathbf{v}_z=\widehat{\mathbf{v}}_z} \right) \Delta \mathbf{v}_z. \quad (\text{C.8})$$

Substituting equation C.8 into C.6 yields

$$\Delta \mathbf{U}_{z+\Delta z}^s = \widehat{\mathbf{E}}_z \Delta \mathbf{U}_z^s + \widehat{\mathbf{E}}_z \left(-i\Delta z \left. \frac{dk_z}{d\mathbf{v}_z} \right|_{\mathbf{v}_z=\widehat{\mathbf{v}}_z} \right) \widehat{\mathbf{U}}_z^s \Delta \mathbf{v}_z. \quad (\text{C.9})$$

We can define a scattering operator $\widehat{\mathbf{G}}_z^s$ that interacts with the background source wavefield as follows:

$$\widehat{\mathbf{G}}_z^s = \left(-i\Delta z \frac{dk_z}{dv_z} \Big|_{\mathbf{v}_z = \widehat{\mathbf{v}}_z} \right) \widehat{\mathbf{U}}_z^s = i\Delta z \frac{\omega^2 / \widehat{\mathbf{v}}_z^3}{\sqrt{\omega^2 / \widehat{\mathbf{v}}_z^2 + \nabla^2}} \widehat{\mathbf{U}}_z^s = \frac{i\Delta z \omega^2}{\widehat{k}_z \widehat{\mathbf{v}}_z^3} \widehat{\mathbf{U}}_z^s. \quad (\text{C.10})$$

Then the perturbed source wavefield for depth $z + \Delta z$ can be rewritten as follows:

$$\Delta \mathbf{U}_{z+\Delta z}^s = \widehat{\mathbf{E}}_z \Delta \mathbf{U}_z^s + \widehat{\mathbf{E}}_z \widehat{\mathbf{G}}_z^s \Delta \mathbf{v}_z. \quad (\text{C.11})$$

We can further write out the recursive equation C.11 for all depths in the following matrix form:

$$\begin{pmatrix} \Delta \mathbf{U}_1^s \\ \Delta \mathbf{U}_2^s \\ \Delta \mathbf{U}_3^s \\ \vdots \\ \Delta \mathbf{U}_n^s \end{pmatrix} = \begin{pmatrix} \mathbf{0} & \mathbf{0} & \mathbf{0} & \cdots & \mathbf{0} & \mathbf{0} \\ \widehat{\mathbf{E}}_1 & \mathbf{0} & \mathbf{0} & \cdots & \mathbf{0} & \mathbf{0} \\ \mathbf{0} & \widehat{\mathbf{E}}_2 & \mathbf{0} & \cdots & \mathbf{0} & \mathbf{0} \\ \vdots & \vdots & \vdots & \vdots & \vdots & \vdots \\ \mathbf{0} & \mathbf{0} & \mathbf{0} & \cdots & \widehat{\mathbf{E}}_{n-1} & \mathbf{0} \end{pmatrix} \begin{pmatrix} \Delta \mathbf{U}_1^s \\ \Delta \mathbf{U}_2^s \\ \Delta \mathbf{U}_3^s \\ \vdots \\ \Delta \mathbf{U}_n^s \end{pmatrix} + \begin{pmatrix} \mathbf{0} & \mathbf{0} & \mathbf{0} & \cdots & \mathbf{0} & \mathbf{0} \\ \widehat{\mathbf{E}}_1 & \mathbf{0} & \mathbf{0} & \cdots & \mathbf{0} & \mathbf{0} \\ \mathbf{0} & \widehat{\mathbf{E}}_2 & \mathbf{0} & \cdots & \mathbf{0} & \mathbf{0} \\ \vdots & \vdots & \vdots & \vdots & \vdots & \mathbf{0} \\ \mathbf{0} & \mathbf{0} & \mathbf{0} & \cdots & \widehat{\mathbf{E}}_{n-1} & \mathbf{0} \end{pmatrix} \begin{pmatrix} \widehat{\mathbf{G}}_1^s & \mathbf{0} & \mathbf{0} & \cdots & \mathbf{0} \\ \mathbf{0} & \widehat{\mathbf{G}}_2^s & \mathbf{0} & \cdots & \mathbf{0} \\ \mathbf{0} & \mathbf{0} & \widehat{\mathbf{G}}_3^s & \cdots & \mathbf{0} \\ \vdots & \vdots & \vdots & \vdots & \vdots \\ \mathbf{0} & \mathbf{0} & \mathbf{0} & \cdots & \widehat{\mathbf{G}}_n^s \end{pmatrix} \begin{pmatrix} \Delta \mathbf{v}_1 \\ \Delta \mathbf{v}_2 \\ \Delta \mathbf{v}_3 \\ \vdots \\ \Delta \mathbf{v}_n \end{pmatrix},$$

or in a more compact notation,

$$\Delta \mathbf{U}^s = \widehat{\mathbf{E}} \Delta \mathbf{U}^s + \widehat{\mathbf{E}} \widehat{\mathbf{G}}^s \Delta \mathbf{v}. \quad (\text{C.12})$$

The solution of equation C.12 can be formally written as follows:

$$\Delta \mathbf{U}^s = \left(\mathbf{1} - \widehat{\mathbf{E}} \right)^{-1} \widehat{\mathbf{E}} \widehat{\mathbf{G}}^s \Delta \mathbf{v}, \quad (\text{C.13})$$

where $\mathbf{1}$ is an identity matrix.

Similarly, the perturbed receiver wavefield satisfies the following recursive relation:

$$\Delta \mathbf{U}_{z+\Delta z}^r = \widehat{\mathbf{E}}_z \Delta \mathbf{U}_z^r + \widehat{\mathbf{E}}_z \widehat{\mathbf{G}}_z^r \Delta \mathbf{v}_z, \quad (\text{C.14})$$

where $\widehat{\mathbf{G}}_z^r$ is the scattering operator, which interacts with the background receiver

wavefield as follows:

$$\widehat{\mathbf{G}}_z^r = \left(-i\Delta z \frac{dk_z}{d\mathbf{v}_z} \Big|_{\mathbf{v}_z=\widehat{\mathbf{v}}_z} \right) \widehat{\mathbf{U}}_z^r = i\Delta z \frac{\omega^2/\widehat{\mathbf{v}}_z^3}{\sqrt{\omega^2/\widehat{\mathbf{v}}_z^2 + \nabla^2}} \widehat{\mathbf{U}}_z^r = \frac{i\Delta z \omega^2}{\widehat{k}_z \widehat{\mathbf{v}}_z^3} \widehat{\mathbf{U}}_z^r. \quad (\text{C.15})$$

We can also write out the recursive equation C.14 for all depth levels in the following matrix form:

$$\begin{pmatrix} \Delta \mathbf{U}_1^r \\ \Delta \mathbf{U}_2^r \\ \Delta \mathbf{U}_3^r \\ \vdots \\ \Delta \mathbf{U}_n^r \end{pmatrix} = \begin{pmatrix} \mathbf{0} & \mathbf{0} & \mathbf{0} & \cdots & \mathbf{0} & \mathbf{0} \\ \widehat{\mathbf{E}}_1 & \mathbf{0} & \mathbf{0} & \cdots & \mathbf{0} & \mathbf{0} \\ \mathbf{0} & \widehat{\mathbf{E}}_2 & \mathbf{0} & \cdots & \mathbf{0} & \mathbf{0} \\ \vdots & \vdots & \vdots & \vdots & \vdots & \vdots \\ \mathbf{0} & \mathbf{0} & \mathbf{0} & \cdots & \widehat{\mathbf{E}}_{n-1} & \mathbf{0} \end{pmatrix} \begin{pmatrix} \Delta \mathbf{U}_1^r \\ \Delta \mathbf{U}_2^r \\ \Delta \mathbf{U}_3^r \\ \vdots \\ \Delta \mathbf{U}_n^r \end{pmatrix} + \begin{pmatrix} \mathbf{0} & \mathbf{0} & \mathbf{0} & \cdots & \mathbf{0} & \mathbf{0} \\ \widehat{\mathbf{E}}_1 & \mathbf{0} & \mathbf{0} & \cdots & \mathbf{0} & \mathbf{0} \\ \mathbf{0} & \widehat{\mathbf{E}}_2 & \mathbf{0} & \cdots & \mathbf{0} & \mathbf{0} \\ \vdots & \vdots & \vdots & \vdots & \vdots & \mathbf{0} \\ \mathbf{0} & \mathbf{0} & \mathbf{0} & \cdots & \widehat{\mathbf{E}}_{n-1} & \mathbf{0} \end{pmatrix} \begin{pmatrix} \widehat{\mathbf{G}}_1^r & \mathbf{0} & \mathbf{0} & \cdots & \mathbf{0} \\ \mathbf{0} & \widehat{\mathbf{G}}_2^r & \mathbf{0} & \cdots & \mathbf{0} \\ \mathbf{0} & \mathbf{0} & \widehat{\mathbf{G}}_3^r & \cdots & \mathbf{0} \\ \vdots & \vdots & \vdots & \vdots & \vdots \\ \mathbf{0} & \mathbf{0} & \mathbf{0} & \cdots & \widehat{\mathbf{G}}_n^r \end{pmatrix} \begin{pmatrix} \Delta \mathbf{v}_1 \\ \Delta \mathbf{v}_2 \\ \Delta \mathbf{v}_3 \\ \vdots \\ \Delta \mathbf{v}_n \end{pmatrix},$$

or in a more compact notation,

$$\Delta \mathbf{U}^r = \widehat{\mathbf{E}} \Delta \mathbf{U}^r + \widehat{\mathbf{E}} \widehat{\mathbf{G}}^r \Delta \mathbf{v}. \quad (\text{C.16})$$

The solution of equation C.16 can be formally written as follows:

$$\Delta \mathbf{U}^r = \left(\mathbf{1} - \widehat{\mathbf{E}} \right)^{-1} \widehat{\mathbf{E}} \widehat{\mathbf{G}}^r \Delta \mathbf{v}. \quad (\text{C.17})$$

Once we obtain the scattered source and receiver wavefields using equations C.13 and C.17, we can correlate them with the background source and receiver wavefields (equation C.5) to generate the perturbed image. Apparently, the velocity perturbation $\Delta \mathbf{v}$ is linear with respect to both the perturbed source wavefield $\Delta \mathbf{U}^s$ and the receiver wavefield $\Delta \mathbf{U}^r$, and the correlation in the perturbed imaging condition (equation C.5) is also linear with respect to the scattered wavefields. Therefore, we have derived a linear operator that maps the velocity perturbation to the image perturbation. The pseudo-code for implementing the forward tomographic operator is shown in Algorithm 2.

Algorithm 2 Numerical implementation of the forward tomographic operator

```

for ishot = 1  $\cdots$   $N_s$  do
  for  $\omega = \omega_{\min} \cdots \omega_{\max}$  do
    read  $\mathbf{f}_s$  at  $\omega$  and ishot
    read  $\mathbf{d}_{\text{obs}}$  at  $\omega$  and ishot
     $\widehat{\mathbf{U}}_{z=z_{\min}}^s = \bar{\mathbf{f}}_s$ 
     $\widehat{\mathbf{U}}_{z=z_{\min}}^r = \mathbf{d}_{\text{obs}}$ 
    for  $z = z_{\min} \cdots z_{\max} - \Delta z$  do
      read  $\widehat{\mathbf{v}}_z$  at  $z$ 
       $\widehat{\mathbf{U}}_{z+\Delta z}^s = \widehat{\mathbf{E}}_z \widehat{\mathbf{U}}_z^s$ 
       $\widehat{\mathbf{U}}_{z+\Delta z}^r = \widehat{\mathbf{E}}_z \widehat{\mathbf{U}}_z^r$ 
    end for
     $\Delta \mathbf{U}_{z=z_{\min}}^s = \mathbf{0}$ 
     $\Delta \mathbf{U}_{z=z_{\min}}^r = \mathbf{0}$ 
    for  $z = z_{\min} + \Delta z \cdots z_{\max}$  do
      read  $\widehat{\mathbf{v}}_{z-\Delta z}$  at  $z - \Delta z$ 
      read  $\Delta \mathbf{v}_{z-\Delta z}$  at  $z - \Delta z$ 
      read  $\Delta \mathbf{m}_z$  at  $z$ 
       $\Delta \mathbf{U}_{z-\Delta z}^s + = \widehat{\mathbf{G}}_{z-\Delta z}^s \Delta \mathbf{v}_z$ 
       $\Delta \mathbf{U}_{z-\Delta z}^r + = \widehat{\mathbf{G}}_{z-\Delta z}^r \Delta \mathbf{v}_z$ 
       $\Delta \mathbf{U}_z^s = \widehat{\mathbf{E}}_{z-\Delta z} \Delta \mathbf{U}_{z-\Delta z}^s$ 
       $\Delta \mathbf{U}_z^r = \widehat{\mathbf{E}}_{z-\Delta z} \Delta \mathbf{U}_{z-\Delta z}^r$ 
      for  $\mathbf{x} = \mathbf{x}_{\min} \cdots \mathbf{x}_{\max}$  do
        for  $\mathbf{h} = \mathbf{h}_{\min} \cdots \mathbf{h}_{\max}$  do
           $\Delta m_z(\mathbf{x}, \mathbf{h}) + = U_z^s(\mathbf{x} - \mathbf{h}) U_z^r(\mathbf{x} + \mathbf{h})$ 
        end for
      end for
      write  $\Delta \mathbf{m}_z$  at  $z$ 
    end for
  end for
end for

```

Application of the adjoint tomographic operator

Now let us examine how to evaluate the adjoint tomographic operator. Since the velocity perturbation $\Delta \mathbf{v}$ is linearly related to the perturbed wavefields, $\Delta \mathbf{U}^s$ and $\Delta \mathbf{U}^r$, to obtain the back-projected velocity perturbation, we first compute the back-projected perturbed wavefields from the perturbed image $\Delta \mathbf{m}$. The back-projected perturbed source and receiver wavefields at each depth level are obtained by using the adjoint of the imaging condition (equation C.5) as follows:

$$\Delta U_z^s(\mathbf{x} - \mathbf{h}) = \overline{\widehat{U}_z^r(\mathbf{x} + \mathbf{h})} \Delta m_z(\mathbf{x}, \mathbf{h}), \quad (\text{C.18})$$

and

$$\Delta U_z^r(\mathbf{x} + \mathbf{h}) = \overline{\widehat{U}_z^s(\mathbf{x} - \mathbf{h})} \Delta m_z(\mathbf{x}, \mathbf{h}), \quad (\text{C.19})$$

where the overlines denote taking complex conjugate. Then the adjoint equations of C.13 and C.17 are used to get the back-projected velocity perturbation $\Delta \mathbf{v}$.

Let us first look at the adjoint equation of C.13, which can be written as follows:

$$\Delta \mathbf{v}^s = (\widehat{\mathbf{G}}^s)^* \widehat{\mathbf{E}}^* (\mathbf{1} - \widehat{\mathbf{E}}^*)^{-1} \Delta \mathbf{U}^s, \quad (\text{C.20})$$

where $*$ denotes taking the adjoint. To recursively solve the above equation, we define a temporary wavefield $\Delta \mathbf{P}^s$ that satisfies the following equation:

$$\Delta \mathbf{P}^s = \widehat{\mathbf{E}}^* (\mathbf{1} - \widehat{\mathbf{E}}^*)^{-1} \Delta \mathbf{U}^s. \quad (\text{C.21})$$

After some simple algebra, the above equation can be rewritten as follows:

$$\Delta \mathbf{P}^s = \widehat{\mathbf{E}}^* \Delta \mathbf{P}^s + \widehat{\mathbf{E}}^* \Delta \mathbf{U}^s, \quad (\text{C.22})$$

or in recursive form for all depths:

$$\begin{pmatrix} \Delta \mathbf{P}_1^s \\ \Delta \mathbf{P}_2^s \\ \Delta \mathbf{P}_3^s \\ \vdots \\ \Delta \mathbf{P}_n^s \end{pmatrix} = \begin{pmatrix} 0 & \widehat{\mathbf{E}}_1^* & 0 & \cdots & 0 & 0 \\ 0 & 0 & \widehat{\mathbf{E}}_2^* & \cdots & 0 & 0 \\ 0 & 0 & 0 & \cdots & 0 & 0 \\ \vdots & \vdots & \vdots & \ddots & \vdots & \vdots \\ 0 & 0 & 0 & \cdots & 0 & 0 \end{pmatrix} \begin{pmatrix} \Delta \mathbf{P}_1^s \\ \Delta \mathbf{P}_2^s \\ \Delta \mathbf{P}_3^s \\ \vdots \\ \Delta \mathbf{P}_n^s \end{pmatrix} + \begin{pmatrix} 0 & \widehat{\mathbf{E}}_1^* & 0 & \cdots & 0 & 0 \\ 0 & 0 & \widehat{\mathbf{E}}_2^* & \cdots & 0 & 0 \\ 0 & 0 & 0 & \cdots & 0 & 0 \\ \vdots & \vdots & \vdots & \ddots & \vdots & \vdots \\ 0 & 0 & 0 & \cdots & 0 & 0 \end{pmatrix} \begin{pmatrix} \Delta \mathbf{U}_1^s \\ \Delta \mathbf{U}_2^s \\ \Delta \mathbf{U}_3^s \\ \vdots \\ \Delta \mathbf{U}_n^s \end{pmatrix}.$$

Therefore, $\Delta \mathbf{P}^s$ can be obtained by recursive upward continuation, where the back-projected source-wavefield perturbation $\Delta \mathbf{U}^s$ is injected at each depth level. The back-projected velocity perturbation from the perturbed source wavefield is then obtained by applying the adjoint of the scattering operator $\widehat{\mathbf{G}}^s$ to the wavefield $\Delta \mathbf{P}^s$ as follows:

$$\Delta \mathbf{v}^s = (\widehat{\mathbf{G}}^s)^* \Delta \mathbf{P}^s, \quad (\text{C.23})$$

or:

$$\begin{pmatrix} \Delta \mathbf{v}_1^s \\ \Delta \mathbf{v}_2^s \\ \Delta \mathbf{v}_3^s \\ \vdots \\ \Delta \mathbf{v}_n^s \end{pmatrix} = \begin{pmatrix} (\widehat{\mathbf{G}}_1^s)^* & 0 & 0 & \cdots & 0 \\ 0 & (\widehat{\mathbf{G}}_2^s)^* & 0 & \cdots & 0 \\ 0 & 0 & (\widehat{\mathbf{G}}_3^s)^* & \cdots & 0 \\ \vdots & \vdots & \vdots & \ddots & \vdots \\ 0 & 0 & 0 & \cdots & (\widehat{\mathbf{G}}_n^s)^* \end{pmatrix} \begin{pmatrix} \Delta \mathbf{P}_1^s \\ \Delta \mathbf{P}_2^s \\ \Delta \mathbf{P}_3^s \\ \vdots \\ \Delta \mathbf{P}_n^s \end{pmatrix}. \quad (\text{C.24})$$

Similarly, the adjoint equation of C.17 reads as follows:

$$\Delta \mathbf{v}^r = (\widehat{\mathbf{G}}^r)^* \widehat{\mathbf{E}}^* (\mathbf{1} - \widehat{\mathbf{E}}^*)^{-1} \Delta \mathbf{U}^r. \quad (\text{C.25})$$

We can also define a temporary wavefield $\Delta \mathbf{P}^r$ that satisfies the following equation:

$$\Delta \mathbf{P}^r = \widehat{\mathbf{E}}^* (\mathbf{1} - \widehat{\mathbf{E}}^*)^{-1} \Delta \mathbf{U}^r. \quad (\text{C.26})$$

After rewriting it, we get the following relation:

$$\Delta \mathbf{P}^r = \widehat{\mathbf{E}}^* \Delta \mathbf{P}^r + \widehat{\mathbf{E}}^* \Delta \mathbf{U}^r, \quad (\text{C.27})$$

or in recursive form for all depths:

$$\begin{pmatrix} \Delta \mathbf{P}_1^r \\ \Delta \mathbf{P}_2^r \\ \Delta \mathbf{P}_3^r \\ \vdots \\ \Delta \mathbf{P}_n^r \end{pmatrix} = \begin{pmatrix} \mathbf{0} & \widehat{\mathbf{E}}_1^* & \mathbf{0} & \cdots & \mathbf{0} & \mathbf{0} \\ \mathbf{0} & \mathbf{0} & \widehat{\mathbf{E}}_2^* & \cdots & \mathbf{0} & \mathbf{0} \\ \mathbf{0} & \mathbf{0} & \mathbf{0} & \cdots & \mathbf{0} & \mathbf{0} \\ \vdots & \vdots & \vdots & \ddots & \vdots & \vdots \\ \mathbf{0} & \mathbf{0} & \mathbf{0} & \cdots & \mathbf{0} & \widehat{\mathbf{E}}_{n-1}^* \end{pmatrix} \begin{pmatrix} \Delta \mathbf{P}_1^r \\ \Delta \mathbf{P}_2^r \\ \Delta \mathbf{P}_3^r \\ \vdots \\ \Delta \mathbf{P}_n^r \end{pmatrix} + \begin{pmatrix} \mathbf{0} & \widehat{\mathbf{E}}_1^* & \mathbf{0} & \cdots & \mathbf{0} & \mathbf{0} \\ \mathbf{0} & \mathbf{0} & \widehat{\mathbf{E}}_2^* & \cdots & \mathbf{0} & \mathbf{0} \\ \mathbf{0} & \mathbf{0} & \mathbf{0} & \cdots & \mathbf{0} & \mathbf{0} \\ \vdots & \vdots & \vdots & \ddots & \vdots & \vdots \\ \mathbf{0} & \mathbf{0} & \mathbf{0} & \cdots & \mathbf{0} & \widehat{\mathbf{E}}_{n-1}^* \end{pmatrix} \begin{pmatrix} \Delta \mathbf{U}_1^r \\ \Delta \mathbf{U}_2^r \\ \Delta \mathbf{U}_3^r \\ \vdots \\ \Delta \mathbf{U}_n^r \end{pmatrix},$$

where $\Delta \mathbf{P}^r$ is also obtained by recursive upward continuation with injection of the back-projected receiver-wavefield perturbation $\Delta \mathbf{U}^r$ at each depth level.

The back-projected velocity perturbation from the perturbed receiver wavefield is then obtained by applying the adjoint of the scattering operator $\widehat{\mathbf{G}}^r$ to the wavefield $\Delta \mathbf{P}^r$ as follows:

$$\Delta \mathbf{v}^r = (\widehat{\mathbf{G}}^r)^* \Delta \mathbf{P}^r, \quad (\text{C.28})$$

or:

$$\begin{pmatrix} \Delta \mathbf{v}_1^r \\ \Delta \mathbf{v}_2^r \\ \Delta \mathbf{v}_3^r \\ \vdots \\ \Delta \mathbf{v}_n^r \end{pmatrix} = \begin{pmatrix} (\widehat{\mathbf{G}}_1^r)^* & \mathbf{0} & \mathbf{0} & \cdots & \mathbf{0} \\ \mathbf{0} & (\widehat{\mathbf{G}}_2^r)^* & \mathbf{0} & \cdots & \mathbf{0} \\ \mathbf{0} & \mathbf{0} & (\widehat{\mathbf{G}}_3^r)^* & \cdots & \mathbf{0} \\ \vdots & \vdots & \vdots & \ddots & \vdots \\ \mathbf{0} & \mathbf{0} & \mathbf{0} & \cdots & (\widehat{\mathbf{G}}_n^r)^* \end{pmatrix} \begin{pmatrix} \Delta \mathbf{P}_1^r \\ \Delta \mathbf{P}_2^r \\ \Delta \mathbf{P}_3^r \\ \vdots \\ \Delta \mathbf{P}_n^r \end{pmatrix}. \quad (\text{C.29})$$

The total back-projected slowness perturbation is obtained by adding $\Delta \mathbf{v}^s$ and $\Delta \mathbf{v}^r$ together, and summing contributions from all frequencies and shots:

$$\Delta \mathbf{v} = \sum_{\omega} \sum_{\text{shots}} (\Delta \mathbf{v}^s + \Delta \mathbf{v}^r). \quad (\text{C.30})$$

The pseudo-code for implementing the adjoint tomographic operator is shown in Algorithm 3.

Algorithm 3 Numerical implementation of the adjoint tomographic operator

```

for ishot = 1  $\cdots$   $N_s$  do
  for  $\omega = \omega_{\min} \cdots \omega_{\max}$  do
    read  $\mathbf{f}_s$  at  $\omega$  and ishot
    read  $\mathbf{d}_{\text{obs}}$  at  $\omega$  and ishot
     $\widehat{\mathbf{U}}_{z=z_{\min}}^s = \mathbf{f}_s$ 
     $\widehat{\mathbf{U}}_{z=z_{\min}}^r = \mathbf{d}_{\text{obs}}$ 
    for  $z = z_{\min} \cdots z_{\max} - \Delta z$  do
      read  $\widehat{\mathbf{v}}_z$  at  $z$ 
       $\widehat{\mathbf{U}}_{z+\Delta z}^s = \widehat{\mathbf{E}}_z \widehat{\mathbf{U}}_z^s$ 
       $\widehat{\mathbf{U}}_{z+\Delta z}^r = \widehat{\mathbf{E}}_z \widehat{\mathbf{U}}_z^r$ 
    end for
     $\Delta \mathbf{U}_{z=z_{\max}}^s = \mathbf{0}$ 
     $\Delta \mathbf{U}_{z=z_{\max}}^r = \mathbf{0}$ 
    for  $z = z_{\max} - \Delta z \cdots z_{\min}$  do
      read  $\widehat{\mathbf{v}}_z$  at  $z$ 
      read  $\Delta \mathbf{v}_z$  at  $z$ 
      read  $\Delta \mathbf{m}_{z+\Delta z}$  at  $z + \Delta z$ 
      for  $\mathbf{x} = \mathbf{x}_{\min} \cdots \mathbf{x}_{\max}$  do
        for  $\mathbf{h} = \mathbf{h}_{\min} \cdots \mathbf{h}_{\max}$  do
           $\Delta U_{z+\Delta z}^s(\mathbf{x} - \mathbf{h})_+ = \overline{U_{z+\Delta z}^r(\mathbf{x} + \mathbf{h})} m_{z+\Delta z}(\mathbf{x}, \mathbf{h})$ 
           $\Delta U_{z+\Delta z}^r(\mathbf{x} + \mathbf{h})_+ = \overline{U_{z+\Delta z}^s(\mathbf{x} - \mathbf{h})} m_{z+\Delta z}(\mathbf{x}, \mathbf{h})$ 
        end for
      end for
       $\Delta \mathbf{U}_z^s = \widehat{\mathbf{E}}_z^* \Delta \mathbf{U}_{z+\Delta z}^s$ 
       $\Delta \mathbf{U}_z^r = \widehat{\mathbf{E}}_z^* \Delta \mathbf{U}_{z+\Delta z}^r$ 
       $\mathbf{v}_{z+} = (\widehat{\mathbf{G}}^s)^* \Delta \mathbf{U}_z^s$ 
       $\mathbf{v}_{z+} = (\widehat{\mathbf{G}}^r)^* \Delta \mathbf{U}_z^r$ 
      write  $\Delta \mathbf{v}_z$  at  $z$ 
    end for
  end for
end for

```

Appendix D

3-D conical-wave migration

This appendix demonstrates that the acquisition mask operator can be ignored when calculating the gradient of equation 4.6. As in Chapter 4, the gradient of equation 4.6 is

$$m(\mathbf{x}, \mathbf{h}) = \sum_{\omega} |\omega|^3 \sum_{y_s} \sum_{p_{s_x}} \sum_{\mathbf{x}_r} G^*(\mathbf{x} + \mathbf{h}, \mathbf{x}_r, \omega) d_{\text{obs}}(\mathbf{x}_r, p_{s_x}, y_s, \omega) \sum_{x_s} W^*(\mathbf{x}_r, x_s, y_s) f_s^*(\omega) G^*(\mathbf{x} - \mathbf{h}, x_s, y_s, \omega) e^{-i\omega p_{s_x} x_s}, \quad (\text{D.1})$$

where $d_{\text{obs}}(\mathbf{x}_r, p_{s_x}, y_s, \omega)$ is the data after the 3-D conical-wave transform obtained as follows:

$$d_{\text{obs}}(\mathbf{x}_r, p_{s_x}, y_s, \omega) = \sum_{x_s} W(\mathbf{x}_r, x_s, y_s) d_{\text{obs}}(\mathbf{x}_r, x_s, y_s, \omega) e^{i\omega p_{s_x} x_s}. \quad (\text{D.2})$$

If we ignore the acquisition mask operator W in equation D.1, we obtain

$$\dot{m}(\mathbf{x}, \mathbf{h}) = \sum_{\omega} |\omega|^3 \sum_{y_s} \sum_{p_{s_x}} \sum_{\mathbf{x}_r} G^*(\mathbf{x} + \mathbf{h}, \mathbf{x}_r, \omega) d_{\text{obs}}(\mathbf{x}_r, p_{s_x}, y_s, \omega) \sum_{x_s} f_s^*(\omega) G^*(\mathbf{x} - \mathbf{h}, x_s, y_s, \omega) e^{-i\omega p_{s_x} x_s}. \quad (\text{D.3})$$

Now I demonstrate the equivalence of equations D.1 and D.3 by showing that both equations converge to the same well-known shot-profile migration, provided that the inline ray parameter p_{s_x} is sufficiently well sampled. Substituting equation D.2 into D.1 and rearranging the order of summation yield

$$\begin{aligned}
m(\mathbf{x}, \mathbf{h}) &= \sum_{\omega} |\omega|^3 \sum_{y_s} \sum_{\mathbf{x}_r} G^*(\mathbf{x} + \mathbf{h}, \mathbf{x}_r, \omega) \\
&\times \sum_{x_s} W^*(\mathbf{x}_r, x_s, y_s) f_s^*(\omega) G^*(\mathbf{x} - \mathbf{h}, x_s, y_s, \omega) \\
&\times \sum_{x'_s} W(\mathbf{x}_r, x'_s, y_s) d_{\text{obs}}(\mathbf{x}_r, x'_s, y_s, \omega) \sum_{p_{s_x}} e^{-i\omega p_{s_x}(x_s - x'_s)}. \quad (\text{D.4})
\end{aligned}$$

If the inline ray parameter p_{s_x} is sufficiently well sampled, we approximately have

$$\sum_{p_{s_x}} e^{-i\omega p_{s_x}(x_s - x'_s)} \approx \frac{1}{|\omega|} \delta(x_s - x'_s). \quad (\text{D.5})$$

Since the acquisition mask operator is a diagonal matrix, it has the following property:

$$W(\mathbf{x}_r, x_s, y_s) = W^*(\mathbf{x}_r, x_s, y_s) = W^2(\mathbf{x}_r, x_s, y_s). \quad (\text{D.6})$$

Substituting equations D.5 and D.6 into D.4 yields the well-known shot-profile migration

$$\begin{aligned}
m(\mathbf{x}, \mathbf{h}) &\approx \sum_{\omega} |\omega|^2 \sum_{y_s} \sum_{x_s} f_s^*(\omega) G^*(\mathbf{x} - \mathbf{h}, x_s, y_s, \omega) \\
&\times \sum_{\mathbf{x}_r} W^*(\mathbf{x}_r, x_s, y_s) G^*(\mathbf{x} + \mathbf{h}, \mathbf{x}_r, \omega) d_{\text{obs}}(\mathbf{x}_r, x_s, y_s, \omega). \quad (\text{D.7})
\end{aligned}$$

Similarly, substituting equation D.2 into D.3 yields

$$\begin{aligned}
\mathring{m}(\mathbf{x}, \mathbf{h}) &= \sum_{\omega} |\omega|^3 \sum_{y_s} \sum_{\mathbf{x}_r} G^*(\mathbf{x} + \mathbf{h}, \mathbf{x}_r, \omega) \\
&\times \sum_{x_s} f_s^*(\omega) G^*(\mathbf{x} - \mathbf{h}, x_s, y_s, \omega) \\
&\times \sum_{x'_s} W(\mathbf{x}_r, x'_s, y_s) d_{\text{obs}}(\mathbf{x}_r, x'_s, y_s, \omega) \sum_{p_{sx}} e^{-i\omega p_{sx}(x_s - x'_s)}. \quad (\text{D.8})
\end{aligned}$$

Using equations D.5 and D.6, equation D.8 also converges to the shot-profile migration:

$$\begin{aligned}
\mathring{m}(\mathbf{x}, \mathbf{h}) &\approx \sum_{\omega} |\omega|^2 \sum_{y_s} \sum_{x_s} f_s^*(\omega) G^*(\mathbf{x} - \mathbf{h}, x_s, y_s, \omega) \\
&\times \sum_{\mathbf{x}_r} W^*(\mathbf{x}_r, x_s, y_s) G^*(\mathbf{x} + \mathbf{h}, \mathbf{x}_r, \omega) d_{\text{obs}}(\mathbf{x}_r, x_s, y_s, \omega). \quad (\text{D.9})
\end{aligned}$$

Therefore, the acquisition mask operator can be ignored in equation 4.9 in Chapter 4.

Appendix E

Seismic visibility analysis

Seismic visibility is defined to be the intensity of the reflection wavefield recorded at the receivers, which can provide a quantitative estimate of which part of the data contributes most to the target region for a given prestack acquisition geometry (Jin and Xu, 2010). Instead of using only the zero-subsurface-offset reflectivity image for modeling, as in Jin and Xu (2010), I extend it to include modeling of nonzero subsurface-offset images to take into account the inaccuracies in velocities. I develop the theory for both point- and plane-wave-source acquisition geometries.

POINT-SOURCE CASE

For acquisition geometry using point sources, the synthesized data d_{point} using generalized Born wavefield modeling (Chapter 3) is

$$d_{\text{point}}(\mathbf{x}_r, \mathbf{x}_s, \omega) = \sum_{\mathbf{x}} \sum_{\mathbf{h}} \omega^2 f_s(\omega) G(\mathbf{x} - \mathbf{h}, \mathbf{x}_s, \omega) G(\mathbf{x} + \mathbf{h}, \mathbf{x}_r, \omega) m(\mathbf{x}, \mathbf{h}), \quad (\text{E.1})$$

where ω is the frequency and $f_s(\omega)$ is the source function; $m(\mathbf{x}, \mathbf{h})$ is the target reflectivity model parameterized as a function of both spatial coordinates $\mathbf{x} = (x, y, z)$ and the subsurface offset $\mathbf{h} = (h_x, h_y, 0)$; G is the Green's function; \mathbf{x}_s and \mathbf{x}_r are the source and receiver locations, respectively.

Seismic visibility is defined to be the intensity of d_{point} as follows:

$$Q_{\text{point}}(\mathbf{x}_r, \mathbf{x}_s, \omega) = |d_{\text{point}}(\mathbf{x}_r, \mathbf{x}_s, \omega)|^2, \quad (\text{E.2})$$

The seismic visibility Q_{point} is a five dimensional object, which is a function of source position, receiver position and frequency. The average source visibility is defined to be the average of Q_{point} over all receiver positions as follows:

$$Q_{\text{point}}^s(\mathbf{x}_s, \omega) = \sum_{\mathbf{x}_r} Q_{\text{point}}(\mathbf{x}_r, \mathbf{x}_s, \omega). \quad (\text{E.3})$$

Similarly, the average receiver visibility is defined to be the average of Q_{point} over all source positions as follows:

$$Q_{\text{point}}^r(\mathbf{x}_r, \omega) = \sum_{\mathbf{x}_s} Q_{\text{point}}(\mathbf{x}_r, \mathbf{x}_s, \omega). \quad (\text{E.4})$$

PLANE-WAVE-SOURCE CASE

For acquisition geometry using plane-wave sources, the synthesized data can be expressed as follows:

$$d_{\text{plane}}(\mathbf{x}_r, \mathbf{p}_s, \omega) = \sum_{\mathbf{x}} \sum_{\mathbf{h}} \omega^2 f_s(\omega) G(\mathbf{x} - \mathbf{h}, \mathbf{p}_s, \omega) G(\mathbf{x} + \mathbf{h}, \mathbf{x}_r, \omega) m(\mathbf{x}, \mathbf{h}), \quad (\text{E.5})$$

where $\mathbf{p}_s = (p_{s_x}, p_{s_y})$ is the horizontal component of the ray parameter for the plane-wave sources, and $G(\mathbf{x}, \mathbf{p}_s, \omega)$ is the plane-wave domain Green's function defined as follows:

$$G(\mathbf{x}, \mathbf{p}_s, \omega) = \sum_{\mathbf{x}_s} G(\mathbf{x}, \mathbf{x}_s, \omega) e^{i\omega \mathbf{p}_s \cdot \mathbf{x}_s}. \quad (\text{E.6})$$

Therefore, the plane-wave domain visibility is

$$Q_{\text{plane}}(\mathbf{x}_r, \mathbf{p}_s, \omega) = |d_{\text{plane}}(\mathbf{x}_r, \mathbf{p}_s, \omega)|^2. \quad (\text{E.7})$$

The average source visibility reads

$$Q_{\text{plane}}^s(\mathbf{p}_s, \omega) = \sum_{\mathbf{x}_r} Q_{\text{plane}}(\mathbf{x}_r, \mathbf{p}_s, \omega), \quad (\text{E.8})$$

and the average receiver visibility reads

$$Q_{\text{plane}}^r(\mathbf{x}_r, \omega) = \sum_{\mathbf{p}_s} Q_{\text{plane}}(\mathbf{x}_r, \mathbf{p}_s, \omega). \quad (\text{E.9})$$

Figure 4.10 in Chapter 4 shows the 3-D plane-wave-domain average source visibility $Q_{\text{plane}}^s(\mathbf{p}_s, \omega)$.

Bibliography

- Al-Yahya, K., 1989, Velocity analysis by iterative profile migration: *Geophysics*, **54**, 718–729.
- Albertin, U., P. Sava, J. Etgen, and M. Maharramov, 2006, Adjoint wave-equation velocity analysis: *SEG Technical Program Expanded Abstracts*, **25**, 3345–3349.
- Albertin, U., D. Yingst, P. Kitchenside, and V. Tcheverda, 2004, True-amplitude beam migration: *SEG Technical Program Expanded Abstracts*, **23**, 949–952.
- Artman, B., G. Alvarez, and K. Matson, 2007, Image-space surface-related multiple prediction: *Geophysics*, **72**, S113–S122.
- Ayeni, G., Y. Tang, and B. Biondi, 2009, Joint preconditioned least-squares inversion of simultaneous source time-lapse seismic data sets: *SEG Technical Program Expanded Abstracts*, **28**, 3914–3918.
- Beasley, C. J., 2008, A new look at marine simultaneous sources: *The Leading Edge*, **27**, 914–917.
- Beasley, C. J., R. E. Chambers, and Z. Jiang, 1998, A new look at simultaneous sources: *SEG Technical Program Expanded Abstracts*, **17**, 133–135.
- Berkhout, A. J. G., 2008, Changing the mindset in seismic data acquisition: *The Leading Edge*, **27**, 924–938.
- Beylkin, G., 1985, Imaging of discontinuities in the inverse scattering problem by inversion of a causal generalized radon transform: *J. Math. Phys.*, **26**, 99–108.
- Biondi, B., 1990, Seismic velocity estimation by beam stack: PhD thesis, Stanford University.
- , 2002, Stable wide-angle Fourier finite-difference downward extrapolation of 3-D wavefields: *Geophysics*, **67**, 872–882.

- , 2006, Prestack exploding-reflectors modeling for migration velocity analysis: SEG Technical Program Expanded Abstracts, **25**, 3056–3060.
- , 2007, Prestack modeling of image events for migration velocity analysis: **SEP-131**, 101–118.
- Biondi, B., S. Fomel, and N. Chemingui, 1998, Azimuth moveout for 3-D prestack imaging: *Geophysics*, **63**, 574–588.
- Biondi, B. and P. Sava, 1999, Wave-equation migration velocity analysis: SEG Technical Program Expanded Abstracts, **18**, 1723–1726.
- Biondi, B. and W. W. Symes, 2004, Angle-domain common-image gathers for migration velocity analysis by wavefield-continuation imaging: *Geophysics*, **69**, 1283–1298.
- Bishop, T. N., K. P. Bube, R. T. Cutler, R. T. Langan, P. L. Love, J. R. Resnick, R. T. Shuey, D. A. Spindler, and H. W. Wyld, 1985, Tomographic determination of velocity and depth in laterally varying media: *Geophysics*, **50**, 903–923.
- Bleistein, N. and H. Jaramillo, H., 2000, A platform for Kirchhoff data mapping in scalar models of data acquisition: *Geophysical Prospecting*, **48**, 135–161.
- Bunks, C., F. M. Saleck, S. Zaleski, and G. Chavent, 1995, Multiscale seismic waveform inversion: *Geophysics*, **60**, 1457–1473.
- Chavent, G. and E. Clement, 1993, Waveform inversion through MBTT formulation: Institut National de Recherche en Informatique et Automatique Report, 1839.
- Chavent, G. and R.-E. Plessix, 1999, An optimal true-amplitude least-squares prestack depth-migration operator: *Geophysics*, **64**, 508–515.
- Claerbout, J., 1998, Multidimensional recursive filters via a helix: *Geophysics*, **63**, 1532–1541.
- Claerbout, J. F., 1971, Toward a unified theory of reflector mapping: *Geophysics*, **36**, 467–481.
- , 1985, *Imaging the earth's interior*: Blackwell Scientific Publication.
- , 1992, *Earth soundings analysis: Processing versus inversion*: Blackwell Scientific Publication.
- , 2008, *Image estimation by example: Geophysical sounding image construction: Multidimensional autoregression*: Stanford University.

- Clapp, M. L., 2005, Imaging under salt: Illumination compensation by regularized inversion: PhD thesis, Stanford University.
- Clapp, R., 2003, Geologically constrained migration velocity analysis: PhD thesis, Stanford University.
- Clayton, R. W. and R. H. Stolt, 1981, A Born-WKBJ inversion method for acoustic reflection data: *Geophysics*, **46**, 1559–1567.
- Docherty, P., 1991, A brief comparison of some Kirchhoff integral formulas for migration and inversion: *Geophysics*, **56**, 1164–1169.
- Duquet, B. and P. Lailly, 2006, Efficient 3D wave-equation migration using virtual planar sources: *Geophysics*, **71**, S185–S197.
- Duquet, B., P. Lailly, and A. Ehinger, 2001, 3D plane wave migration of streamer data: *SEG Technical Program Expanded Abstracts*, **20**, 1033–1036.
- Etgen, J. T., 1993, Interval velocity estimation using residual prestack migration: *SEG Technical Program Expanded Abstracts*, **12**, 669–672.
- , 2005, How many angles do we really need for delayed-shot migration?: *SEG Technical Program Expanded Abstracts*, **24**, 1985–1988.
- Fei, W. and P. Williamson, 2010, On the gradient artifacts in migration velocity analysis based on differential semblance optimization: *SEG Technical Program Expanded Abstracts*, **29**, 4071–4076.
- Fei, W., P. Williamson, and A. Khoury, 2009, 3-D common-azimuth wave-equation migration velocity analysis: *SEG Technical Program Expanded Abstracts*, **28**, 2283–2287.
- Fomel, S., P. Sava, J. Rickett, and J. F. Claerbout, 2003, The Wilson–Burg method of spectral factorization with application to helical filtering: *Geophysical Prospecting*, **51**, 409–420.
- Gelius, L.-J., I. Lecomte, and H. Tabti, 2002, Analysis of the resolution function in seismic prestack imaging: *Geophysical Prospecting*, **50**, 505–515.
- Gray, R. and L. D. Davisson, 2003, *Introduction to statistical signal processing*: Cambridge University Press.
- Guerra, C., 2010, Migration-velocity analysis using image-space generalized wavefields: PhD thesis, Stanford University.

- Guerra, C., Y. Tang, and B. Biondi, 2009, Wave-equation tomography using image-space phase encoded data: SEG Technical Program Expanded Abstracts, **28**, 3964–3968.
- Guillon, A., 2004, Amplitude and kinematic corrections of migrated images for nonunitary imaging operators: *Geophysics*, **69**, 1017–1024.
- Hale, D., 2007, Local dip filtering with directional laplacians: CWP Project Review, **567**, 91–102.
- Hampson, G., J. Stefani, and F. Herkenhoff, 2008, Acquisition using simultaneous sources: *The Leading Edge*, **27**, 918–923.
- Hoffmann, J., 2001, Illumination, resolution, and image quality of PP- and PS-waves for survey planning: *The Leading Edge*, **20**, 1008–1014.
- Howard, M. S. and N. Moldoveanu, 2006, Marine survey design for rich-azimuth seismic using surface streamers: 76rd Ann. Internat. Mtg., Expanded Abstracts, 2915–2919, Soc. of Expl. Geophys.
- Hubral, P., J. Schleicher, and M. Tygel, 1996, A unified approach to 3-D seismic reflection imaging, part I: Basic concepts: *Geophysics*, **61**, 742–758.
- Jannane, M., W. Beydoun, E. Crase, D. Cao, Z. Koren, E. Landa, M. Mendes, A. Pica, M. Noble, G. Roeth, S. Singh, R. Snieder, A. Tarantola, D. Trezeguet, and M. Xie, 1989, Wavelengths of earth structures that can be resolved from seismic reflection data: *Geophysics*, **54**, 906–910.
- Jin, S. and S. Xu, 2010, Visibility analysis for target-oriented reverse time migration and optimizing acquisition parameters: *The Leading Edge*, **29**, 1372–1377.
- Keggin, J., T. Manning, W. Rietveld, C. Page, E. Fromyr, and R. Borselen, 2006, Key aspects of multi-azimuth acquisition and processing: 76rd Ann. Internat. Mtg., Expanded Abstracts, 2886–2890, Soc. of Expl. Geophys.
- Kosloff, D., J. Sherwood, Z. Koren, E. Machet, and Y. Falkovitz, 1996, Velocity and interface depth determination by tomography of depth migrated gathers: *Geophysics*, **61**, 1511–1523.
- Krebs, J. R., J. E. Anderson, D. Hinkley, R. Neelamani, S. Lee, A. Baumstein, and M.-D. Lacasse, 2009, Fast full-wavefield seismic inversion using encoded sources: *Geophysics*, **74**, WCC177–WCC188.

- Kühl, H. and M. D. Sacchi, 2003, Least-squares wave-equation migration for AVP/AVA inversion: *Geophysics*, **68**, 262–273.
- Lailly, P., 1983, The seismic inverse problem as a sequence of before stack migration: Proc. Conf. on Inverse Scattering, Theory and Applications, Expanded Abstracts, Philadelphia, SIAM.
- LeBras, R. and R. W. Clayton, 1988, An iterative inversion of back-scattered acoustic waves: *Geophysics*, **53**, 501–508.
- Lecomte, I., 2008, Resolution and illumination analyses in PSDM: A ray-based approach: *The Leading Edge*, **27**, no. 5, 650–663.
- Lecomte, I. and L.-J. Gelius, 1998, Have a look at the resolution of prestack depth migration for any model, survey and wavefields: SEG Technical Program Expanded Abstracts, **17**, 1112–1115.
- Liu, F., D. W. Hanson, N. D. Whitmore, R. S. Day, and R. H. Stolt, 2006, Toward a unified analysis for source plane-wave migration: *Geophysics*, **71**, no. 4, S129–S139.
- Maurer, H., A. Curtis, and D. E. Boerner, 2010, Recent advances in optimized geophysical survey design: *Geophysics*, **75**, 75A177–75A194.
- Michell, S., E. Shoshitaishvili, D. Chergotis, J. Sharp, and J. Etgen, 2006, Wide azimuth streamer imaging of mad dog: Have we solved the subsalt imaging problem?: 76rd Ann. Internat. Mtg., Expanded Abstracts, 2905–2909, Soc. of Expl. Geophys.
- Mora, P., 1987, Elastic wavefield inversion: PhD thesis, Stanford University.
- , 1989, Inversion = migration + tomography: *Geophysics*, **54**, 1575–1586.
- Nemeth, T., C. Wu, and G. T. Schuster, 1999, Least-squares migration of incomplete reflection data: *Geophysics*, **64**, 208–221.
- Nocedal, J. and S. Wright, 2000, Numerical optimization: Springer Verlag.
- Paffenholz, J., J. Stefani, B. McLain, and K. Bishop, 2002, SIGSBEE 2A Synthetic subsalt dataset - Image quality as function of migration algorithm and velocity model error: 64th Annual International Meeting, European Association of Geoscience Engineers, Extended Abstracts, B019.
- Plessix, R.-E., 2006, A review of the adjoint-state method for computing the gradient of a functional with geophysical applications: *Geophys. J. Int.*, **167**, 495–503.

- Plessix, R.-E. and W. A. Mulder, 2004, Frequency-domain finite-difference amplitude-preserving migration: *Geophys. J. Int.*, **157**, 975–987.
- Pratt, R. G., 1999, Seismic waveform inversion in the frequency domain, Part 1: Theory and verification in a physical scale model: *Geophysics*, **64**, 888–901.
- Pratt, R. G., C. Shin, and G. J. Hicks, 1998, Gauss-Newton and full Newton methods in frequency-space seismic waveform inversion: *Geophys. J. Int.*, **133**, 341–362.
- Prucha, M. L. and B. L. Biondi, 2002, Subsalt event regularization with steering filters: *SEG Technical Program Expanded Abstracts*, **21**, 1176–1179.
- Rickett, J. E., 2003, Illumination-based normalization for wave-equation depth migration: *Geophysics*, **68**, 1371–1379.
- Rickett, J. E. and P. C. Sava, 2002, Offset and angle-domain common image-point gathers for shot-profile migration: *Geophysics*, **67**, 883–889.
- Ristow, D. and T. Rühl, 1994, Fourier finite-difference migration: *Geophysics*, **59**, 1882–1893.
- Romero, L. A., D. C. Ghiglia, C. C. Ober, and S. A. Morton, 2000, Phase encoding of shot records in prestack migration: *Geophysics*, **65**, 426–436.
- Sacchi, M. D. and T. J. Ulrych, 1995, High-resolution velocity gathers and offset space reconstruction: *Geophysics*, **60**, 1169–1177.
- Sava, P., 2004, Migration and velocity analysis by wavefield extrapolation: PhD thesis, Stanford University.
- Sava, P. and B. Biondi, 2004a, Wave-equation migration velocity analysis-I: Theory: *Geophysical Prospecting*, **52**, 593–606.
- , 2004b, Wave-equation migration velocity analysis-II: Examples: *Geophysical Prospecting*, **52**, 607–623.
- Sava, P. and S. Fomel, 2006, Time-shift imaging condition in seismic migration: *Geophysics*, **71**, S209–S217.
- Sava, P. and A. Guitton, 2005, Multiple attenuation in the image space: *Geophysics*, **70**, V10–V20.
- Sava, P. and I. Vlad, 2008, Numeric implementation of wave-equation migration velocity analysis operators: *Geophysics*, **73**, VE145–VE159.
- Sava, P. C. and S. Fomel, 2003, Angle-domain common-image gathers by wavefield

- continuation methods: *Geophysics*, **68**, 1065–1074.
- Shen, P., 2004, Wave-equation migration velocity analysis by differential semblance optimization: PhD thesis, Rice University.
- Shen, P. and W. W. Symes, 2008, Automatic velocity analysis via shot profile migration: *Geophysics*, **73**, VE49–VE59.
- Shen, P., W. W. Symes, S. Morton, A. Hess, and H. Calandra, 2005, Differential semblance velocity analysis via shot profile migration: *SEG Technical Program Expanded Abstracts*, **24**, 2249–2252.
- Sjoeberg, T. A., L.-J. Gelius, and I. Lecomte, 2003, 2-D deconvolution of seismic image blur: *SEG Technical Program Expanded Abstracts*, **22**, 1055–1058.
- Soubaras, R. and B. Gratacos, 2007, Velocity model building by semblance maximization of modulated-shot gathers: *Geophysics*, **72**, U67–U73.
- Stoffa, P. L., J. T. Fokkema, R. M. de Luna Freire, and W. P. Kessinger, 1990, Split-step Fourier migration: *Geophysics*, **55**, 410–421.
- Stolt, R. H. and A. Benson, 1986, *Seismic migration: Theory and practice*: Geophysical Press.
- Stork, C., 1992, Reflection tomography in the postmigrated domain: *Geophysics*, **57**, 680–692.
- Stork, C. and J. Kapoor, 2004, How many P values do you want to migrate for delayed shot wave equation migration?: *SEG Technical Program Expanded Abstracts*, **23**, 1041–1044.
- , 2006, On “Delayed-shot 3D depth migration”: *Geophysics*, **71**, no. 5, X25–X27.
- Symes, W. W., 2008, Approximate linearized inversion by optimal scaling of prestack depth migration: *Geophysics*, **73**, R23–R35.
- Symes, W. W. and J. J. Carazzone, 1991, Velocity inversion by differential semblance optimization: *Geophysics*, **56**, 654–663.
- Tang, Y., 2007, Selective stacking in the reflection-angle and azimuth domain: *SEG Technical Program Expanded Abstracts*, **26**, 2320–2324.
- , 2008, Modeling, migration and inversion in the generalized source and receiver domain: **SEP-136**, 97–112.

- , 2009, Target-oriented wave-equation least-squares migration/inversion with phase-encoded Hessian: *Geophysics*, **74**, WCA95–WCA107.
- Tang, Y. and B. Biondi, 2009, Least-squares migration/inversion of blended data: SEG Technical Program Expanded Abstracts, **28**, 2859–2863.
- , 2011, Target-oriented wavefield tomography using synthesized Born data: *Geophysics*, Accepted.
- Tang, Y., C. Guerra, and B. Biondi, 2008, Image-space wave-equation tomography in the generalized source domain: **SEP-136**, 1–22.
- Tang, Y. and S. Lee, 2010, Preconditioning full waveform inversion with phase-encoded Hessian: SEG Technical Program Expanded Abstracts, **29**, 1034–1038.
- Tarantola, A., 1984, Inversion of seismic reflection data in the acoustic approximation: *Geophysics*, **49**, 1259–1266.
- , 1987, *Inverse problem theory: Methods for data fitting and model parameter estimation*: Elsevier.
- Trad, D. O., T. J. Ulrych, and M. D. Sacchi, 2002, Accurate interpolation with high-resolution time-variant radon transforms: *Geophysics*, **67**, 644–656.
- Valenciano, A., 2008, *Imaging by wave-equation inversion*: PhD thesis, Stanford University.
- Valenciano, A. A., B. Biondi, and A. Guitton, 2006, Target-oriented wave-equation inversion: *Geophysics*, **71**, no. 4, A35–A38.
- van Vliet, L. J. and P. W. Verbeek, 1995, Estimators for orientation and anisotropy in digitized images: *ASCI95, Proc. First Annual Conference of the Advanced School for Computing and Imaging (Heijen, NL, May 16-18)*, *ASCI*, 442–450.
- Vyas, M. and Y. Tang, 2010, Gradients for wave-equation migration velocity analysis: SEG Technical Program Expanded Abstracts, **29**, 4077–4081.
- Whitmore, N. D., 1995, *An imaging hierarchy for common angle plane wave seismogram*: PhD thesis, University of Tulsa.
- Woodward, M., 1989, *Wave equation tomography*: PhD thesis, Stanford University.
- Woodward, M. J., 1992, Wave-equation tomography: *Geophysics*, **57**, 15–26.
- Wu, R.-S. and M. N. Toksöz, 1987, Diffraction tomography and multisource holography applied to seismic imaging: *Geophysics*, **52**, 11–25.

- Xie, X.-B., S. Jin, and R.-S. Wu, 2006, Wave-equation-based seismic illumination analysis: *Geophysics*, **71**, no. 5, S169–S177.
- Yu, J., J. Hu, G. T. Schuster, and R. Estill, 2006, Prestack migration deconvolution: *Geophysics*, **71**, no.2, S53–S62.
- Zhang, Y., J. Sun, C. Notfors, S. H. Gray, L. Chernis, and J. Young, 2005, Delayed-shot 3D depth migration: *Geophysics*, **70**, E21–E28.
- , 2006, Reply to the discussion: *Geophysics*, **71**, no. 5, X27–X29.